

AD-A240 743



2

NAVAL POSTGRADUATE SCHOOL Monterey, California



DTIC
SELECTE
SEP 26 1991
S D

THESIS

HEAT TRANSFER, ADIABATIC EFFECTIVENESS AND INJECTANT DISTRIBUTIONS DOWNSTREAM OF SINGLE AND DOUBLE ROWS OF FILM-COOLING HOLES WITH SIMPLE AND COMPOUND ANGLES.

BY

Salvatore Ciriello Jr.

March 1991

Thesis Advisor:

Phillip M. Ligrani

Approved for public release; distribution is unlimited.

91-11503



9 1 0 2 0 5 3

Unclassified

Security Classification of this page

REPORT DOCUMENTATION PAGE

1a Report Security Classification Unclassified	1b Restrictive Markings
2a Security Classification Authority	3 Distribution Availability of Report Approved for public release; distribution is unlimited.
2b Declassification/Downgrading Schedule	
4 Performing Organization Report Number(s)	5 Monitoring Organization Report Number(s)
6a Name of Performing Organization Naval Postgraduate School	6b Office Symbol <i>(If Applicable)</i> 34
6c Address (city, state, and ZIP code) Monterey, CA 93943-5000	7a Name of Monitoring Organization Naval Postgraduate School
	7b Address (city, state, and ZIP code) Monterey, CA 93943-5000
8a Name of Funding/Sponsoring Organization Wright Aeronautical Laboratories	8b Office Symbol
8c Address (city, state, and ZIP code) Dayton, OH 45433	9 Procurement Instrument Identification Number <i>(If Applicable)</i>
	10 Source of Funding Numbers MIPR FY 1455-89-N0670
	Program Element Number Project No Task No Work Unit Accession No

11 Title (Include Security Classification) **HEAT TRANSFER, ADIABATIC EFFECTIVENESS AND INJECTANT DISTRIBUTIONS DOWNSTREAM OF SINGLE AND DOUBLE ROWS OF FILM-COOLING HOLES WITH SIMPLE AND COMPOUND ANGLES**

12 Personal Author(s) **Salvatore Ciriello Jr.**
13a Type of Report **Master's Thesis** | 13b Time Covered From To | 14 Date of Report (year, month, day) **1991, March 28** | 15 Page Count **288**

16 Supplementary Notation **The views expressed in this thesis are those of the author and do not reflect the official policy or position of the Department of Defense or the U.S. Government.**

17 Cosati Code^a | 18 Subject Terms (continue on reverse if necessary and identify by block number)
Compound Angle Injection, Simple Angle Injection, Film-cooling, Turbulent Boundary Layer

Field	Group	Subgroup

19 Abstract (continue on reverse if necessary and identify by block number)
Experimental results are presented which describe the development and structure of flow downstream of single and double rows of film-cooling holes with both simple and compound angle orientations. Two configurations are investigated, a simple angle injection system in which the injectant is introduced into the freestream parallel to the main flow (as viewed in streamwise/spanwise planes), and a compound angle injection system in which the injectant is introduced with spanwise velocity components. Results indicate that effectiveness depends mostly on four parameters: simple or compound angle injection, spanwise hole spacing, one or two rows of holes, and blowing ratio. In general, for a given m, for all the configurations tested, effectiveness is greatest at low x/d values, and decreases with increasing x/d. As blowing ratio increases, effectiveness generally decreases, particularly at low x/d values because of lift-off effects. Iso-energetic Stanton number ratios vary between 1.0 and 1.25 for all cases, and generally increase with increasing blowing ratio at any given x/d. Effectiveness values measured downstream of two rows of holes are higher than values measured downstream of one row of holes. Adiabatic film-cooling effectiveness data for both the compound angle injection system and the simple angle injection collapse with minimal scatter in η/m vs x_l/s coordinates.

20 Distribution/Availability of Abstract unclassified/unlimited same as report DTIC users | 21 Abstract Security Classification **Unclassified**

22a Name of Responsible Individual **Phillip M. Ligrani** | 22b Telephone (Include Area code) **(408) 646-3382** | 22c Office Symbol **MELi**

Approved for public release; distribution is unlimited.

**Heat Transfer, Adiabatic Effectiveness and Injectant
Distributions Downstream of Single and Double Rows of Film-
Cooling Holes with Simple and Compound Angles.**

by

**Salvatore Ciriello, Jr.
Lieutenant, United States Navy
B.A., Manhattanville College, 1979
M.S., University of Rhode Island, 1982**

Submitted in partial fulfillment of the requirements
for the degree of

**MASTER OF SCIENCE IN MECHANICAL
ENGINEERING**

from the

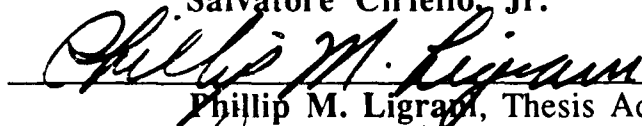
**NAVAL POSTGRADUATE SCHOOL
March 1991**

Author:

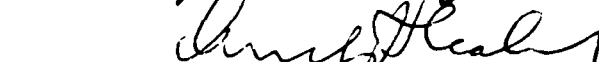


Salvatore Ciriello, Jr.

Approved by:



Phillip M. Ligrani, Thesis Advisor



Anthony J. Healey, Chairman, Department of Mechanical
Engineering

ABSTRACT

Experimental results are presented which describe the development and structure of flow downstream of single and double rows of film-cooling holes with both simple and compound angle orientations. Two configurations are investigated, a simple angle injection system in which the injectant is introduced into the freestream parallel to the main flow (as viewed in streamwise/spanwise planes), and a compound angle injection system in which the injectant is introduced with spanwise velocity components. Results indicate that effectiveness depends mostly on four parameters: simple or compound angle injection, spanwise hole spacing, one or two rows of holes, and blowing ratio. In general, for a given m , for all the configurations tested, effectiveness is greatest at low x/d values, and decreases with increasing x/d . As blowing ratio increases, effectiveness generally decreases, particularly at low x/d values because of lift-off effects. Iso-energetic Stanton number ratios vary between 1.0 and 1.25 for all cases, and generally increase with increasing blowing ratio at any given x/d . Effectiveness values measured downstream of two rows of holes are higher than values measured downstream of one row of holes. Adiabatic film-cooling effectiveness data for both the compound angle injection system and the simple angle injection collapse with minimal scatter in η/m vs xI/s coordinates.



Accession For	NTIS CRA&I DTIC TAB Unannounced Justification	J
By	DTIC	
Availability		
Dist	A-1	

TABLE OF CONTENTS

I. INTRODUCTION.....	1
A. BACKGROUND/THEORY	1
B. PRESENT STUDY	6
C. EXPERIMENTAL OUTLINE	7
D. THESIS ORGANIZATION	8
II. EXPERIMENTAL APPARATUS AND PROCEDURES.....	9
A. WIND TUNNEL	9
B. INJECTION HOLE CONFIGURATION.....	10
C. INJECTION SYSTEM	11
D. HEAT TRANSFER SURFACE	12
E. TEMPERATURE MEASUREMENTS	14
F. MEAN VELOCITY MEASUREMENTS	16
III. EXPERIMENTAL RESULTS.....	18
A. PLATE 1, COMPOUND ANGLE	18
1. Two rows of film-cooling holes with $m=0.5$	18
2. Two rows of film-cooling holes with $m=1.0$	
a. Heat Transfer Measurements.....	18
b. Five Hole Pressure Probe Survey.....	19
c. Injectant Distribution.....	19
3. Two rows of film-cooling holes with $m=1.5$	19
4. Two rows of film-cooling holes with $m=1.74$	20
B. PLATE 2, SIMPLE ANGLE	20
1. One row of film-cooling holes with $m=0.5$	
a. Heat Transfer Measurements.....	20
b. Five Hole Pressure Probe Survey.....	20
c. Injectant Distribution.....	21
2. One row of film-cooling holes with $m=1.0$	

a. Heat Transfer Measurements.....	21
b. Five Hole Pressure Probe Survey.....	21
c. Injectant Distribution.....	21
3. One row of film-cooling holes with $m=1.5$	
a. Heat Transfer Measurements.....	22
b. Five Hole Pressure Probe Survey.....	22
c. Injectant Distribution.....	22
4. Two rows of film-cooling holes with $m=0.5$	
a. Heat Transfer Measurements.....	23
b. Five Hole Pressure Probe Survey.....	23
c. Injectant Distribution.....	23
5. Two rows of film-cooling holes with $m=1.0$	
a. Heat Transfer Measurements.....	24
b. Five Hole Pressure Probe Survey.....	24
c. Injectant Distribution.....	24
6. Two rows of film-cooling holes with $m=1.5$	
a. Heat Transfer Measurements.....	25
b. Five Hole Pressure Probe Survey.....	25
c. Injectant Distribution.....	25
C. COMPARISON OF RESULTS FROM THE SIMPLE ANGLE AND COMPOUND ANGLE FILM-COOLING HOLE CONFIGURATIONS.....	26
D. CORRELATIONS OF ADIABATIC FILM-COOLING EFFECTIVENESS DATA.....	27
E. DIRECT MEASUREMENT OF ADIABATIC FILM-COOLING EFFECTIVENESS.....	28

IV. SUMMARY AND CONCLUSIONS 30
APPENDIX A FIGURES 32
APPENDIX B UNCERTAINTY ANALYSIS 239
APPENDIX C DATA ACQUISITION, PROCESSING
AND PLOTTING PROGRAMS 240
APPENDIX D DATA FILE DIRECTORY..... 243
REFERENCES..... 263
INITIAL DISTRIBUTION LIST..... 265

LIST OF FIGURES

Figure 1. Test Section Coordinate System, Plate 1, Compound Angle	33
Figure 2. Test Section Coordinate System, Plate 2, Simple Angle	34
Figure 3. Top View Schematic of Wind Tunnel Test Section, Plate 1, Compound Angle.....	35
Figure 4. Top View Schematic of Wind Tunnel Test Section, Plate 2, Simple Angle.....	36
Figure 5. Injection Hole Configuration, Compound Angle	37
Figure 6. Injection Hole Configuration, Simple Angle.....	38
Figure 7. Coefficient of Discharge (C_d) versus Reynolds number (Re) for Injection System, Bishop [Ref. 6].....	39
Figure 8. Injectant Temperature versus Plenum Temperature, Bishop [Ref. 6]	40
Figure 9. Baseline Stanton number comparison between Exact Solution and Experimental Measurements, Compound Angle.....	41
Figure 10. Baseline Stanton number comparison between Exact Solution and Experimental Measurements, Simple Angle.....	42
Figure 11. St/St_0 vs θ , Compound Angle, 2 rows, $m=0.5$, $x/d=6.7$, $z=0.0$	43
Figure 12. St/St_0 vs θ , Compound Angle, 2 rows, $m=0.5$, $x/d=17.2$, $z=0.0$	44
Figure 13. St/St_0 vs θ , Compound Angle, 2 rows, $m=0.5$, $x/d=33.1$, $z=0.0$	45
Figure 14. St/St_0 vs θ , Compound Angle, 2 rows, $m=0.5$, $x/d=54.3$, $z=0.0$	46
Figure 15. St/St_0 vs θ , Compound Angle, 2 rows, $m=0.5$, $x/d=75.4$, $z=0.0$	47
Figure 16. St/St_0 vs θ , Compound Angle, 2 rows, $m=0.5$, $x/d=96.6$, $z=0.0$	48
Figure 17. η , vs x/d , Compound Angle, 2 rows, $m=0.5$, Spanwise Average....	49
Figure 18. St_t/St_0 vs x/d , Compound Angle, 2 rows, $m=0.5$, Spanwise Average.....	50
Figure 19. Spanwise Variation of η , Compound Angle, 2 rows, $m=0.5$	51

Figure 20. Spanwise Variation of St/St_0 , Compound Angle, 2 rows, $m=0.5$, $\theta=1.256$	52
Figure 21. Spanwise Variation of St_f/St_0 , Compound Angle, 2 rows, $m=0.5$,...	53
Figure 22. St/St_0 vs θ , Compound Angle, 2 rows, $m=1.0$, $x/d=6.7$, $z=0.0$	54
Figure 23. St/St_0 vs θ , Compound Angle, 2 rows, $m=1.0$, $x/d=17.2$, $z=0.0$	55
Figure 24. St/St_0 vs θ , Compound Angle, 2 rows, $m=1.0$, $x/d=33.1$, $z=0.0$	56
Figure 25. St/St_0 vs θ , Compound Angle, 2 rows, $m=1.0$, $x/d=54.3$, $z=0.0$	57
Figure 26. St/St_0 vs θ , Compound Angle, 2 rows, $m=1.0$, $x/d=75.4$, $z=0.0$	58
Figure 27. St/St_0 vs θ , Compound Angle, 2 rows, $m=1.0$, $x/d=96.6$, $z=0.0$	59
Figure 28. η , vs x/d , Compound Angle, 2 rows, $m=1.0$, Spanwise Average....	60
Figure 29. St_f/St_0 vs x/d , Compound Angle, 2 rows, $m=1.0$, Spanwise Average.....	61
Figure 30. Spanwise Variation of η , Compound Angle, 2 rows, $m=1.0$	62
Figure 31. Spanwise Variation of St/St_0 , Compound Angle, 2 rows, $m=1.0$, $\theta=1.443$	63
Figure 32. Spanwise Variation of St_f/St_0 , Compound Angle, 2 rows, $m=1.0$,...	64
Figure 33. Streamwise Velocity Field, Compound Angle, 2 rows, $m=1.0$, $x/d=11.4$	65
Figure 34. Streamwise Velocity Field, Compound Angle, 2 rows, $m=1.0$, $x/d=45.7$	66
Figure 35. Streamwise Velocity Field, Compound Angle, 2 rows, $m=1.0$, $x/d=87.2$	67
Figure 36. Streamwise Pressure Field, Compound Angle, 2 rows, $m=1.0$, $x/d=11.4$	68
Figure 37. Streamwise Pressure Field, Compound Angle, 2 rows, $m=1.0$, $x/d=45.7$	69
Figure 38. Streamwise Pressure Field, Compound Angle, 2 rows, $m=1.0$, $x/d=87.2$	70
Figure 39. Streamwise Injectant Distribution, Compound Angle, 2 rows, $m=1.0$, $x/d=11.4$	71

Figure 40. Streamwise Injectant Distribution, Compound Angle, 2 rows, m=1.0, x/d=45.7	72
Figure 41. Streamwise Injectant Distribution, Compound Angle, 2 rows, m=1.0, x/d=87.2	73
Figure 42. St/St ₀ vs θ , Compound Angle, 2 rows, m=1.5, x/d=6.7, z=0.0	74
Figure 43. St/St ₀ vs θ , Compound Angle, 2 rows, m=1.5, x/d=17.2, z=0.0	75
Figure 44. St/St ₀ vs θ , Compound Angle, 2 rows, m=1.5, x/d=33.1, z=0.0	76
Figure 45. St/St ₀ vs θ , Compound Angle, 2 rows, m=1.5, x/d=54.3, z=0.0	77
Figure 46. St/St ₀ vs θ , Compound Angle, 2 rows, m=1.5, x/d=75.4, z=0.0	78
Figure 47. St/St ₀ vs θ , Compound Angle, 2 rows, m=1.5, x/d=96.6, z=0.0	79
Figure 48. η , vs x/d, Compound Angle, 2 rows, m=1.5, Spanwise Average....	80
Figure 49. St _f /St ₀ vs x/d, Compound Angle, 2 rows, m=1.5, Spanwise Average.....	81
Figure 50. Spanwise Variation of η , Compound Angle, 2 rows, m=1.5	82
Figure 51. Spanwise Variation of St/St ₀ , Compound Angle, 2 rows, m=1.5, $\theta=1.433$	83
Figure 52. Spanwise Variation of St _f /St ₀ , Compound Angle, 2 rows, m=1.5,...	84
Figure 53. St/St ₀ vs θ , Compound Angle, 2 rows, m=1.74, x/d=6.7, z=0.0	85
Figure 54. St/St ₀ vs θ , Compound Angle, 2 rows, m=1.74, x/d=17.2, z=0.0...	86
Figure 55. St/St ₀ vs θ , Compound Angle, 2 rows, m=1.74, x/d=33.1, z=0.0...	87
Figure 56. St/St ₀ vs θ , Compound Angle, 2 rows, m=1.74, x/d=54.3, z=0.0...	88
Figure 57. St/St ₀ vs θ , Compound Angle, 2 rows, m=1.74, x/d=75.4, z=0.0 ..	89
Figure 58. St/St ₀ vs θ , Compound Angle, 2 rows, m=1.74, x/d=96.6, z=0.0...	90
Figure 59. η , vs x/d, Compound Angle, 2 rows, m=1.74, Spanwise Average ..	91
Figure 60. St _f /St ₀ vs x/d, Compound Angle, 2 rows, m=1.74, Spanwise Average.....	92
Figure 61. Spanwise Variation of η , Compound Angle, 2 rows, m=1.74	93
Figure 62. Spanwise Variation of St/St ₀ , Compound Angle, 2 rows, m=1.74, $\theta=1.355$	94
Figure 63. Spanwise Variation of St _f /St ₀ , Compound Angle, 2 rows,	

$m=1.74,$	95
Figure 64. St/St_0 vs θ , Simple Angle, 1 row, $m=0.5$, $x/d=6.8$, $z=0.0$	96
Figure 65. St/St_0 vs θ , Simple Angle, 1 row, $m=0.5$, $x/d=17.4$, $z=0.0$	97
Figure 66. St/St_0 vs θ , Simple Angle, 1 row, $m=0.5$, $x/d=33.2$, $z=0.0$	98
Figure 67. St/St_0 vs θ , Simple Angle, 1 row, $m=0.5$, $x/d=54.4$, $z=0.0$	99
Figure 68. St/St_0 vs θ , Simple Angle, 1 row, $m=0.5$, $x/d=75.6$, $z=0.0$	100
Figure 69. St/St_0 vs θ , Simple Angle, 1 row, $m=0.5$, $x/d=96.7$, $z=0.0$	101
Figure 70. η , vs x/d , Simple Angle, 1 row, $m=0.5$, Spanwise Average.....	102
Figure 71. St_f/St_0 vs x/d , Simple Angle, 1 row, $m=0.5$, Spanwise Average....	103
Figure 72. Spanwise Variation of η , Simple Angle, 1 row, $m=0.5$	104
Figure 73. Spanwise Variation of St/St_0 , Simple Angle. 1 row, $m=0.5$, $\theta=1.477$	105
Figure 74. Spanwise Variation of St_f/St_0 , Simple Angle, 1 row, $m=0.5$	106
Figure 75. Streamwise Velocity Field, Simple, 1 row, $m=0.5$, $x/d=9.4$	107
Figure 76. Streamwise Velocity Field, Simple Angle, 1 row, $m=0.5$, $x/d=43.7$	108
Figure 77. Streamwise Velocity Field, Simple Angle, 1 row, $m=0.5$, $x/d=85.2$	109
Figure 78. Streamwise Pressure Field, Simple Angle, 1 row, $m=0.5$, $x/d=9.4$	110
Figure 79. Streamwise Pressure Field, Simple Angle, 1 row, $m=0.5$, $x/d=43.7$	111
Figure 80. Streamwise Pressure Field, Simple Angle, 1 row, $m=0.5$, $x/d=85.2$	112
Figure 81. Streamwise Injectant Distribution. Simple Angle, 1 row, $m=0.5$, $x/d=9.4$	113
Figure 82. Streamwise Injectant Distribution, Simple Angle, 1 row, $m=0.5$, $x/d=43.7$	114
Figure 83. Streamwise Injectant Distribution, Simple Angle, 1 row, $m=0.5$, $x/d=85.2$	115

Figure 84. St/St_0 vs θ , Simple Angle, 1 row, $m=1.0$, $x/d=6.8$, $z=0.0$	116
Figure 85. St/St_0 vs θ , Simple Angle, 1 row, $m=1.0$, $x/d=17.4$, $z=0.0$	117
Figure 86. St/St_0 vs θ , Simple Angle, 1 row, $m=1.0$, $x/d=33.2$, $z=0.0$	118
Figure 87. St/St_0 vs θ , Simple Angle, 1 row, $m=1.0$, $x/d=54.4$, $z=0.0$	119
Figure 88. St/St_0 vs θ , Simple Angle, 1 row, $m=1.0$, $x/d=75.6$, $z=0.0$	120
Figure 89. St/St_0 vs θ , Simple Angle, 1 row, $m=1.0$, $x/d=96.7$, $z=0.0$	121
Figure 90. η , vs x/d , Simple Angle, 1 row, $m=1.0$, Spanwise Average.....	122
Figure 91. St_f/St_0 vs x/d , Simple Angle, 1 row, $m=1.0$, Spanwise Average....	123
Figure 92. Spanwise Variation of η , Simple Angle, 1 row, $m=1.0$	124
Figure 93. Spanwise Variation of St/St_0 , Simple Angle, 1 row, $m=1.0$, $\theta=1.644$	125
Figure 94. Spanwise Variation of St_f/St_0 , Simple Angle, 1 row, $m=1.0$	126
Figure 95. Streamwise Velocity Field, Simple, 1 row, $m=1.0$, $x/d=9.4$	127
Figure 96. Streamwise Velocity Field, Simple Angle, 1 row, $m=1.0$, $x/d=43.7$	128
Figure 97. Streamwise Velocity Field, Simple Angle, 1 row, $m=1.0$, $x/d=85.2$	129
Figure 98. Streamwise Pressure Field, Simple Angle, 1 row, $m=1.0$, $x/d=9.4$	130
Figure 99. Streamwise Pressure Field, Simple Angle, 1 row, $m=1.0$, $x/d=43.7$	131
Figure 100. Streamwise Pressure Field, Simple Angle, 1 row, $m=1.0$, $x/d=85.2$	132
Figure 101. Streamwise Injectant Distribution, Simple Angle, 1 row, $m=1.0$, $x/d=9.4$	133
Figure 102. Streamwise Injectant Distribution, Simple Angle, 1 row, $m=1.0$, $x/d=43.7$	134
Figure 103. Streamwise Injectant Distribution, Simple Angle, 1 row, $m=1.0$, $x/d=85.2$	135
Figure 104. St/St_0 vs θ , Simple Angle, 1 row, $m=1.5$, $x/d=6.8$, $z=0.0$	136

Figure 105. St/St_0 vs θ , Simple Angle, 1 row, $m=1.5$, $x/d=17.4$, $z=0.0$	137
Figure 106. St/St_0 vs θ , Simple Angle, 1 row, $m=1.5$, $x/d=33.2$, $z=0.0$	138
Figure 107. St/St_0 vs θ , Simple Angle, 1 row, $m=1.5$, $x/d=54.4$, $z=0.0$	139
Figure 108. St/St_0 vs θ , Simple Angle, 1 row, $m=1.5$, $x/d=75.6$, $z=0.0$	140
Figure 109. St/St_0 vs θ , Simple Angle, 1 row, $m=1.5$, $x/d=96.7$, $z=0.0$	141
Figure 110. η , vs x/d , Simple Angle, 1 row, $m=1.5$, Spanwise Average	142
Figure 111. St_f/St_0 vs x/d , Simple Angle, 1 row, $m=1.5$, Spanwise Average..	143
Figure 112. Spanwise Variation of η , Simple Angle, 1 row, $m=1.5$	144
Figure 113. Spanwise Variation of St/St_0 , Simple Angle, 1 row, $m=1.5$, $\theta=1.626$	145
Figure 114. Spanwise Variation of St_f/St_0 , Simple Angle, 1 row, $m=1.5$	146
Figure 115. Streamwise Velocity Field, Simple, 1 row, $m=1.5$, $x/d=9.4$	147
Figure 116. Streamwise Velocity Field, Simple Angle, 1 row, $m=1.5$, $x/d=43.7$	148
Figure 117. Streamwise Velocity Field, Simple Angle, 1 row, $m=1.5$, $x/d=85.2$	149
Figure 118. Streamwise Pressure Field, Simple Angle, 1 row, $m=1.5$, $x/d=9.4$	150
Figure 119. Streamwise Pressure Field, Simple Angle, 1 row, $m=1.5$, $x/d=43.7$	151
Figure 120. Streamwise Pressure Field, Simple Angle, 1 row, $m=1.5$, $x/d=85.2$	152
Figure 121. Streamwise Injectant Distribution, Simple Angle, 1 row, $m=1.5$, $x/d=9.4$	153
Figure 122. Streamwise Injectant Distribution, Simple Angle, 1 row, $m=1.5$, $x/d=43.7$	154
Figure 123. Streamwise Injectant Distribution, Simple Angle, 1 row, $m=1.5$, $x/d=85.2$	155
Figure 124. St/St_0 vs θ , Simple Angle, 2 rows, $m=0.5$, $x/d=6.8$, $z=0.0$	156
Figure 125. St/St_0 vs θ , Simple Angle, 2 rows, $m=0.5$, $x/d=17.4$, $z=0.0$	157

Figure 126. St/St_0 vs θ , Simple Angle, 2 rows, $m=0.5$, $x/d=33.2$, $z=0.0$	158
Figure 127. St/St_0 vs θ , Simple Angle, 2 rows, $m=0.5$, $x/d=54.4$, $z=0.0$	159
Figure 128. St/St_0 vs θ , Simple Angle, 2 rows, $m=0.5$, $x/d=75.6$, $z=0.0$	160
Figure 129. St/St_0 vs θ , Simple Angle, 2 rows, $m=0.5$, $x/d=96.7$, $z=0.0$	161
Figure 130. η , vs x/d , Simple Angle, 2 rows, $m=0.5$, Spanwise Average	162
Figure 131. St_f/St_0 vs x/d , Simple Angle, 2 rows, $m=0.5$, Spanwise Average.	163
Figure 132. Spanwise Variation of η , Simple Angle, 2 rows, $m=0.5$	164
Figure 133. Spanwise Variation of St/St_0 , Simple Angle, 2 rows, $m=0.5$, $\theta=1.450$	165
Figure 134. Spanwise Variation of St_f/St_0 , Simple Angle, 2 rows, $m=0.5$	166
Figure 135. Streamwise Velocity Field, Simple, 2 rows, $m=0.5$, $x/d=9.4$	167
Figure 136. Streamwise Velocity Field, Simple Angle, 2 rows, $m=0.5$, $x/d=43.7$	168
Figure 137. Streamwise Velocity Field, Simple Angle, 2 rows, $m=0.5$, $x/d=85.2$	169
Figure 138. Streamwise Pressure Field, Simple Angle, 2 rows, $m=0.5$, $x/d=9.4$	170
Figure 139. Streamwise Pressure Field, Simple Angle, 2 rows, $m=0.5$, $x/d=43.7$	171
Figure 140. Streamwise Pressure Field, Simple Angle, 2 rows, $m=0.5$, $x/d=85.2$	172
Figure 141. Streamwise Injectant Distribution, Simple Angle, 2 rows, $m=0.5$, $x/d=9.4$	173
Figure 142. Streamwise Injectant Distribution, Simple Angle, 2 rows, $m=0.5$, $x/d=43.7$	174
Figure 143. Streamwise Injectant Distribution, Simple Angle, 2 rows, $m=0.5$, $x/d=85.2$	175
Figure 144. St/St_0 vs θ , Simple Angle, 2 rows, $m=1.0$, $x/d=6.8$, $z=0.0$	176
Figure 145. St/St_0 vs θ , Simple Angle, 2 rows, $m=1.0$, $x/d=17.4$, $z=0.0$	177
Figure 146. St/St_0 vs θ , Simple Angle, 2 rows, $m=1.0$, $x/d=33.2$, $z=0.0$	178

Figure 147. St/St_0 vs θ , Simple Angle, 2 rows, $m=1.0$, $x/d=54.4$, $z=0.0$	179
Figure 148. St/St_0 vs θ , Simple Angle, 2 rows, $m=1.0$, $x/d=75.6$, $z=0.0$	180
Figure 149. St/St_0 vs θ , Simple Angle, 2 rows, $m=1.0$, $x/d=96.7$, $z=0.0$	181
Figure 150. η , vs x/d , Simple Angle, 2 rows, $m=1.0$, Spanwise Average	182
Figure 151. St_f/St_0 vs x/d , Simple Angle, 2 rows, $m=1.0$, Spanwise Average.	183
Figure 152. Spanwise Variation of η , Simple Angle, 2 rows, $m=1.0$	184
Figure 153. Spanwise Variation of St/St_0 , Simple Angle, 2 rows, $m=1.0$, $\theta=1.500$	185
Figure 154. Spanwise Variation of St_f/St_0 , Simple Angle, 2 rows, $m=1.0$	186
Figure 155. Streamwise Velocity Field, Simple, 2 rows, $m=1.0$, $x/d=9.4$	187
Figure 156. Streamwise Velocity Field, Simple Angle, 2 rows, $m=1.0$, $x/d=43.7$	188
Figure 157. Streamwise Velocity Field, Simple Angle, 2 rows, $m=1.0$, $x/d=85.2$	189
Figure 158. Streamwise Pressure Field, Simple Angle, 2 rows, $m=1.0$, $x/d=9.4$	190
Figure 159. Streamwise Pressure Field, Simple Angle, 2 rows, $m=1.0$, $x/d=43.7$	191
Figure 160. Streamwise Pressure Field, Simple Angle, 2 rows, $m=1.0$, $x/d=85.2$	192
Figure 161. Streamwise Injectant Distribution, Simple Angle, 2 rows, $m=1.0$, $x/d=9.4$	193
Figure 162. Streamwise Injectant Distribution, Simple Angle, 2 rows, $m=1.0$, $x/d=43.7$	194
Figure 163. Streamwise Injectant Distribution, Simple Angle, 2 rows, $m=1.0$, $x/d=85.2$	195
Figure 164. St/St_0 vs θ , Simple Angle, 2 rows, $m=1.5$, $x/d=6.8$, $z=0.0$	196
Figure 165. St/St_0 vs θ , Simple Angle, 2 rows, $m=1.5$, $x/d=17.4$, $z=0.0$	197
Figure 166. St/St_0 vs θ , Simple Angle, 2 rows, $m=1.5$, $x/d=33.2$, $z=0.0$	198
Figure 167. St/St_0 vs θ , Simple Angle, 2 rows, $m=1.5$, $x/d=54.4$, $z=0.0$	199

Figure 168. St/St_0 vs θ , Simple Angle, 2 rows, $m=1.5$, $x/d=75.6$, $z=0.0$	200
Figure 169. St/St_0 vs θ , Simple Angle, 2 rows, $m=1.5$, $x/d=96.7$, $z=0.0$	201
Figure 170. η , vs x/d , Simple Angle, 2 rows, $m=1.5$, Spanwise Average	202
Figure 171. St_f/St_0 vs x/d , Simple Angle, 2 rows, $m=1.5$, Spanwise Average.	203
Figure 172. Spanwise Variation of η , Simple Angle, 2 rows, $m=1.5$	204
Figure 173. Spanwise Variation of St/St_0 , Simple Angle, 2 rows, $m=1.5$, $\theta=1.574$	205
Figure 174. Spanwise Variation of St_f/St_0 , Simple Angle, 2 rows, $m=1.5$	206
Figure 175. Streamwise Velocity Field, Simple, 2 rows, $m=1.5$, $x/d=9.4$	207
Figure 176. Streamwise Velocity Field, Simple Angle, 2 rows, $m=1.5$, $x/d=43.7$	208
Figure 177. Streamwise Velocity Field, Simple Angle, 2 rows, $m=1.5$, $x/d=85.2$	209
Figure 178. Streamwise Pressure Field, Simple Angle, 2 rows, $m=1.5$, $x/d=9.4$	210
Figure 179. Streamwise Pressure Field, Simple Angle, 2 rows, $m=1.5$, $x/d=43.7$	211
Figure 180. Streamwise Pressure Field, Simple Angle, 2 rows, $m=1.5$, $x/d=85.2$	212
Figure 181. Streamwise Injectant Distribution, Simple Angle, 2 rows, $m=1.5$, $x/d=9.4$	213
Figure 182. Streamwise Injectant Distribution, Simple Angle, 2 rows, $m=1.5$, $x/d=43.7$	214
Figure 183. Streamwise Injectant Distribution, Simple Angle, 2 rows, $m=1.5$, $x/d=85.2$	215
Figure 184. Comparison of η for Compound Angle Injection System at Different Blow Ratios, 1 row	216
Figure 185. Comparison of St_f/St_0 , for Compound Angle Injection System at Different Blow Ratios, 1 row.....	217

Figure 186. Comparison of η for Compound Angle Injection System at Different Blow Ratios, 2 rows	218
Figure 187. Comparison of Stf/Sto , for Compound Angle Injection System at Different Blow Ratios, 2 rows	219
Figure 188. Comparison of η for Simple Angle Injection System at Different Blow Ratios, 1 row	220
Figure 189. Comparison of Stf/Sto , for Simple Angle Injection System at Different Blow Ratios, 1 row	221
Figure 190. Comparison of η for Simple Angle Injection System at Different Blow Ratios, 2 rows	222
Figure 191. Comparison of Stf/Sto , for Simple Angle Injection System at Different Blow Ratios, 2 rows	223
Figure 192. Comparison of η of Compound Angle Injection System to Simple Angle Injection System, 1 row	224
Figure 193. Comparison of Stf/Sto , of Compound Angle Injection System to Simple Angle Injection System, 1 row	225
Figure 194. Comparison of η of Compound Angle Injection System to Simple Angle Injection System, 2 rows	226
Figure 195. Comparison of Stf/Sto , of Compound Angle Injection System to Simple Angle Injection System, 2 rows	227
Figure 196. ETA/m vs XI/s , Compound Angle Injection System vs Simple Angle Injection System, 1 row	228
Figure 197. ETA/m vs XI/s , Compound Angle Injection System vs Simple Angle Injection System, 2 rows	229
Figure 198. ETA/I vs XI/s , Compound Angle Injection System vs Simple Angle Injection System, 1 row	230
Figure 199. ETA/I vs XI/s , Compound Angle Injection System vs Simple Angle Injection System, 2 rows	231
Figure 200. ETA vs $X/(ms)*Re^{-0.25}$, Compound Angle Injection System vs Simple Angle Injection System, 1 row	232

Figure 201. ETA vs $X/(ms) \cdot Re^{-0.25}$, Compound Angle Injection System vs Simple Angle Injection System, 2 rows.....	233
Figure 202. ETA vs Xm/s , Compound Angle Injection System vs Simple Angle Injection System, 1 row	234
Figure 203. ETA vs Xm/s , Compound Angle Injection System vs Simple Angle Injection System, 2 rows.....	235
Figure 204. ETA vs $X/(ms)$, Compound Angle Injection System vs Simple Angle Injection System, 1 row	236
Figure 205. ETA vs $X/(ms)$, Compound Angle Injection System vs Simple Angle Injection System, 2 rows.....	237
Figure 206. η vs x/d . Superposition vs. Direct Measurement.....	238

LIST OF SYMBOLS

- C_d - coefficient of discharge
- C_f - skin friction coefficient
- d - injection hole diameter (0.945 cm)
- h - average heat transfer coefficient
- I - momentum flux ratio, $\frac{\rho_c U_c^2}{\rho_m U_m^2}$
- k - thermal conductivity
- m - blowing ratio, $\frac{\rho_c U_c}{\rho_m U_m}$
- Pr - Prandtl number
- Re - Reynolds number
- s - spanwise hole spacing
- St - Stanton number
- St_f - Iso-energetic Stanton number
- St_0 - Baseline Stanton number, no film cooling
- T - static temperature
- T_{amb} - ambient temperature
- T_{av} - average plate temperature
- T_c - coolant temperature
- T_{inj} - injectant temperature
- T_{plenum} - plenum temperature
- T_w - wall temperature
- T_∞ - freestream temperature

- U - mean velocity
- U' - longitudinal turbulence intensity
- U^+ - turbulent flow parameter
- U_τ - friction velocity
- U_∞ - freestream velocity
- X - downstream distance measured from the leading edge of the boundary layer trip
- x/d - dimensionless streamwise position : streamwise distance measured from the downstream edges of the injection holes divided by the the injection hole diameter
- Y - distance normal to the test surface
- Y^+ - turbulent flow parameter
- Y/δ - non-dimensional height
- Z - spanwise distance measured from the test surface centerline
- Z/d - dimensionless spanwise position

Greek Symbols

- α - thermal diffusivity
- β_1 - complete beta function
- β_{u1} - incomplete beta function
- δ - boundary layer thickness based on the position y where $U=0.99 U_\infty$
- δ_1 - momentum thickness
- δ_2 - energy thickness
- ξ - unheated starting length
- η - adiabatic film cooling effectiveness

ν - kinematic viscosity

θ - non-dimensional temperature, $\frac{T_c - T_\infty}{T_w - T_\infty}$

ρ - density

Subscripts

ad - adiabatic condition

c - coolant

f - film flow

m - freestream

o - stagnation condition

w - wall

∞ - freestream

ACKNOWLEDGMENTS

This research was sponsored by Wright Aeronautical Laboratories, Wright-Patterson Air Force Base, MIPR FY 1455-89-N0670. Program monitor was Dr. Bill Troha.

I wish to express my deep appreciation to Professor Phillip Ligrani who was a very influential and important driving force behind the composition of this study. Dr. Chelakara Subramanian was extremely helpful with his knowledge of computer programming and technical familiarity of all laboratory procedures employed. I wish to thank both Professor Phillip Ligrani and Dr. Subramanian for their patience, guidance and never ending enthusiasm for this study.

In addition, I wish to thank the entire staff of the NPS Department of Mechanical Engineering, especially Thomas H. McCord, Charles E. Crow, Thomas Christian, James T. Scholfield, Mardo Blanco, and Jim Selby who were always willing to lend a hand in the manufacture and repair of equipment at a moments notice. Last, but not least, I am deeply indebted to my wife, Margaret, for her support throughout this research.

I. INTRODUCTION

A. BACKGROUND/THEORY

Current turbine inlet temperatures of gas turbines are approaching 2000 K. These extreme temperatures, in combination with the high rotational speeds, put extraordinary stress on component materials, especially on the blades of the first turbine stage. For long, safe, and reliable operation, an efficient means of cooling these blades is thus a necessity to avoid excessive thermal stresses. Film cooling is one method of protection for these gas turbine surfaces, and is extensively used in commercial and military applications. In the past, simple angle injection has been the film-cooling method employed most frequently on turbine blades, turbine endwalls, combustion chamber linings, and afterburner linings. Simple angle injection refers to situations in which the film is injected with holes inclined to the test surface such that injectant is issued approximately in the direction of the mainstream flow.

More recently, gas turbine components include film holes with compound angle orientations, from which the injectant provides better protection and higher film effectiveness than injectant from simple angle orientations. Compound angle orientations are ones in which the film is injected with holes inclined to the test surface such that the injectant is issued with a spanwise velocity component relative to the mainstream flow. Although film-cooling is a common means of turbine blade protection, there is little data which is available in the archival literature on heat transfer and boundary layer behavior downstream of film cooling holes with compound angle orientations. Some data

does exist, however, and most of this is currently under the category of corporate knowledge.

References 1 through 8 study the effectiveness of film-cooling using single and multiple film-cooling holes. Of these references, 2, 3, 4, 5, 7, and 8, present results on the effects of film-cooling as influenced by embedded, longitudinal vortices. More recently, Mitchell [Ref. 7], studied the effect of embedded vortices on heat transfer downstream of injection holes with compound angle orientations. Bishop [Ref. 6], studied the flow field downstream of injection holes with compound angle orientations without embedded vortices.

In the present study, new Stanton number, iso-energetic Stanton number, adiabatic film effectiveness, mean velocity, mean total pressure, and injectant distribution data are presented and analyzed for the same compound angle configuration used by Bishop [Ref. 6], as well as for a simple angle injection hole configuration. Adiabatic film cooling effectiveness values are determined using linear superposition theory from Stanton number ratios measured at different injection temperatures. This is possible since the three-dimensional energy equation which describes the flow field is linear and homogeneous in its dependent variable, temperature. This equation is of the form :

$$\alpha \left(\frac{\partial^2 T}{\partial x^2} + \frac{\partial^2 T}{\partial y^2} + \frac{\partial^2 T}{\partial z^2} \right) = u \frac{\partial T}{\partial x} + v \frac{\partial T}{\partial y} + w \frac{\partial T}{\partial z} \quad (\text{Equation 1.1})$$

where $\alpha = \frac{k}{\rho c}$. (Equation 1.2)

The technique of superposition was first applied to film cooling by Metzger, Carper and Swank [Ref. 1]. They examined the effect of secondary fluid injection through nontangential slots on the heat transfer in regions near the injection site. They found differences in the various tangential injection geometries employed, as reflected in rather large variations of the adiabatic wall temperature. These authors employ the parameter Φ , which depends on a temperature difference ratio (θ) and a mass velocity ratio (m), to facilitate comparisons of various film cooling schemes. The parameter Φ is defined as :

$$\Phi = \frac{h_{\text{with film injection}}}{h_{\text{without injection}}} = \frac{h}{h_o} \quad (\text{Equation 1.3})$$

In a comment on the Metzger, Carper and Swank paper, E.R.G. Eckert relates Φ to the adiabatic wall temperature (T_{ad}). The adiabatic wall temperature (T_{ad}), is defined as the temperature which the film-cooled wall assumes when the heat flux \dot{q} in the following equation is zero.

$$\dot{q} = h_f A (T_w - T_{ad}) \quad (\text{Equation 1.4})$$

Equation 1.4 relates heat transfer to the difference between the actual wall temperature and the adiabatic wall temperature with the iso-energetic heat transfer coefficient h_f . Under the condition, $\dot{q} = 0$, $T_w = T_{ad}$. The inverse of the adiabatic film-cooling effectiveness is given by:

$$\theta_{ad} = \frac{T_f - T_m}{T_{ad} - T_m} \quad (\text{Equation 1.5})$$

Alternatively,

$$\eta_{ad} = \frac{T_{ad} - T_m}{T_f - T_m} = \frac{1}{\theta_{ad}} \quad (\text{Equation 1.6})$$

Equation 1.4 for heat flux may also be expressed in terms of the difference between the actual wall temperature and the freestream temperature using the equation given by:

$$\dot{q} = hA(T_w - T_m) \quad (\text{Equation 1.7})$$

Setting Equations 1.4 and 1.7 equal then yields:

$$h = h_f \frac{T_w - T_{ad}}{T_w - T_m} \quad (\text{Equation 1.8})$$

Adding and subtracting T_m to the numerator of the temperature term of Equation 1.8 yields:

$$\frac{T_w - T_{ad}}{T_w - T_m} = \frac{(T_w - T_m) - (T_{ad} - T_m)}{(T_w - T_m)} = 1 - \frac{(T_{ad} - T_m)}{(T_w - T_m)} \quad (\text{Equation 1.9})$$

Multiplying numerator and denominator of the right hand term of Equation 1.9 by $(T_f - T_m)$ and using Equation 1.6 then yields:

$$\frac{T_w - T_{ad}}{T_w - T_m} = (1 - \theta \eta_{ad}) \quad (\text{Equation 1.10})$$

Substituting Equation 1.10 into Equation 1.8 finally yields:

$$h = h_f(1 - \theta \eta_{ad}) \quad (\text{Equation 1.11})$$

where;

$$\theta = \frac{T_f - T_m}{T_w - T_m} \quad (\text{Equation 1.12})$$

In this study heat transfer data is normalized with baseline heat transfer coefficients, h_o , obtained with no injectant. Dividing Equation 1.11 by h_o , and then expressing h and h_o in terms of Stanton numbers, St and St_o , Equation 1.11 finally becomes:

$$\frac{St}{St_o} = \frac{St_f}{St_o}(1 - \theta \eta_{ad}) \quad (\text{Equation 1.13})$$

Equation 1.13 is a linear relation between St/St_o and θ . A plot of St/St_o versus θ , gives a straight line with a vertical axis intercept of St_f/St_o , and a horizontal axis intercept of θ_{ad} , provided temperature variations are small enough that fluid properties are invariant with respect to distance. Thus, by extrapolating to the axis intercepts of this straight line, both the iso-energetic Stanton number ratio St_f/St_o , and the adiabatic film cooling effectiveness η_{ad} , can be determined. St_f/St_o is the ratio of the iso-energetic Stanton number to the Stanton number without film-cooling. The iso-energetic Stanton number is based

on the heat transfer coefficient with film cooling when the temperature of the injectant is equal to the temperature of the freestream, $\theta=0$.

Now, if St/St_0 is set equal to zero in Equation 1.13, the case of no heat transfer at the wall, then it then becomes :

$$(1 - \theta\eta_{ad}) = 0 \quad \text{(Equation 1.14)}$$

Thus, adiabatic effectiveness is given by;

$$\eta_{ad} = \frac{1}{\theta} \quad \text{(Equation 1.15)}$$

at the horizontal intercept of the straight line.

B. PRESENT STUDY

The objective of the present work is to determine Stanton numbers at theta values ranging from $\theta=0$, to $\theta=3.0$, at x/d ratios of 6.7, 17.2, 33.1, 54.3, 75.4 and 96.6, for a compound angle injection system, plate 1, and x/d values of 6.8, 17.4, 33.2, 54.4, 75.5, and 96.7 for a simple angle injection system, plate 2. With the compound angle configuration, plate 1, holes are inclined at 35 degrees with respect to the test surface when projected into the streamwise/normal plane, and 30 degrees with respect to the test surface when projected into the spanwise/normal plane. With the simple angle configuration, plate 2, holes are inclined at 35 degrees with respect to the test surface in the streamwise/normal plane. With each configuration, two staggered rows of holes are used. Within each row, holes are spaced 6 hole diameters apart for the simple angle

configuration and 7.8 hole diameters apart for the compound angle configuration. Results presented include distributions of surface heat transfer, adiabatic film cooling effectiveness deduced from heat transfer coefficients using superposition, and injectant distributions. Also presented are plots showing the streamwise development of distributions of mean velocity and mean temperature.

C. EXPERIMENTAL OUTLINE

Three different types of measurements are made in the present study:

1. Heat transfer distributions including Stanton numbers, Stanton number ratios and adiabatic film cooling effectiveness at 21 spanwise locations at x/d ratios of 6.7, 17.2, 33.1, 54.3, 75.4 and 96.6 for plate 1, and x/d ratios of 6.8, 17.4, 33.2, 54.4, 75.5, and 96.7 for plate 2.

2. Mean velocity and total pressure surveys in Y-Z planes at x/d values of 11.4, 45.7, and 87.2 for plate 1, and 9.4, 43.7, and 85.2 for plate 2.

3. Mean temperature ($T - T_{\infty}$) surveys in Y-Z planes at x/d values of 11.4, 45.7, and 87.2 for plate 1, and 9.4, 43.7, and 85.2 for plate 2, to provide information on injectant distributions.

These data are obtained for the ten different injection configurations as well as with no film-cooling. The following configurations are presented: (1) two staggered rows of compound angle film-cooling holes with a blowing ratio of $m=0.5$, (2) two staggered rows of compound angle film-cooling holes with a blowing ratio of $m=1.0$, (3) two staggered rows of compound angle film-cooling holes with a blowing ratio of $m=1.5$, and (4) two staggered rows of compound angle film-cooling holes with a blowing ratio of $m=1.74$, (5) one row of simple angle film-cooling holes with a blowing ratio of $m=0.5$, (6) one row of simple

angle film-cooling holes with a blowing ratio of $m=1.0$, (7) one row of simple angle film-cooling holes with a blowing ratio of $m=1.5$, (8) two staggered rows of simple angle film-cooling holes with a blowing ratio of $m=0.5$, (9) two staggered rows of simple angle film-cooling holes with a blowing ratio of $m=1.0$, and (10) two staggered rows of simple angle film-cooling holes with a blowing ratio of $m=1.5$. (11) No film-cooling.

D. THESIS ORGANIZATION

The remainder of this thesis is organized as follows. Chapter II discusses the experimental apparatus and procedures. Chapter III contains experimental results. Chapter IV then presents a summary and conclusions. Appendix A contains all of the figures. Appendix B gives the uncertainty levels developed by Schwartz [Ref. 8], for the parameters measured and calculated. Appendix C discusses all of the data acquisition, processing and plotting programs developed and used for this thesis. Appendix D contains a data file directory listing the names of all data files contained on micro floppy disks.

II. EXPERIMENTAL APPARATUS AND PROCEDURES

A. WIND TUNNEL

The wind tunnel employed is an open-circuit, subsonic wind tunnel located in the laboratories of the Department of Mechanical Engineering of the Naval Postgraduate School. This is the same wind tunnel described by References 2 through 8. The source of the flow is a variable speed centrifugal blower located at the upstream end. A coarse filter located on the inlet of the blower removes dirt from the surrounding room air. The blower is followed by a diffuser, within which is located a fine grade filter to aid in removal of small air particulates. Four baffle vanes are also contained to minimize noise and flow separation. The inlet air then passes into a header box which contains three screens and a honeycomb to further reduce spatial non-uniformities of the flow. After the header, the flow enters a 16 to 1 ratio nozzle and exits into the wind tunnel test section.

The test section is a rectangular duct 3.05 m long and 0.61 m wide with an adjustable top wall to permit changes in the streamwise pressure gradient. The test section contains the constant heat flux transfer surface as well as the two rows of film-cooling injection holes. For the present study, a zero pressure gradient is maintained along the length of the test section (without the film cooling) to within 0.01 inches of water differential pressure. The freestream velocity is adjustable from 1 m/s to 40 m/s, and the freestream turbulence intensity is approximately 0.1 percent for a freestream velocity of 30 m/s. The boundary layer is tripped near the nozzle exit 1.072 m upstream of the constant heat flux transfer surface for the compound angle injection system, plate 1, and

1.097 m for the simple angle injection system, plate 2. Figures 1 and 2 show the test section coordinate system as well as the locations of the injection holes. Locations of the thermocouple rows within the heated test surface are also shown. Figures 3 and 4 show a top view of the test surface at the injection locations for plates 1 and 2, respectively. When the heat transfer section is in operation, an unheated starting length of 1.072 m exists for plate 1, and 1.097 m for plate 2. The direction of heat transfer is thus from the constant heat flux surface to the air.

B. INJECTION HOLE CONFIGURATION

The injection hole configurations consists of two staggered rows of holes, where each row contains five injection cooling holes with a nominal inside diameter of 0.945 cm. Two injection plates were tested.

Plate 1, a compound angle injection system, is shown in Figures 3 and 5. Within each row of holes, centerlines are spaced $7.8d$ apart in the spanwise direction. Centerlines of holes in separate rows are separated by $5.2d$ in the streamwise direction. The holes in the two rows are staggered, with spanwise distances between hole centerlines from different rows of $3.9d$. The plane of each injection hole is angled at 50.5 degrees from the streamwise/normal (X-Y) plane. Within the plane of each hole, centerlines are oriented at angles of 24 degrees from the X-Z plane of the test surface. When projected into spanwise/normal (Y-Z) planes, holes are inclined at an angle of 30 degrees with respect to the test surface. When projected into streamwise/normal (X-Y) planes, holes are inclined at an angle of 35 degrees from the test surface.

Plate 2, a simple-angle injection system, is shown Figures 4 and 6. Within each row of holes, centerlines are spaced $6d$ apart in the spanwise direction. Centerlines of holes in separate rows are separated by $3.9d$ in the streamwise direction. The holes in the two rows are staggered, with spanwise distances between hole centerlines from different rows of $3.0d$. Planes of each injection hole are contained within the streamwise/normal (X-Y) plane, within which, holes are inclined at an angle of 35 degrees from the test surface.

C. INJECTION SYSTEM

Film coolant is injected from injection holes into the boundary layer developing along the bottom wall of the test section. Air for the film coolant injection is provided by two 1.5 hp DR513 Rotron Blowers, each capable of producing 30 cfm at 2.5 psig. From blowers, air flows through a regulating valve, a Fisher and Porter rotometer, a diffuser, and finally into the injection heat exchanger and plenum chamber. The heat exchanger allows heating of the injectant above the ambient air temperature. The upper surface of the plenum chamber contains ten brass injection tubes, each three inches long, which terminate in the two rows, of five injection cooling holes.

The present injection system is qualified from measurements of discharge coefficients as a function of injection Reynolds number. Bishop [Ref. 6], gives plots of the coefficient of discharge (C_d) versus Reynolds number (Re), one of which is shown in Figure 7. Because the range and magnitudes of these data are as expected, the injection system is considered to be operating normally.

All film cooling parameters, such as the blowing ratio, are calculated using the temperature at the exits of the injection holes, (T_{inj}). Qualification tests,

performed by Bishop [Ref. 6], led to a relation between injection plenum temperature T_{plenum} and T_{inj} . A plot of his results is shown in Figure 8. The equation relating the two temperatures is given by:

$$T_{\text{inj}} (\text{°C}) = 2.2907 + 0.85948 * T_{\text{plenum}} (\text{°C}) \quad (\text{Equation. 2.1})$$

This equation represents an empirical fit to experimental data for blowing ratios ranging from 0 to 1.5, and ranges of injection temperature from 0 to 100 degrees Celsius. With this arrangement, the injection temperature may be calculated after measurement of the plenum temperature.

When only the downstream row of injection holes is used, the upstream holes are plugged and covered with cellophane tape.

D. HEAT TRANSFER SURFACE

The heat transfer test surface is designed to provide constant heat flux over most of its area. This plate is inserted into the bottom wall of the wind tunnel test section such that the upper surface of the plate is maintained level with the test surface and adjacent to the wind tunnel airstream. This is accomplished using height adjustment screws mounted in the plexiglass support frame. The test surface is made of stainless steel foil, with dimensions of 1.3 m x 0.476 m x 0.20 mm. The portion of the foil adjacent to the airstream is coated with seven layers of liquid crystals. Copper-constantan thermocouples are attached to the underside of the stainless steel foil in six rows of 21 thermocouples per row, with a spanwise spacing of 1.27 cm between individual thermocouples. Thermocouple lead wires are embedded in grooves cut into a triple sheet of

0.254 mm thick double sided tape. RTV epoxy is then used to fill spaces around thermocouple lead wires within these grooves. Electrobond epoxy is used to attach a foil heater, with dimensions of 1.0 mm x 1.118 m x 0.438 m and manufactured by the Electrofilm Corporation, to the underside of the double sided tape. The heater is rated at 120 volts and 1500 watts, with interior foil designed to maintain uniform dissipation of heat over the surface of the heater. A 12.7 mm thick Lexan sheet, followed by 25.4 mm of foam insulation, an 82.55 mm thick Styrofoam layer, three sheets of 0.254 mm thick Lexan, and one 9.53 mm thick sheet of balsa wood make up the remaining insulation. A plexiglass support frame then encases the bottom portion of the test surface and provides support. This frame is then mounted on the underside of the wind tunnel.

The energy balance by Ortiz [Ref. 2] is used to determine conductive heat losses from the heat transfer plate. These amount to approximately 1.5 to 2.5 percent of the total power into the heater, whereas radiation losses average about 8.5 percent of the total power. The contact resistance between the thermocouples and the upper foil is given by Joseph [Ref. 9], but later verified by Williams [Ref. 4].

To provide a baseline data check, Stanton numbers, measured without film injection present, are compared to an empirical relationship given by Kays and Crawford [Ref. 10]. This particular relationship represents turbulent boundary layer flow in a zero pressure gradient over a constant heat flux surface just downstream of an unheated starting length. The equation is given by :

$$StPr^{0.4} = 0.03Re^{-0.2} \times \frac{\beta_1(19,109)}{\beta_{u1}(19,109)} \quad (\text{Equation 2.2})$$

Here, β_1 and β_{u1} are the Beta function and the incomplete Beta function, respectively. The term $u1$ is defined as :

$$u1 = 1 - \left(\frac{\xi_1}{X} \right)^{\frac{9}{10}} \quad (\text{Equation 2.3})$$

Equation 2.2 is compared to the baseline data in Figures 9 and 10. For x/d values greater than about 33, experimental data values are within ± 17 percent of Equation 2.2 for plate 1, and within ± 8 percent for plate 2, providing a check on spanwise-averaged Stanton number behavior with no film injection present.

E. TEMPERATURE MEASUREMENTS

All temperature measurements are made using calibrated copper-constantan thermocouples. These include heat transfer surface temperatures, the freestream temperature, local boundary layer temperatures, and the injection plenum temperature. The calibration equation used for heat transfer surface temperatures is given by Ortiz [Ref. 2]. These are connected to channels 1 - 126 of the data acquisition system. The calibration equation for the test bed thermocouples is given by;

$$T(^{\circ}\text{C}) = 0.018205 + 0.025846 * E - 0.000000581 * E * E$$

(Equation 2.7)

where E is in microvolts.

The calibration equation used for the freestream thermocouple is given by Williams [Ref. 4]. This thermocouple is connected to data acquisition channel 147. Its calibration equation is given by;

$$T(^{\circ}\text{C}) = -2.602912 + 32.177745 * E - 5.483059 * E * E + 1.24739 * E * E * E$$

(Equation 2.8)

where E is in millivolts.

Thermocouples employed in the plenum chamber, used to measure film injectant temperatures in the boundary layer, were calibrated by Bishop [Ref. 6]. From this calibration, the polynomial representing temperature as a function of thermocouple output voltage (E-volts) is given by;

$$T(^{\circ}\text{C}) = 0.0858454 + 26017.4569 * E - 740382.8 * E * E + 35639480 * E * E * E$$

(Equation 2.9)

where E is in volts. This same equation applies to all new thermocouples employed. Two are used on channels 149 and 150 for measurement of plenum temperature. One of these same thermocouples is also employed on channel 153 when boundary layer temperatures are measured to determine injection distributions.

Temperature surveys to determine injectant distributions are performed using a thermocouple traversed through the boundary layer in conjunction with a

thermocouple to measure freestream temperature. For these tests, freestream temperature is maintained at ambient temperature while injectant is heated to 50 degrees Celsius in the injection plenum, with no power applied to the heat transfer test plate. For each survey, local temperatures are taken at 800 (20 x 40) locations in the Y-Z plane at a particular x/d location. The spatial resolution between sampling points is 0.508 cm in each direction (Y and Z), and the overall sampling plane dimensions are 10.2 cm x 20.3 cm.

The traversing device consists of spanwise and vertical traversing blocks allowing two degrees of freedom. Each block is mounted on a separate assembly consisting of two steel case hardened support shafts and a 20 thread per inch pitch drive screw. Separate M092-FD310 stepping motors are used to drive each of the two shafts. A two-axis Motion Controller (MITAS), equipped with 2K bytes of memory and a MC68000 16 bit microprocessor controls a motor drive which runs the motors. The motors, controller and drive are manufactured by the Superior Electric Company. Software within a Hewlett-Packard Series 9000 Model 310 computer provides instructions which control operation of the controller and traversing device.

A Hewlett-Packard 3497A Data acquisition/Control Unit with a Hewlett-Packard 3498A extender is used to collect all voltages from the thermocouples used. These units are also controlled by a Hewlett-Packard Series 9000 Model 310 computer.

F. MEAN VELOCITY MEASUREMENTS

A DC-250-24CD five hole pressure probe manufactured by the United Sensors and Control Corporation is used to measure the three mean velocity

components. The pressure probe has a tip diameter of 6.25 mm and is mounted on the automated traversing device discussed in the temperature measurements section above. Calibration characteristics, given by Williams [Ref. 4], are used to convert the pressure coefficients into velocity components. During these surveys, the freestream temperature, heat transfer surface temperatures, and the plenum injectant temperature are maintained at ambient conditions. A separate Celesco model LCVR differential pressure transducer is used to measure the pressure from each of the five ports of the pressure probe. Each transducer has a full scale pressure range of 2.0 cm of differential water pressure. Transducer output signals are converted to D.C. voltage by five Celesco CD-10D carrier demodulators. The converted voltages are then sent to the Hewlett-Packard 3497A Data Acquisition Unit.

III. EXPERIMENTAL RESULTS

Experimental results are presented first for the compound angle injection system, plate 1, and then for the simple angle injection system, plate 2. For plate 2, heat transfer data, velocity/pressure surveys, and injectant distributions are presented for both 1 row and 2 rows of holes at various blowing ratios. For plate 1, heat transfer data are given for all blowing ratios tested, whereas velocity/pressure data and injectant distributions are given only for $m=1.0$.

A. Plate 1, COMPOUND ANGLE

1. Two rows of film cooling holes with $m=0.5$

Figures 11 - 16 present St/St_0 vs θ for $x/d=6.7, 17.2, 33.1, 54.3, 75.4,$ and 96.4 . Figures 17 and 18 present η and Stf/St_0 vs x/d , respectively. Figures 19, 20, and 21 show streamwise and spanwise variations of η , St/St_0 , and Stf/St_0 , respectively. Figure 17 shows that effectiveness is greatest at $x/d=6.7$. As x/d increases, effectiveness drops. Spatially resolved plots of η at $x/d=6.7$ in figure 19 show spanwise periodicity which becomes less pronounced with streamwise development.

2. Two rows of film cooling holes with $m=1.0$

a. Heat Transfer Measurements.

Figures 22 - 27 present St/St_0 vs θ for $x/d=6.7, 17.2, 33.1, 54.3,$ $75.4,$ and 96.4 . Figures 28 and 29 present η and Stf/St_0 vs x/d , respectively. Figures 30, 31, and 32 show streamwise and spanwise variations of η , St/St_0 , and Stf/St_0 , respectively. Spatially resolved plots of η at $x/d=6.7$ in Figure 30 show spanwise periodicity which becomes less pronounced with streamwise

development. Compared to results from $m=0.5$, effectiveness is higher at x/d values larger than 17.2 due to the larger amounts of injectant. At low x/d , effectiveness is lower than that at $m=0.5$ due to lift-off effects. Again, as x/d increases, effectiveness drops.

b. Five Hole Pressure Probe Survey.

Figures 33, 34, and 35 show streamwise velocity surveys for $x/d=11.4, 45.7,$ and 87.2 . Figures 36, 37, and 38 show total pressure surveys for these same locations. Velocity/pressure deficits are apparent as a result of accumulation of injectant at injectant hole locations. These deficits are non-circular, and spanwise periodic at the wall, existing at x/d values as high as 87.2.

c. Injectant Distributions.

Figures 39, 40, and 41 show temperature survey results which provide information on distributions of injectant. Near the wall, injectant distributions are non-circular, and spanwise periodic across the span of the test surface. Similarity in every other pattern is apparent because of the staggered arrangement of the film-cooling holes in the two rows.

3. Two rows of film cooling holes with $m=1.5$

Figures 42 - 47 present St/St_0 vs θ for $x/d=6.7, 17.2, 33.1, 54.3, 75.4,$ and 96.4 . Figures 48 and 49 present η and Stf/St_0 vs x/d , respectively. Figures 50, 51, and 52 show streamwise and spanwise variations of η , St/St_0 , and Stf/St_0 , respectively. Spatially resolved plots of η at $x/d=6.7$ in Figure 50 show spanwise periodicity which becomes less pronounced with streamwise development. Because of lift-off effects, effectiveness values in Figure 48 drop significantly at $m=1.5$ for x/d values less than about 33.1, compared to data at $m=0.5$. Again effectiveness decreases as x/d increases for each m studied.

4. Two rows of film cooling holes with $m=1.74$

Figures 53 - 58 present St/St_0 vs θ for $x/d=6.7, 17.2, 33.1, 54.3, 75.4,$ and 96.4 . Figures 59 and 60 present η and Stf/St_0 vs x/d , respectively. Figures 61, 62, and 63 show streamwise and spanwise variations of η , St/St_0 , and Stf/St_0 , respectively. Spatially resolved plots of η at $x/d=6.7$ in Figure 61 show spanwise periodicity which becomes less pronounced with streamwise development. As for $m=1.5$ data, effectiveness values drop as lift-off becomes more pronounced.

B. Plate 2, SIMPLE ANGLE

1. One row of film cooling holes with $m=0.5$

a. Heat Transfer Measurements.

Figures 64 - 69 present St/St_0 vs θ for $x/d=6.8, 17.4, 33.2, 54.4, 75.6,$ and 96.7 . Figures 70 and 71 present η and Stf/St_0 vs x/d , respectively. Figures 72, 73, and 74 show streamwise and spanwise variations of η , St/St_0 , and Stf/St_0 , respectively. Spatially resolved plots of η at $x/d=6.8$ in Figure 72 show spanwise periodicity which becomes less pronounced with streamwise development. Effectiveness drops as x/d increases, with low values compared to $m=1.0$ and $m=1.5$ data, due to the limited coverage of the surface by injectant.

b. Five Hole Pressure Probe Surveys.

Figures 75, 76, and 77 show streamwise velocity surveys for $x/d=9.4, 43.7,$ and 85.2 , respectively. Figures 78, 79, and 80 show total pressure surveys at the same locations. Velocity/pressure deficits are apparent as a result of accumulation of injectant at the spanwise positions of hole locations. These deficits are circular, and spanwise periodic at the wall, and exist at x/d values as high as 85.2 .

c. Injectant Distributions.

Figures 81, 82, and 83 show temperature survey results which provide information on distributions of injectant. Injectant distributions are circular, and spanwise periodic near the wall of the test surface.

2. One row of film cooling holes with $m=1.0$

a. Heat Transfer Measurements.

Figures 84 - 89 present St/St_0 vs θ for $x/d=6.8, 17.4, 33.2, 54.4, 75.6,$ and 96.7 . Figures 90 and 91 present η and Stf/St_0 , vs x/d respectively. Figures 92, 93, and 94 show streamwise and the spanwise variations of η , St/St_0 , and Stf/St_0 , respectively. Spatially resolved plots of η at $x/d=6.8$ in Figure 92 show spanwise periodicity which becomes less pronounced with streamwise development. Compared to results for $m=0.5$, effectiveness values are lower due to lift-off effects.

b. Five Hole Pressure Probe Surveys.

Figures 95, 96, and 97 show streamwise velocity surveys for $x/d=9.4, 43.7,$ and 85.2 , respectively. Figures 98, 99, and 100 show total pressure surveys at these same locations. Again, velocity/pressure deficits are apparent as a result of accumulation of injectant at the spanwise locations of injectant holes. Deficits are circular, and spanwise periodic at the wall, and exist at x/d values as high as 85.2 .

c. Injectant Distributions.

Figures 101, 102, and 103 show temperature survey results which provide information on distributions of injectant. Near the wall, injectant distributions are circular, and spanwise periodic across the span of the test

surface. Injectant distribution patterns show concentrations of injectant which are positioned higher off the test surface compared to results for $m=0.5$.

3. One row of film cooling holes with $m=1.5$

a. Heat Transfer Measurements.

Figures 104 - 109 present St/St_0 vs θ for $x/d=6.8, 17.4, 33.2, 54.4, 75.6,$ and 96.7 . Figures 110 and 111 present η and Stf/St_0 vs x/d , respectively. Figures 112, 113, and 114, show streamwise and spanwise variations of η , St/St_0 , and Stf/St_0 , respectively. Spatially resolved plots of η at $x/d=6.8$ in Figure 112 show spanwise periodicity which becomes less pronounced with streamwise development. Compared to results for $m=1.0$, effectiveness values are lower due to lift-off effects.

b. Five Hole Pressure Probe Surveys.

Figures 115, 116, and 117 show streamwise velocity surveys for $x/d=9.4, 43.7,$ and 85.2 , respectively. Figures 118, 119, and 120 show total pressure surveys at these same locations. As before, velocity/pressure deficits are apparent as a result of accumulation of injectant at the spanwise locations of injectant holes. These deficits are circular, and spanwise periodic at the wall, and exist at x/d values as high as 85.2 .

c. Injectant Distributions.

Figures 121, 122, and 123 show temperature survey results which provide information on distributions of injectant. As before, injectant distributions are circular near the wall, and spanwise periodic across the span of the test surface.

4. Two rows of film cooling holes with $m=0.5$

a. Heat Transfer Measurements.

Figures 124 - 129 present St/St_o vs θ for $x/d=6.8, 17.4, 33.2, 54.4, 75.6,$ and 96.7 . Figures 130 and 131 present η and Stf/St_o vs x/d , respectively. Figures 132, 133, and 134 show streamwise and spanwise variations of η , St/St_o , and Stf/St_o , respectively. Spatially resolved plots of η at $x/d=6.8$ in Figure 132 show spanwise periodicity which becomes less pronounced with streamwise development. Compared to the results for $m=0.5$ with 1 row of holes, effectiveness is significantly higher due to more thorough coverage by injectant from 2 staggered row of holes.

b. Five Hole Pressure Probe Surveys.

Figures 135, 136, and 137 show streamwise velocity surveys for $x/d=9.4, 43.7,$ and 85.2 , respectively. Figures 138, 139, and 140 show total pressure surveys at these same locations. Again, velocity/pressure deficits are evident at the spanwise positions of injectant holes due to accumulation of injectant. These deficits are circular and spanwise periodic at the wall.

c. Injectant Distributions.

Figures 141, 142, and 143 show temperature survey results which provide information on distributions of injectant. Near the wall, injectant distributions are circular, and spanwise periodic across the span of the test surface. Similarity in every other pattern is apparent because of the staggered arrangement of the film-cooling holes in the two different rows. From these figures, the thorough coverage provided by injectant from two staggered rows of holes is apparent. As x/d increases, injectant from different holes coalesces together to form a continuous protective film over the surface.

5. Two rows of film cooling holes with $m=1.0$

a. Heat Transfer Measurements.

Figures 144 - 149 present St/St_0 vs θ for $x/d=6.8, 17.4, 33.2, 54.4, 75.6,$ and 96.7 . Figures 150 and 151 present η and Stf/St_0 vs x/d , respectively. Figures 152, 153, and 154 show streamwise and spanwise variations of η , St/St_0 , and Stf/St_0 , respectively. Spatially resolved plots of η at $x/d=6.8$ in Figure 152 show spanwise periodicity which becomes less pronounced with streamwise development. Compared to results obtained for $m=0.5$, effectiveness is lower at x/d values below about 54 due to lift-off effects. At higher x/d , effectiveness values are higher than at $m=0.5$ due to the larger amounts of injectant next to the test surface.

b. Five Hole Pressure Probe Surveys.

Figures 155, 156, and 157 show streamwise velocity surveys for $x/d=9.4, 43.7,$ and 85.2 , respectively. Figures 158, 159, and 160 show total pressure surveys for the same locations. Again, velocity/pressure deficits are evident at the spanwise positions of injectant holes due to accumulation of injectant. These deficits are circular and spanwise periodic at the wall.

c. Injectant Distributions.

Figures 161, 162, and 163 show temperature survey results which provide information on distributions of injectant. Again, near the wall, injectant distributions are circular, and spanwise periodic across the span of the test surface. Similarity in every other pattern is apparent because of the staggered nature of the film-cooling holes in the two separate rows. As x/d increases, the injectant from the different holes coalesces together to form a continuous protective film over the surface. Comparing these figures to those obtained at

$m=0.5$, it is evident that lift-off occurs at $x/d=9.4$ for $m=1.0$. Consequently, better surface coverage exists for $m=0.5$ at small x/d . At $x/d=43.7$ and larger, higher effectiveness values evidence better surface coverage at $m=1.0$ than at $m=0.5$.

6. Two rows of film cooling holes with $m=1.5$

a. Heat Transfer Measurements.

Figures 164 - 169 present St/St_0 vs θ for $x/d=6.8, 17.4, 33.2, 54.4, 75.6,$ and 96.7 . Figures 170 and 171 present η and Stf/St_0 vs x/d , respectively. Figures 172, 173, and 174 show streamwise and spanwise variations of η , St/St_0 , and Stf/St_0 , respectively. Spatially resolved plots of η at $x/d=6.8$ in Figure 172 show spanwise periodicity which becomes less pronounced with streamwise development. Compared to results obtained for $m=1.0$, effectiveness is lower at x/d values below 33.2 due to lift-off effects at the higher m . At x/d greater than 33.2, effectiveness values are higher than at $m=1.0$ due to the larger amounts of injectant along the test surface.

b. Five Hole Pressure Probe Surveys.

Figures 175, 176, and 177 present the streamwise velocity surveys for $x/d=9.4, 43.7,$ and 85.2 , respectively. Figures 178, 179, and 180 present total pressure surveys for these same locations. Again, velocity/pressure deficits are evident at the spanwise locations of injection holes due to accumulation of injectant. These deficits are circular and spanwise periodic near the wall.

c. Injectant Distributions.

Figures 181, 182, and 183 show temperature survey results which provide information on distributions of injectant. Again, near the wall, injectant distributions are circular, and spanwise periodic across the span of the test

surface. Similarity in every other pattern is apparent because of the staggered nature of the film-cooling holes in the two separate rows.

C. COMPARISON OF RESULTS FROM THE SIMPLE ANGLE AND COMPOUND ANGLE FILM-COOLING HOLE CONFIGURATIONS.

Experimental results for compound angle injection system, plate 1, and for simple angle injection system, plate 2, are compared in this section. The effects of blowing ratio, injectant temperature, and position (x/d) are discussed for results obtained downstream of both one and two rows of holes.

Figure 184 presents effectiveness vs x/d , measured downstream of 1 row of plate 1 compound angle holes for various blowing ratios [Ref. 6]. Figure 185 presents iso-energetic Stanton number ratio vs x/d , measured downstream of 1 row of plate 1 compound angle holes for various blowing ratios [Ref. 6]. Figure 186 presents effectiveness vs x/d , measured downstream of 2 rows of plate 1 compound angle holes for various blowing ratios. Figure 187 presents iso-energetic Stanton number ratio vs x/d , measured downstream of 2 rows of plate 1 compound angle holes for various blowing ratios. Figure 188 presents effectiveness vs x/d , measured downstream of 1 row of plate 2 simple angle holes for various blowing ratios. Figure 189 presents iso-energetic Stanton number ratio vs x/d , measured downstream of 1 row of plate 2 simple angle holes for various blowing ratios. Figure 190 presents effectiveness vs x/d , measured downstream of 2 rows of plate 2 simple angle holes for various blowing ratios. Figure 191 presents iso-energetic Stanton number ratio vs x/d , measured downstream of 2 rows of plate 2 simple angle holes for various blowing ratios.

In general, for a given m , for all the configurations tested, effectiveness is greatest at low x/d values, and decreases with increasing x/d as convection takes place between the injectant and the plate, and as diffusion of the injectant occurs. As blowing ratio increases, effectiveness generally decreases, particularly at low x/d values, as the increase of momentum flux ratio causes lift-off of the injectant from the surface. Iso-energetic Stanton number ratios vary between 1.0 and 1.25 for all cases, and generally increase with increasing blowing ratio at any given x/d . This is probably because of increases of boundary layer turbulence levels. Effectiveness values measured downstream of two rows of holes are higher than values measured downstream of one row of holes. This is evident after comparing Figures 184 and 186 for the compound angle injection system, and 188 and 190 for the simple angle injection system. With two rows of holes, the spanwise distance between holes is half that with one row, and thus, there is significantly more injectant coverage along the test surface.

Figures 192 through 195 present the above data on composite graphs. In Figure 192, effectiveness data are given which are measured downstream of one row of holes. In Figure 194, effectiveness data are given which are measured downstream of two rows of holes. With equal spanwise hole spacing it is expected that the effectiveness of the compound angle injection will be comparable or higher than for the simple angle injection system.

D. CORRELATIONS OF ADIABATIC FILM-COOLING EFFECTIVENESS DATA.

In Figures 196 through 205, adiabatic film-cooling effectiveness data for both the compound angle injection system and the simple angle injection system

are presented in several different types of plots. Log-log coordinates are used in each case. Figures 196 and 197 show η/m vs xI/s . Figures 198 and 199 show η/I vs xI/s . Figures 200 and 201 show η vs $x/(ms)*Re^{*-0.25}$. Figures 202 and 203 show η vs xm/s . In each case, data are given which are measured downstream of one row of holes and two rows of holes. Of these correlations, Figures 196 and 197, η/m vs xI/s , collapse the data with the least amount of scatter.

E. DIRECT MEASUREMENT OF ADIABATIC FILM-COOLING EFFECTIVENESS.

In this section, the adiabatic film-cooling effectiveness determined using the principle of superposition is compared to a direct measurement of the same quantity. The adiabatic film-cooling effectiveness is given by:

$$\eta_{ad} = \frac{T_{ad} - T_m}{T_f - T_m} = \frac{1}{\theta_{ad}} \quad (\text{Equation 1.6})$$

The comparison is made for measurements made downstream of one row of holes with $m=0.5$. For the direct measurement, the injectant is heated to about 50 degrees Celsius, with no power is supplied to the test bed. All temperatures are then measured, including wall temperatures. The adiabatic effectiveness is then calculated using an equation given by:

$$\eta_{ad} = \frac{T_w - T_m}{T_f - T_m} + \frac{Q_{corr}}{h(T_f - T_m)} \quad (\text{Equation 3.1})$$

This equation is based on Mick and Mayle [Ref. 11]. In Equation 3.1, Q_{corr} is the sum of the conduction and radiation flux losses from the test surface:

$$Q_{corr} = Q_{cond} + Q_{rad} + Q_{ccv} \quad (\text{Equation 3.2})$$

Conduction and radiation losses are estimated using equations given by Ortiz [Ref.2]. For conduction;

$$Q_{cond} = 0.683 + 0.954(T_{av} - T_{amb}) - 0.016(T_{av} - T_{amb})^2 \quad (\text{Equation 3.3})$$

For radiation;

$$Q_{rad} = 2.169 \times 10^{-8}(T_{av}^4 - T_{amb}^4) \quad (\text{Equation 3.4})$$

Q_{ccv} in Equation 3.2 accounts for additional convective, radiative, and conductive losses. With this term;

$$\frac{Q_{ccv}}{h(T_f - T_m)} = 0.03 \quad (\text{Equation 3.5})$$

Figure 206 shows effectiveness values from direct measurement to be in agreement with ones determined using superposition. The deviation between direct measurement and superposition, is about 7 percent, except at high x/d values for $m=0.5$, where the deviation is 15 percent.

IV. SUMMARY AND CONCLUSIONS

Experimental results are presented which describe the development and structure of flow downstream of single and double rows of film-cooling holes with both simple and compound angle orientations. Two configurations are investigated, a simple angle injection system in which the injectant is introduced into the freestream parallel to the main flow (as viewed in streamwise/spanwise planes), and a compound angle injection system in which the injectant is introduced with spanwise velocity components. The effects of blowing ratio, injectant temperature, and downstream position are determined.

For plate 1, four configurations are used : (1) two staggered rows of film-cooling holes with a blowing ratio of $m=0.5$, (2) two staggered rows of film-cooling holes with a blowing ratio of $m=1.0$, (3) two staggered rows of film-cooling holes with a blowing ratio of $m=1.5$, and (4) two staggered rows of film-cooling holes with a blowing ratio of $m=1.74$.

For plate 2, six configurations were used: (1) one row of film-cooling holes with a blowing ratio of $m=0.5$, (2) one row of film-cooling holes with a blowing ratio of $m=1.0$, (3) one row of film-cooling holes with a blowing ratio of $m=1.5$, (4) two staggered rows of film-cooling holes with a blowing ratio of $m=0.5$, (5) two staggered rows of film-cooling holes with a blowing ratio of $m=1.0$, and (6) two staggered rows of film-cooling holes with a blowing ratio of $m=1.5$.

Results indicate that effectiveness depends mostly on four parameters: simple or compound angle injection, spanwise hole spacing, one or two rows of holes, and blowing ratio. In general, for a given m , for all the configurations tested, effectiveness is greatest at low x/d values, and decreases with increasing x/d as

convection takes place between the injectant and the plate, and as diffusion of the injectant occurs. As blowing ratio increases, effectiveness generally decreases, particularly at low x/d values, as the increase of momentum flux ratio causes lift-off of the injectant from the surface. Iso-energetic Stanton number ratios vary between 1.0 and 1.25 for all cases, and generally increase with increasing blowing ratio at any given x/d . This is probably because of increases of boundary layer turbulence levels. Effectiveness values measured downstream of two rows of holes are higher than values measured downstream of one row of holes. With two rows of holes, the spanwise distance between holes is half that with one row, and thus, there is significantly more injectant coverage along the test surface. Adiabatic film-cooling effectiveness data for both the compound angle injection system and the simple angle injection collapse with minimal scatter in η/m vs x/d coordinates.

Effectiveness values determined from direct measurement are in agreement with ones determined using superposition. The deviation between these, is about 7 percent, except at high x/d values for $m=0.5$, where the deviation is 15 percent.

APPENDIX A

FIGURES

Appendix A contains all of the figures generated for this thesis. These figures include the test set-up, hole configurations, plots of Stanton numbers versus position, and spanwise plots of velocity, pressure and temperature for the ten configurations used.

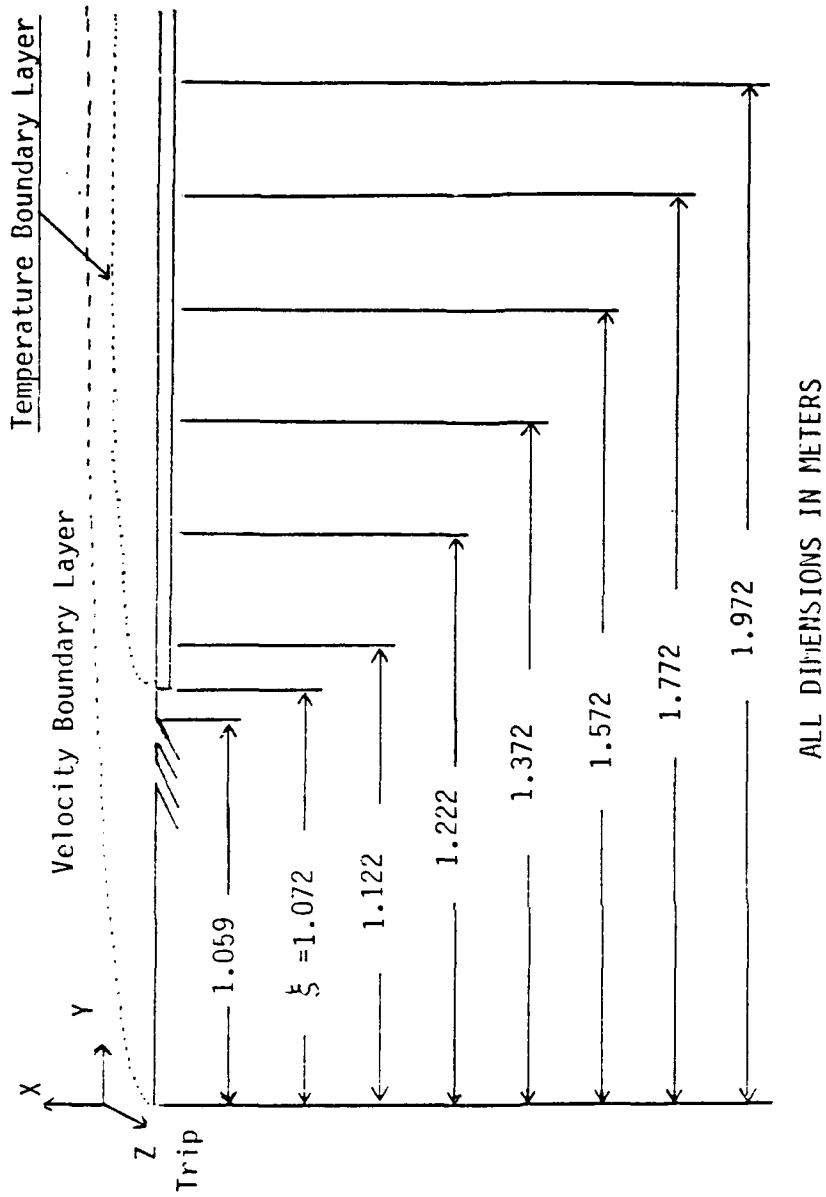


Figure 1. Test Section Coordinate System, Plate I, Compound Angle.

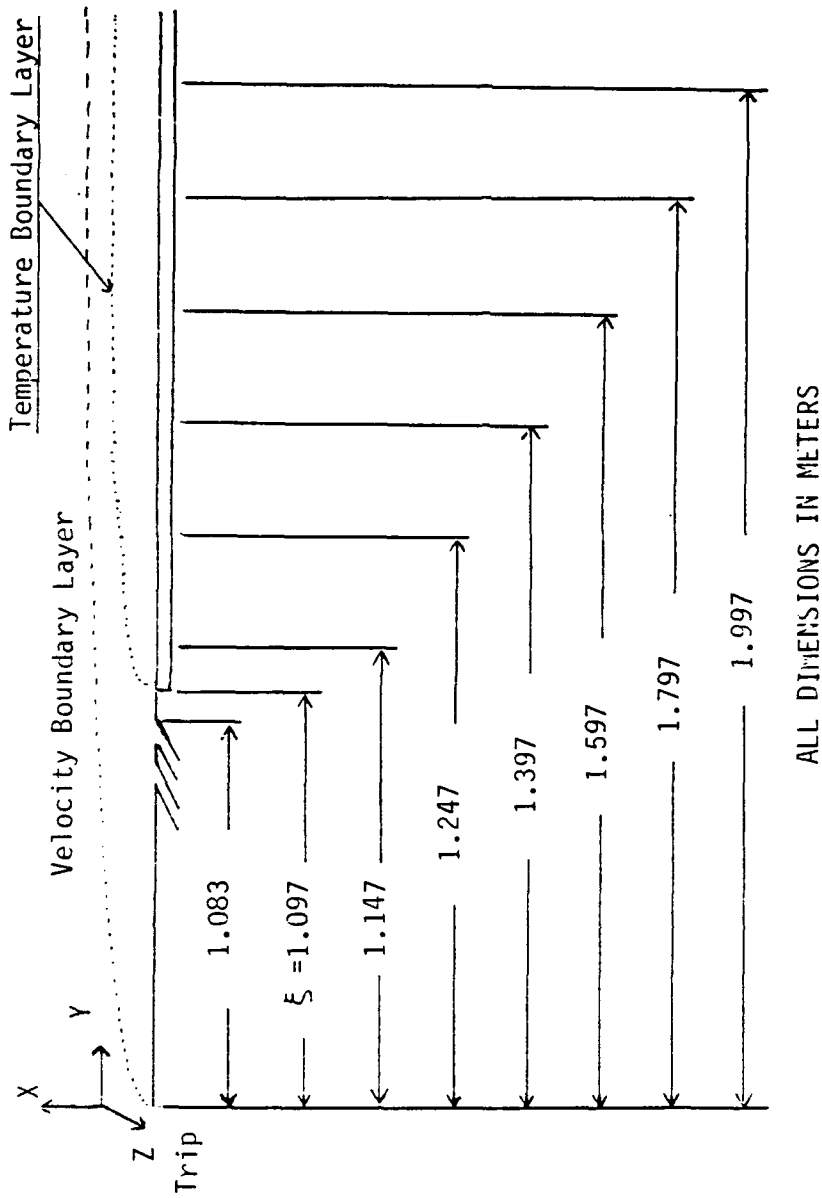


Figure 2. Test Section Coordinate System, Plate I, Simple Angle.

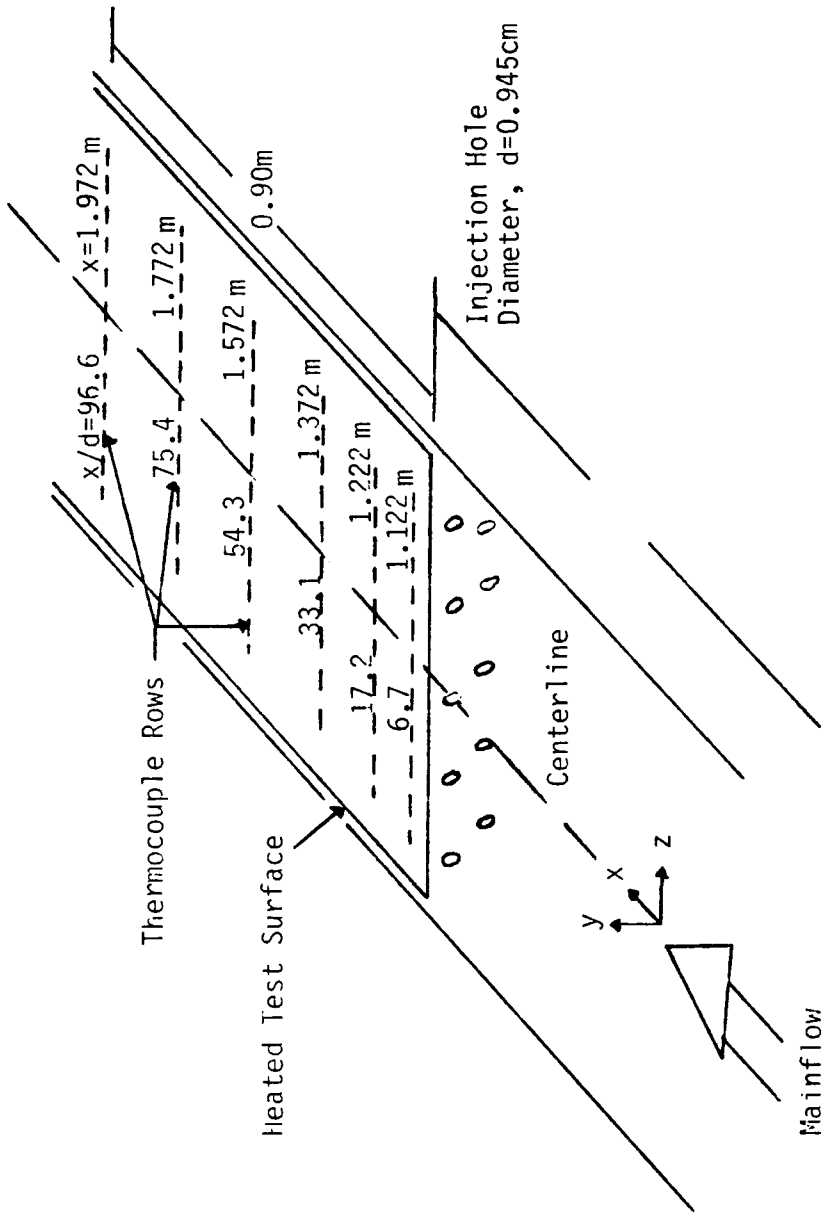


Figure 3. Top View Schematic of Wind Tunnel Test Section, Compound Angle.

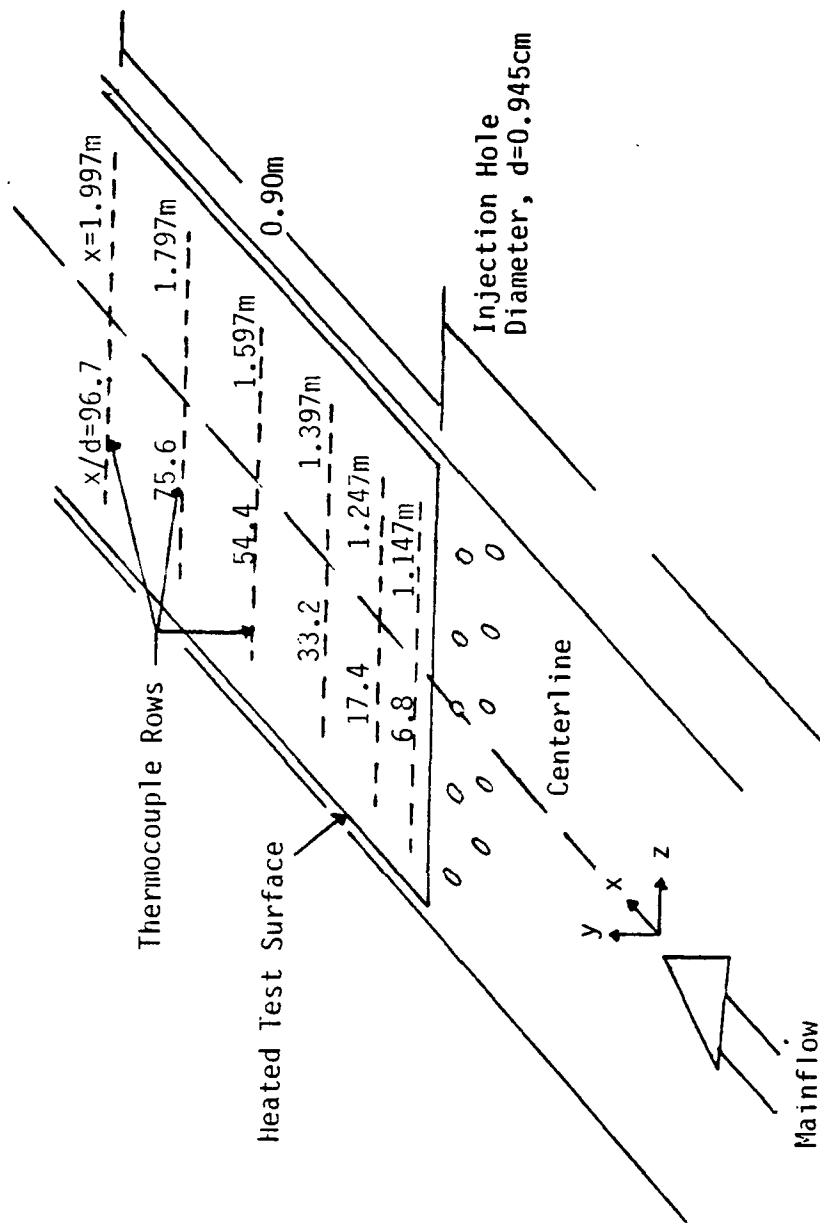


Figure 4. Top View Schematic of Wind Tunnel Test Section, Simple Angle.

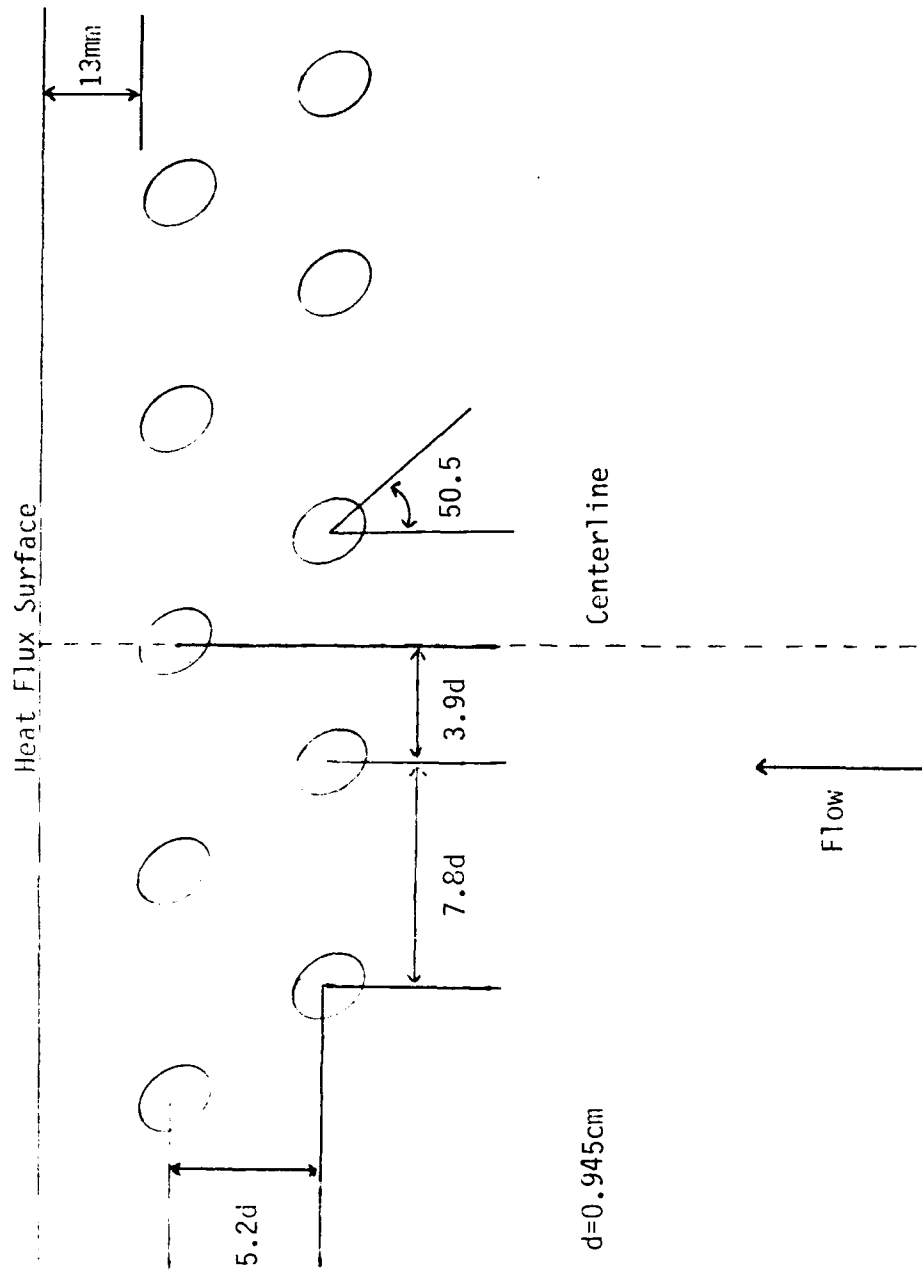


Figure 5. Injection Hole Configuration, Compound Angle.

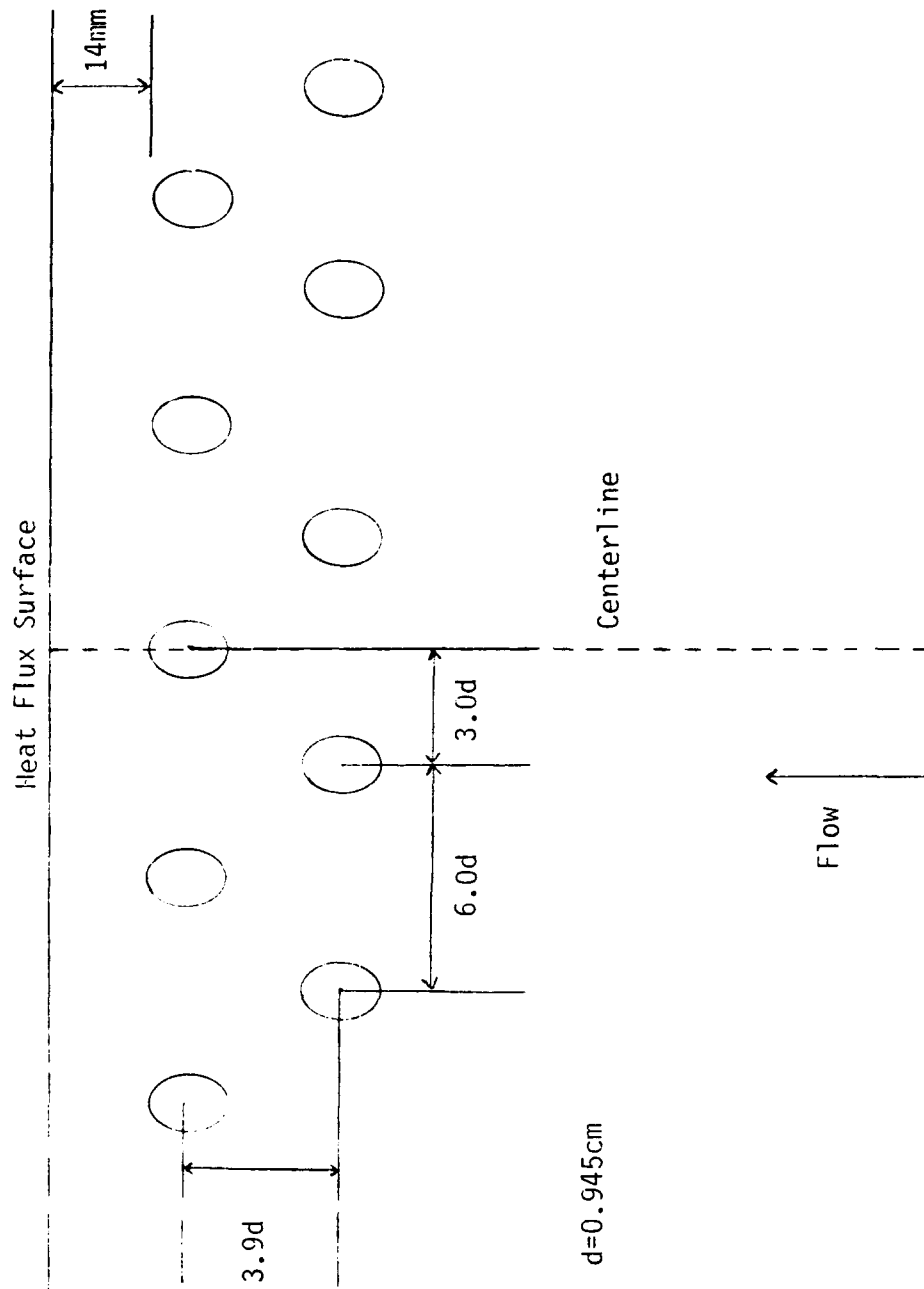


Figure 6. Injection Hole Configuration, Simple Angle.

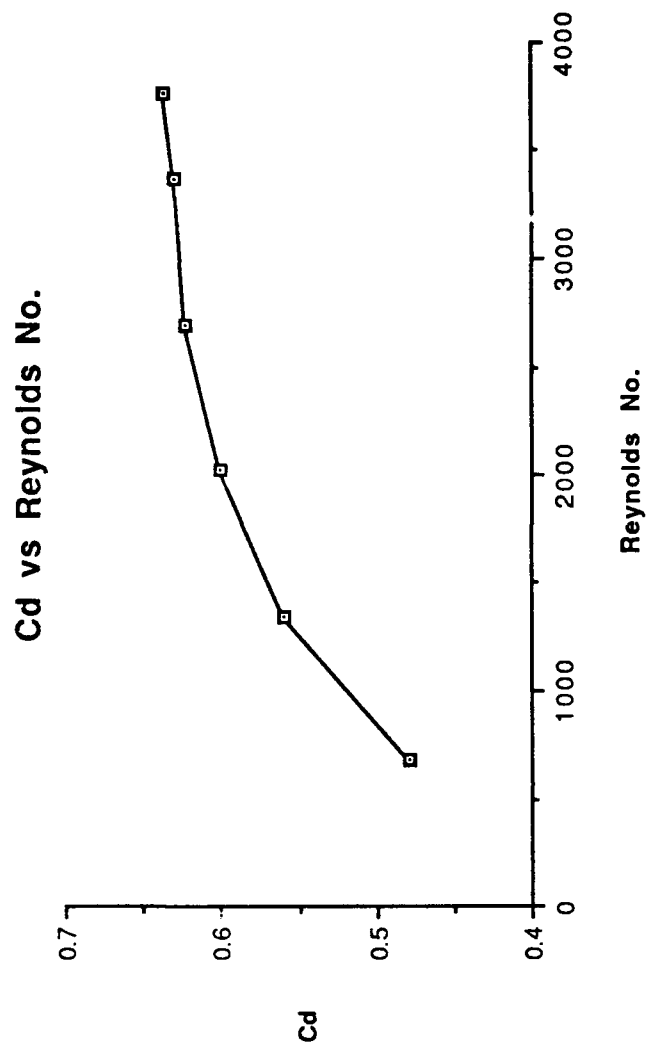


Figure 7. Coefficient of Discharge (C_d) versus Reynolds number (Re) for Injection System, Bishop [Ref. 6].

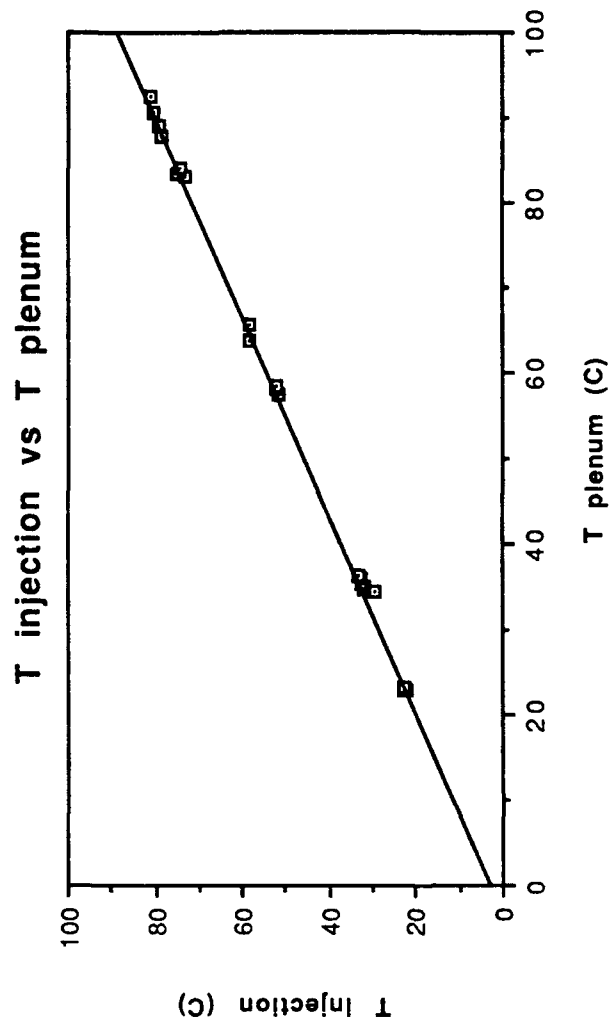


Figure 8. Irjectant Temperature versus Plenum Temperature, Bishop [Ref. 6].

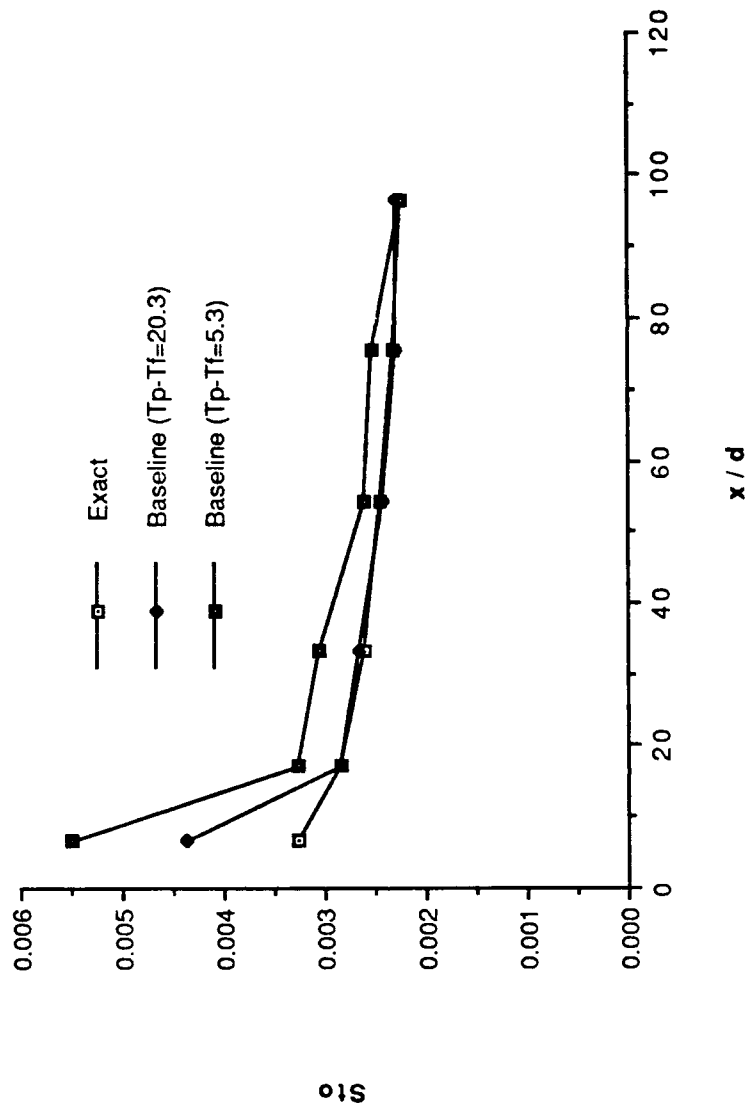


Figure 9. Baseline Stanton number comparison between Exact Solution and Experimental Measurements, Compound Angle.

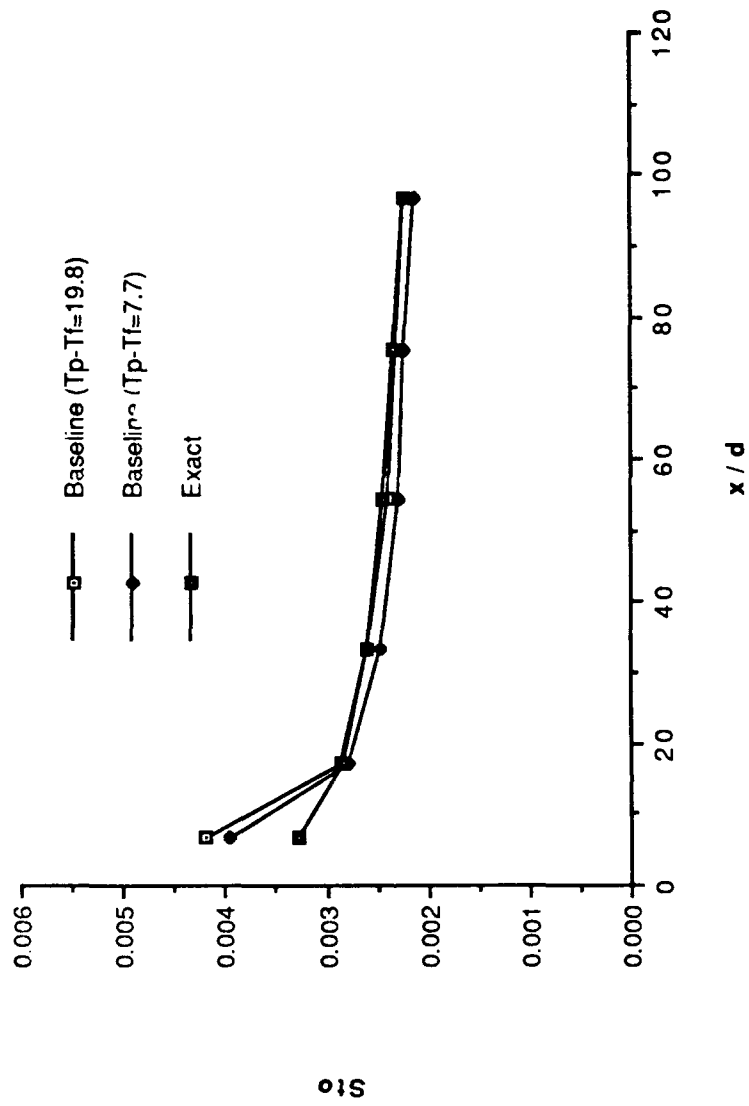


Figure 10. Baseline Stanton number comparison between Exact Solution and Experimental Measurements, Simple Angle.

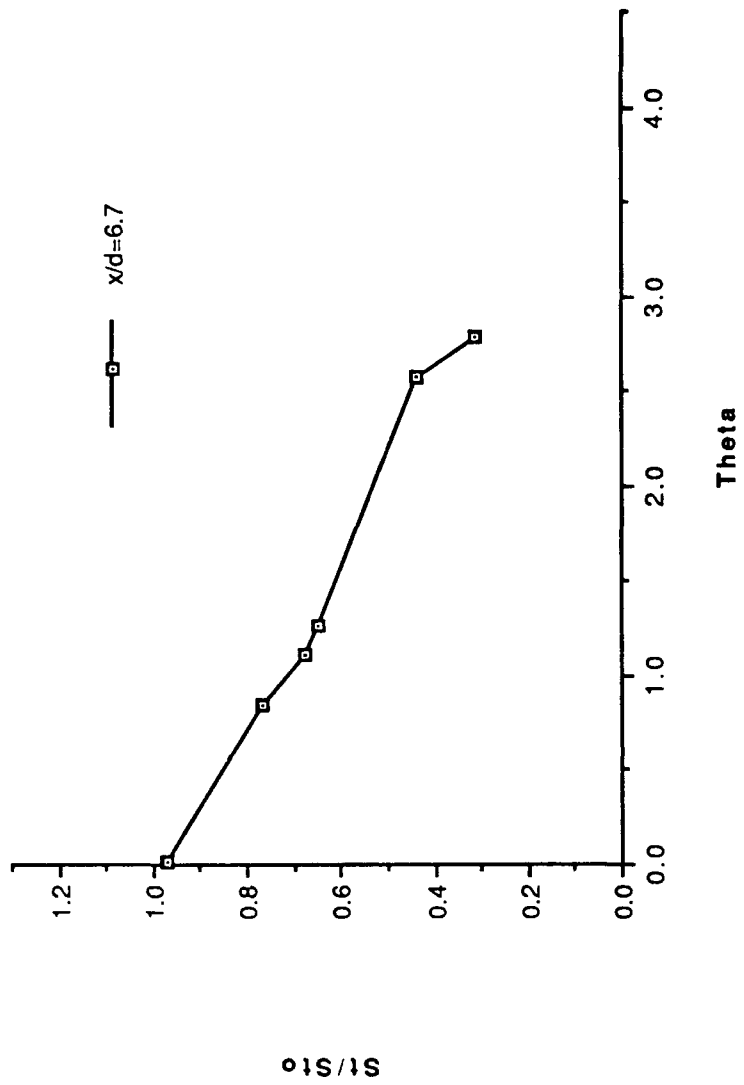


Figure 11. St/St_0 vs θ , Compound Angle, 2 rows, $m=0.5$, $x/d=6.7$, $z=0.0$.

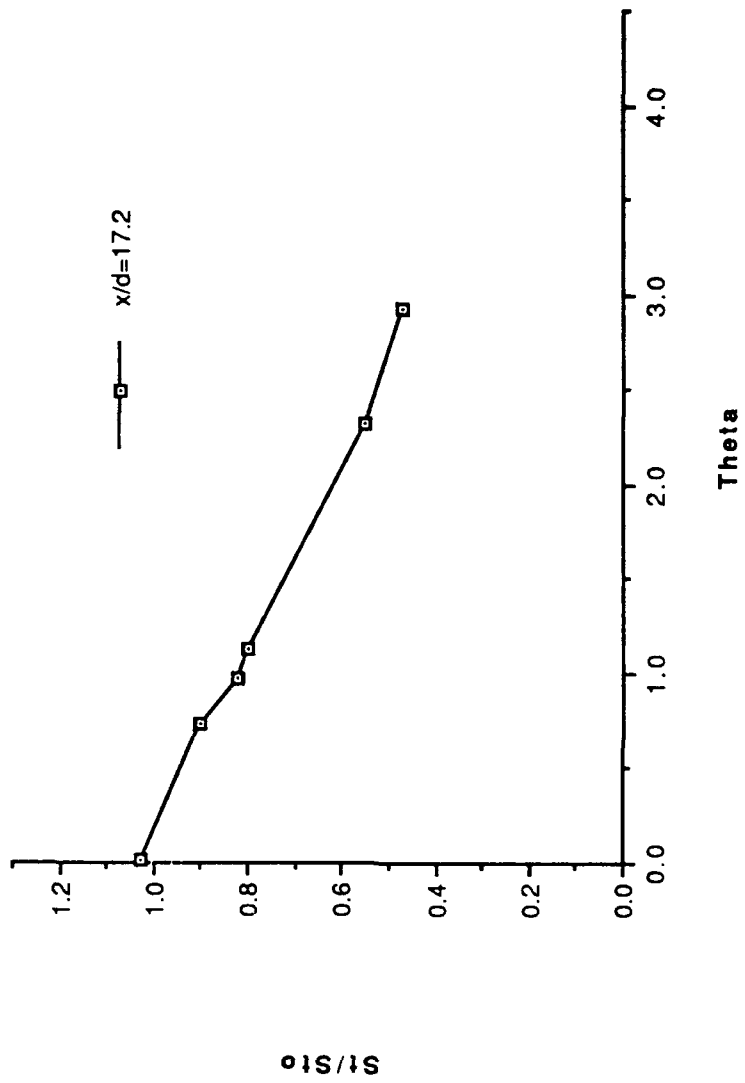


Figure 12. St/St_0 vs θ , Compound Angle, 2 rows, $m=0.5$, $x/d=17.2$, $z=0.0$.

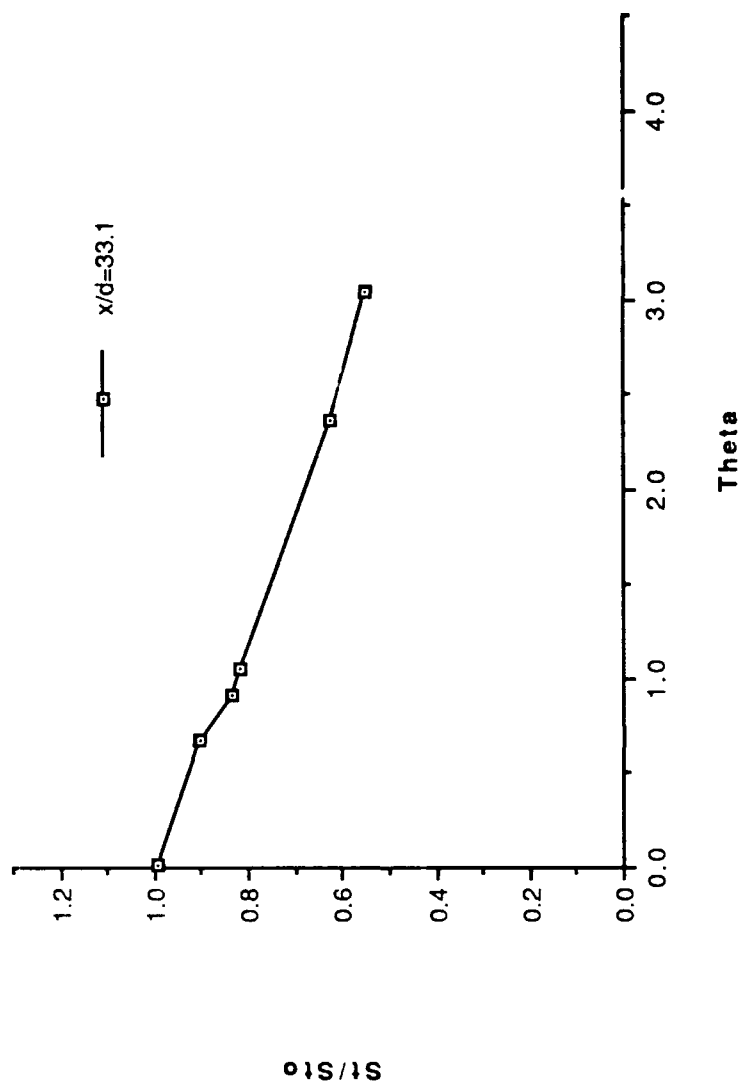


Figure 13. St/St_0 vs θ , Compound Angle, 2 rows, $m=0.5$, $x/d=33.1$, $z=0.0$.

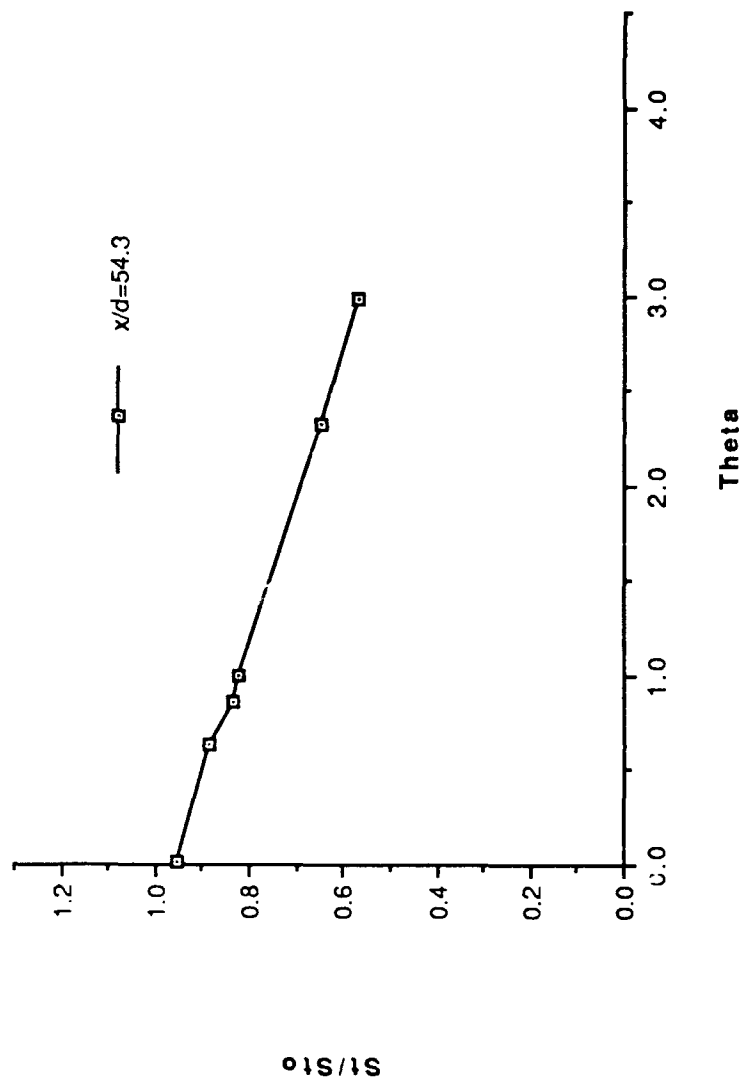


Figure 14. St/St_0 vs θ , Compound Angle, 2 rows, $m=0.5$, $x/d=54.3$, $z=0.0$.

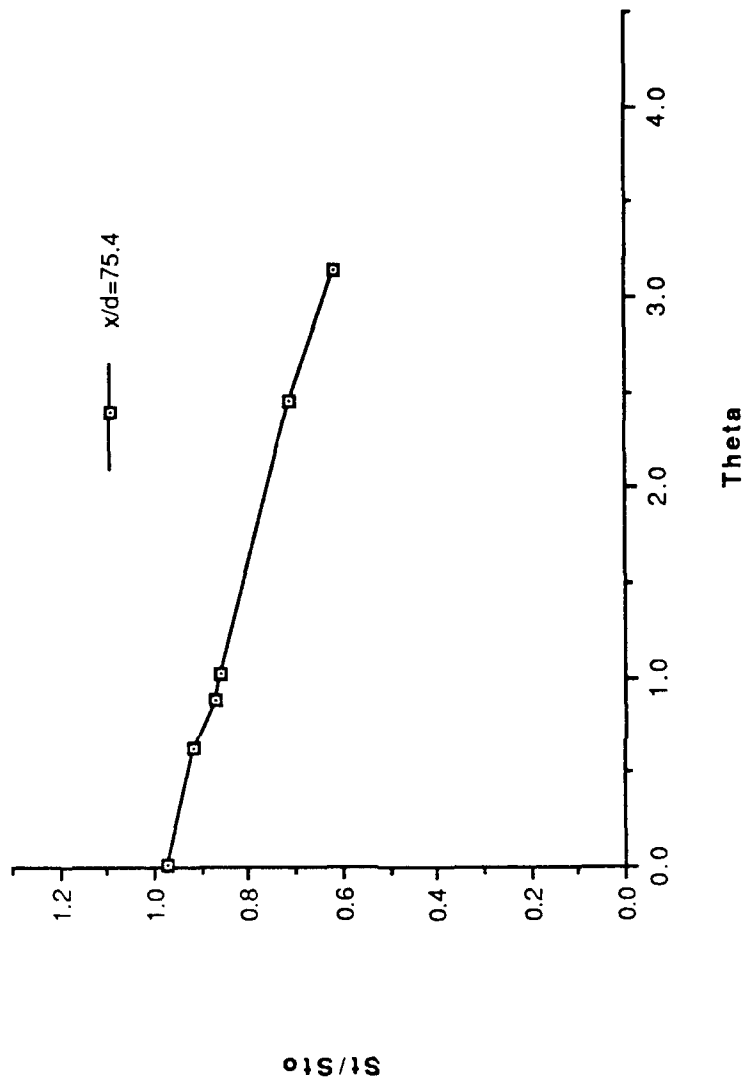


Figure 15. St/St_0 vs θ , Compound Angle, 2 rows, $m=0.5$, $x/d=75.4$, $z=0.0$.

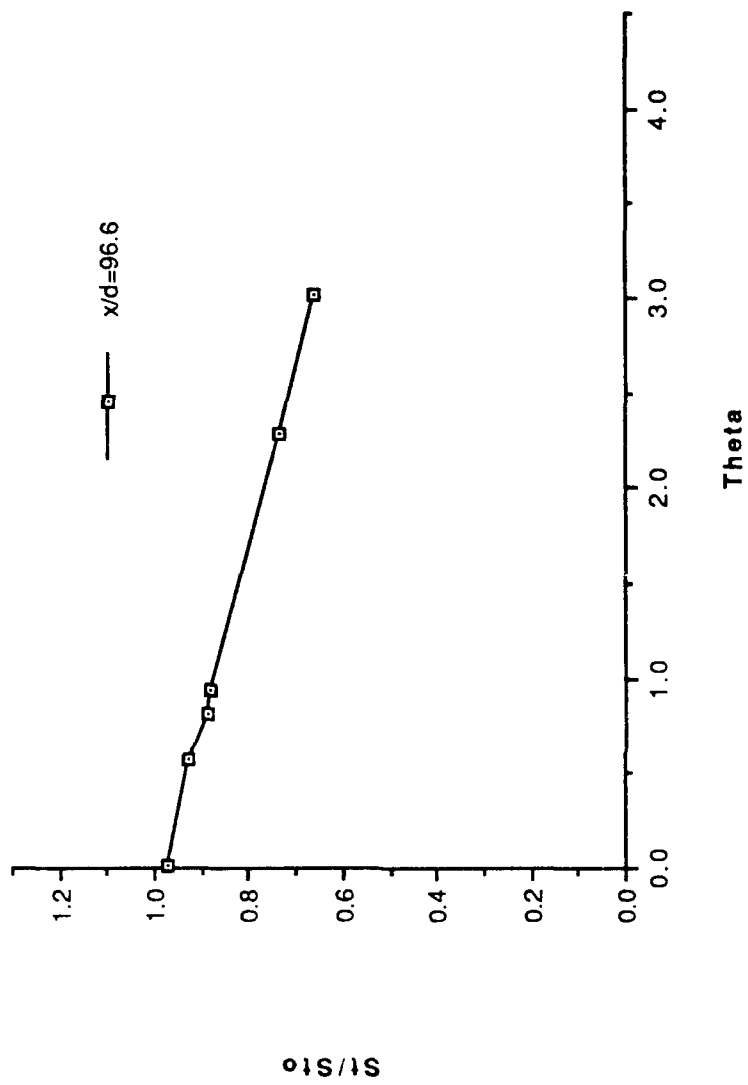


Figure 16. St/St_0 vs θ , Compound Angle, 2 rows, $m=0.5$, $x/d=96.6$, $z=0.0$

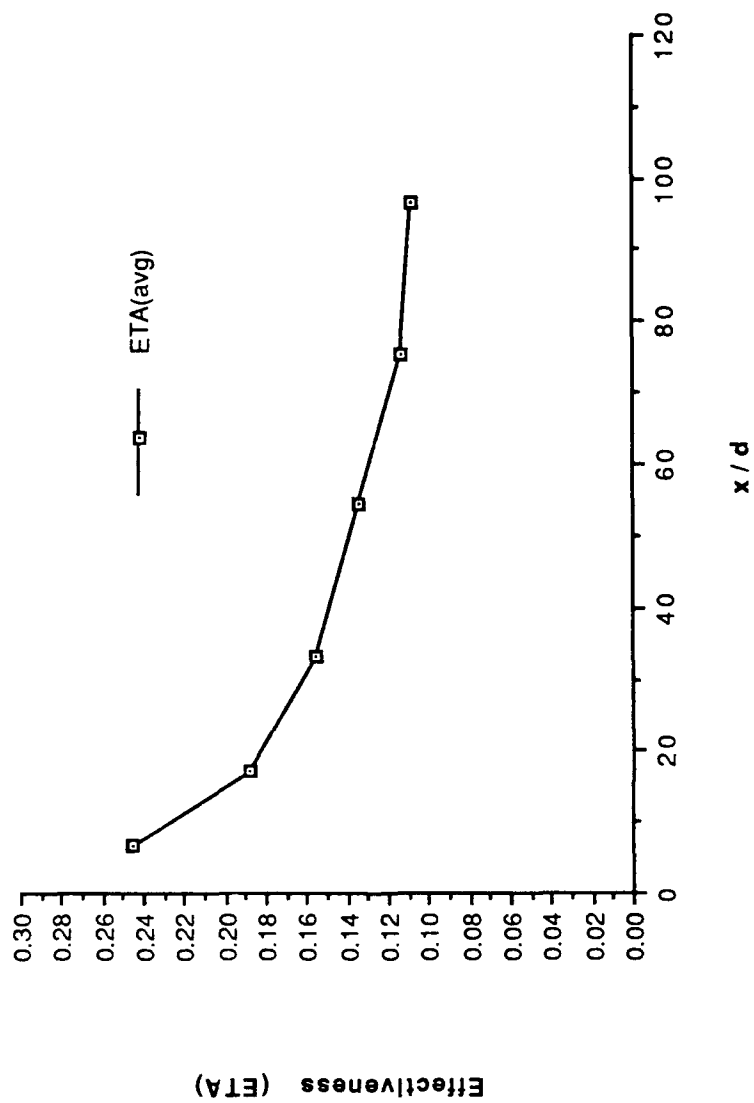


Figure 17. η , vs x/d , Compound Angle, 2 rows, $m=0.5$, Spanwise Average.

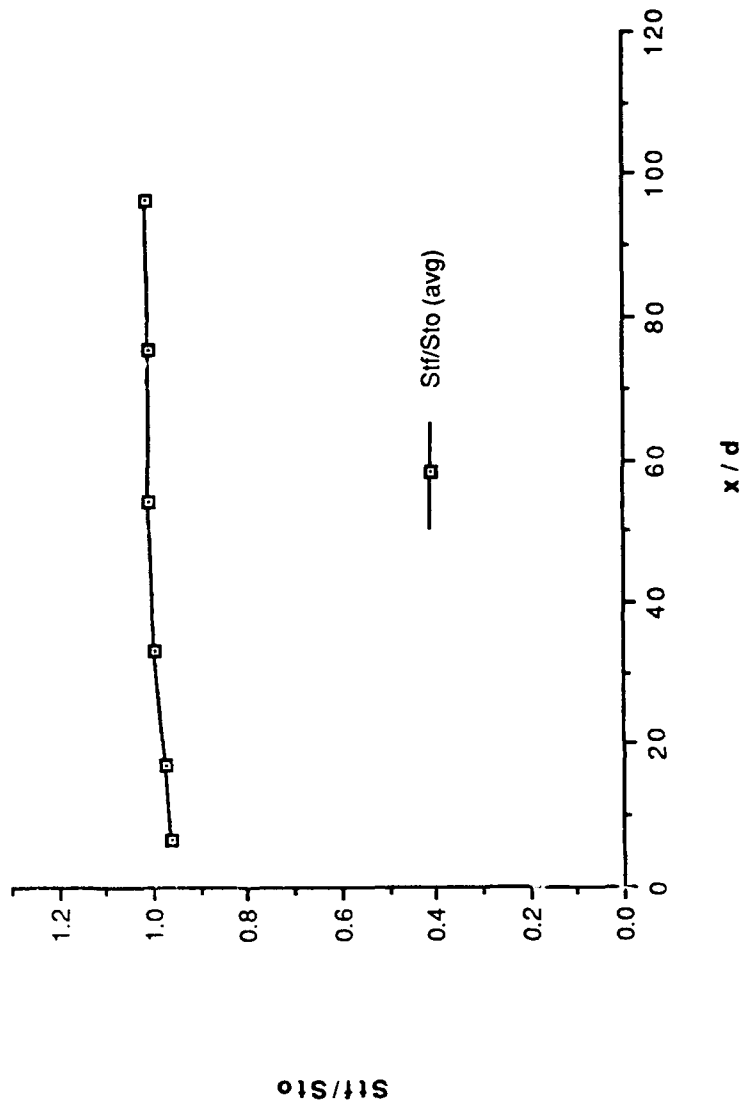


Figure 18. St_f/St_0 vs x/d , Compound Angle, 2 rows, $m=0.5$, Spanwise Average.

FILM-COOLING EFFECTIVENESS

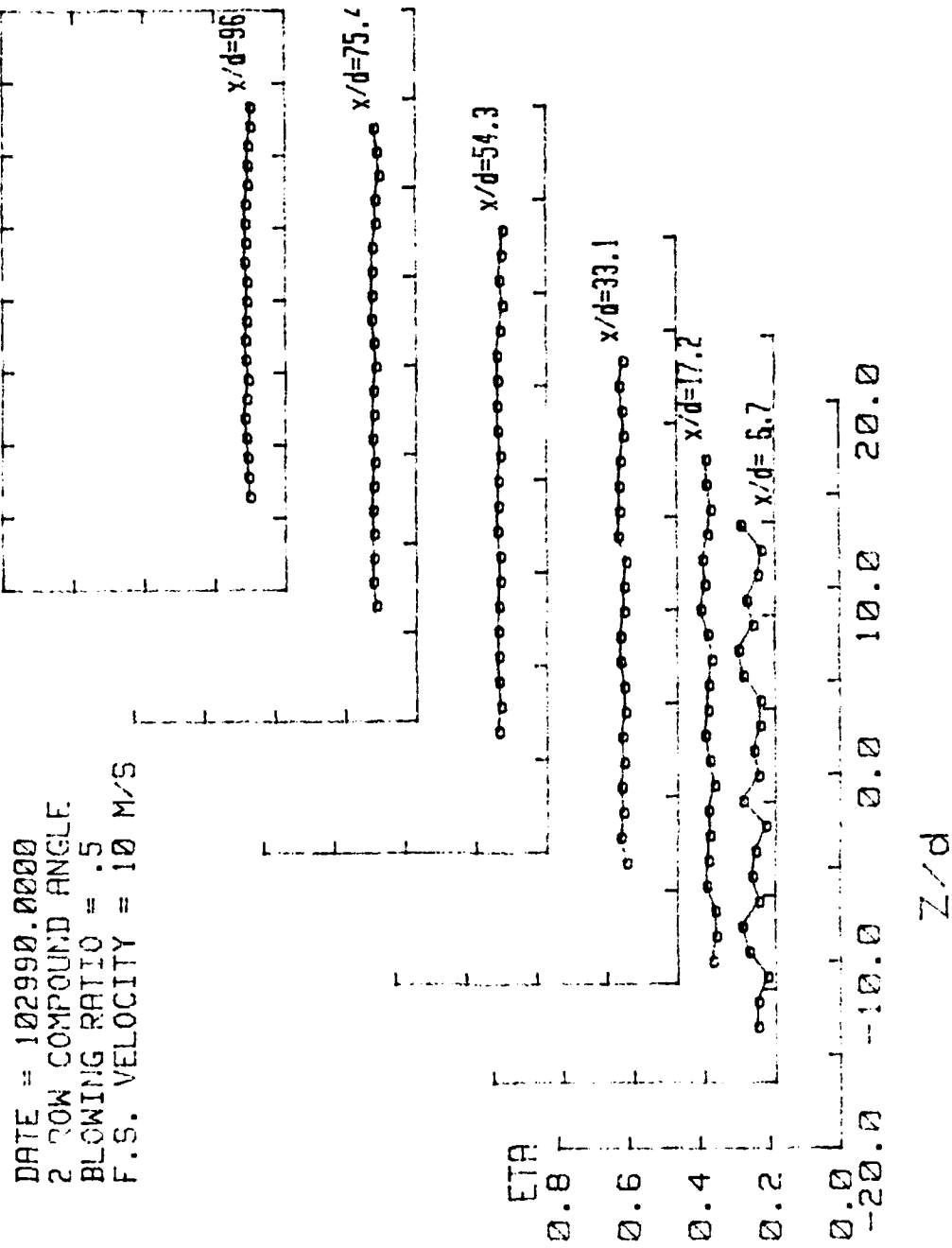


Figure 19. Spanwise Variation of η , Compound Angle, 2 rows, $m=0.5$.

STANTON NUMBER RATIOS

DATE = 102990.1848
 THETA=1.256
 BLOWING RATIO = .5
 F.S. VELOCITY = 10 M/S

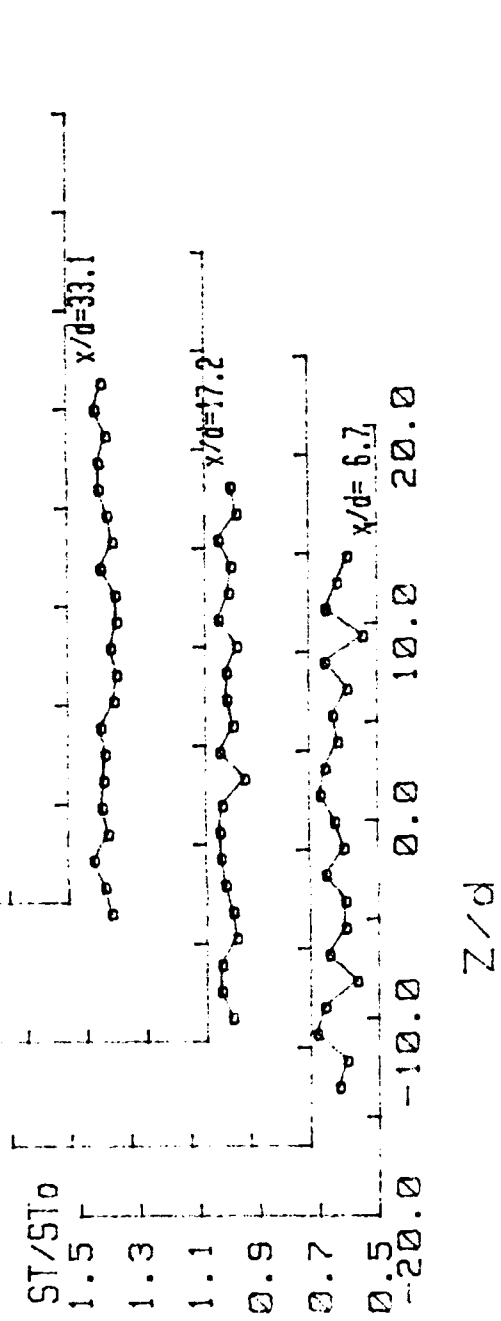


Figure 20. Spanwise Variation of St/St_0 , Compound Angle, 2 rows, $m=0.5$, $\theta=1.256$.

ISO-ENERGETIC STANTON # RATIO

DATE = 102990.0000
 2 ROW COMPOUND ANGLE
 BLOWING RATIO = .5
 F.S. VELOCITY = 10 M/S

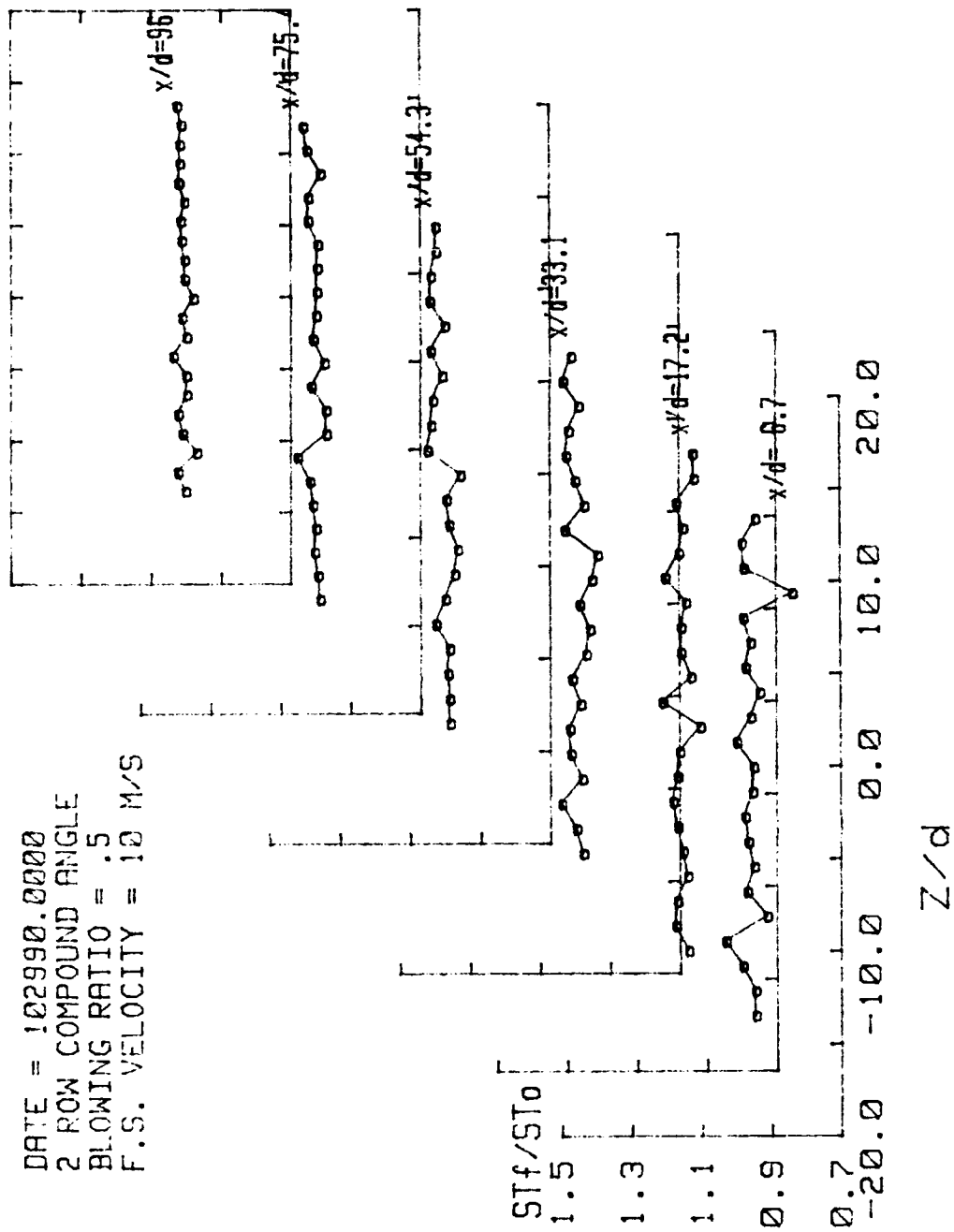


Figure 21. Spanwise Variation of St_f/St_0 , Compound Angle, 2 rows, $m=0.5$.

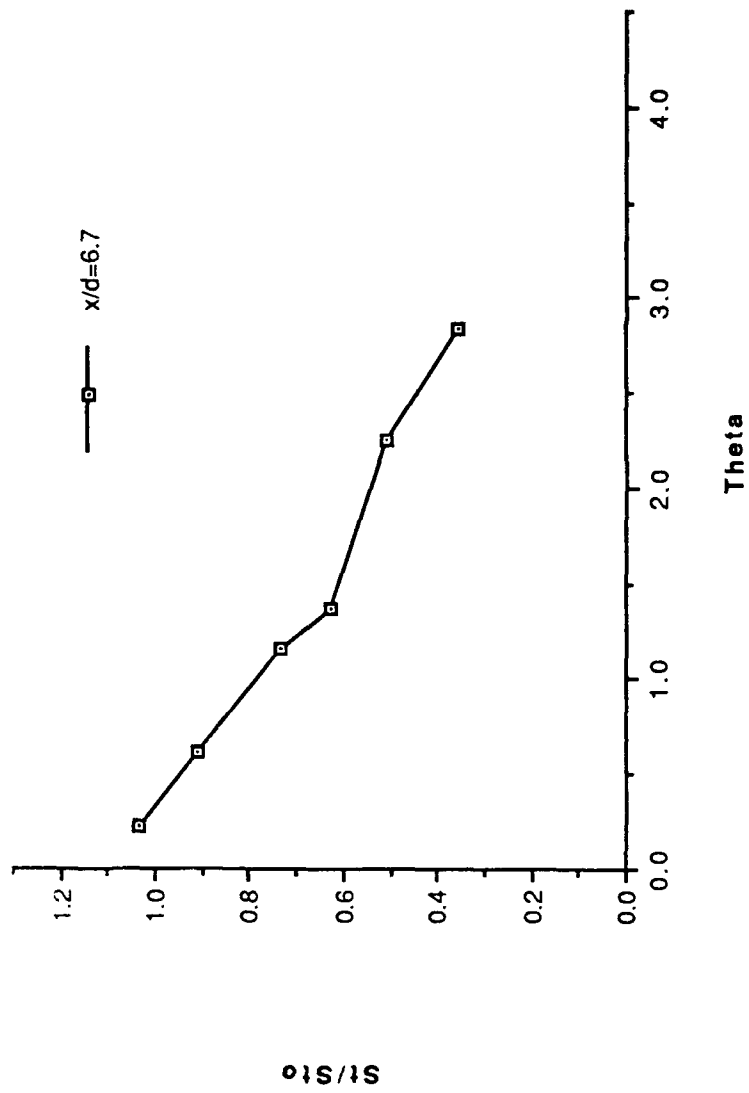


Figure 22. St/St_0 vs θ , Compound Angle, 2 rows, $m=1.0$, $x/d=6.7$, $z=0.0$.

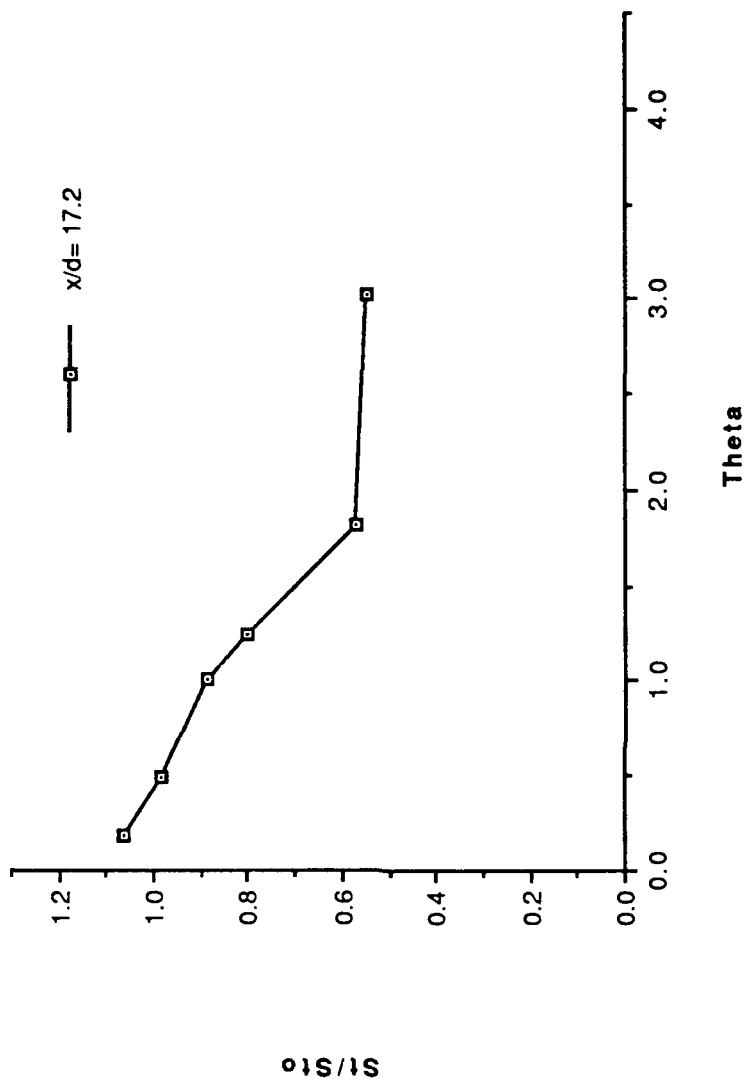


Figure 23. St/St_0 vs θ , Compound Angle, 2 rows, $m=1.0$, $x/d=17.2$, $z=0.0$.

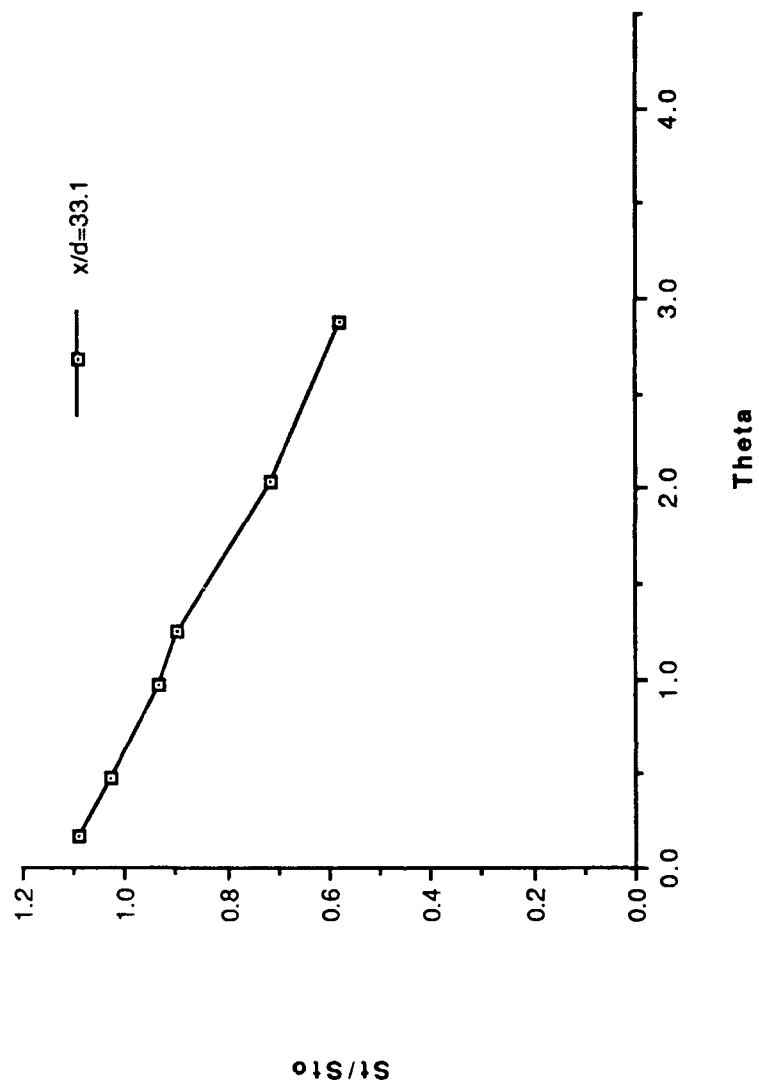


Figure 24. St/St_0 vs θ , Compound Angle, 2 rows, $m=1.0$, $x/d=33.1$, $z=0.0$.

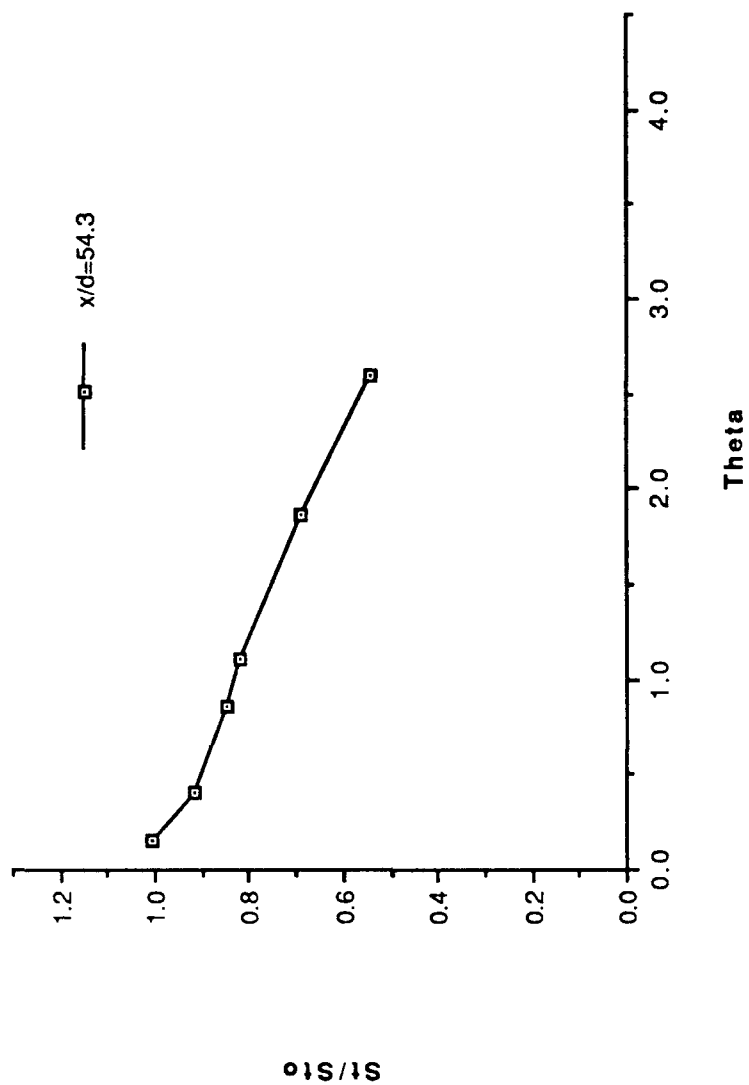


Figure 25. St/St_0 vs θ . Compound Angle, 2 rows, $m=1.0$, $x/d=54.3$, $z=0.0$.

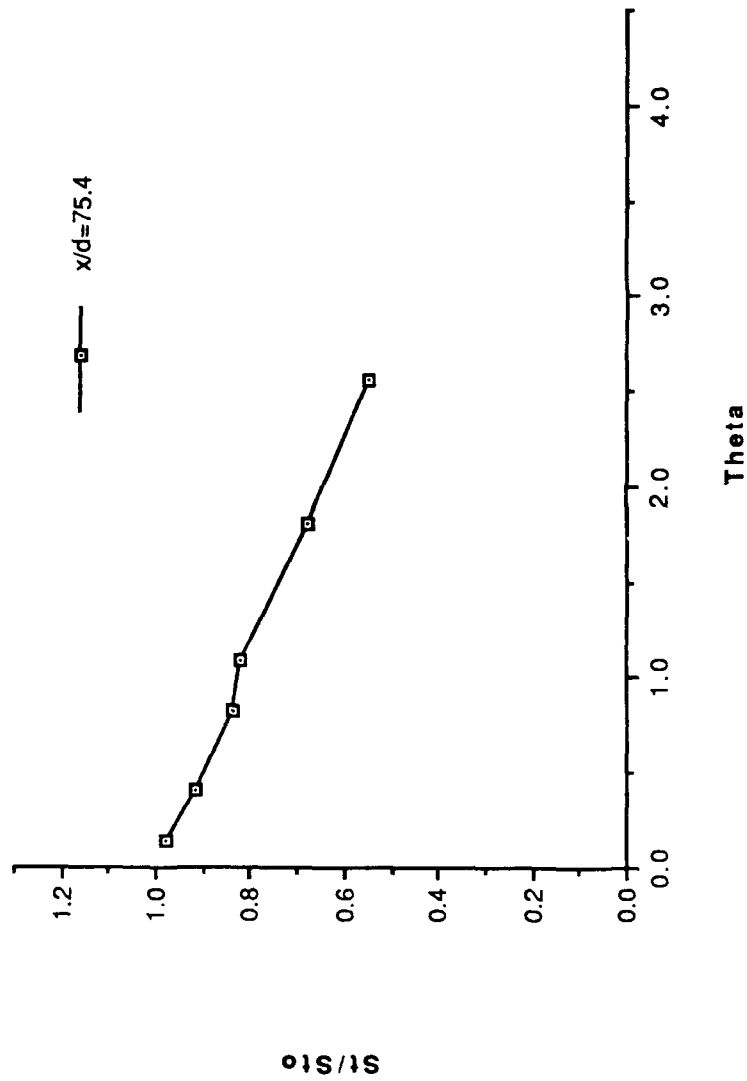


Figure 26. St/St_0 vs θ , Compound Angle, 2 rows, $m=1.0$, $x/d=75.4$, $z=0.0$.

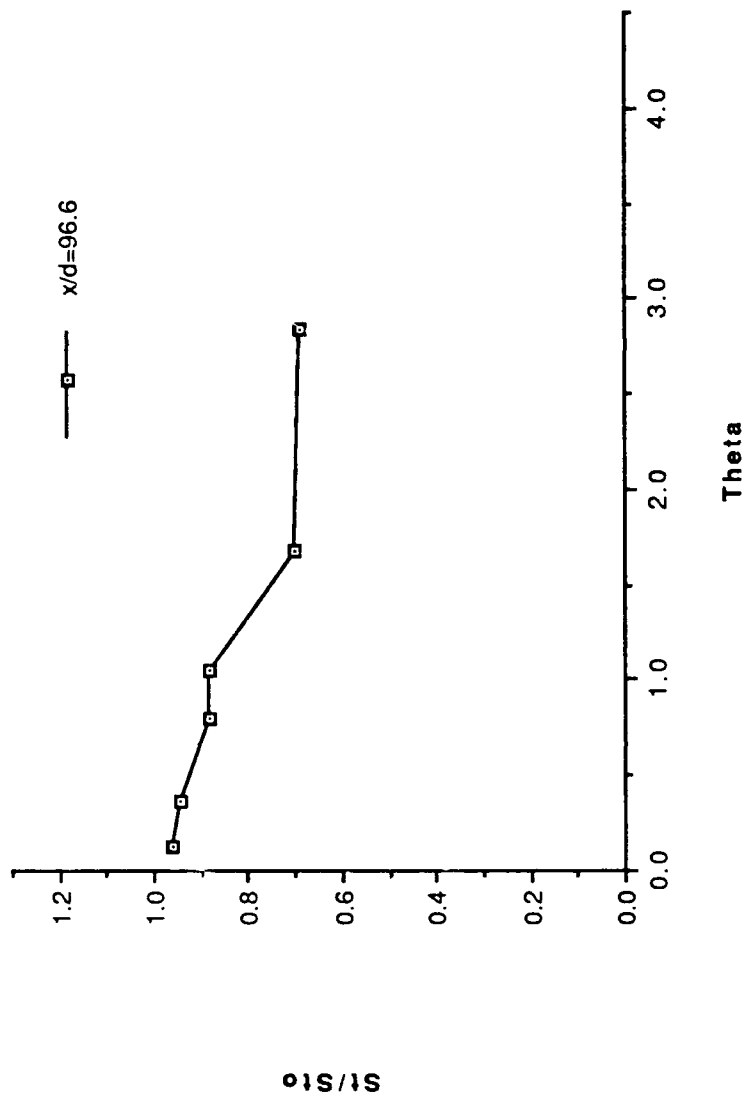


Figure 27. St/St_0 vs θ , Compound Angle, 2 rows, $m=1.0$, $x/d=96.6$, $z=0.0$.

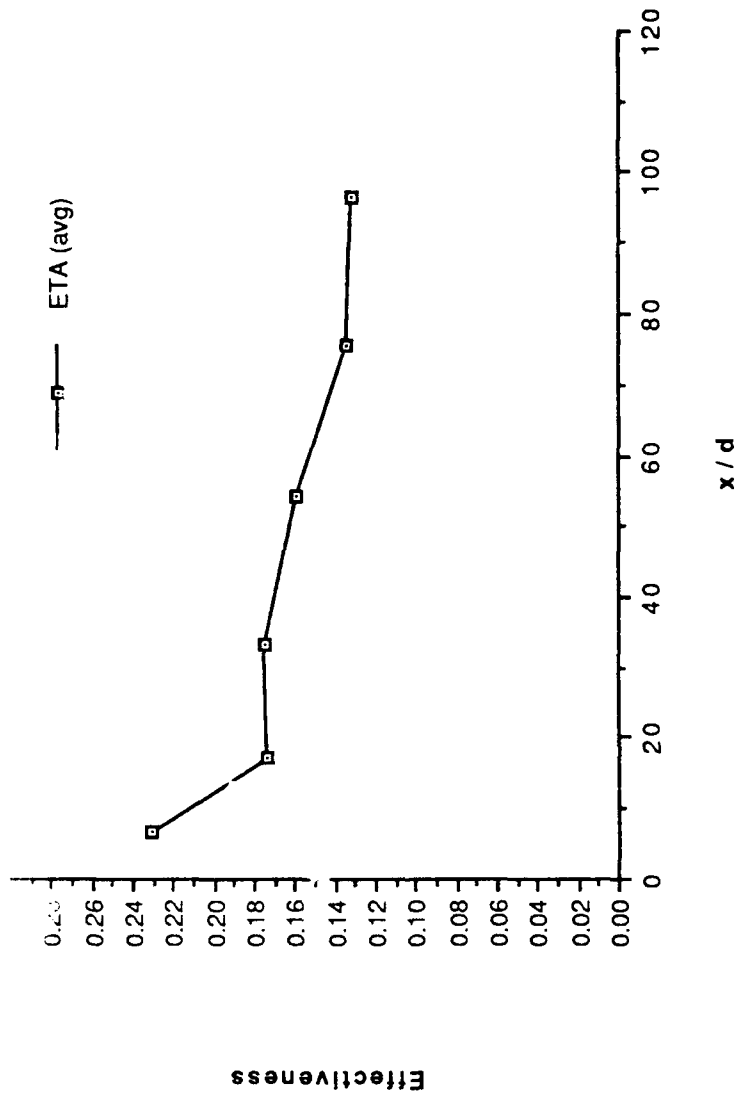


Figure 28. η , vs x/d , Compound Angle, 2 rows, $m=1.0$, Spanwise Average.

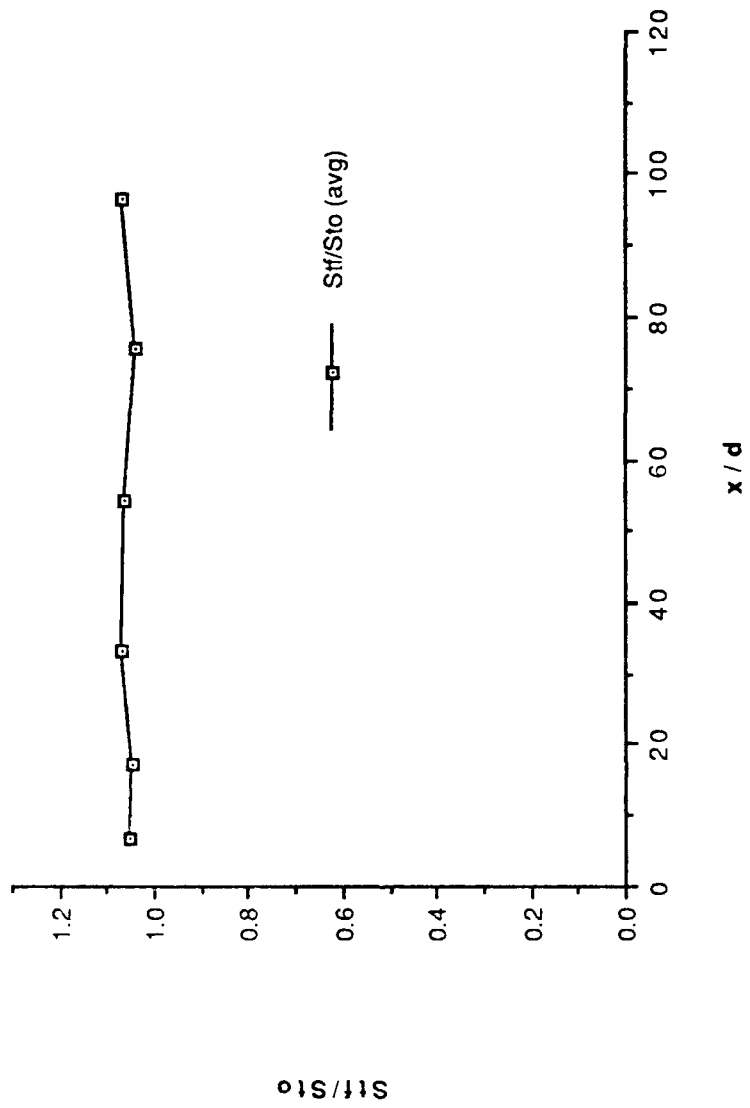


Figure 29. St_f/St_0 vs x/d , Compound Angle, 2 rows, $m=1.0$, Spanwise Average.

FILM-COOLING EFFECTIVENESS

DATE = 100950.0000
 2 ROW COMPOUND ANGLE
 BLOWING RATIO = 1
 F.S. VELOCITY = 10 M/S

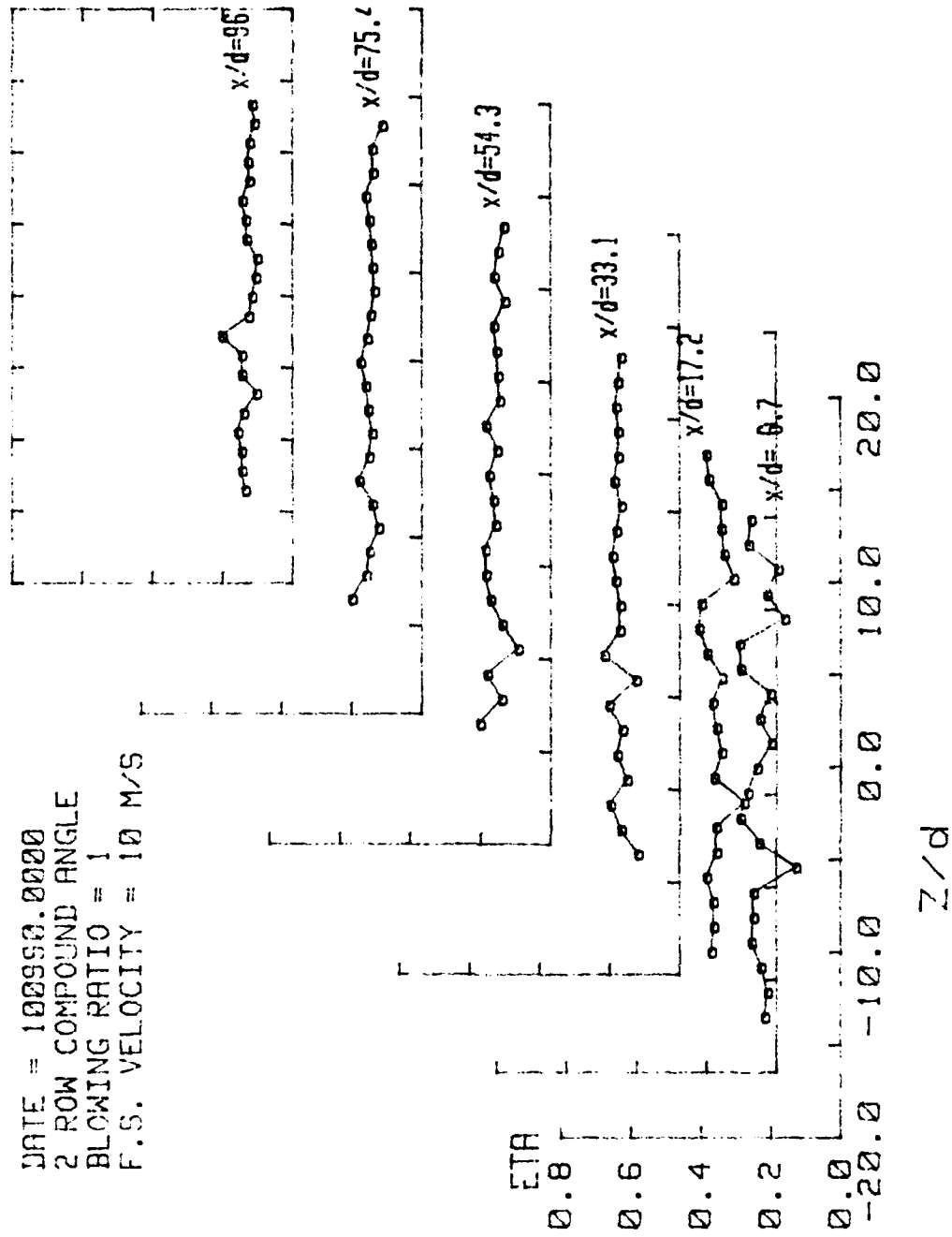


Figure 30. Spanwise Variation of η , Compound Angle, 2 rows, $m=1.0$.

STANTON NUMBER RATIOS

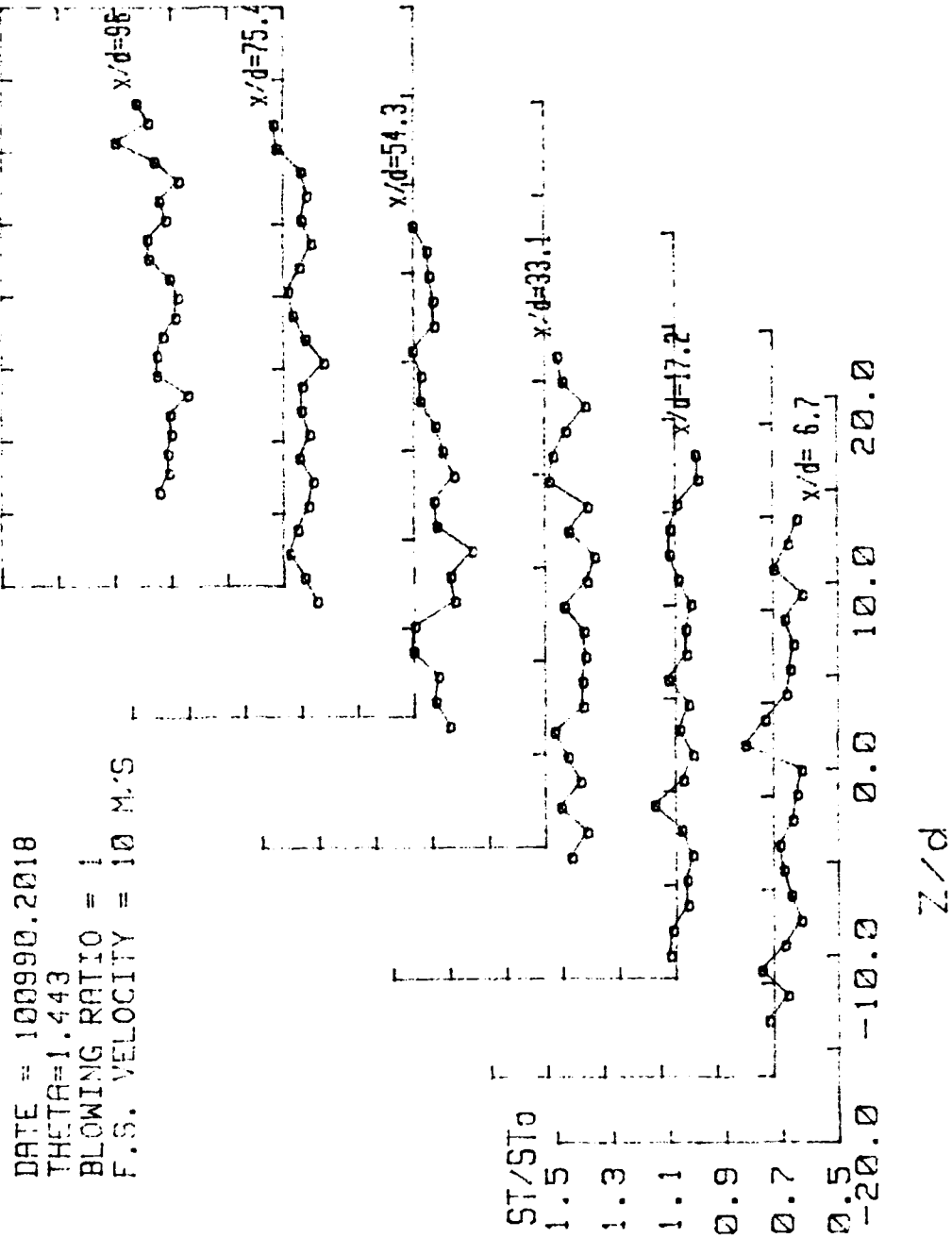


Figure 31. Spanwise Variation of St/St_0 , Compound Angle, 2 rows, $m=1.0$, $\theta=1.443$.

ISO-ENERGETIC STANTON # RATIO

DATE = 100990.0000
 2 ROW COMPOUND ANGLE
 BLOWING RATIO = 1
 F.S. VELOCITY = 10 M/S

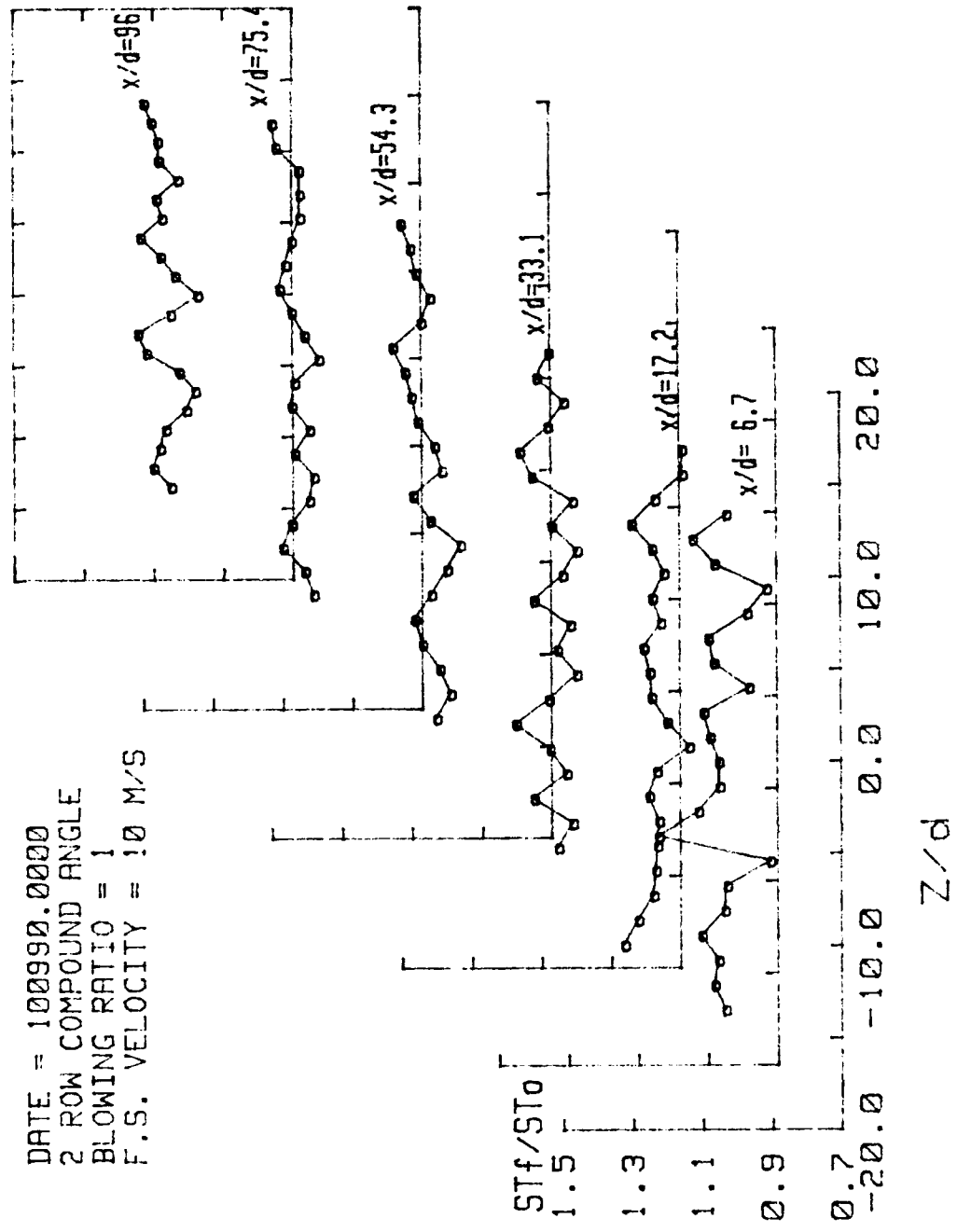
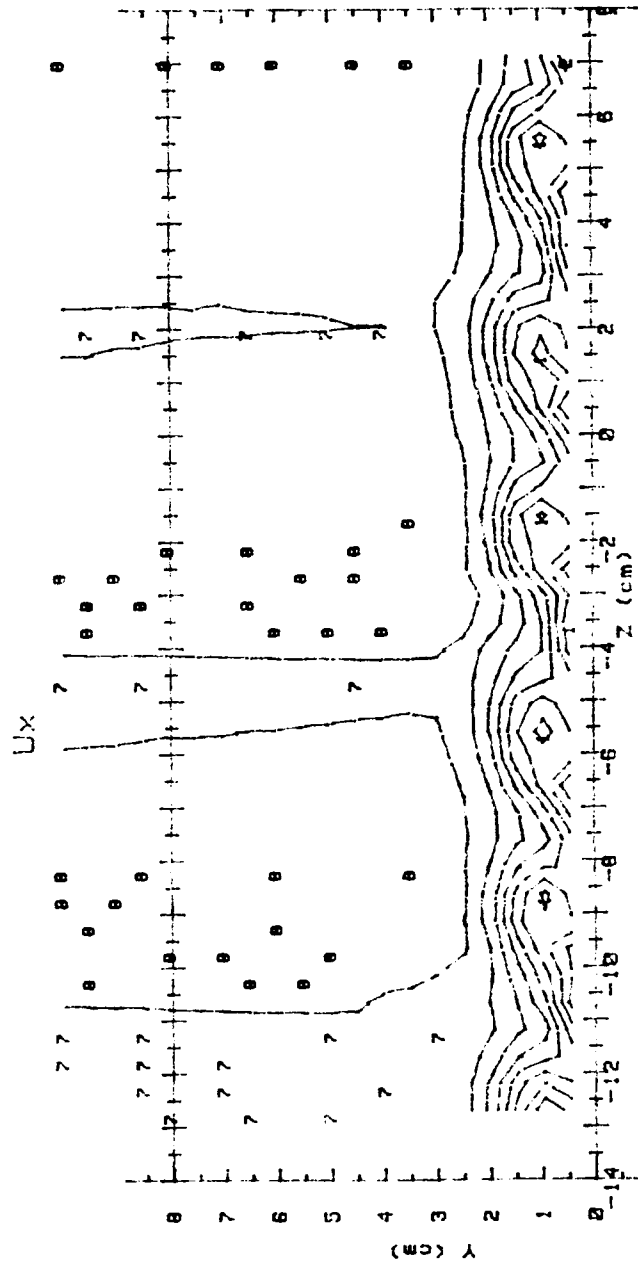


Figure 32. Spanwise Variation of St_f/St_0 , Compound Angle, 2 rows, $m=1.0$.

RUN #112590.0905



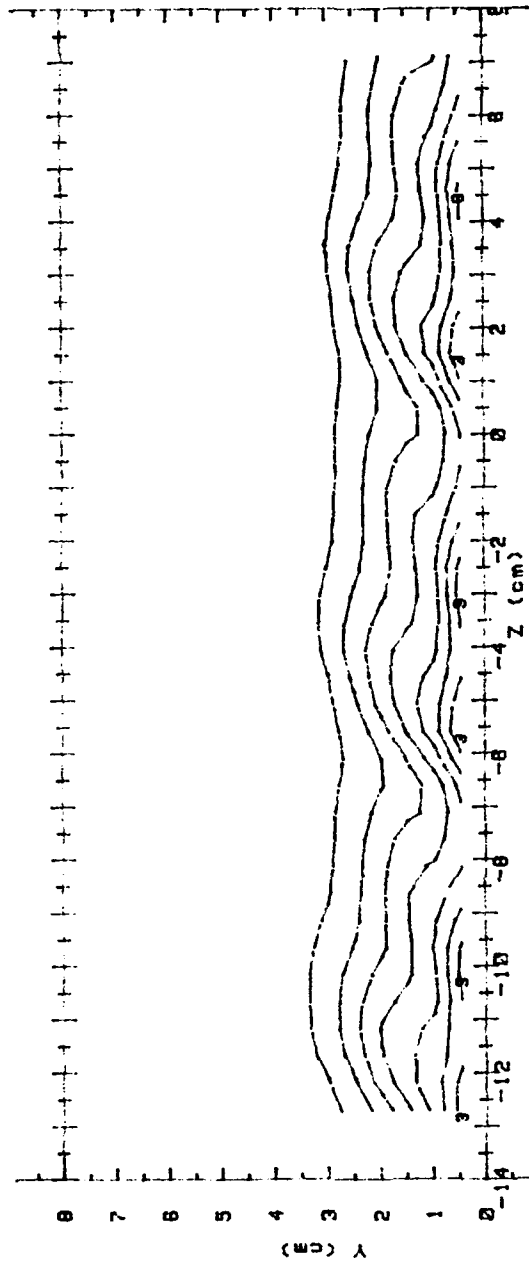
Ux (m/s) RANGES 2 ROW m=1.0 x/d = 11.4

0	< 5.5	5	> 7.5	< 8	
1	> 5.5	< 6	6	> 8	< 8.5
2	> 6	< 6.5	7	> 8.5	< 9
3	> 6.5	< 7	8	> 9	< 9.5
4	> 7	< 7.5	9	> 9.5	< 10
			10	> 10	

Figure 33. Streamwise Velocity Field, Compound Angle, 2 rows, m=1.0, x/d=11.4.

RUN #112090.09

Ux



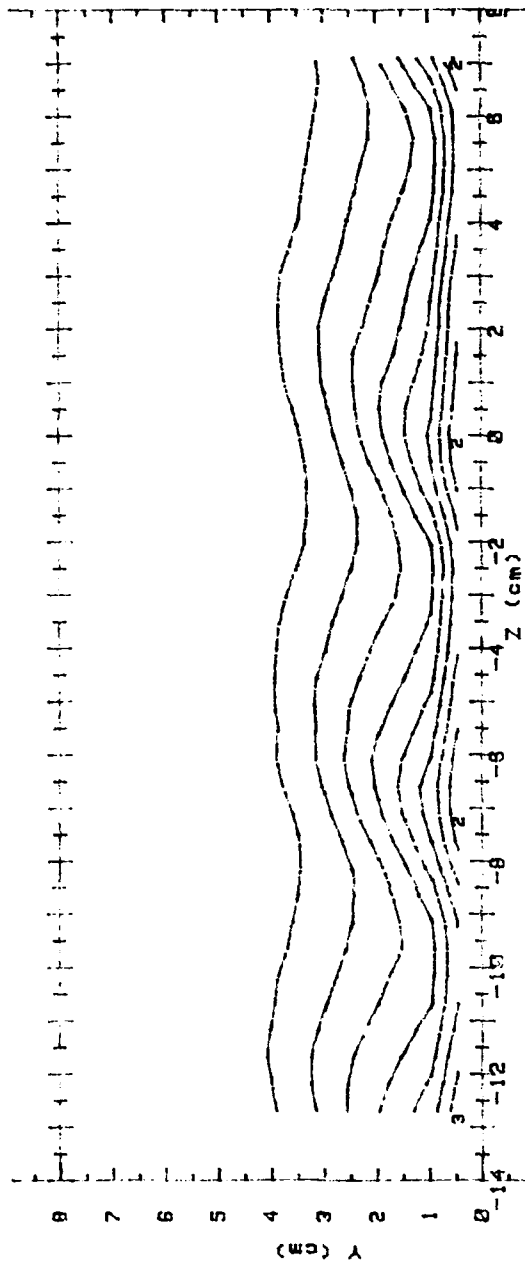
Ux (m/s) RANGES 2 ROW m=1.0 x/d = 45.7

0 :	< 5.5	5 :	7.5 < 8
1 :	5.5 < 6	6 :	8 < 8.5
2 :	6 < 6.5	7 :	8.5 < 9
3 :	6.5 < 7	8 :	9 < 9.5
4 :	7 < 7.5	9 :	9.5 < 10
		10 :	10

Figure 34. Streamwise Velocity Field, Compound Angle, 2 rows, $m=1.0$, $x/d=45.7$.

RUN #111590.14

Ux



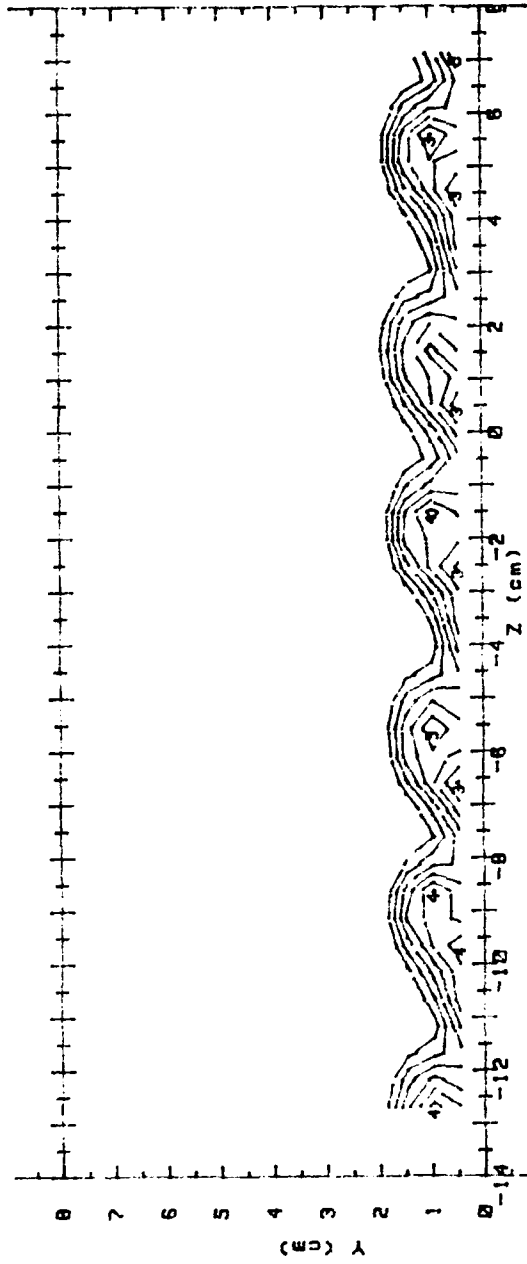
Ux(m/s) RANGES 2 ROW m=1.0 x/d = 87.2

0 1	< 5.5	5 1	> 7.5	< 8	
1 1	> 5.5	< 6	6 1	> 8	< 8.5
2 1	> 6	< 6.5	7 1	> 8.5	< 9
3 1	> 6.5	< 7	8 1	> 9	< 9.5
4 1	> 7	< 7.5	9 1	> 9.5	< 10
			10 1	> 10	

Figure 35. Streamwise Velocity Field, Compound Angle, 2 rows, $m=1.0$, $x/d=87.2$.

RUN #112590.0905

Ptotal

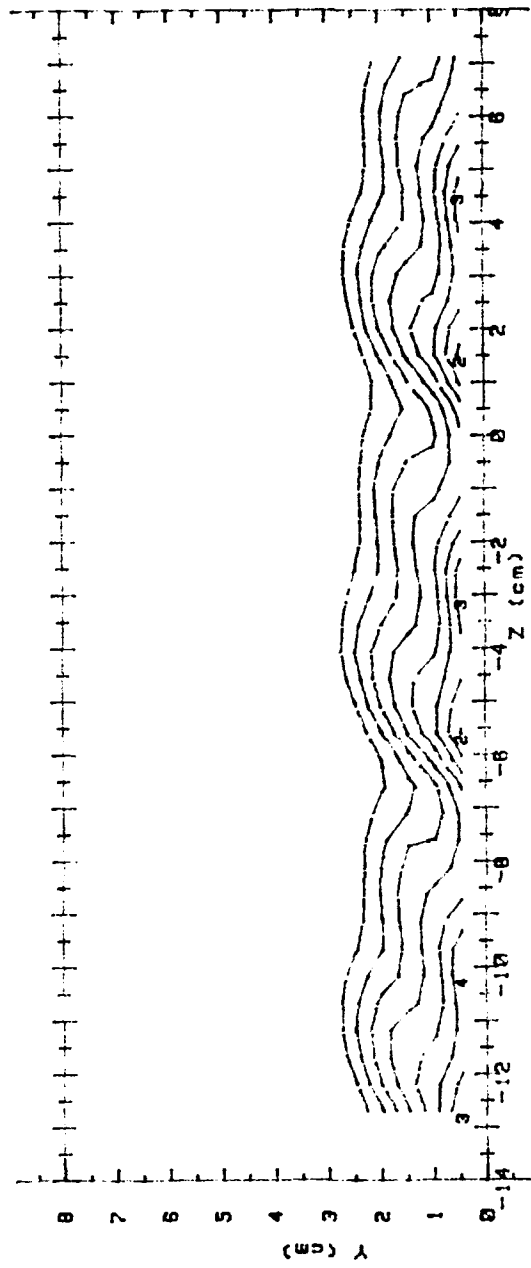


Ptotal(Pascals) RANGES 2 ROW m=1.0 x/d=11.4

0 :	< 20	5 :	36 < 40
1 :	20 < 24	6 :	40 < 44
2 :	24 < 28	7 :	44 < 48
3 :	28 < 32	8 :	48 < 52
4 :	32 < 36	9 :	52 < 56
		10 :	56

Figure 36. Streamwise Pressure Field, Compound Angle, 2 rows, $m=1.0$, $x/d=11.4$.

RUN #112090.09
 Ptotal



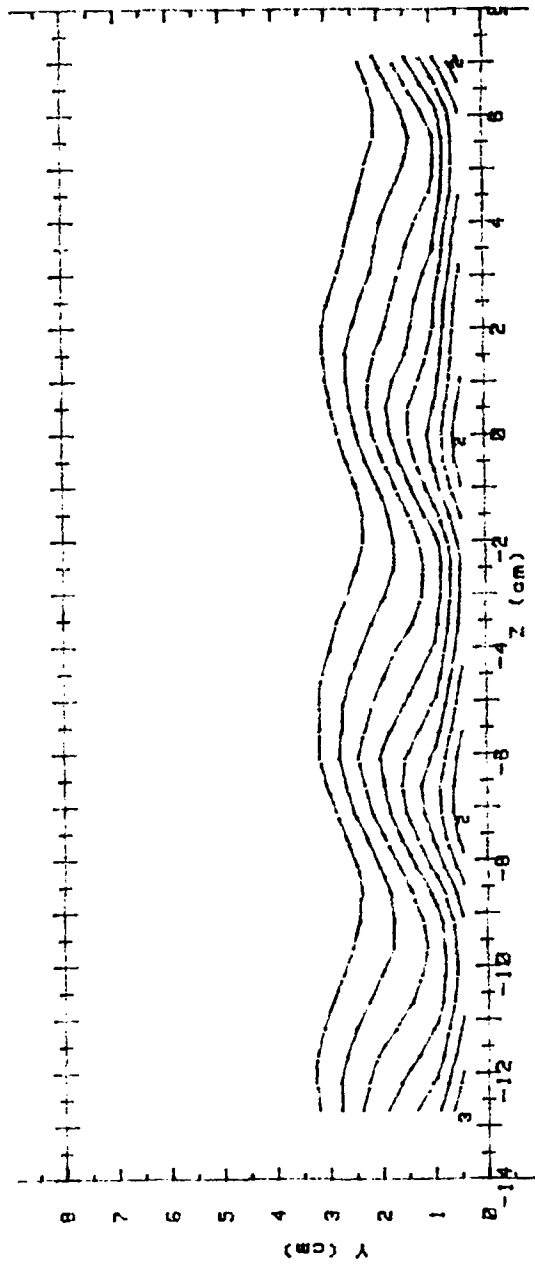
Ptotal (Pascals) RANGES 2 ROW m=1.0 x/d=45.7

0 :	< 20	5 :	36 < 40
1 :	20 < 24	6 :	40 < 44
2 :	24 < 28	7 :	44 < 48
3 :	28 < 32	8 :	48 < 52
4 :	32 < 36	9 :	52 < 56
		10 :	> 56

Figure 37. Streamwise Pressure Field, Compound Angle, 2 rows, $m=1.0$, $x/d=45.7$.

RUN #111590.14

Ptotal



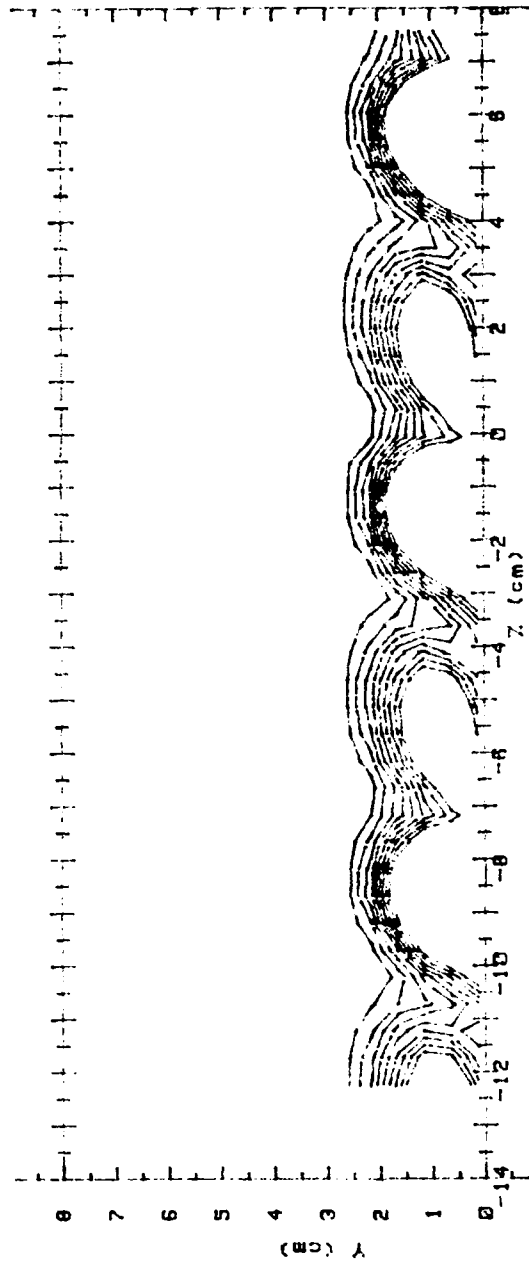
Ptotal(Pascal) RANGES 2 ROW m=1.0 x/d=87.2

0 :	< 20	5 > 36 < 40
1 >	20 < 24	6 > 40 < 44
2 >	24 < 28	7 > 44 < 48
3 >	28 < 32	8 > 48 < 52
4 >	32 < 36	9 > 52 < 56
		10 > 56

Figure 38. Streamwise Pressure Field, Compound Angle, 2 rows, $m=1.0$, $x/d=87.2$.

RUN #120590.1111

T - Tfs



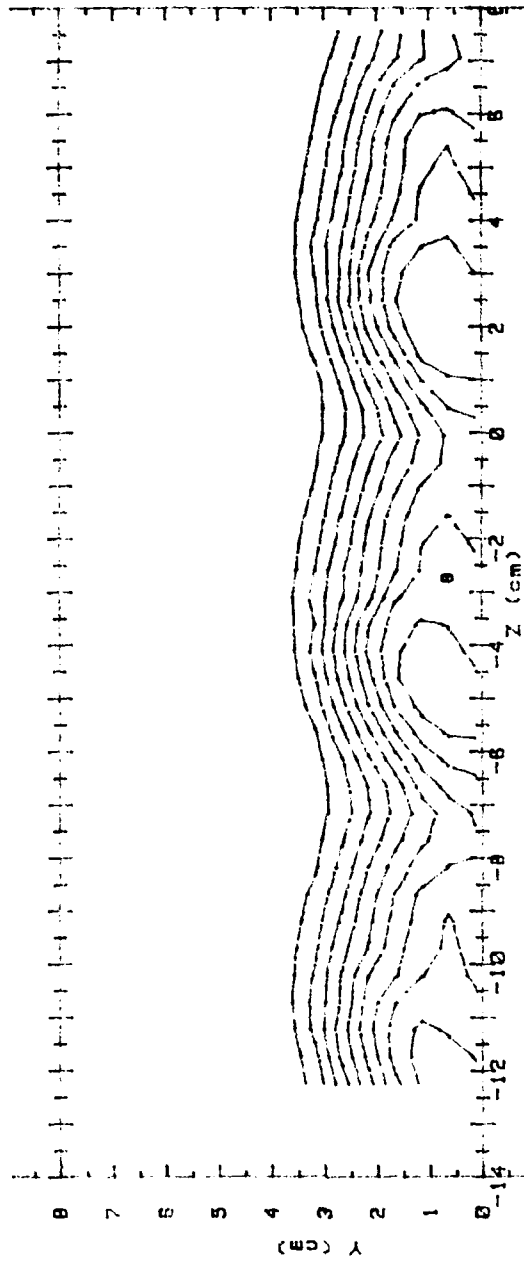
T - Tfe (CELCIUS) RANGES 2 ROW m=1.0 x/d = 11.4

0 :	< .5	5 :	2.5 < 3
1 :	.5 < 1	6 :	3 < 3.5
2 :	1 < 1.5	7 :	3.5 < 4
3 :	1.5 < 2	8 :	4 < 4.5
4 :	2 < 2.5	9 :	4.5

Figure 39. Streamwise Injectant Distribution, Compound Angle, 2 rows, $m=1.0$, $x/d=11.4$.

RUN #120592.1535

T - Tfs



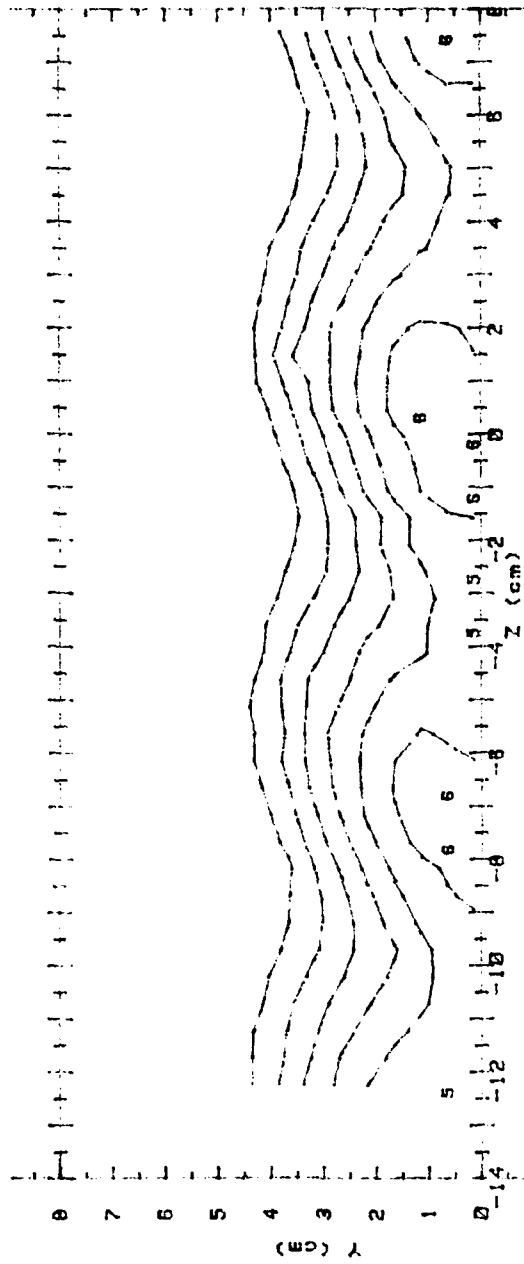
T - Tfs (CELCIUS) RANGES 2 ROW m=1.0 x/d = 45.7

- 0 : < .5
- 1 : .5 < 1
- 2 : 1 < 1.5
- 3 : 1.5 < 2
- 4 : 2 < 2.5
- 5 : 2.5 < 3
- 6 : 3 < 3.5
- 7 : 3.5 < 4
- 8 : 4 < 4.5
- 9 : 4.5

Figure 40. Streamwise Injectant Distribution, Compound Angle, 2 rows, m=1.0, x/d=45.7.

RUN: #120690.:045

T - Tfs



T - Tfs (CELCIUS) RANGES 2 ROW m=1.0 x/d = 87.2

- 0 : < .5
- 1 : .5 < 1
- 2 : 1 < 1.5
- 3 : 1.5 < 2
- 4 : 2 < 2.5
- 5 : 2.5 < 3
- 6 : 3 < 3.5
- 7 : 3.5 < 4
- 8 : 4 < 4.5
- 9 : 4.5

Figure 41. Streamwise Injectant Distribution, Compound Angle, 2 rows, m=1.0, x/d=87.2.

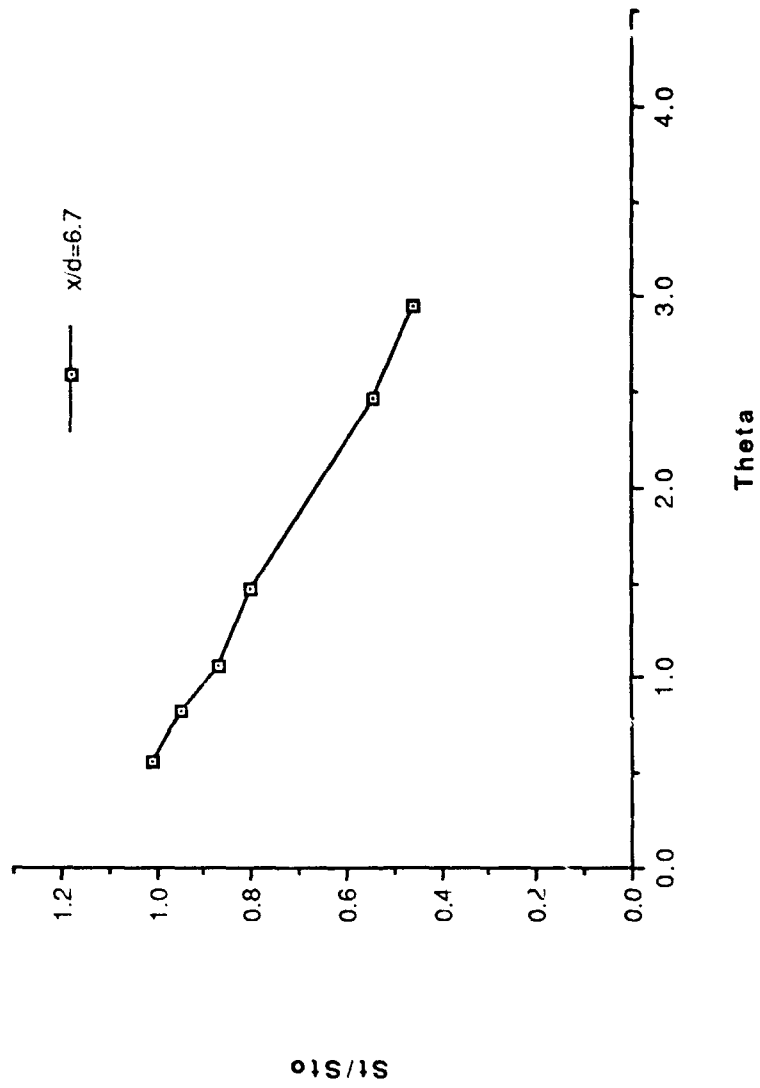


Figure 42. St/St_0 vs θ , Compound Angle, 2 rows, $m=1.5$, $x/d=6.7$, $z=0.0$.

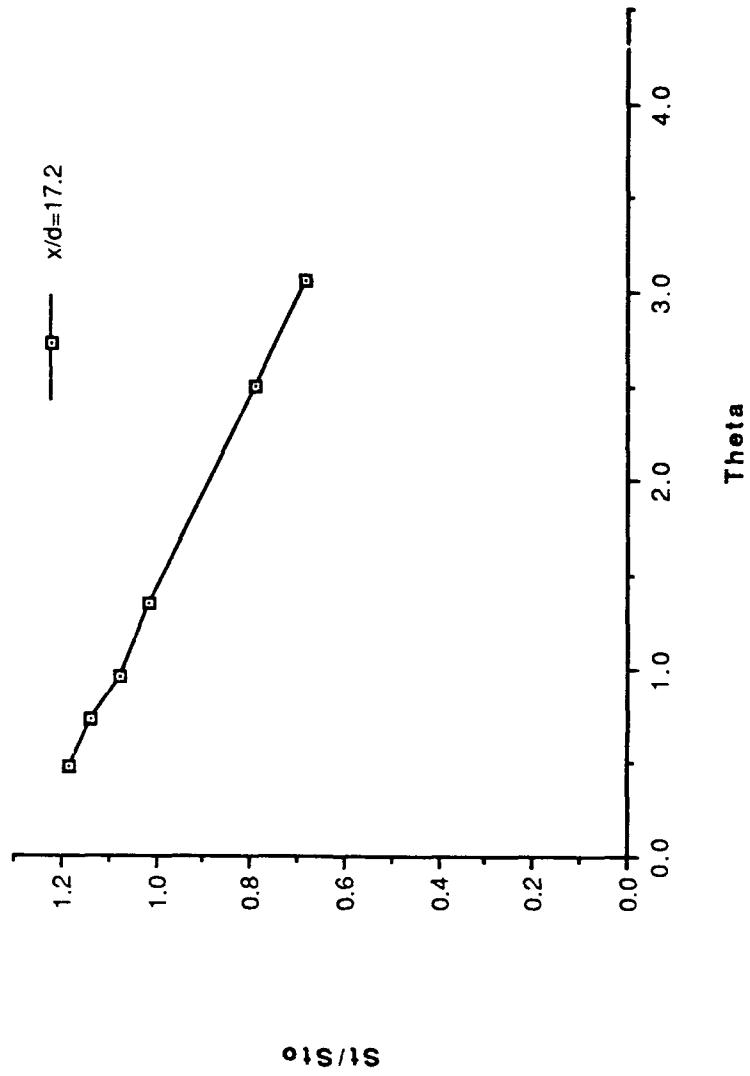


Figure 43. St/St_0 vs θ , Compound Angle, 2 rows, $m=1.5$, $x/d=17.2$, $z=0.0$.

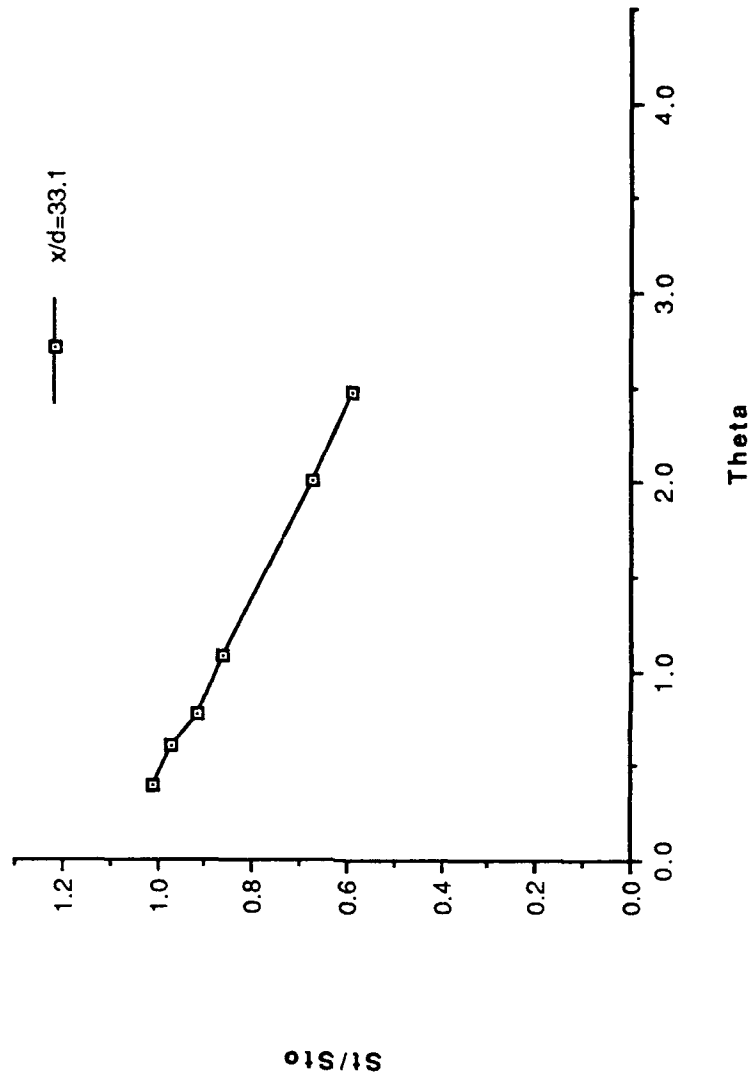


Figure 44. St/St_0 vs θ , Compound Angle, 2 rows, $m=1.5$, $x/d=33.1$, $z=0.0$.

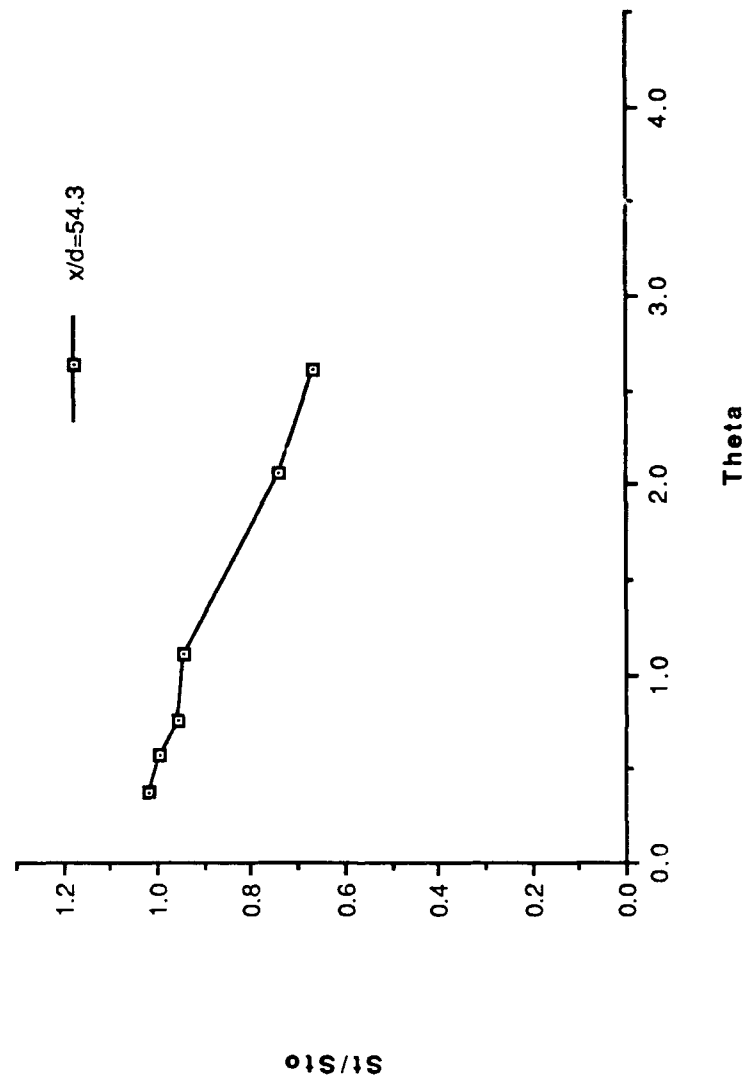


Figure 45. St/St_0 vs θ , Compound Angle, 2 rows, $m=1.5$, $x/d=54.3$, $z=0.0$.

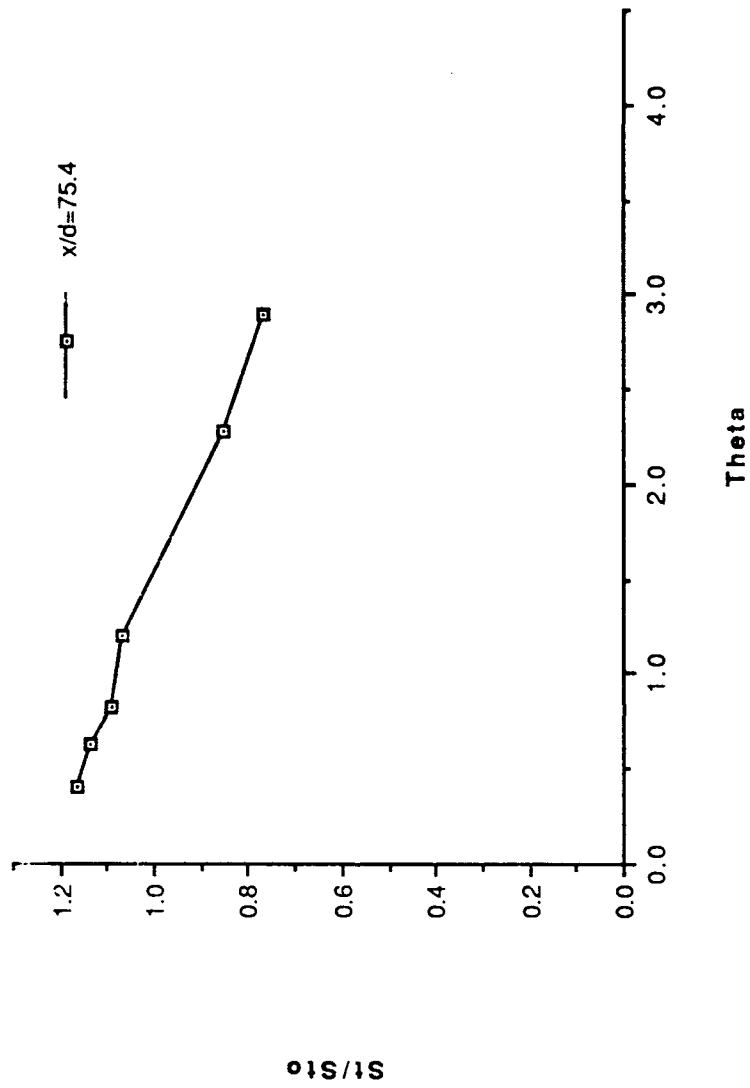


Figure 46. St/St_0 vs θ , Compound Angle, 2 rows, $m=1.5$, $x/d=75.4$, $z=0.0$.

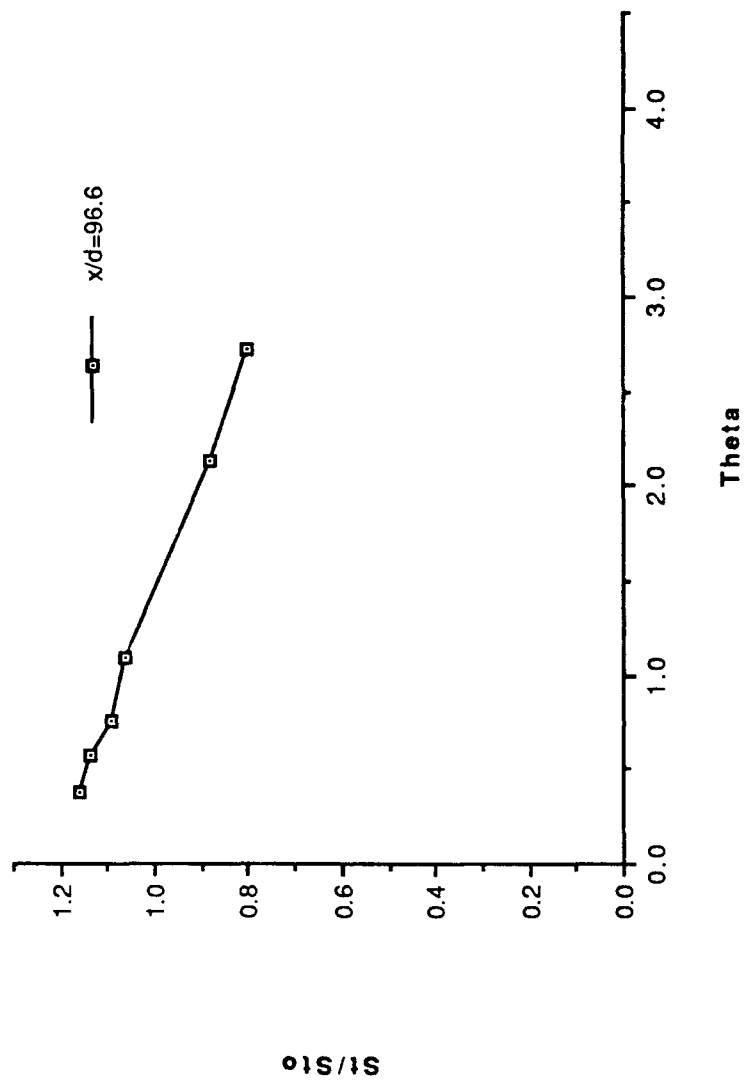


Figure 47. St/St_0 vs θ , Compound Angle, 2 rows, $m=1.5$, $x/d=96.6$, $z=0.0$.

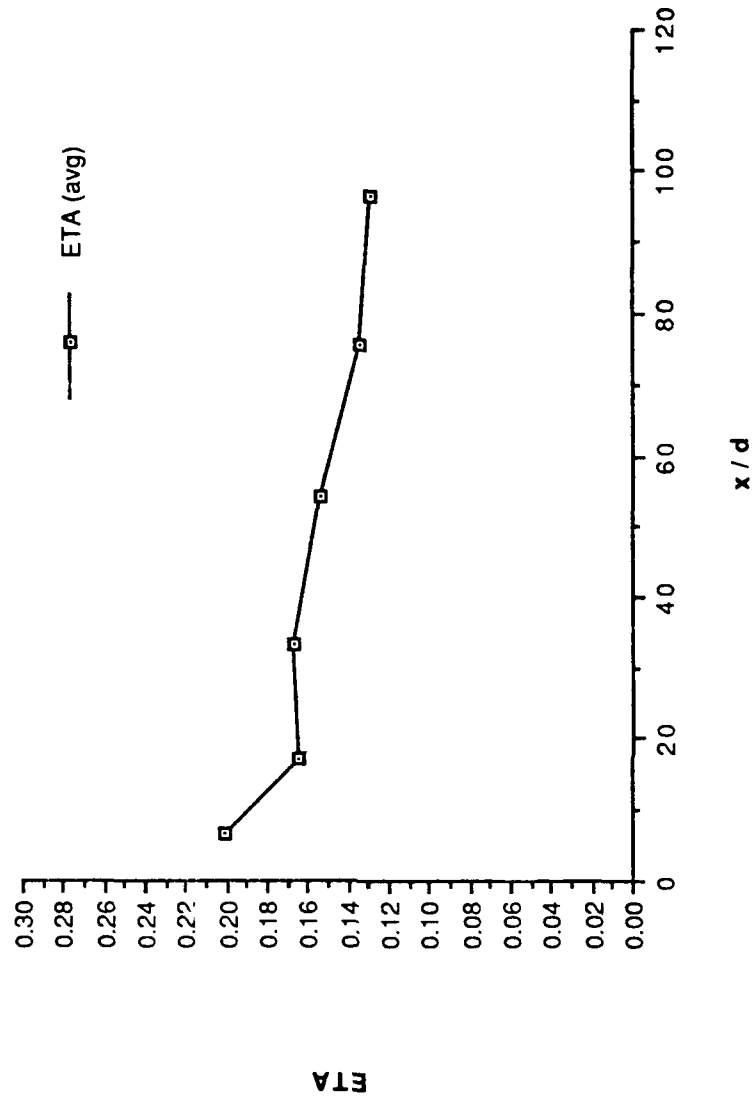


Figure 48. η , vs x/d , Compound Angle, 2 rows, $m=1.5$, Spanwise Average.

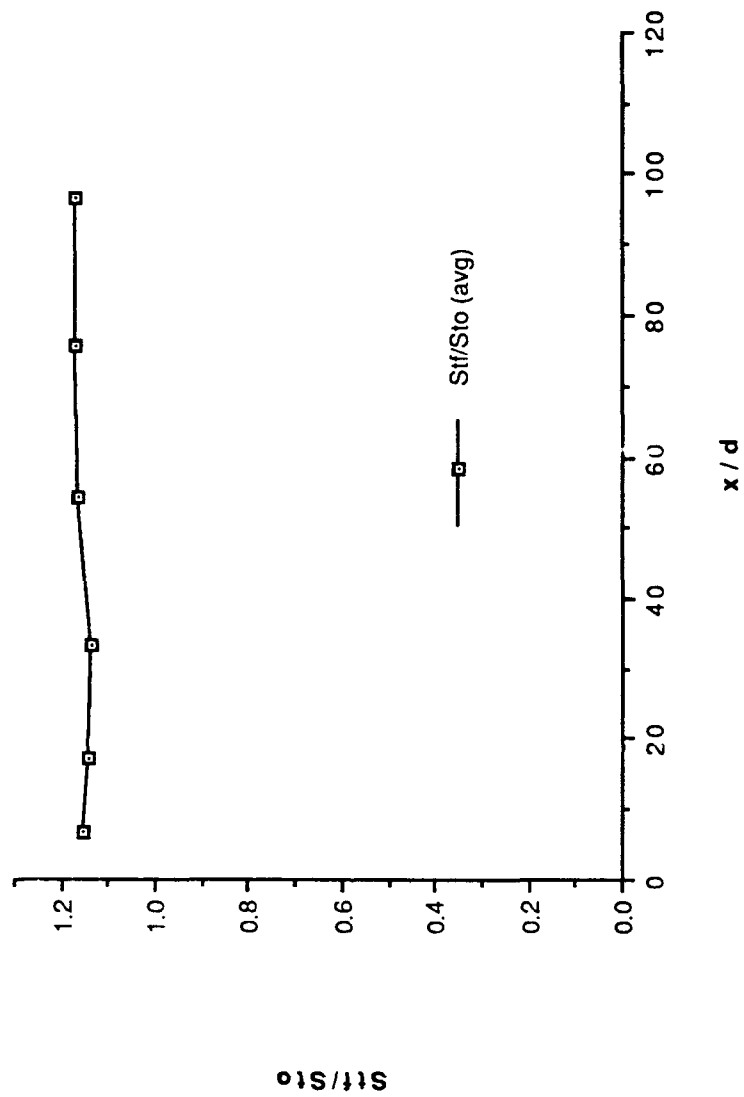


Figure 49. St_f/St_0 vs x/d , Compound Angle, 2 rows, $m=1.5$, Spanwise Average.

FILM-COOLING EFFECTIVENESS

DATE = 102492.0000
 2 ROW COMPOUND ANGLE
 BLOWING RATIO = 1.5
 F.S. VELOCITY = 10 M/S

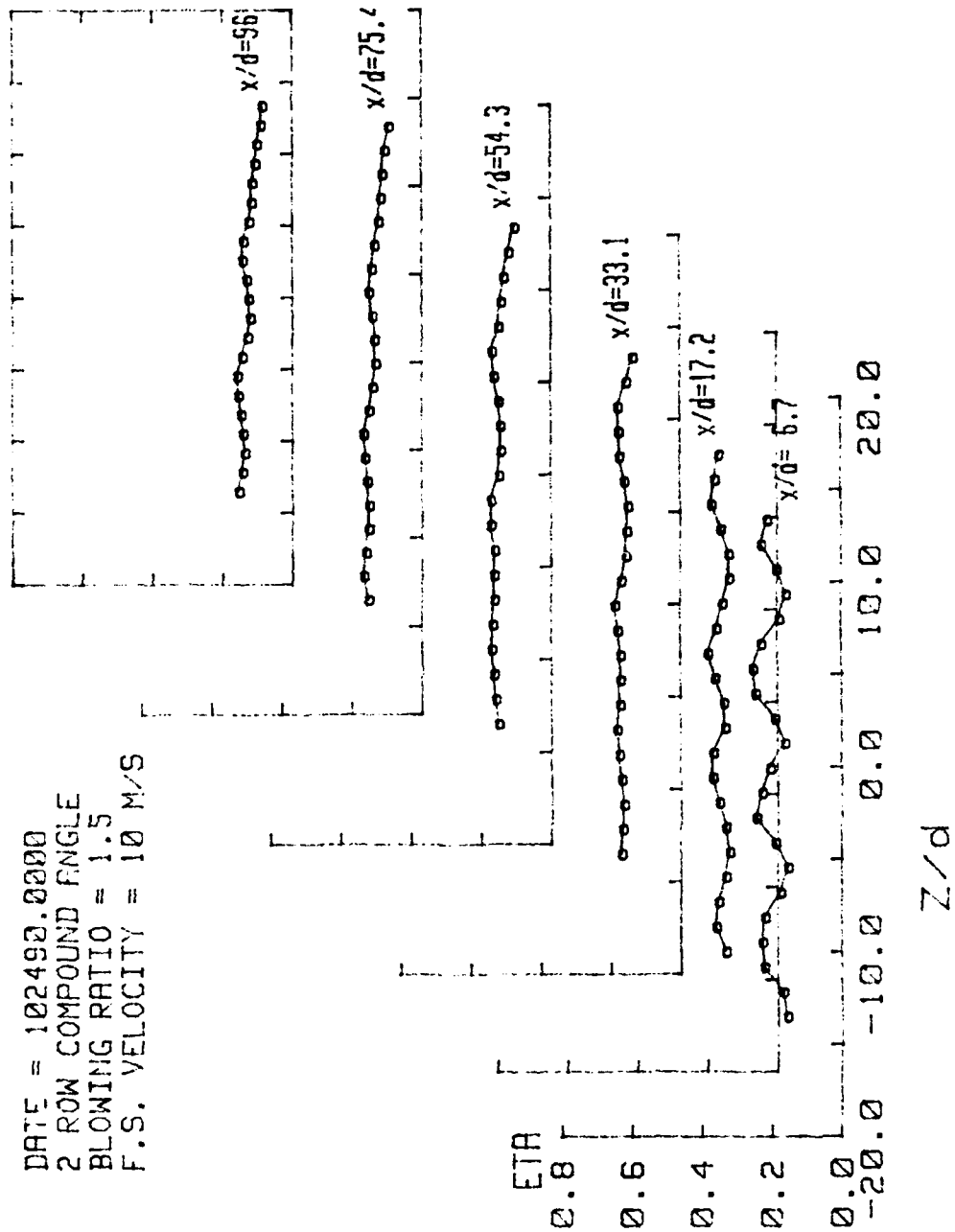


Figure 50. Spanwise Variation of η , Compound Angle, 2 rows, $m=1.5$.

STANTON NUMBER RATIOS

DATE = 102590.1438
 THETA=1.433
 BLOWING RATIO = 1.5
 F.S. VELOCITY = 10 M/S

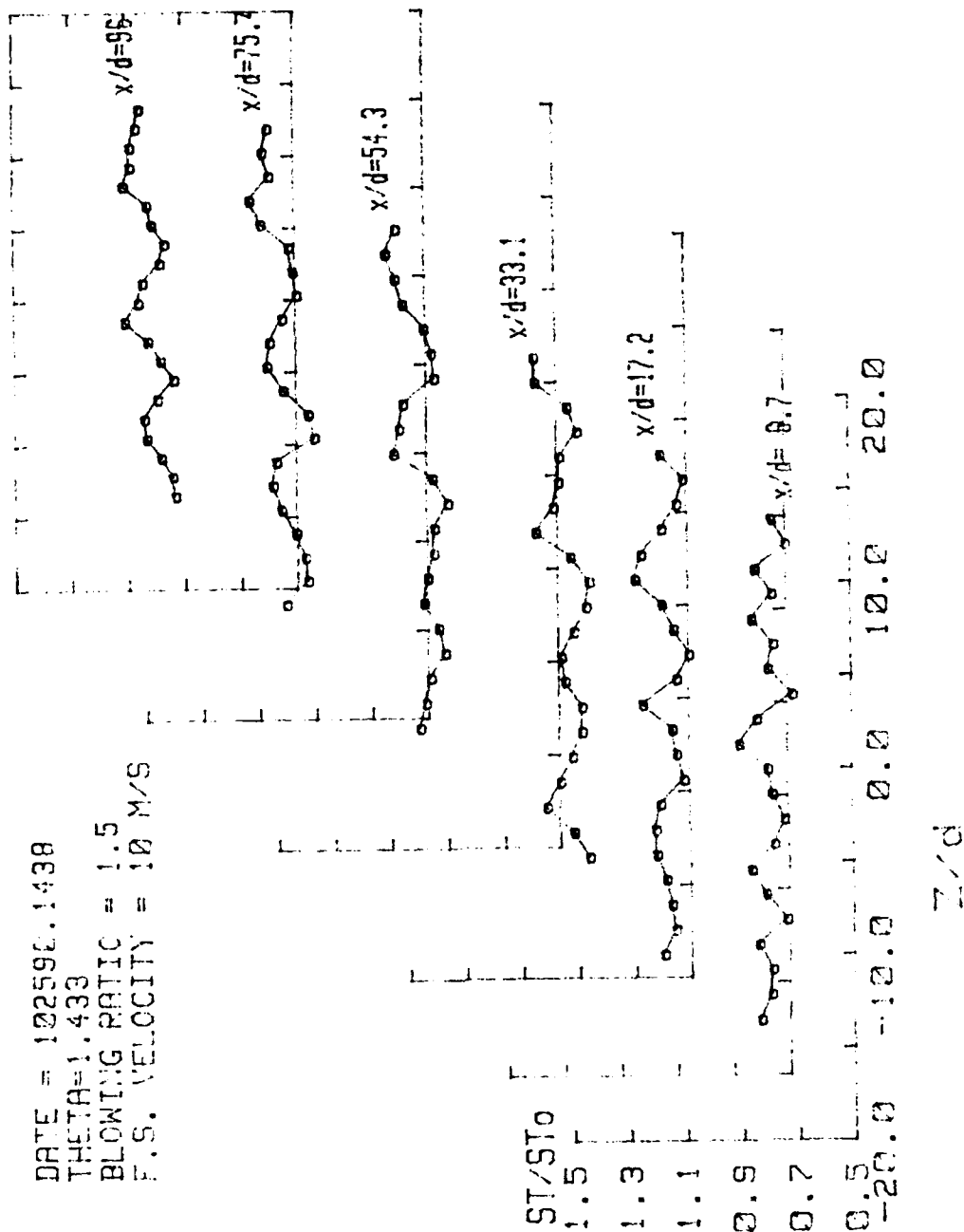


Figure 51. Spanwise Variation of St/St_0 , Compound Angle, 2 rows, $m=1.5$, $\theta=1.433$.

ISO-ENERGETIC STANTON # RATIO

DATE = 102490.0000
 2 ROW COMPOUND ANGLE
 BLOWING RATIO = 1.5
 F.S. VELOCITY = 10 M/S

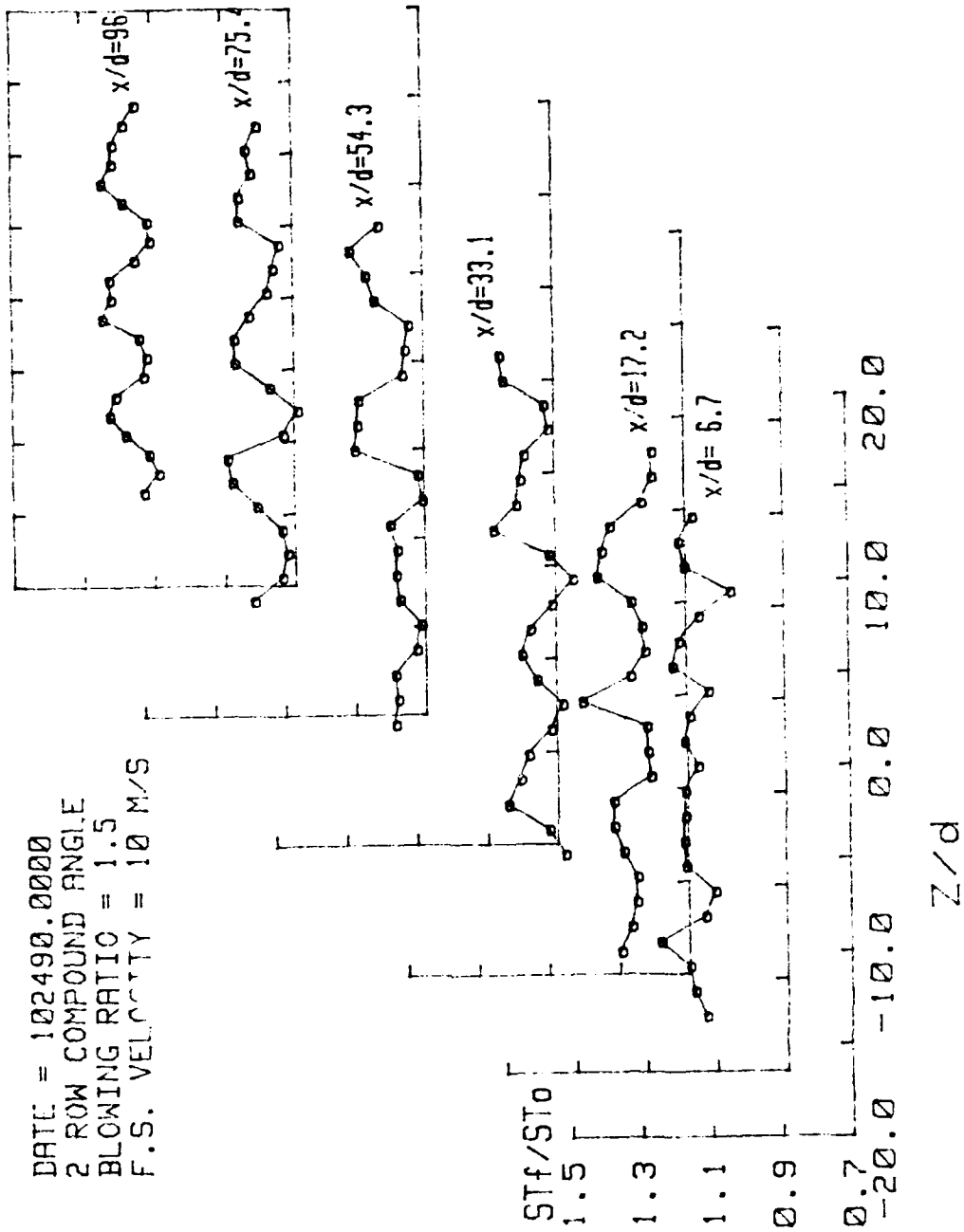


Figure 52. Spanwise Variation of St_f/St_0 , Compound Angle, 2 rows, $m=1.5$.

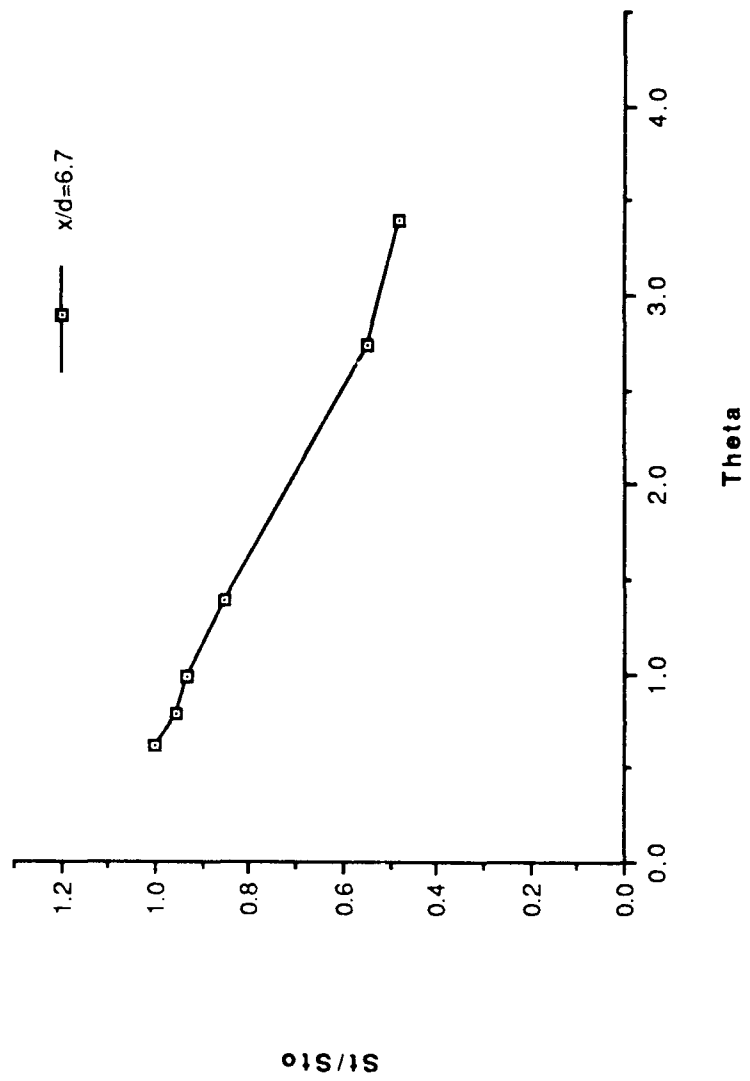


Figure 53. St/St_0 vs θ , Compound Angle, 2 rows, $m=1.74$, $x/d=6.7$, $z=0.0$.

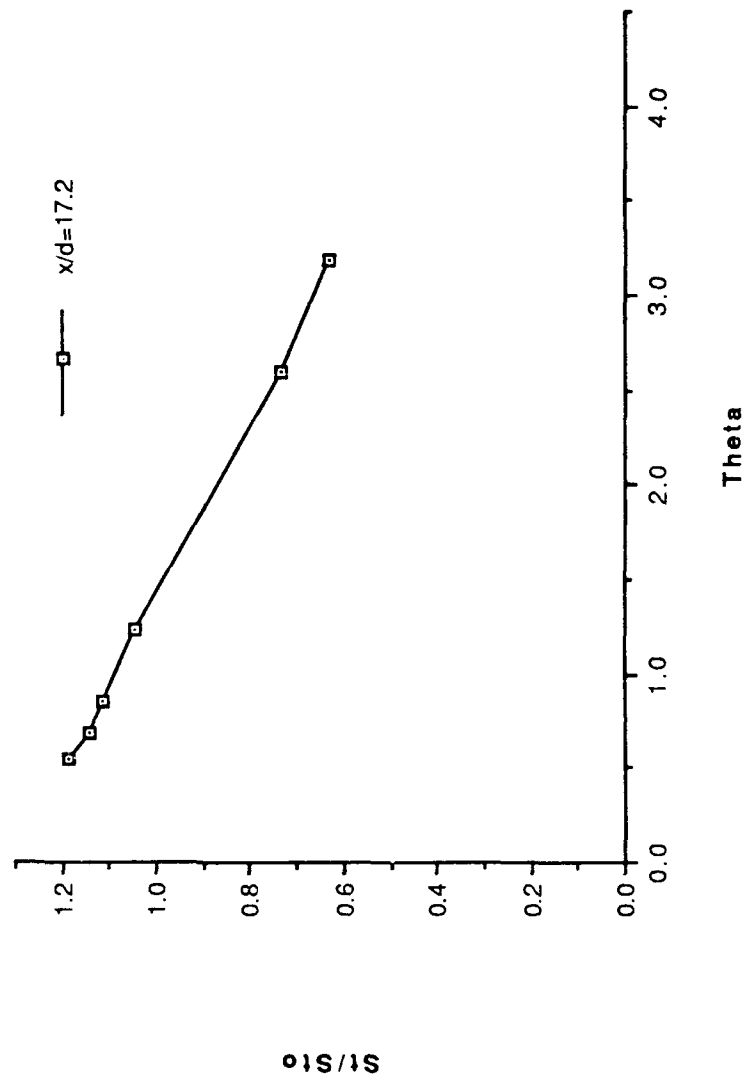


Figure 54. St/St_0 vs θ , Compound Angle, 2 rows, $m=1.74$, $x/d=17.2$, $z=0.0$.

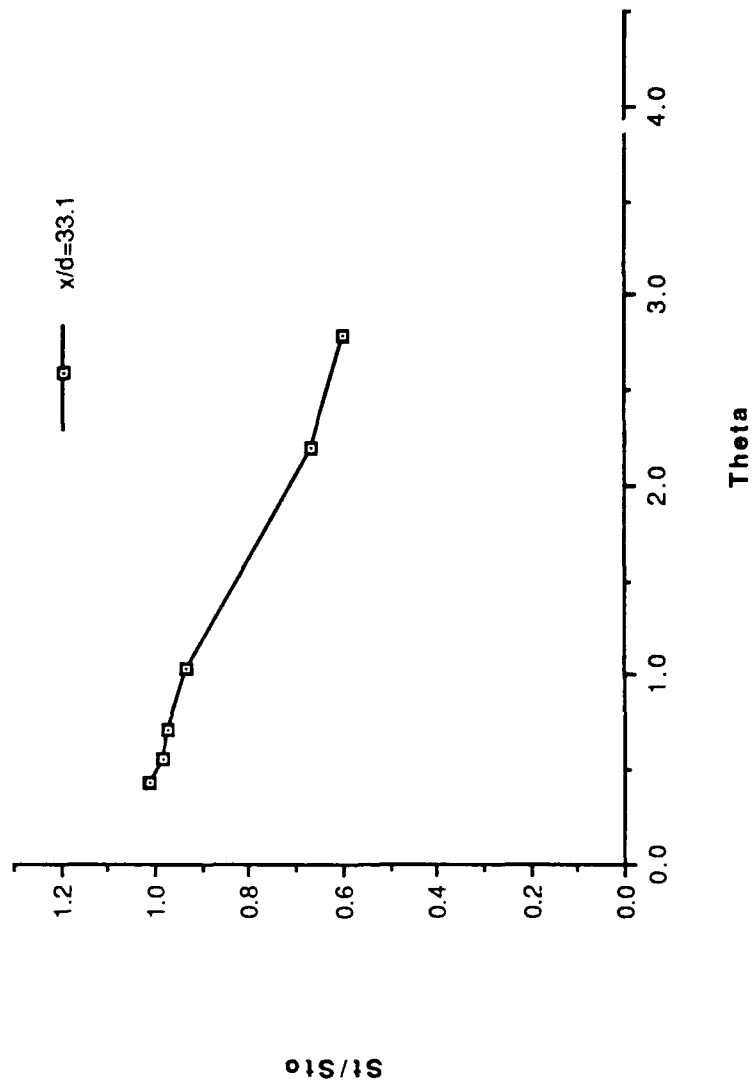


Figure 55. St/St_0 vs θ , Compound Angle, 2 rows, $m=1.74$, $x/d=33.1$, $z=0.0$.

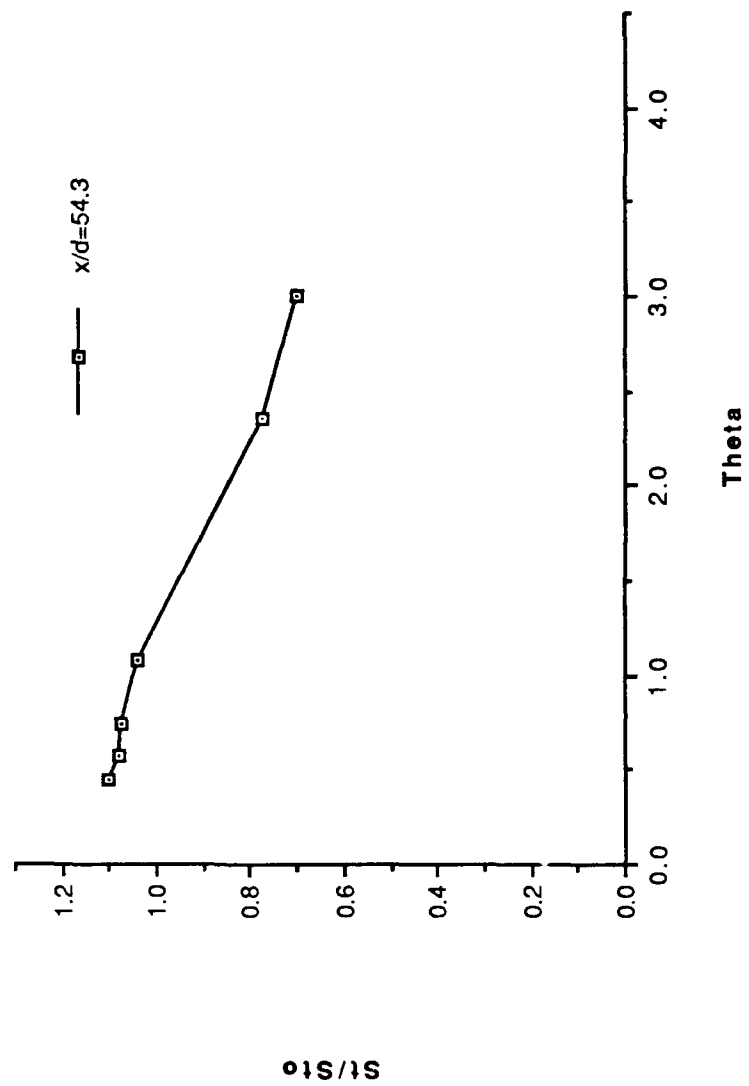


Figure 56. St/St_0 vs θ , Compound Angle, 2 rows, $m=1.74$, $x/d=54.3$, $z=0.0$.

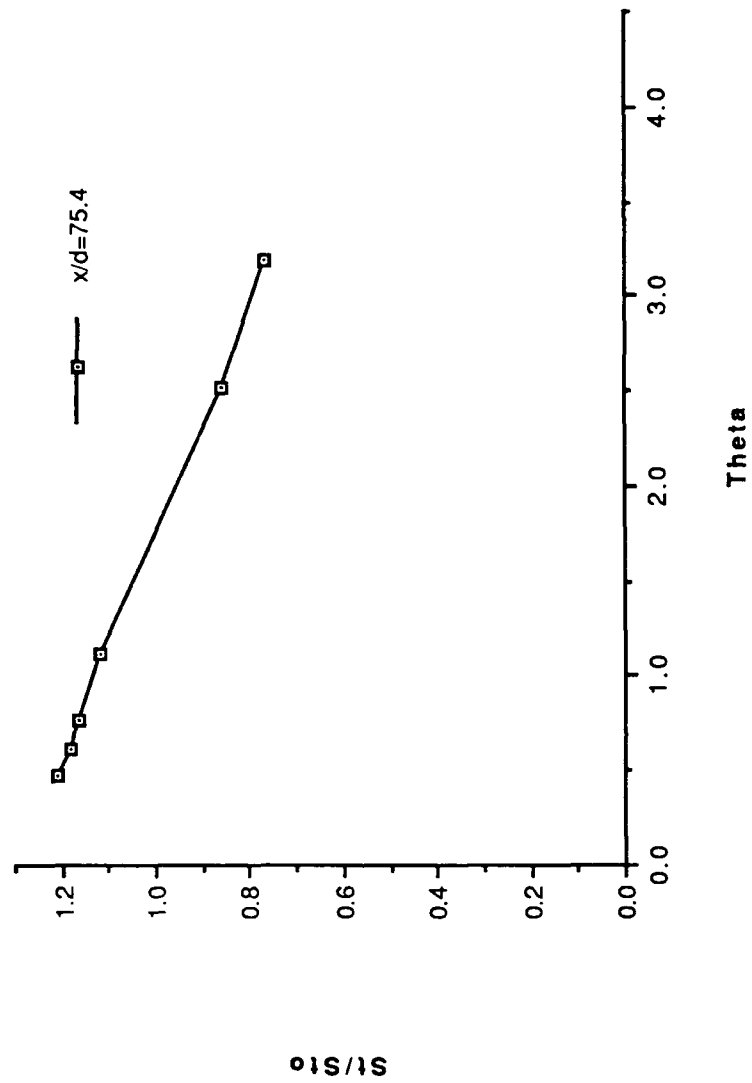


Figure 57. St/St_0 vs θ , Compound Angle, 2 rows, $m=1.74$, $x/d=75.4$, $z=0.0$.

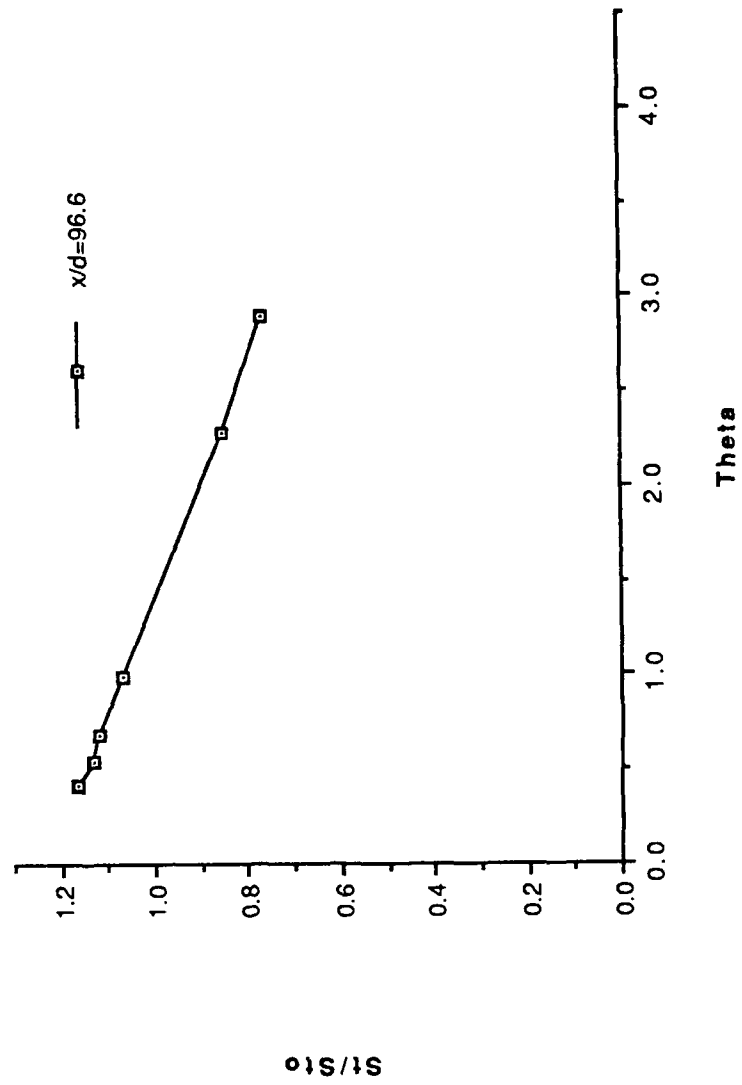


Figure 58. St/St_0 vs θ , Compound Angle, 2 rows, $m=1.74$, $x/d=96.6$, $z=0.0$.

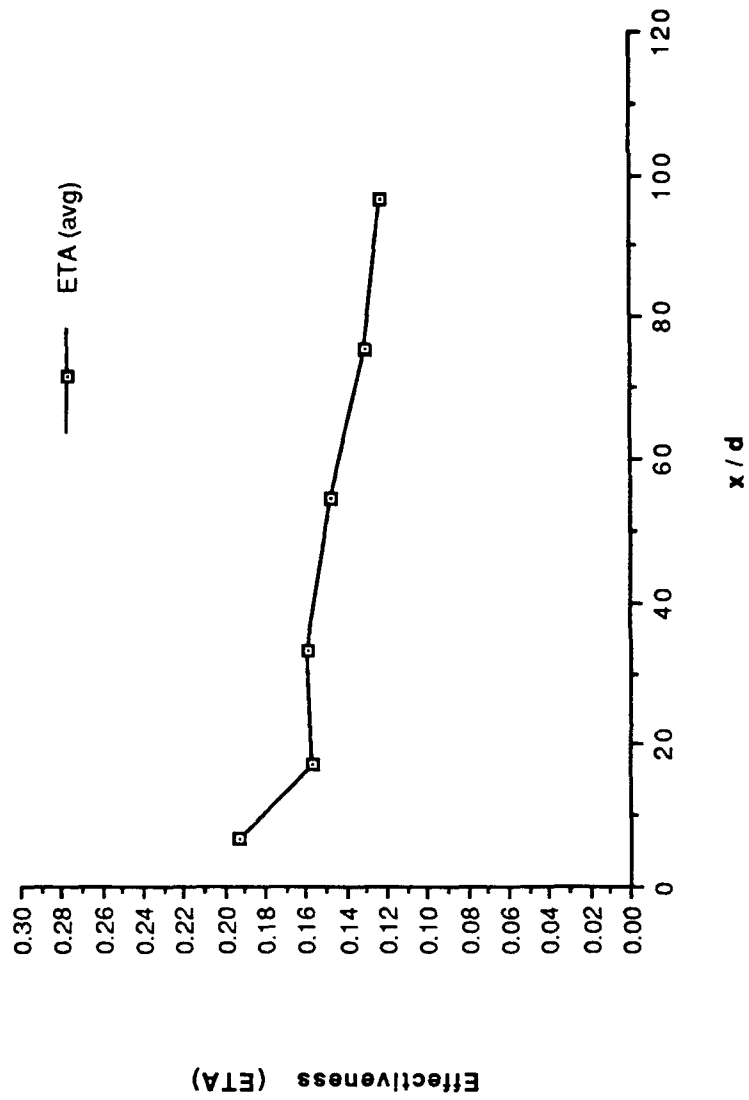


Figure 59. η , vs x/d , Compound Angle, 2 rows, $m=1.74$, Spanwise Average.

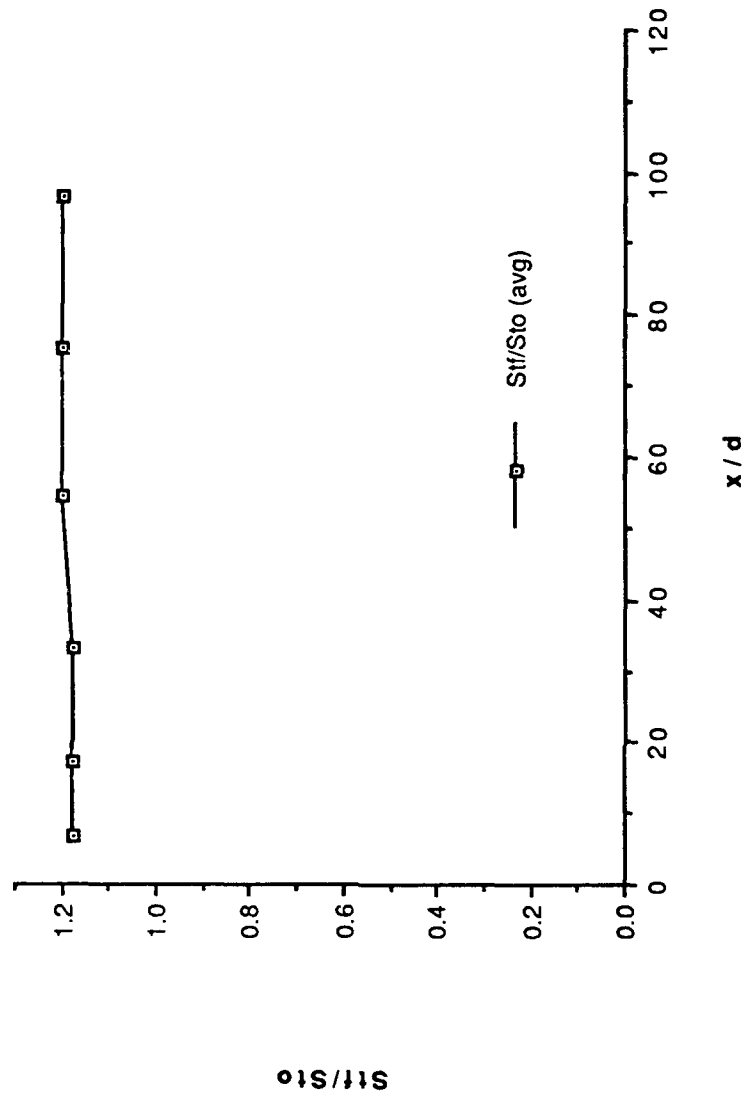


Figure 60. St_f/St_0 vs x/d , Compound Angle, 2 rows, $m=1.74$, Spanwise Average.

FILM-COOLING EFFECTIVENESS

DATE = 103190.0000
 2 ROW COMPOUND ANGLE
 BLOWING RATIO = 1.74
 F.S. VELOCITY = 10 M/S

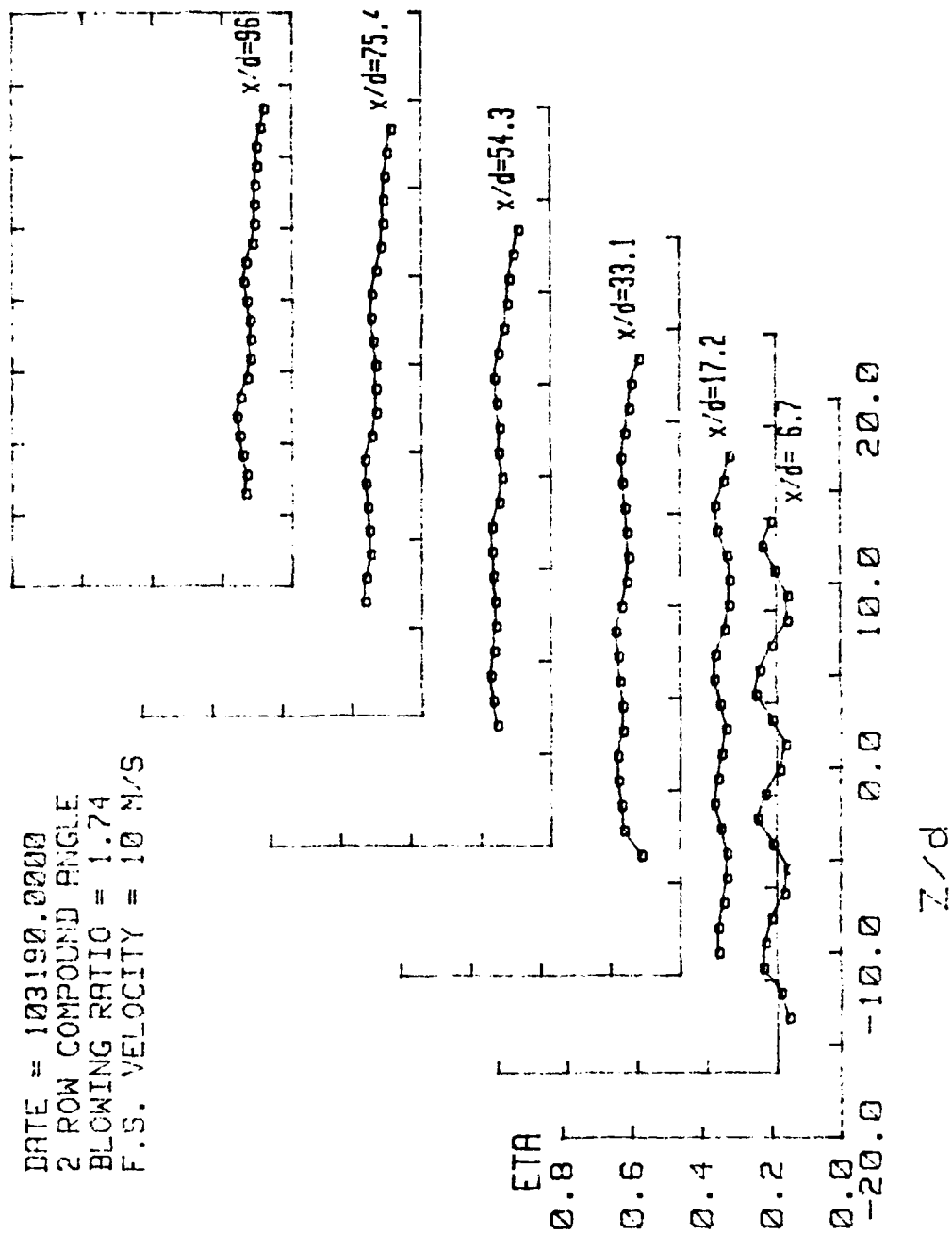


Figure 61. Spanwise Variation of η , Compound Angle, 2 rows, $m=1.74$.

STANTON NUMBER RATIOS

DATE = 103190.1143
 THETA=1.355
 BLOWING RATIO = 1.74
 F.S. VELOCITY = 10 M/S

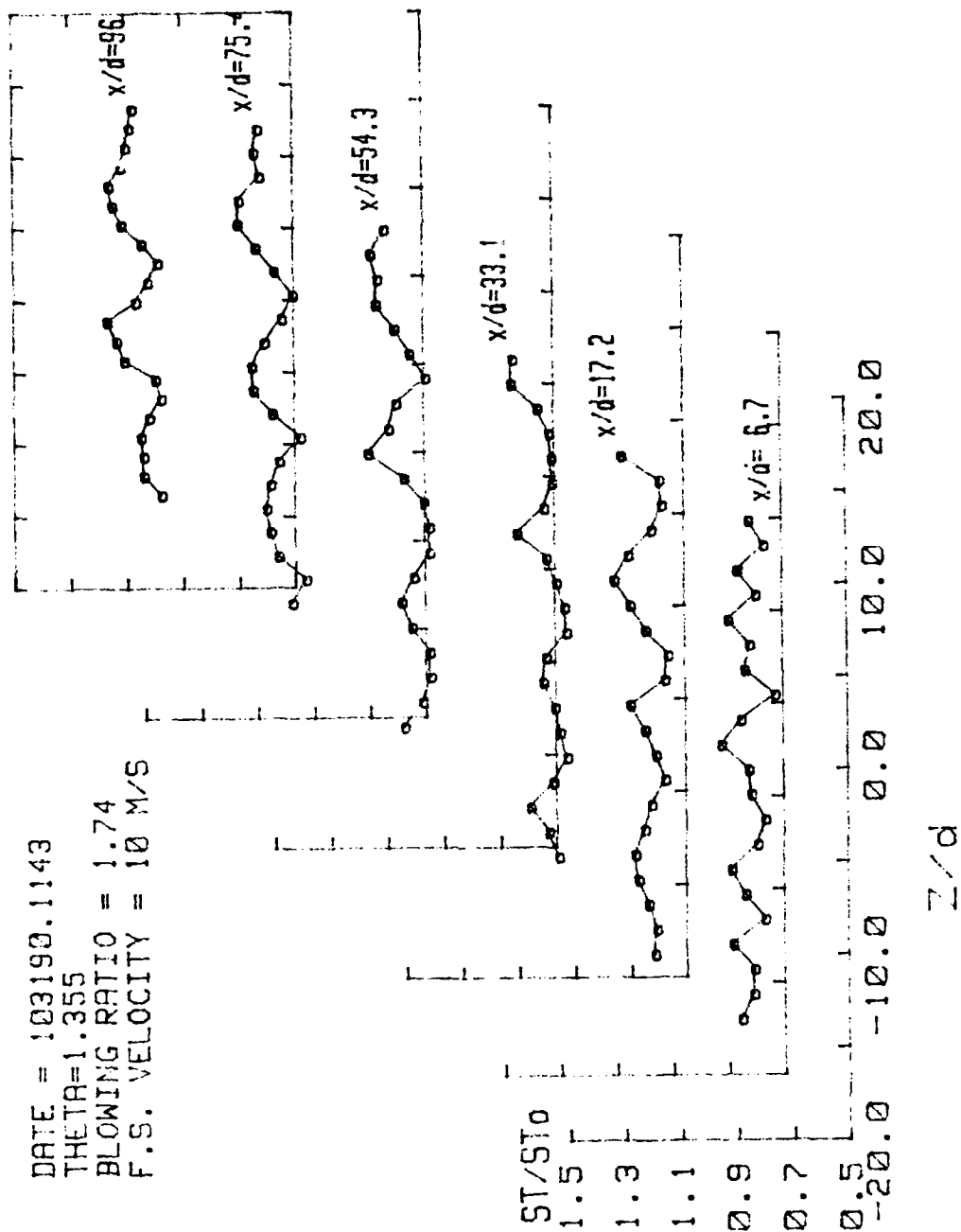


Figure 62. Spanwise Variation of St/St_0 , Compound Angle, 2 rows, $m=1.74$, $\theta=1.355$.

ISO-ENERGETIC STANTON # RATIO

DATE = 103190.0000
 2 ROW COMPOUND ANGLE
 BLOWING RATIO = 1.74
 F.S. VELOCITY = 10 M/S

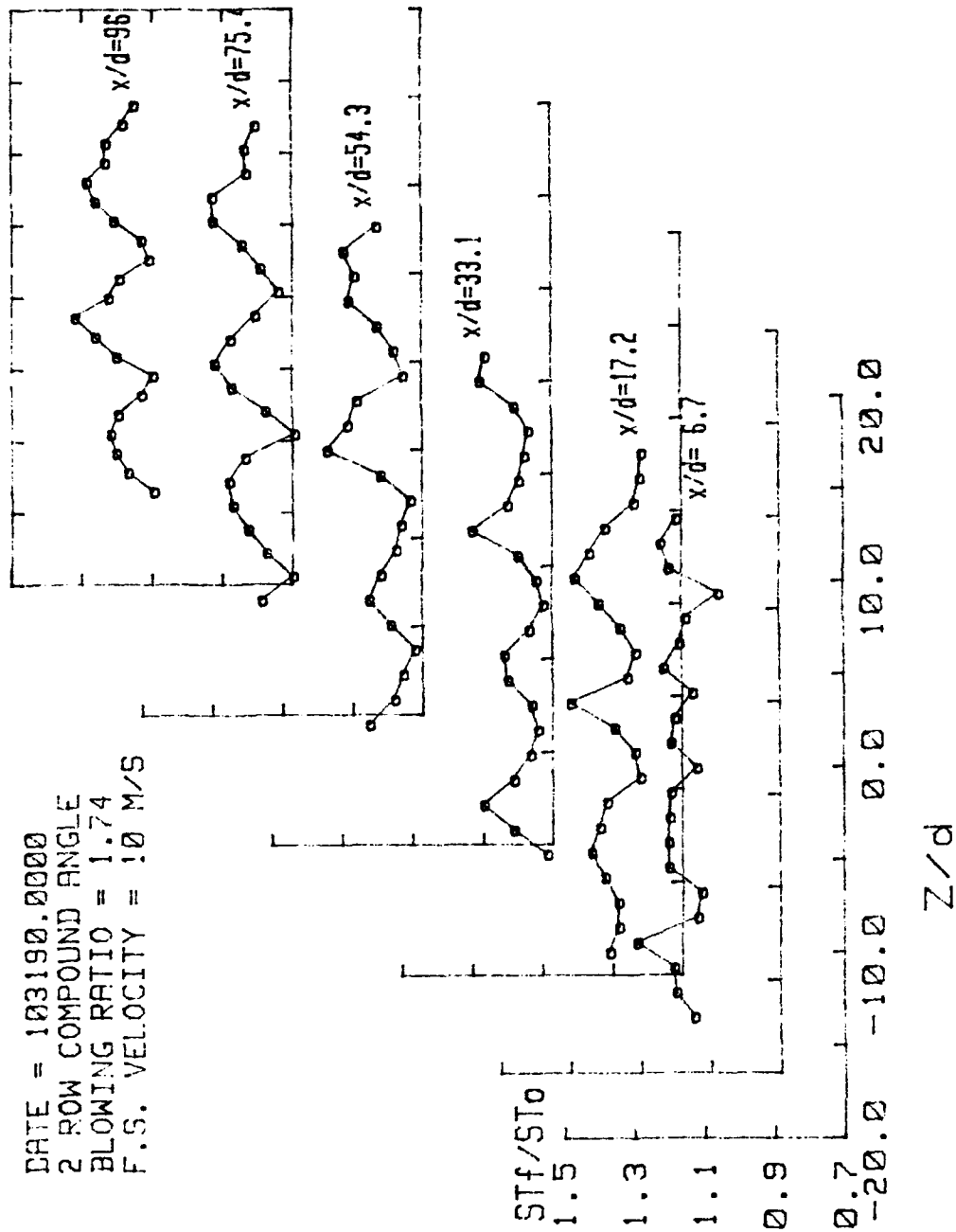


Figure 63. Spanwise Variation of St_f/St_0 , Compound Angle, 2 rows, $m=1.74$.

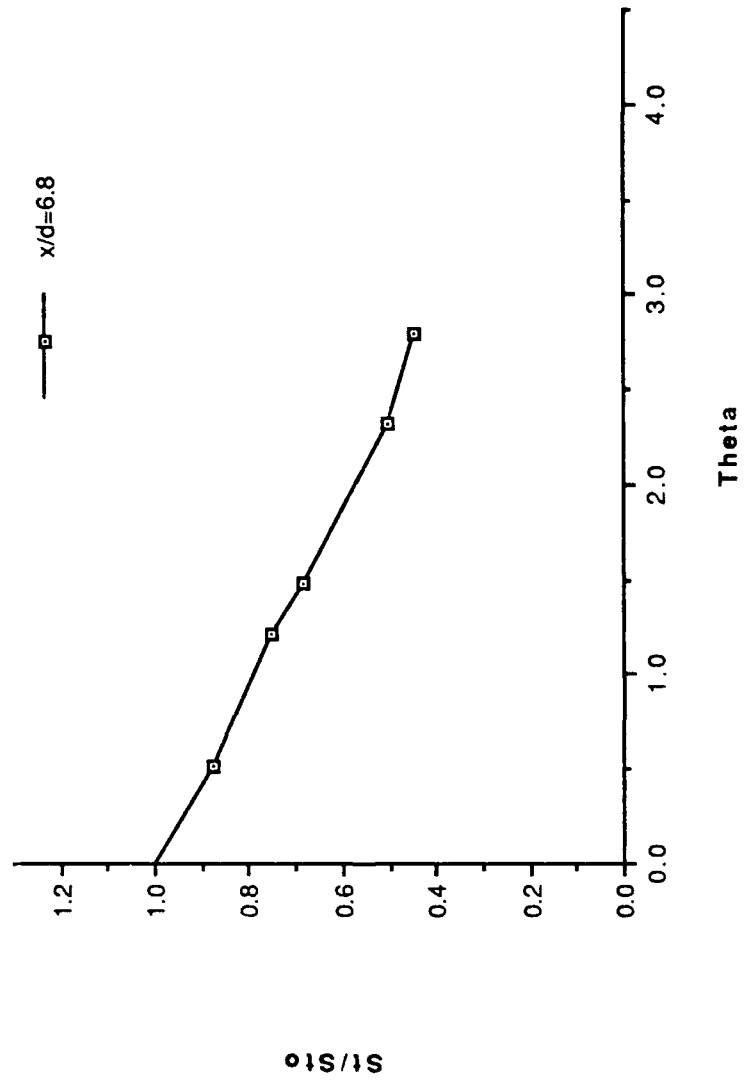


Figure 64. St/St_0 vs θ , Simple Angle, 1 row, $m=0.5$, $x/d=6.8$, $z=0.0$.

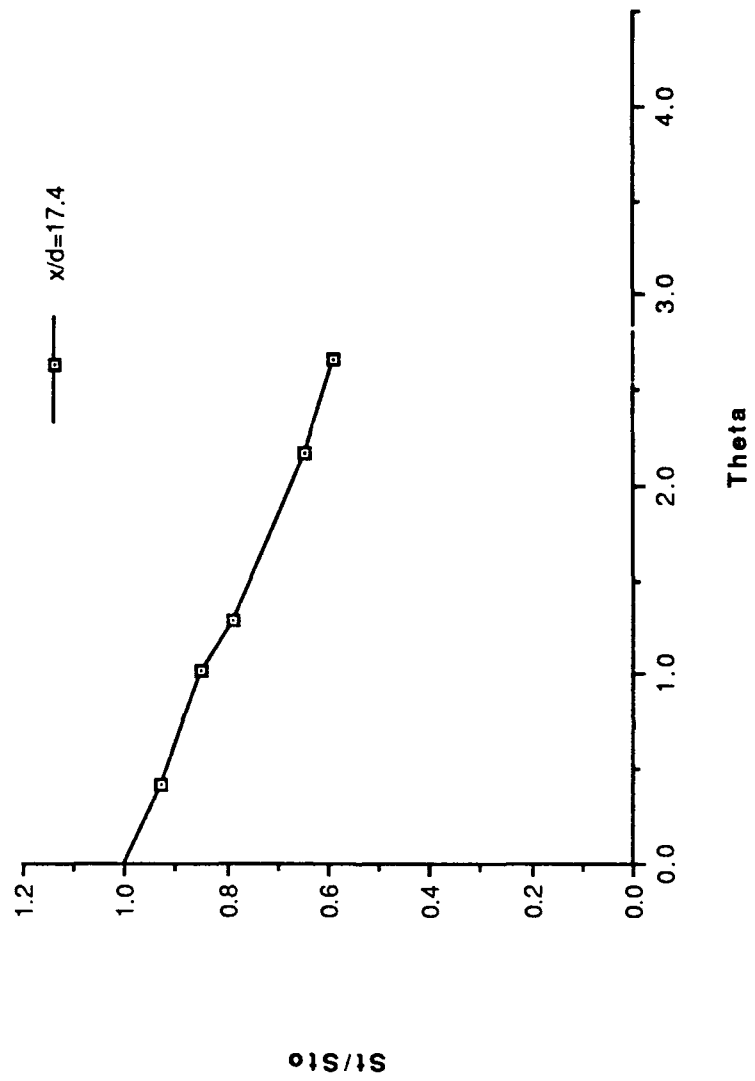


Figure 65. St/St_0 vs θ , Simple Angle, 1 row, $m=0.5$, $x/d=17.4$, $z=0.0$.

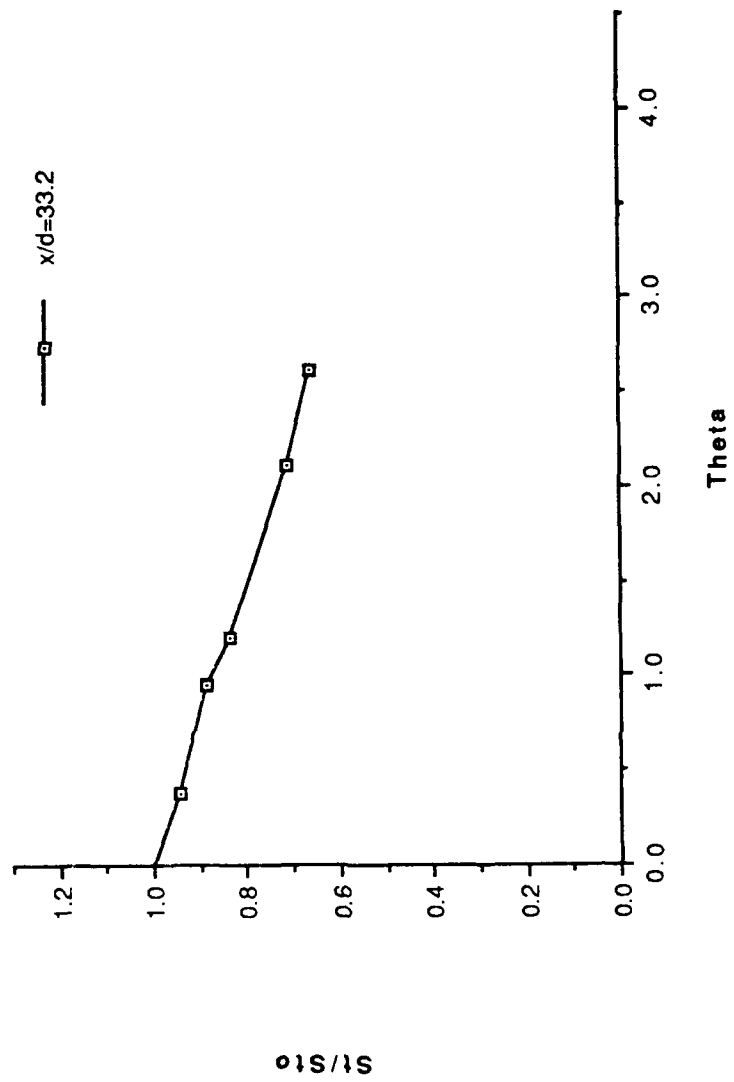


Figure 66. St/St_0 vs θ , Simple Angle, 1 row, $m=0.5$, $x/d=33.2$, $z=0.0$.

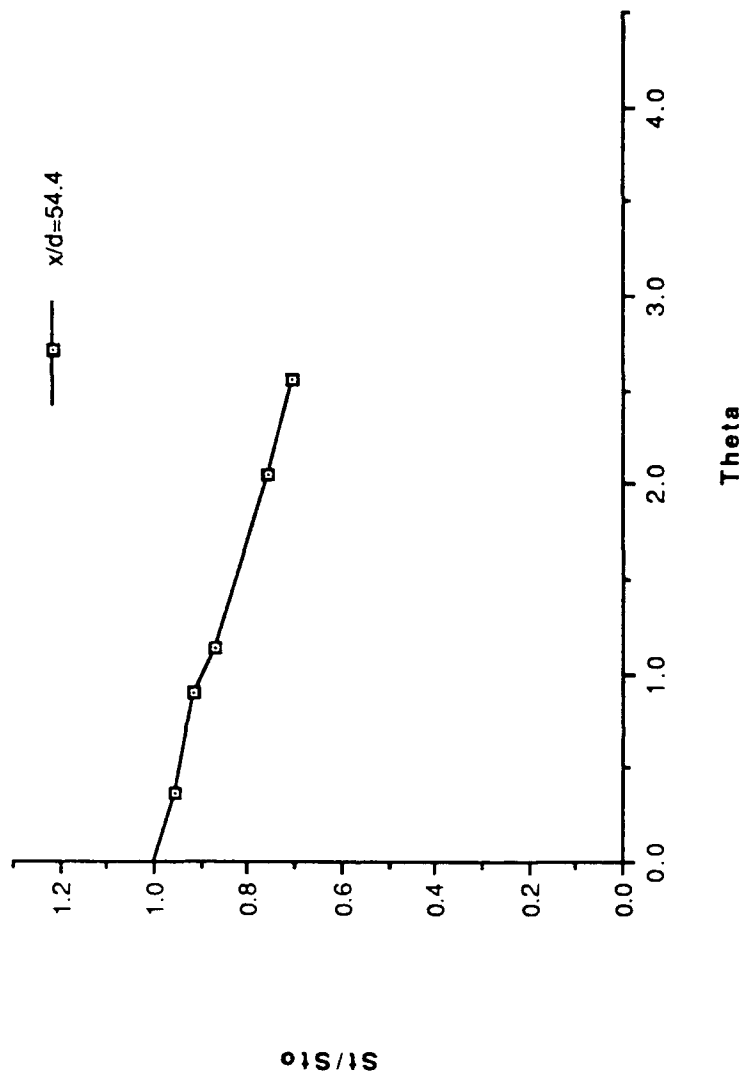


Figure 67. St/St_0 vs θ , Simple Angle, 1 row, $m=0.5$, $x/d=54.4$, $z=0.0$.

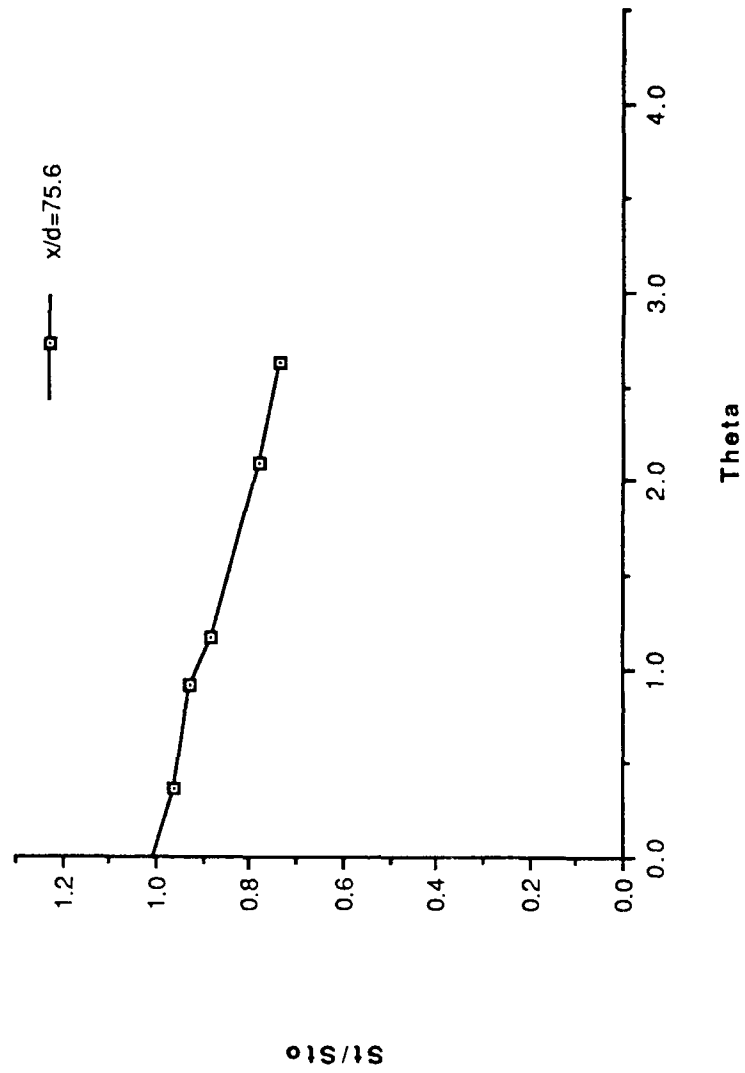


Figure 68. St/St_0 vs θ , Simple Angle, 1 row, $m=0.5$, $x/d=75.6$, $z=0.0$.

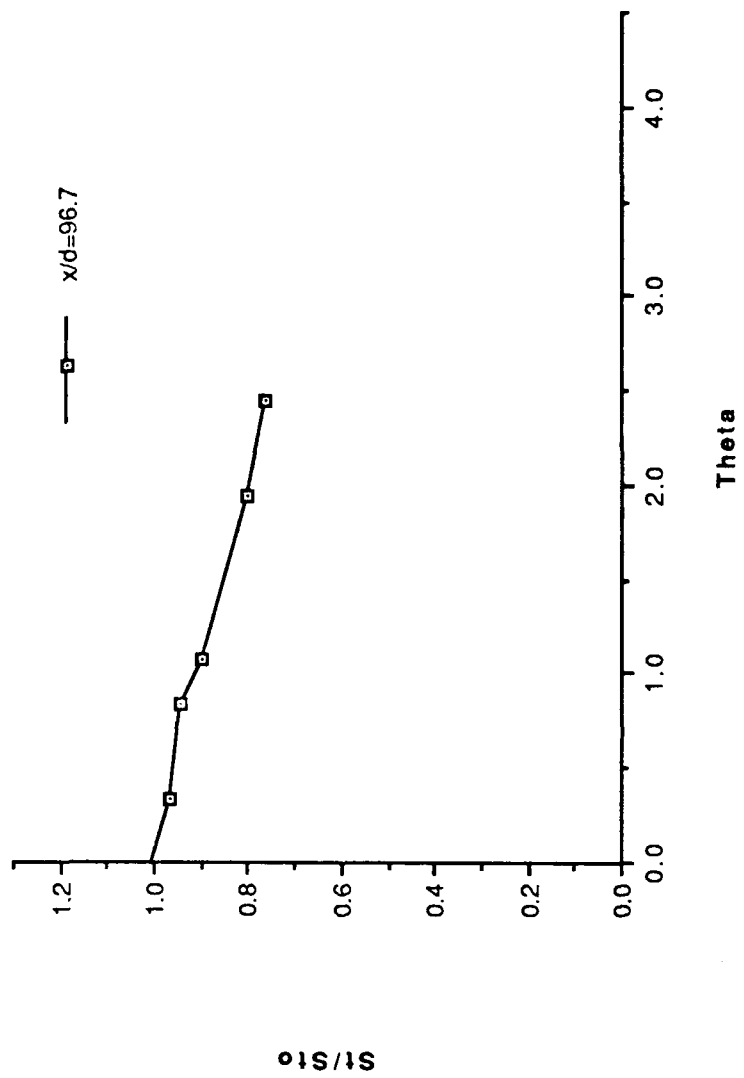


Figure 69. St/St_0 vs θ , Simple Angle, 1 row, $m=0.5$, $x/d=96.7$, $z=0.0$.

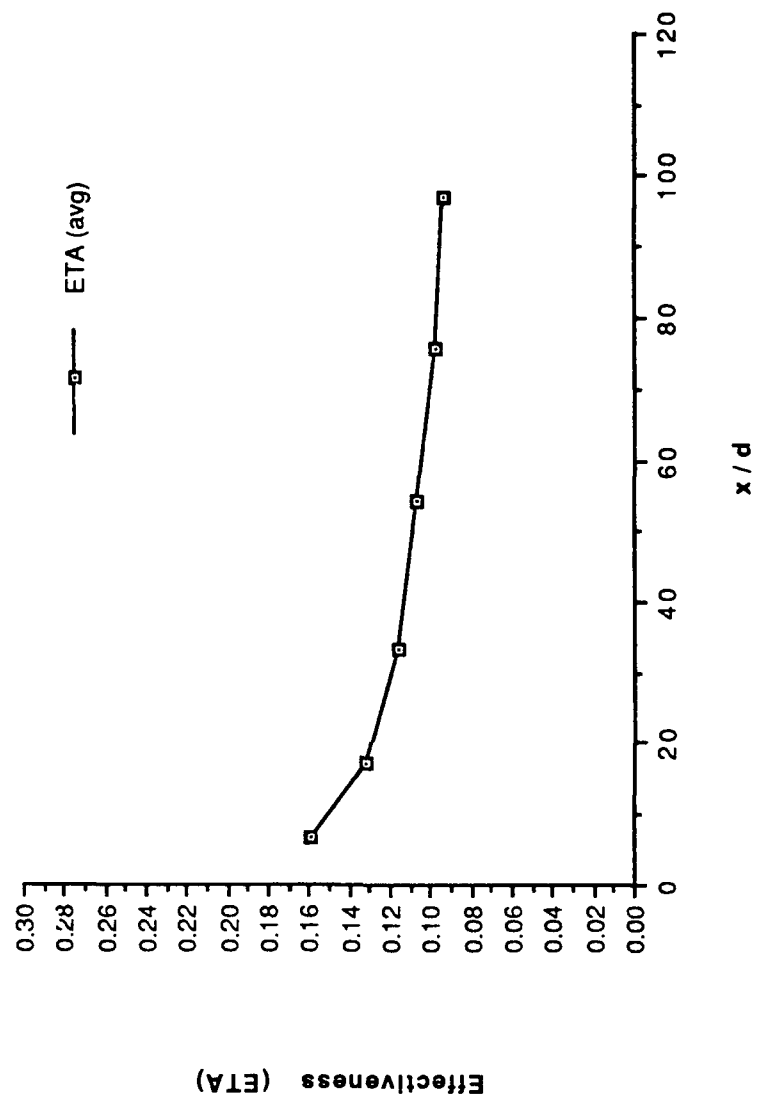


Figure 70. η , vs x/d , Simple Angle, 1 row, $m=0.5$, Spanwise Average.

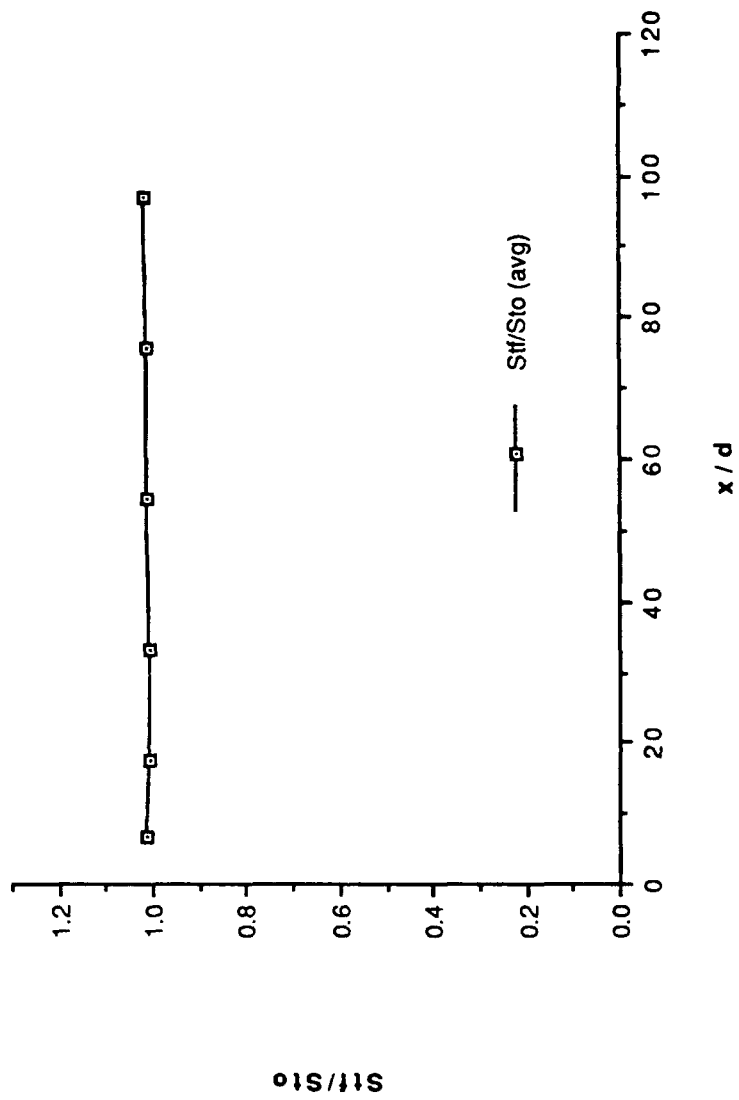


Figure 71. St_f/St_0 vs x/d , Simple Angle, 1 row, $m=0.5$, Spanwise Average.

FILM-COOLING EFFECTIVENESS

DATE = 10491.0000
 1 ROW SIMPLE ANGLE
 BLOWING RATIO = .5
 F.S. VELOCITY = 10 M/S

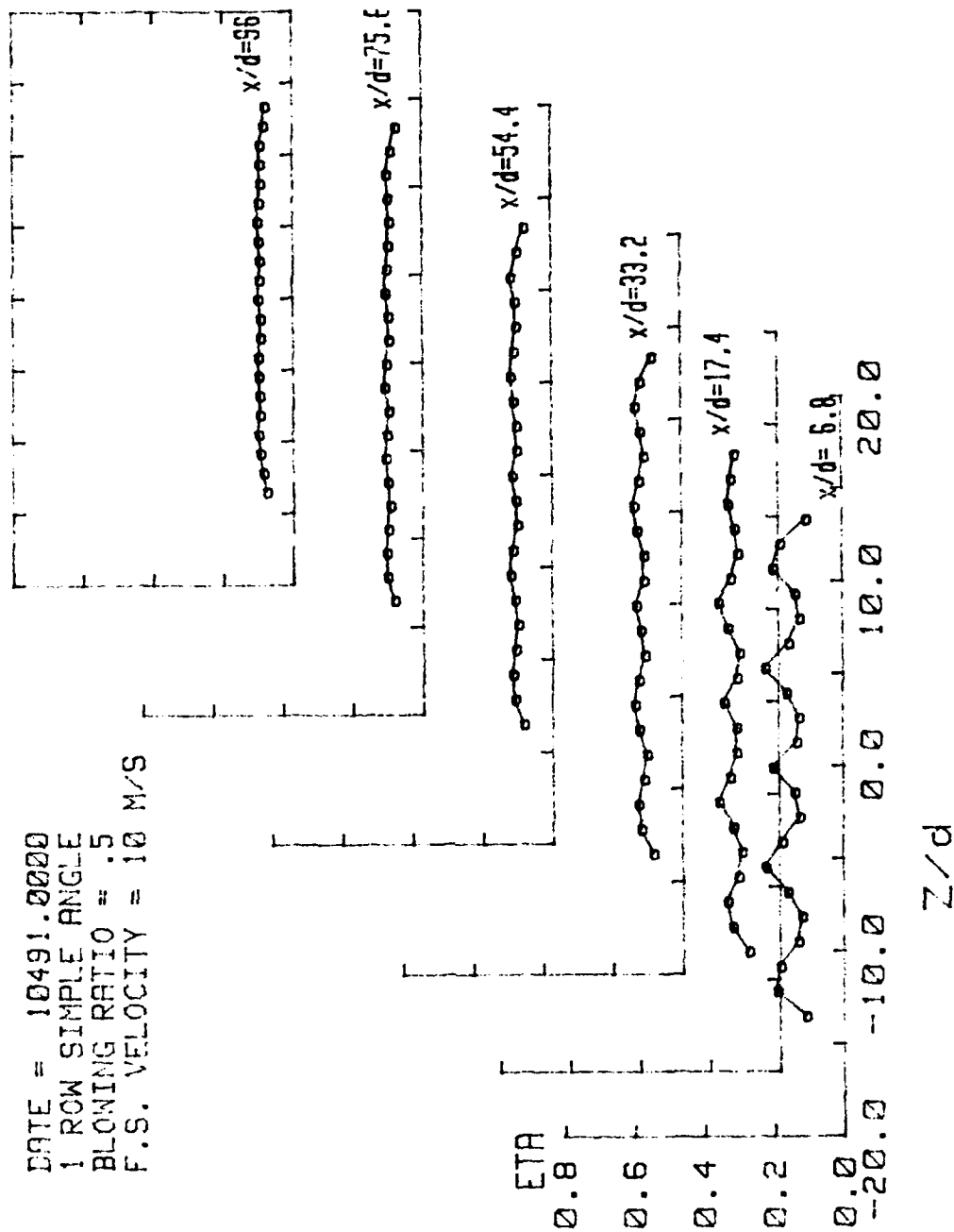


Figure 72. Spanwise Variation of η , Simple Angle, 1 row, $m=0.5$.

STANTON NUMBER RATIOS

DATE = 10491.1558
 THETA=1.477
 BLOWING RATIO = .5
 F.S. VELOCITY = 10 M/S

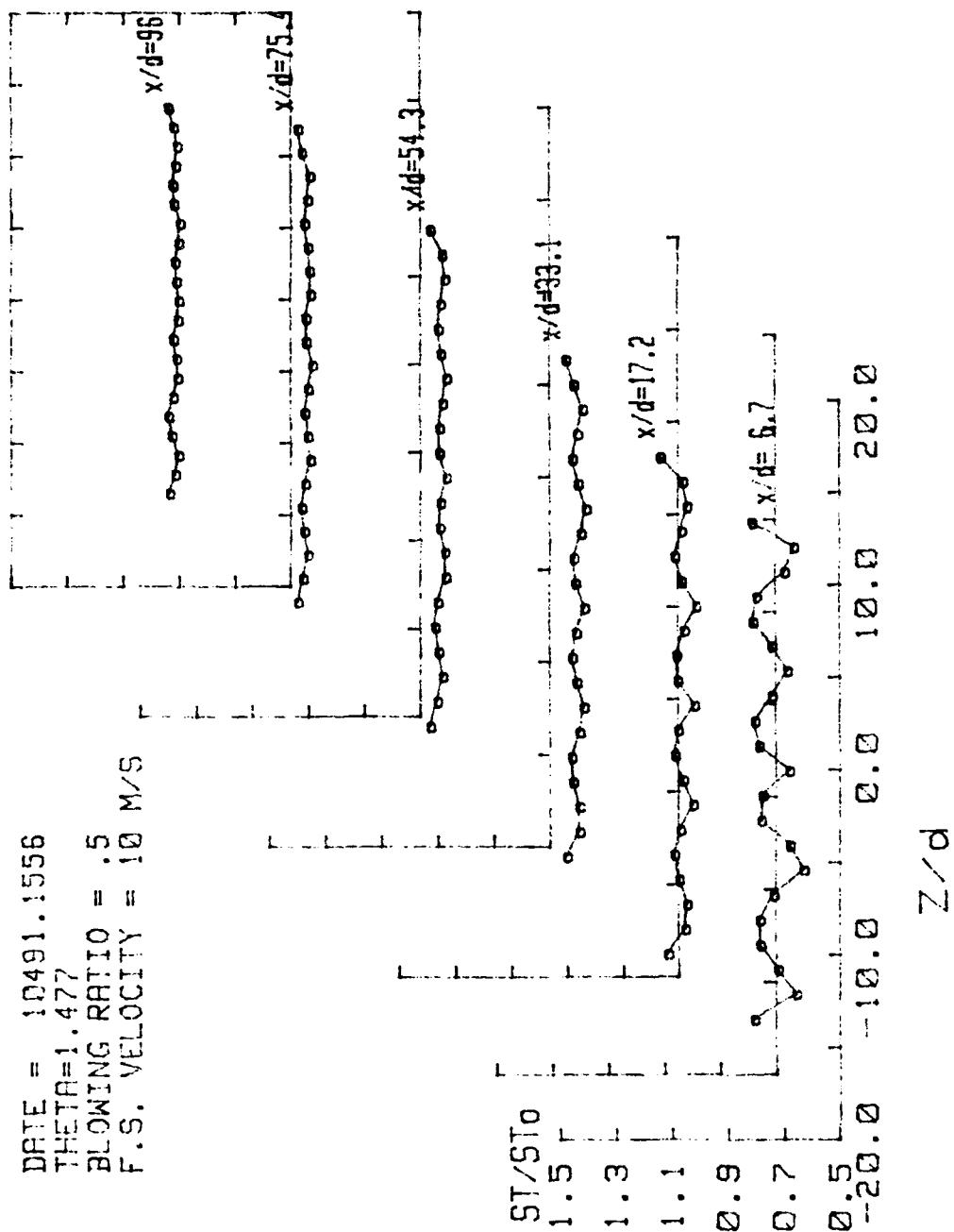


Figure 73. Spanwise Variation of St/St_0 , Simple Angle, 1 row, $m=0.5$, $\theta=1.477$.

ISO-ENERGETIC STANTON # RATIO

DATE = 10491.0000
 1 ROW SIMPLE ANGLE
 BLOWING RATIO = .5
 F.S. VELOCITY = 10 M/S

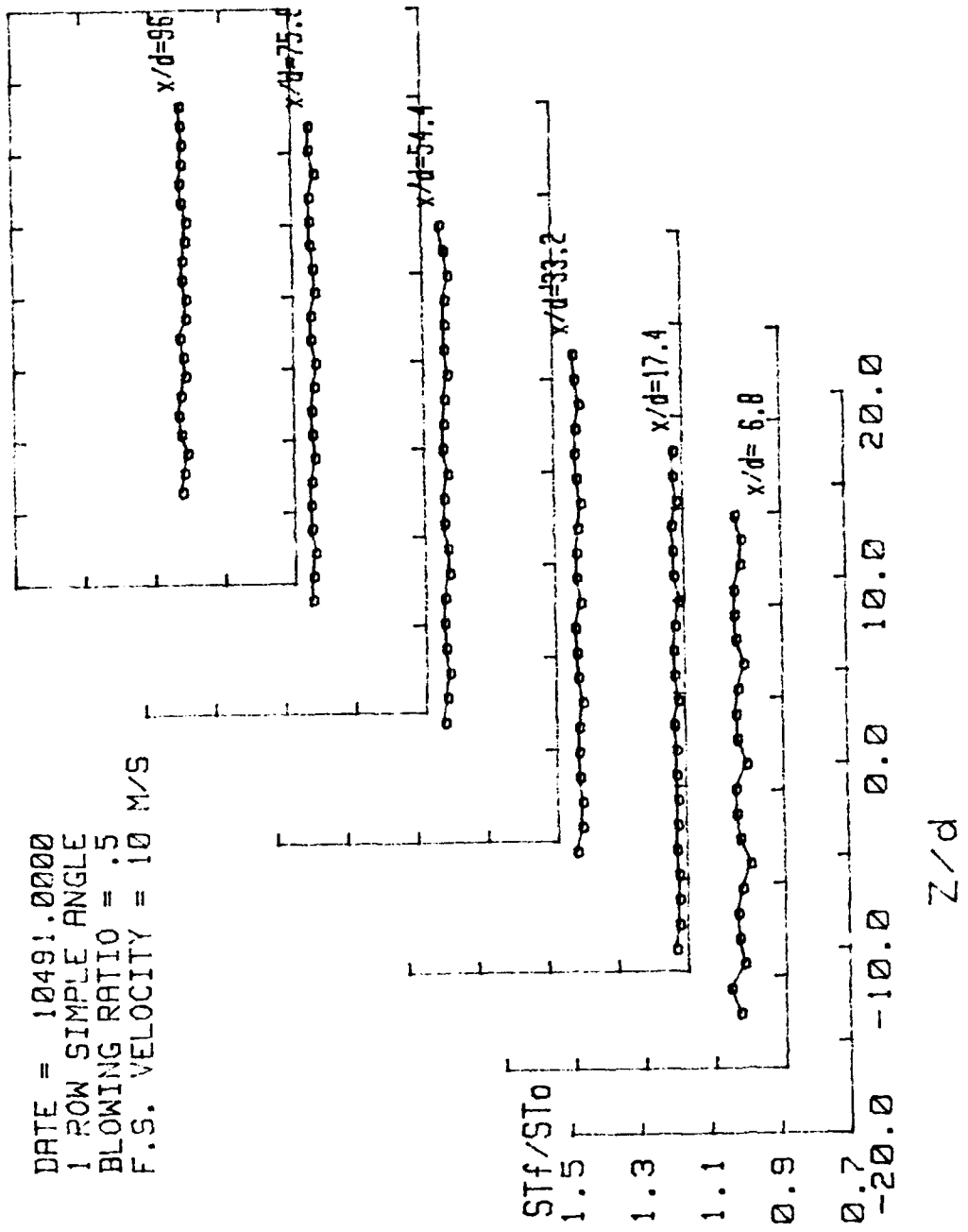
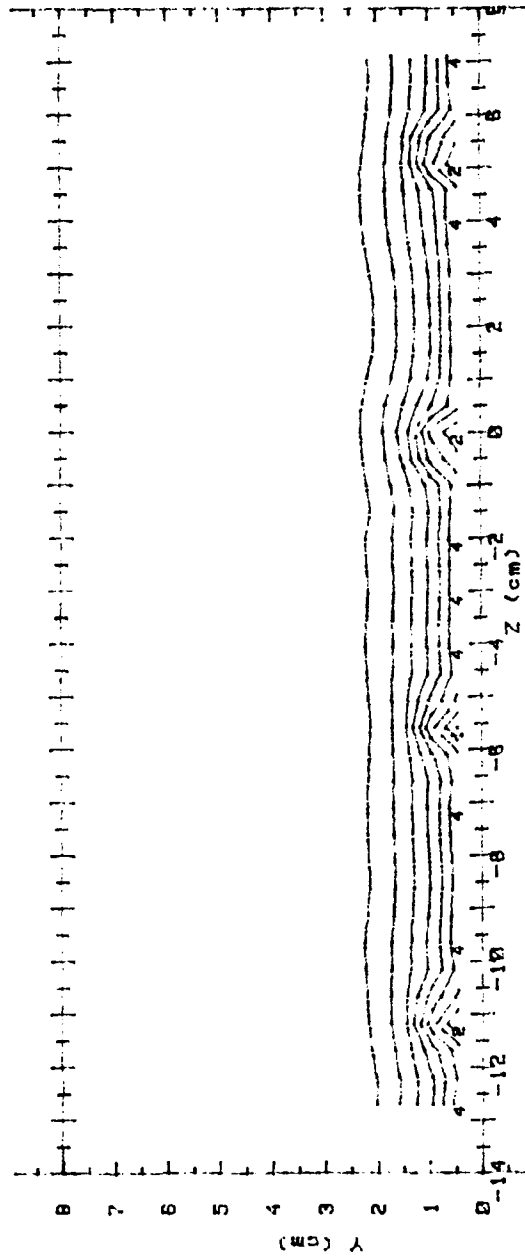


Figure 74. Spanwise Variation of St_f/St_0 , Simple Angle, 1 row, $m=0.5$.

RUN #11451.0044

Ux

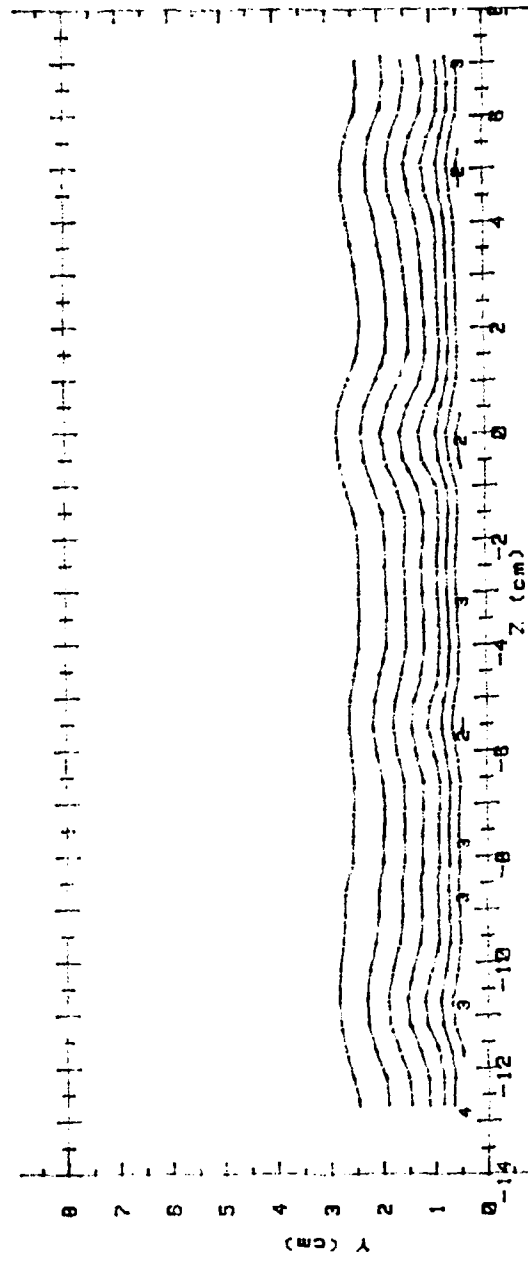


Ux(m/s) RANGES 1 ROW m=0.5 x/d = 9.4

Figure 75. Streamwise Velocity Field, Simple, 1 row, m=0.5, x/d=9.4.

RUN #11291.0831

Ux



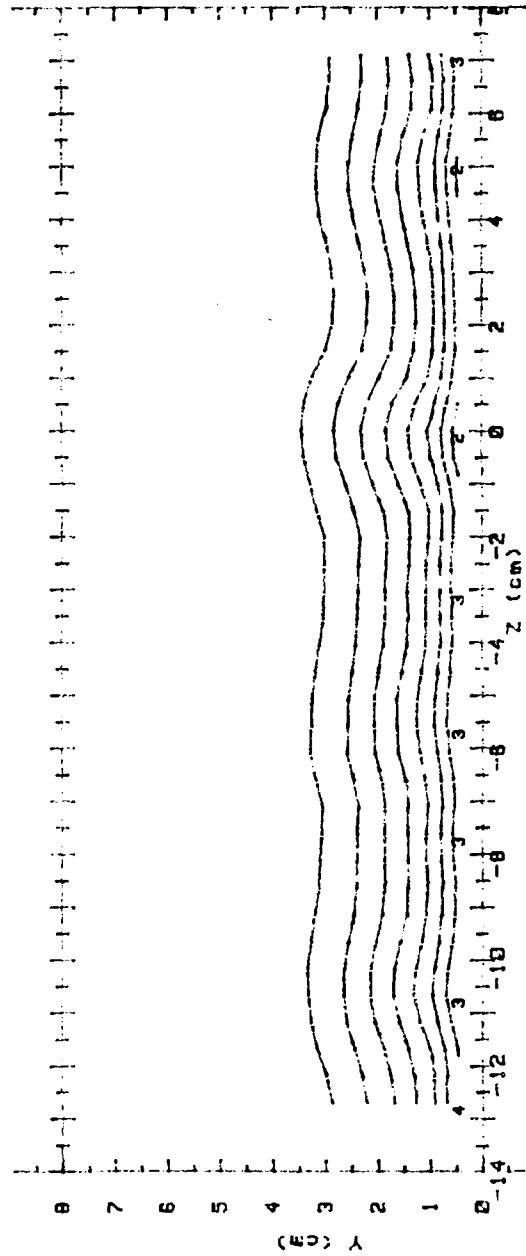
Ux (m/s) RANGES 1 ROW m=0.5 x/d = 43.7

0 :	< 5.5	5 :	7.5 < 8
1 :	5.5 < 6	6 :	8 < 8.5
2 :	6 < 6.5	7 :	8.5 < 9
3 :	6.5 < 7	8 :	9 < 9.5
4 :	7 < 7.5	9 :	9.5 < 10
		10 :	10

Figure 76. Streamwise Velocity Field, Simple Angle, 1 row, $m=0.5$, $x/d=43.7$.

RUN #10991.1106

Ux



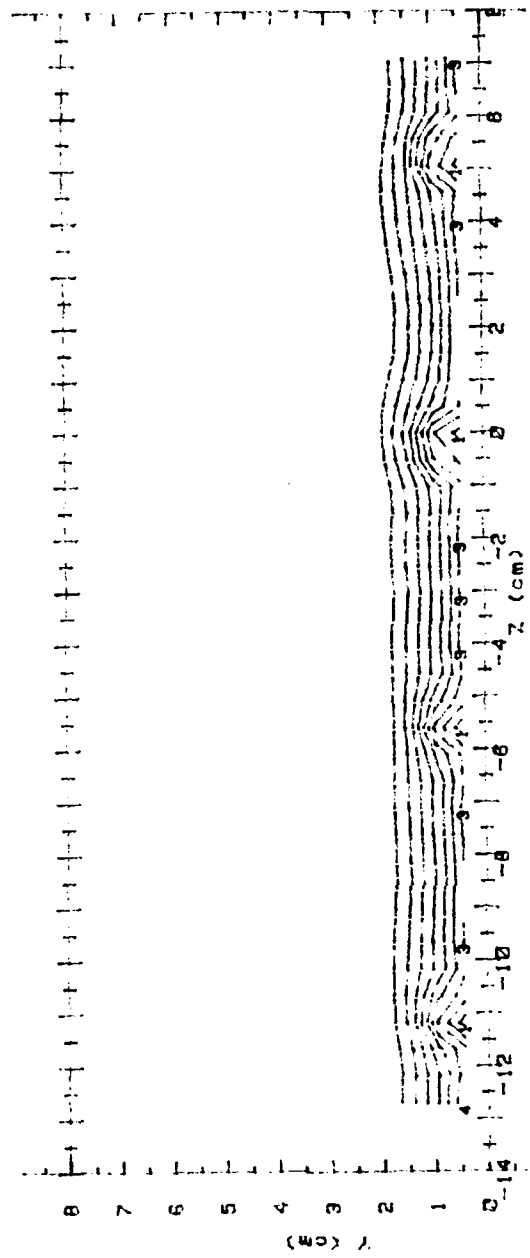
Ux(m/s) RANGES : ROW m=0.5 x/d = 85.2

0 :	< 5.5	5 :	7.5 < 8
1 :	5.5 < 6	6 :	8 < 8.5
2 :	6 < 6.5	7 :	8.5 < 9
3 :	6.5 < 7	8 :	9 < 9.5
4 :	7 < 7.5	9 :	9.5 < 10
		10 :	> 10

Figure 77. Streamwise Velocity Field, Simple Angle, 1 row, $m=0.5$, $x/d=85.2$.

RUN #11491.0844

Ptotal



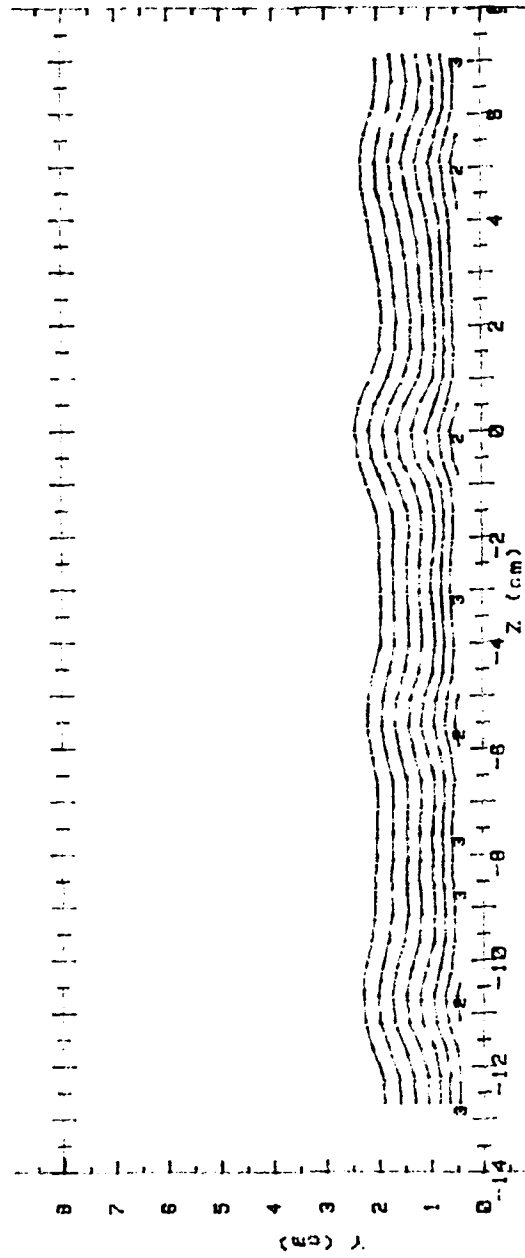
Ptotal (Pascals) RANGES 1 RON m=0.5 x/d=9.4

0 :	< 20	5 :	36 < 40
1 :	20 < 24	6 :	40 < 44
2 :	24 < 28	7 :	44 < 48
3 :	28 < 32	8 :	48 < 52
4 :	32 < 36	9 :	52 < 56
		10 :	56

Figure 78. Streamwise Pressure Field, Simple Angle, 1 row, $m=0.5$, $x/d=9.4$.

RUN #11291.0831

Ptotal



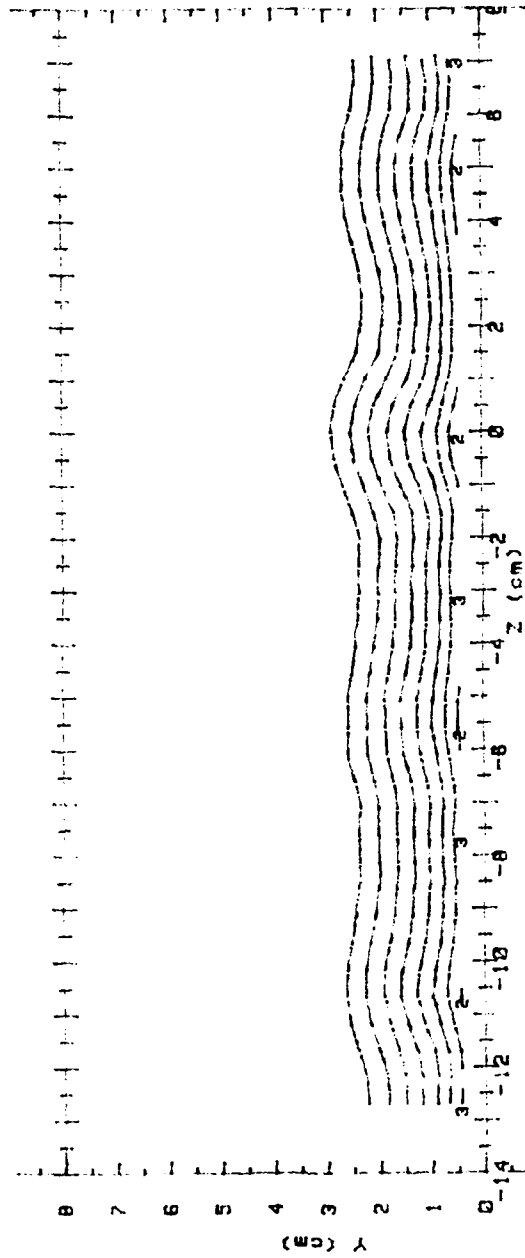
Ptotal(Pascals) RANGES 1 ROW m=0.5 x/d= 43.7

0 :	< 20	5 :	36 < 40
1 :	20 < 24	6 :	40 < 44
2 :	24 < 28	7 :	44 < 48
3 :	28 < 32	8 :	48 < 52
4 :	32 < 36	9 :	52 < 56
		10 :	56

Figure 79. Streamwise Pressure Field, Simple Angle, 1 row, $m=0.5$, $x/d=43.7$.

RUN #10991.1105

Ptotal



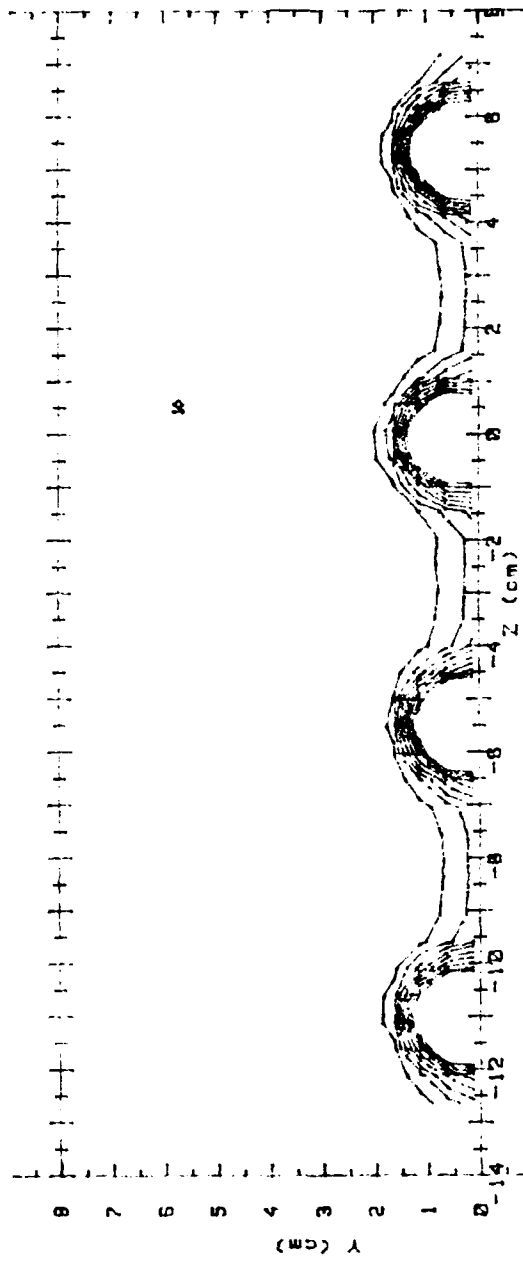
Ptotal (Pascals) RANGES 1 ROW m=0.5 x/d=85.2

0 :	< 20	5 :	36 < 40
1 :	20 < 24	6 :	40 < 44
2 :	24 < 28	7 :	44 < 48
3 :	28 < 32	8 :	48 < 52
4 :	32 < 36	9 :	52 < 56
		10 :	56

Figure 80. Streamwise Pressure Field, Simple Angle, 1 row, $m=0.5$, $x/d=85.2$.

RUN #:0791.2101

T - Tfs



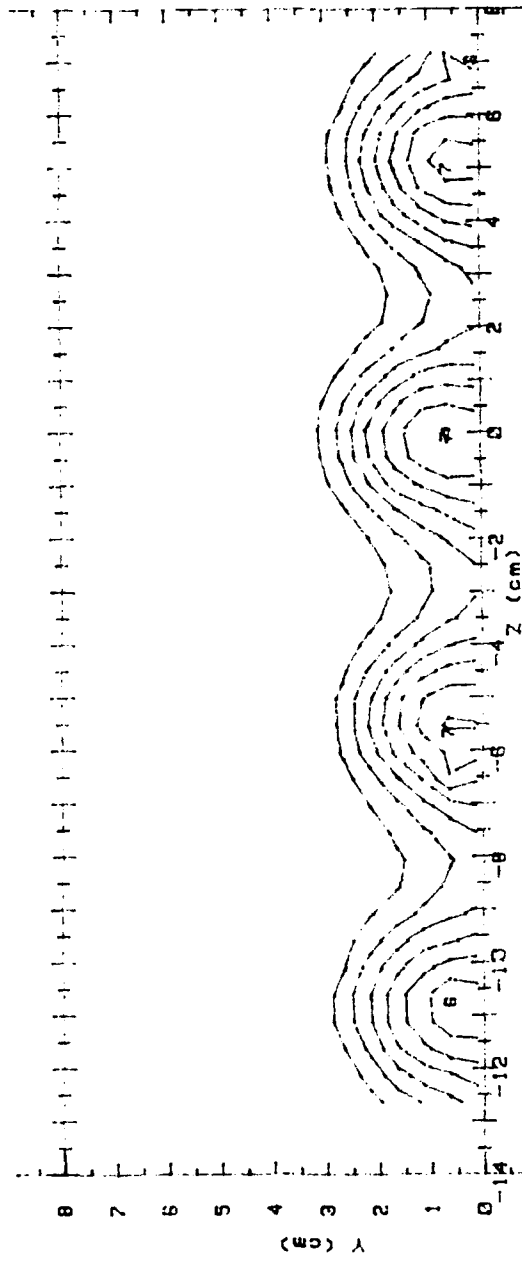
T - Tfs (CELCIUS) RANGES 1 ROW m=0.5 x/d = 9.4

0 :	< .5	5 :	> 2.5	< 3	
1 :	> .5	< 1	6 :	> 3	< 3.5
2 :	> 1	< 1.5	7 :	> 3.5	< 4
3 :	> 1.5	< 2	8 :	> 4	< 4.5
4 :	> 2	< 2.5	9 :	> 4.5	

Figure 81. Streamwise Injectant Distribution, Simple Angle, 1 row, $m=0.5$, $x/d=9.4$.

RUN #10791.1654

T - Tfs



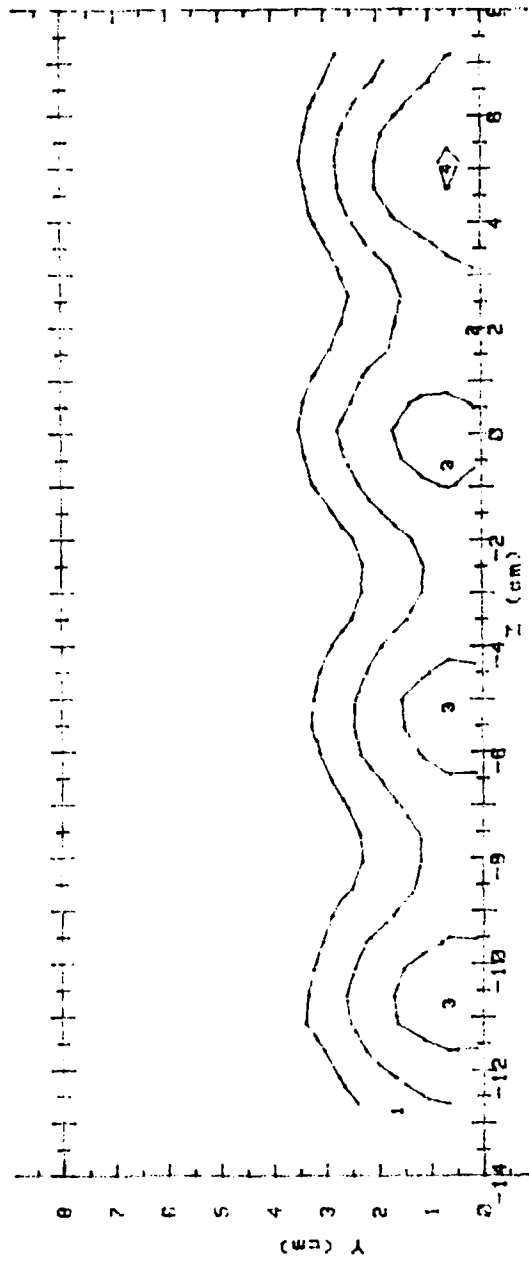
T - Tfs (CELCIUS) RANGES 1 ROW m=0.5 x/d = 43.7

0 :	< .5	5 :	2.5 < 3
1 :	.5 < 1	6 :	3 < 3.5
2 :	1 < 1.5	7 :	3.5 < 4
3 :	1.5 < 2	8 :	4 < 4.5
4 :	2 < 2.5	9 :	4.5

Figure 82. Streamwise Injectant Distribution, Simple Angle, 1 row, $m=0.5$, $x/d=43.7$.

RUN #10791.1119

T - Tfs



T - Tfs (CELCIUS) RANGES 1 ROW m=0.5 x/d = 85.2

0 :	< .5	5 :	2.5 < 3
1 :	.5 < 1	6 :	3 < 3.5
2 :	1 < 1.5	7 :	3.5 < 4
3 :	1.5 < 2	8 :	4 < 4.5
4 :	2 < 2.5	9 :	4.5

Figure 83. Streamwise Injectant Distribution, Simple Angle, 1 row, m=0.5, x/d=85.2.

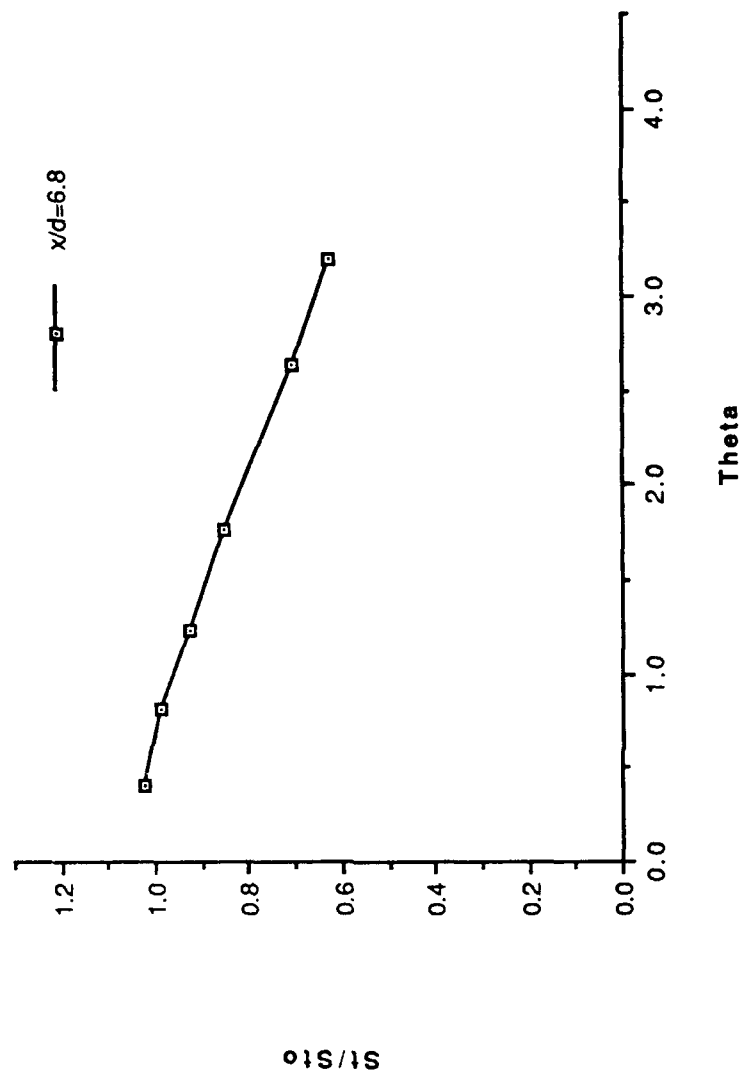


Figure 84. St/St_0 vs θ , Simple Angle, 1 row, $m=1.0$, $x/d=6.8$, $z=0.0$.

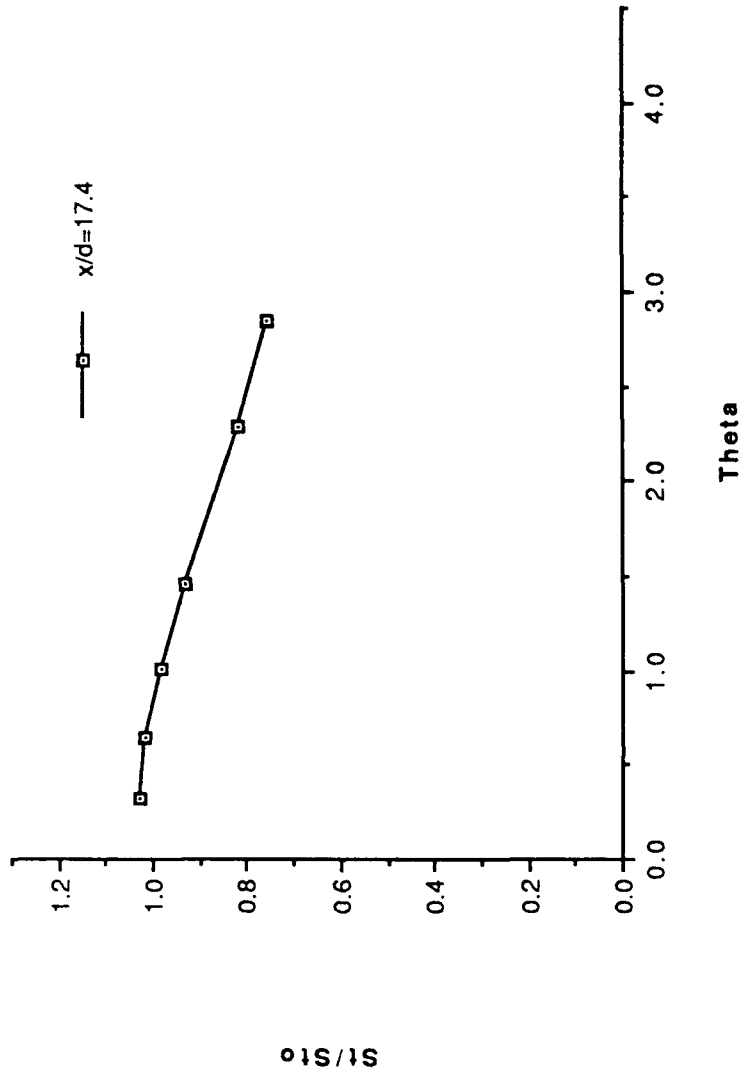


Figure 85. St/St_0 vs θ , Simple Angle, 1 row, $m=1.0$, $x/d=17.4$, $z=0.0$.

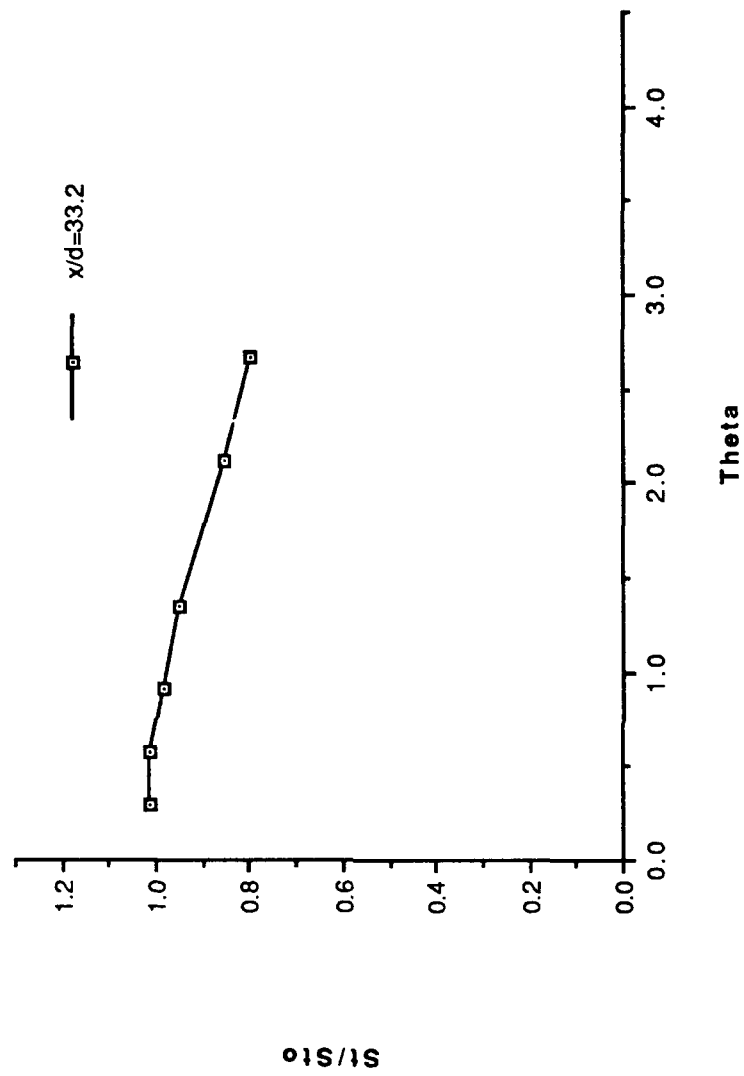


Figure 86. St/St_0 vs θ , Simple Angle, 1 row, $m=1.0$, $x/d=33.2$, $z=0.0$.

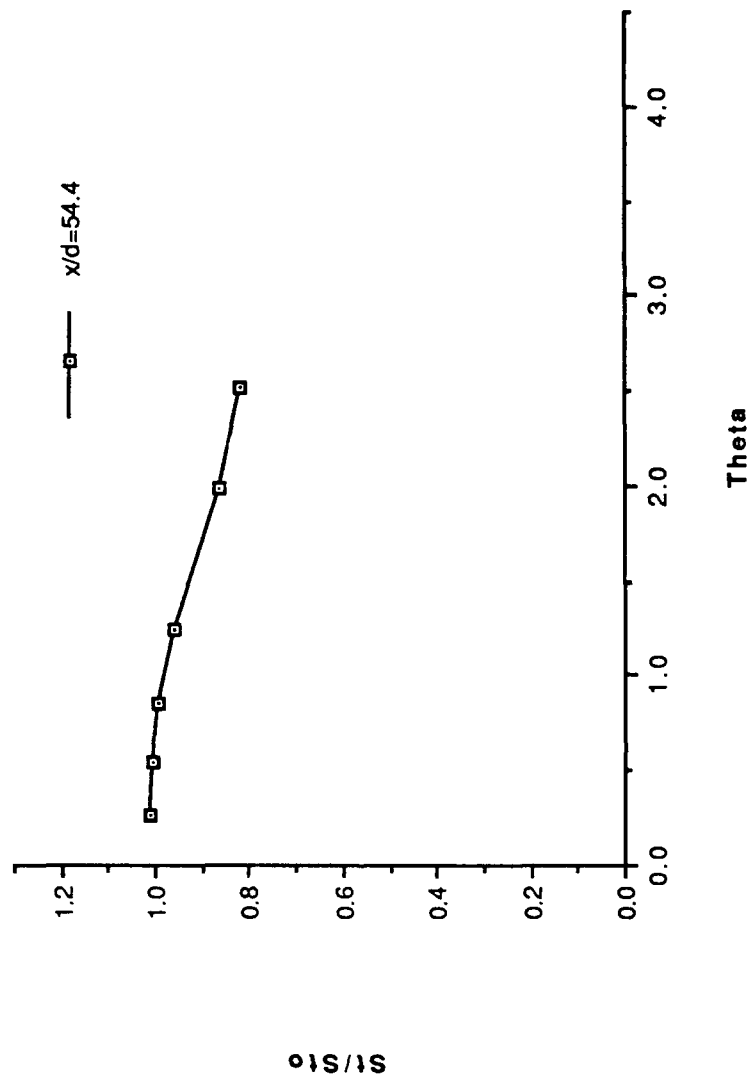


Figure 87. St/St_0 vs θ , Simple Angle, 1 row, $m=1.0$, $x/d=54.4$, $z=0.0$.

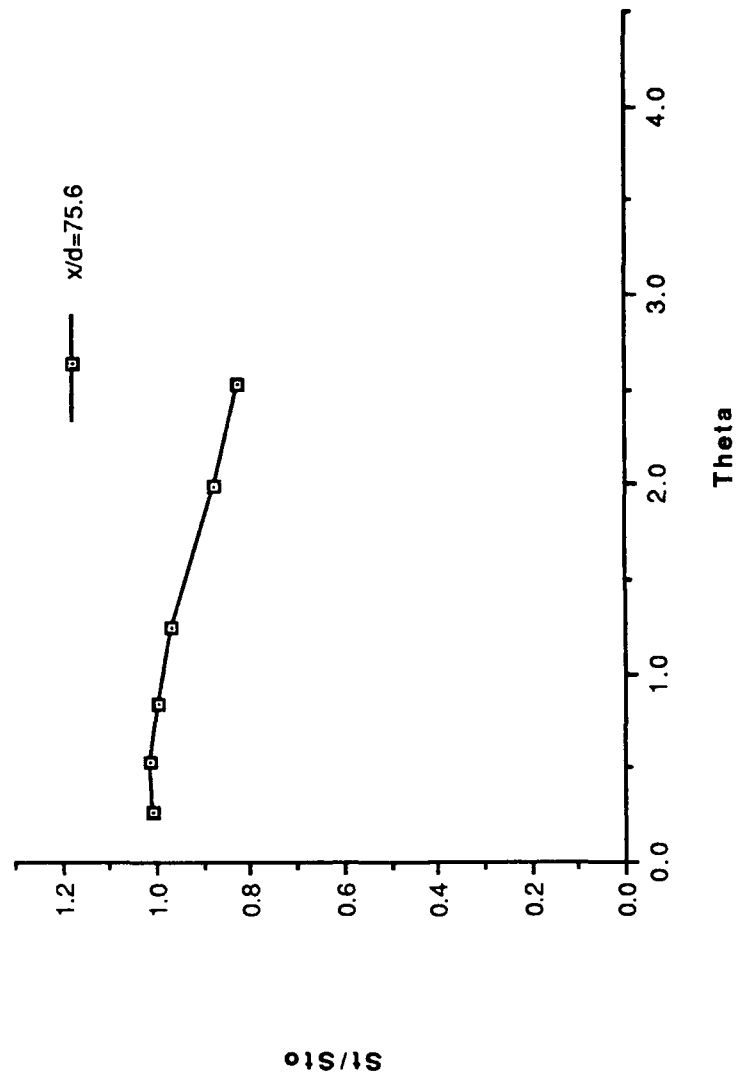


Figure 88. St/St_0 vs θ , Simple Angle, 1 row, $m=1.0$, $x/d=75.6$, $z=0.0$.

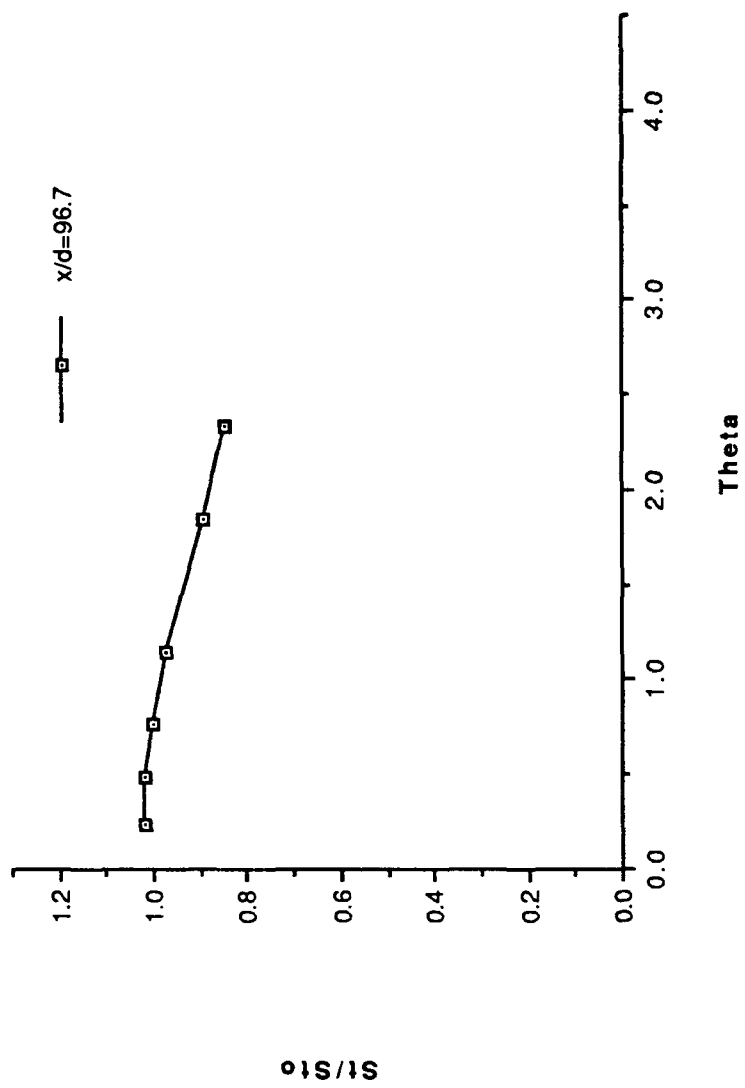


Figure 89. St/St_0 vs θ , Simple Angle, 1 row, $m=1.0$, $x/d=96.7$, $z=0.0$.

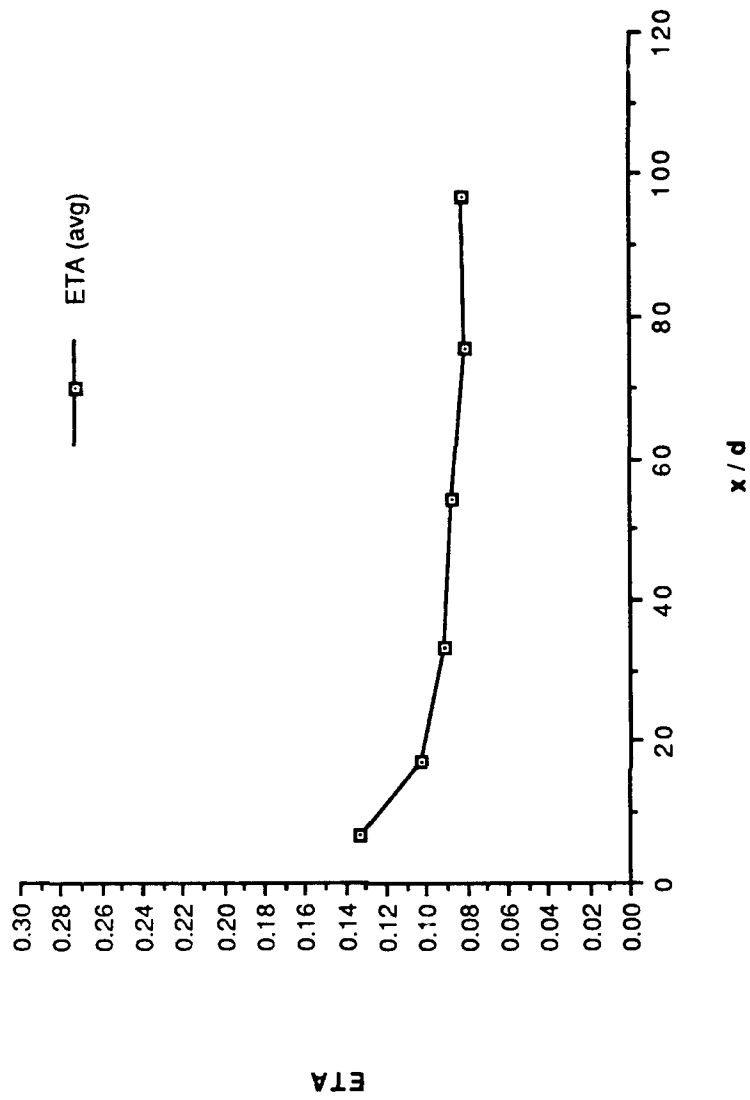


Figure 90. η , vs x/d , Simple Angle, 1 row, $m=1.0$, Spanwise Average.

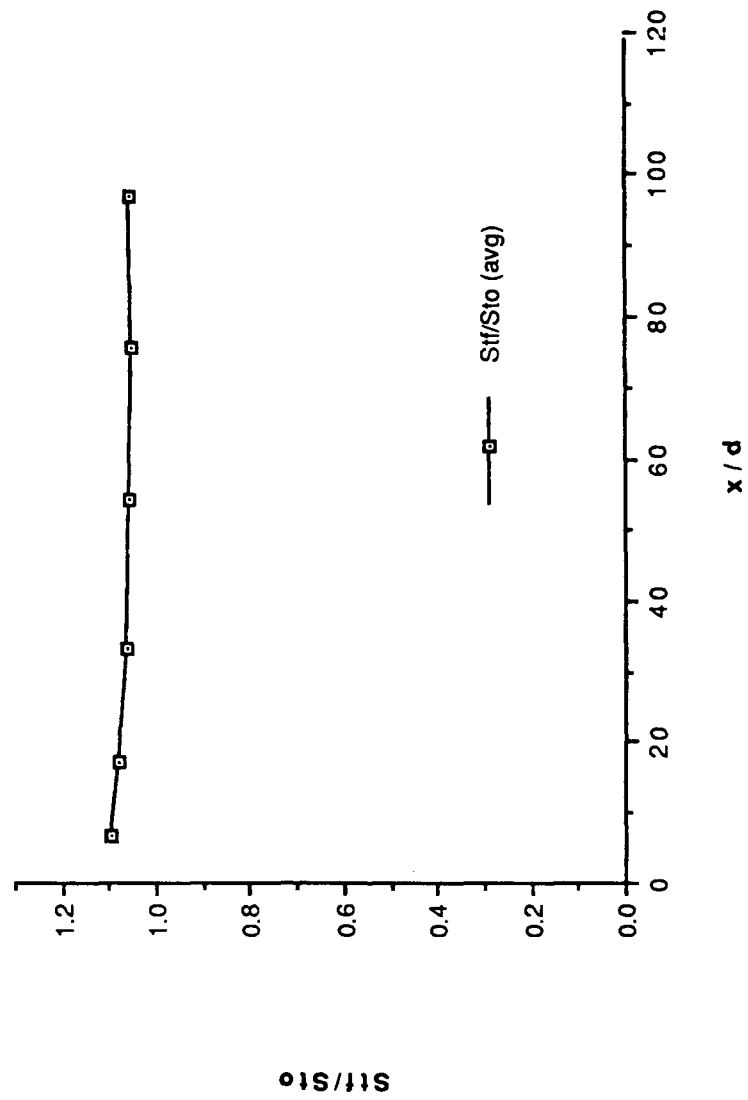


Figure 91. St_f/St_0 vs x/d , Simple Angle, 1 row, $m=1.0$, Spanwise Average.

FILM-COOLING EFFECTIVENESS

DATE = 122090.0000
 1 ROW SIMPLE ANGLE
 BLOWING RATIO = 1
 F.S. VELOCITY = 10 M/S

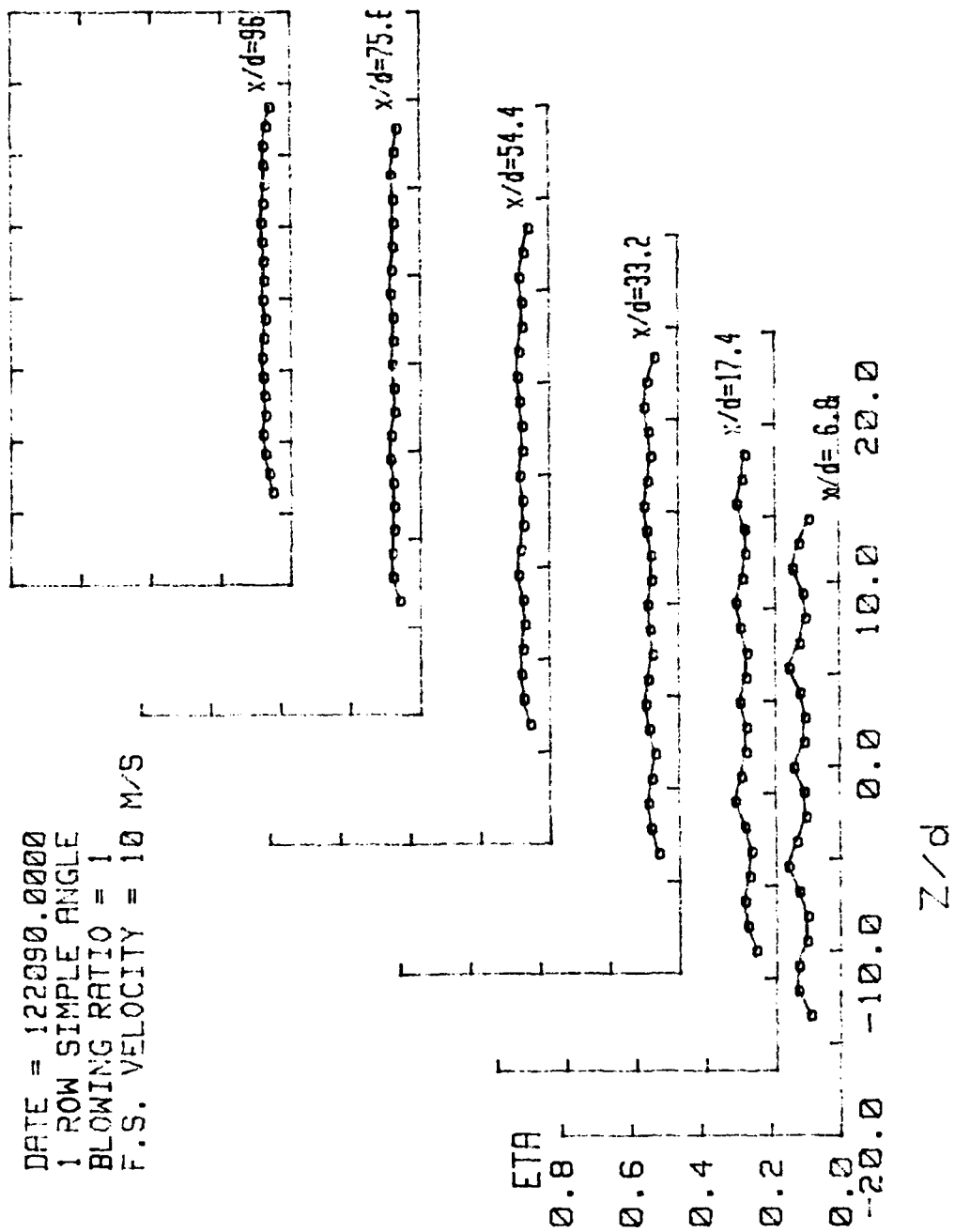


Figure 92. Spanwise Variation of η , Simple Angle, 1 row, $m=1.0$.

STANTON NUMBER RATIOS

DATE = 122098.1601
 THETA=1.644
 BLOWING RATIO = 1
 F.S. VELOCITY = 10 M/S

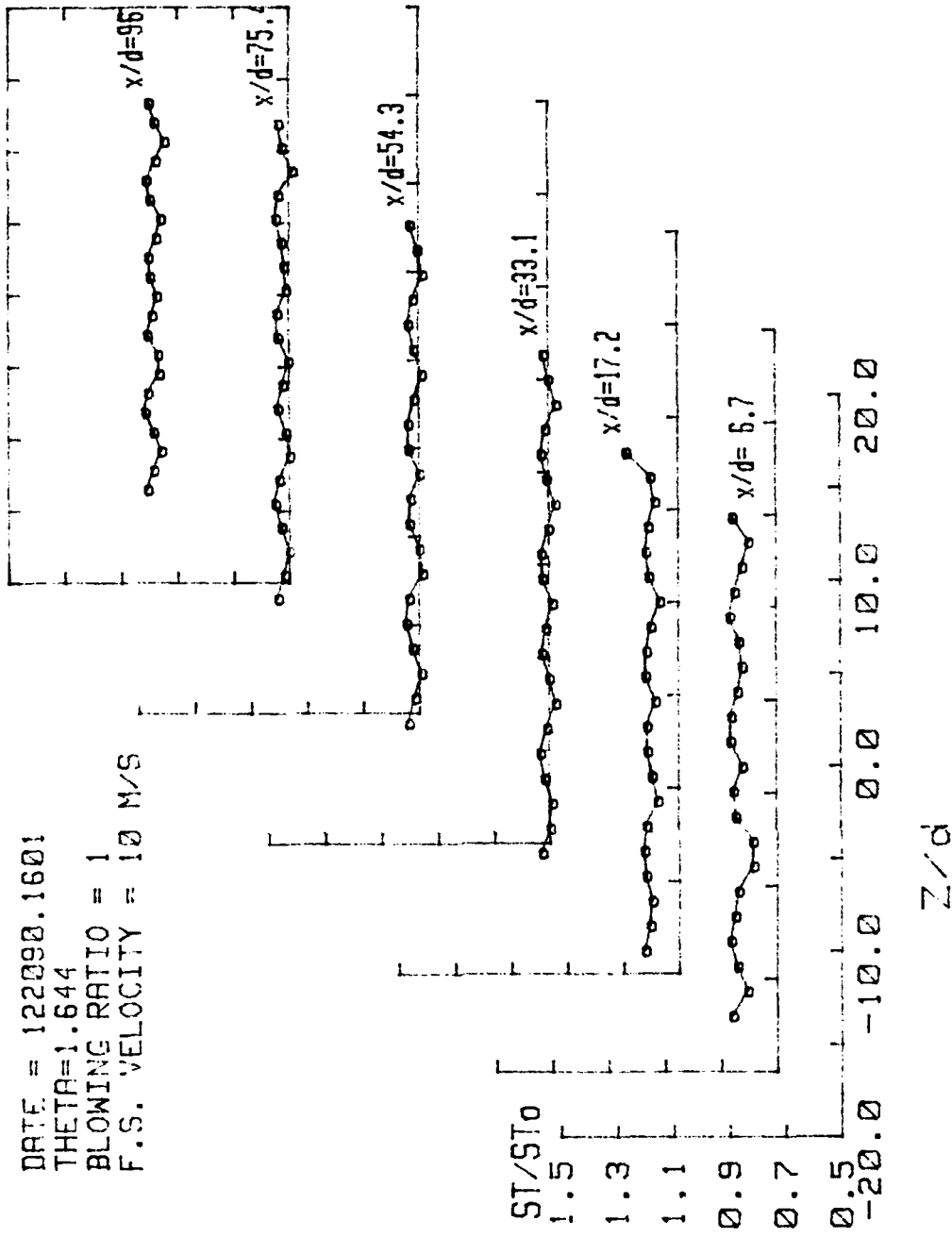


Figure 93. Spanwise Variation of St/St_0 , Simple Angle, 1 row, $m=1.0$, $\theta=1.644$.

ISO-ENERGETIC STANTON # RATIO

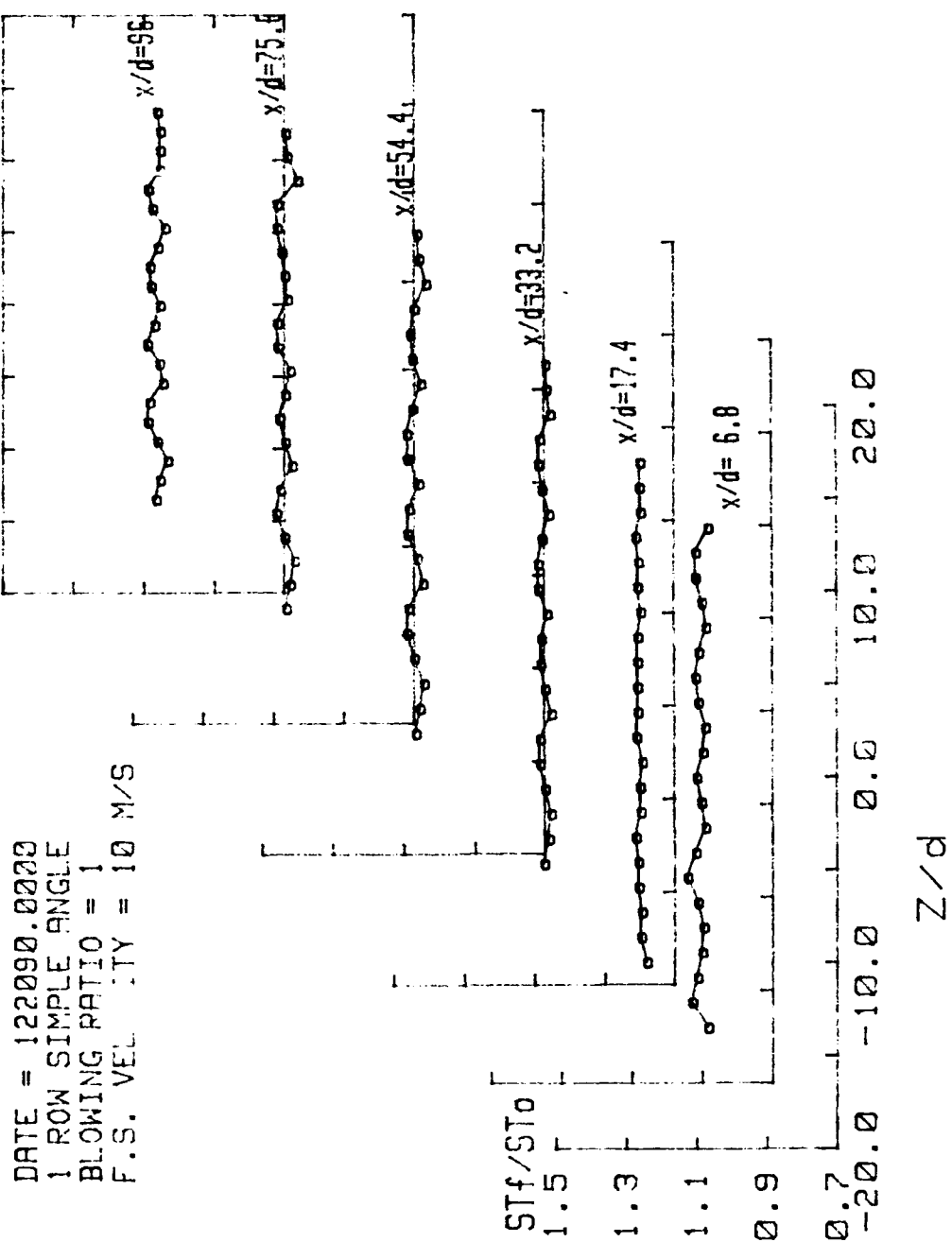


Figure 94. Spanwise Variation of St_f/St_0 , Simple Angle. 1 row, $m=1.0$.

RUN #122390.1646

Ux

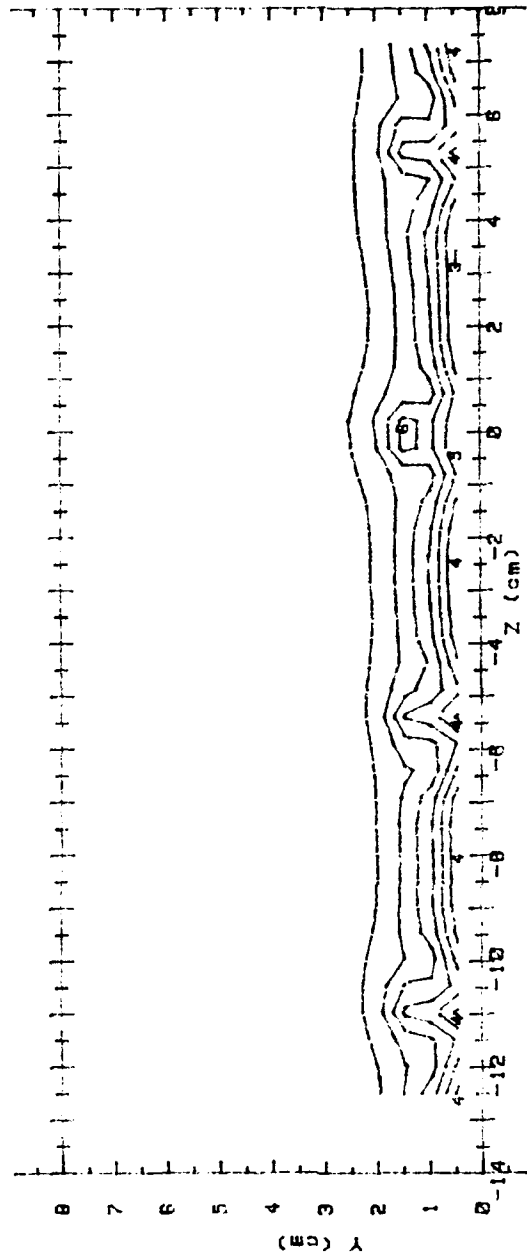


Figure 95. Streamwise Velocity Field, Simple, 1 row, m=1.0, x/d=9.4.

RUN #122290.1815

Ux

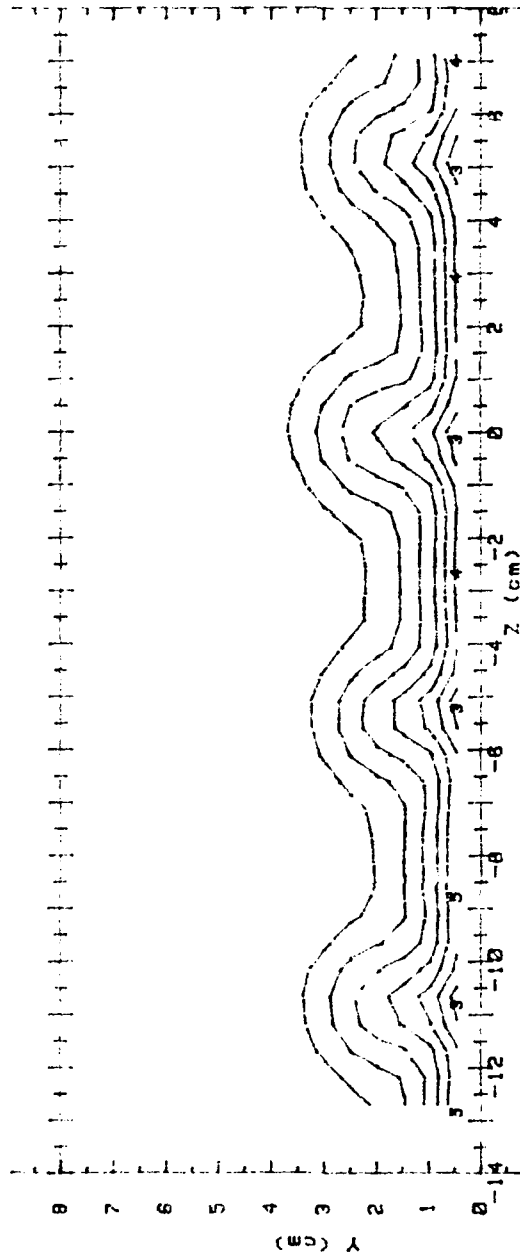
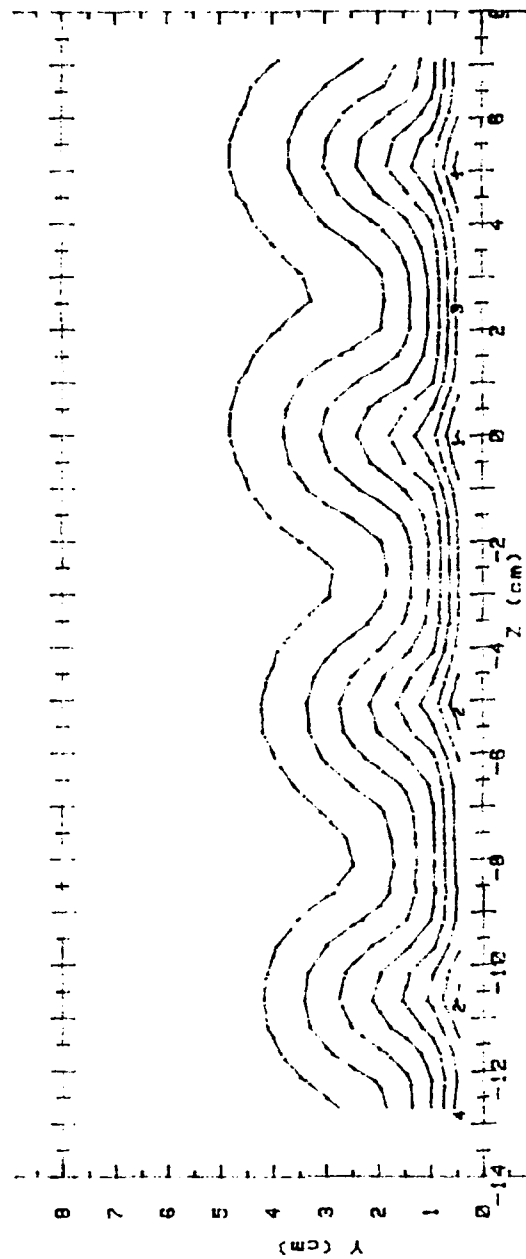


Figure 96. Streamwise Velocity Field, Simple Angle, 1 row, m=1.0, x/d=43.7.

RUN #122290.0655

Ux



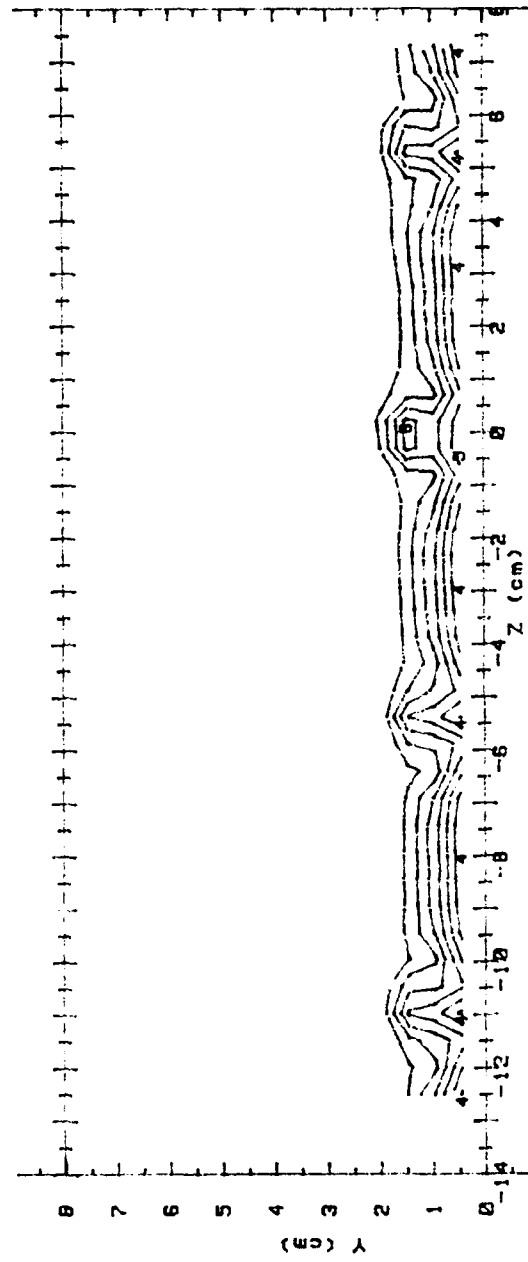
Ux (m/s) RANGES 1 ROW m=1.0 x/d = 85.2

0 :	< 5.5	5 :	> 7.5 < 8
1 :	> 5.5 < 6	6 :	> 8 < 8.5
2 :	> 6 < 6.5	7 :	> 8.5 < 9
3 :	> 6.5 < 7	8 :	> 9 < 9.5
4 :	> 7 < 7.5	9 :	> 9.5 < 10
		10 :	> 10

Figure 97. Streamwise Velocity Field, Simple Angle, 1 row, m=1.0, x/d=85.2.

RUN #122390.1645

Ptotal



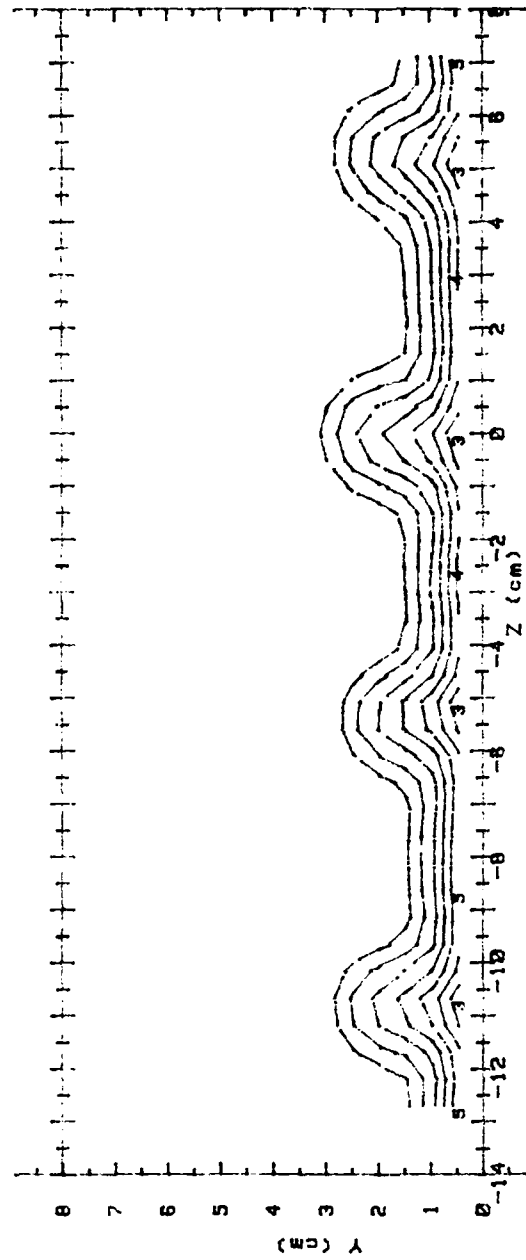
Ptotal(Pascals) RANGES 1 ROW m=1.0 x/d=9.4

0 :	< 20	5 :	36 < 40
1 :	20 < 24	6 :	40 < 44
2 :	24 < 28	7 :	44 < 48
3 :	28 < 32	8 :	48 < 52
4 :	32 < 36	9 :	52 < 56
		10 :	56

Figure 98. Streamwise Pressure Field, Simple Angle, 1 row, $m=1.0$, $x/d=9.4$.

RUN #122290.1015

Ptotal



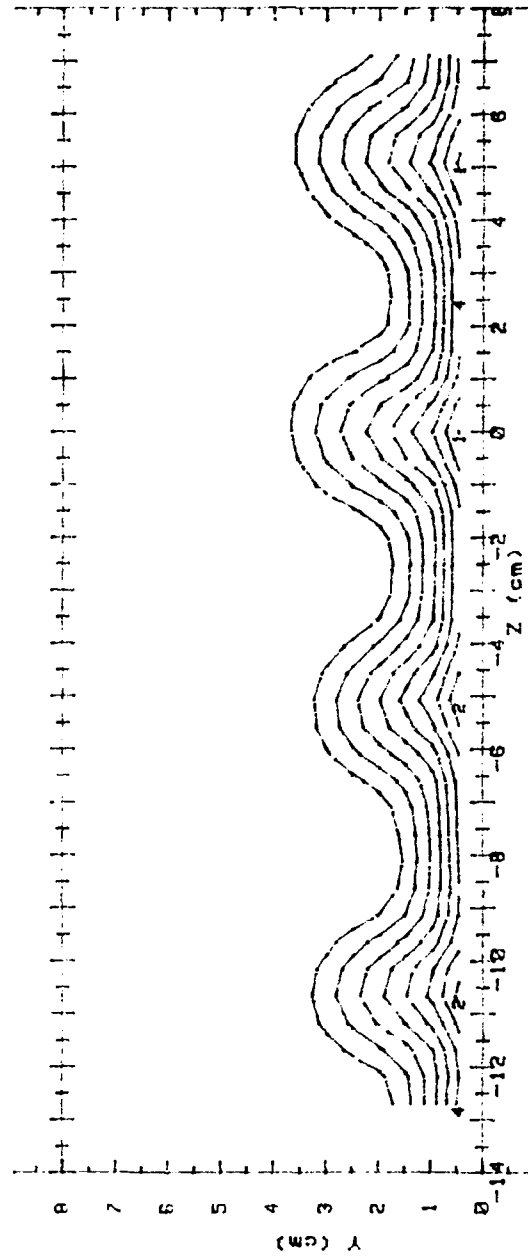
Ptotal(Pascals) RANGES 1 ROW m=1.0 x/d=43.7

0 :	< 20	5 :	36 < 40
1 :	20 < 24	6 :	40 < 44
2 :	24 < 28	7 :	44 < 48
3 :	28 < 32	8 :	48 < 52
4 :	32 < 36	9 :	52 < 56
		10 :	56

Figure 99. Streamwise Pressure Field, Simple Angle, 1 row, $m=1.0$, $x/d=43.7$.

RUN #122290.0055

Ptotal



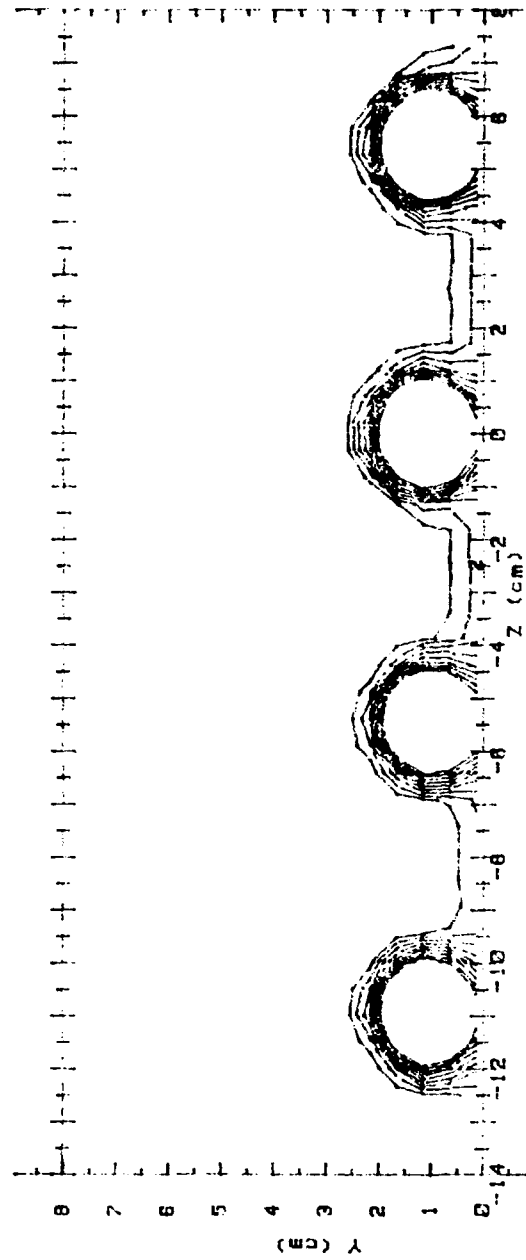
Ptotal(Pascals) RANGES 1 ROW m=1.0 x/d= 85.2

0 :	< 20	5 :	36 < 40
1 :	20 < 24	6 :	40 < 44
2 :	24 < 28	7 :	44 < 48
3 :	28 < 32	8 :	48 < 52
4 :	32 < 36	9 :	52 < 56
		10 :	56

Figure 100. Streamwise Pressure Field, Simple Angle, 1 row, $m=1.0$, $x/d=85.2$.

RUN #122790.1351

T - Tfs



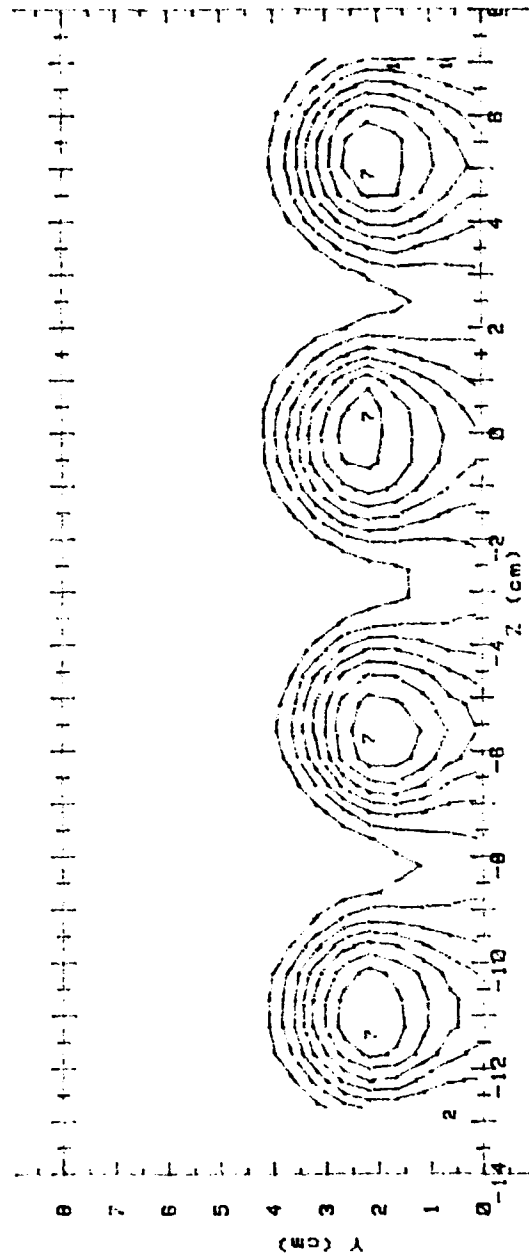
T - Tfs (CELCIUS) RANGES 1 ROW m=1.0 x/d = 9.4

0	< .5	5	> 2.5	< 3	
1	> .5	< 1	6	> 3	< 3.5
2	> 1	< 1.5	7	> 3.5	< 4
3	> 1.5	< 2	8	> 4	< 4.5
4	> 2	< 2.5	9	> 4.5	

Figure 101. Streamwise Injectant Distribution, Simple Angle, 1 row, $m=1.0$, $x/d=9.4$.

RUN #122790.1802

T - Tfs



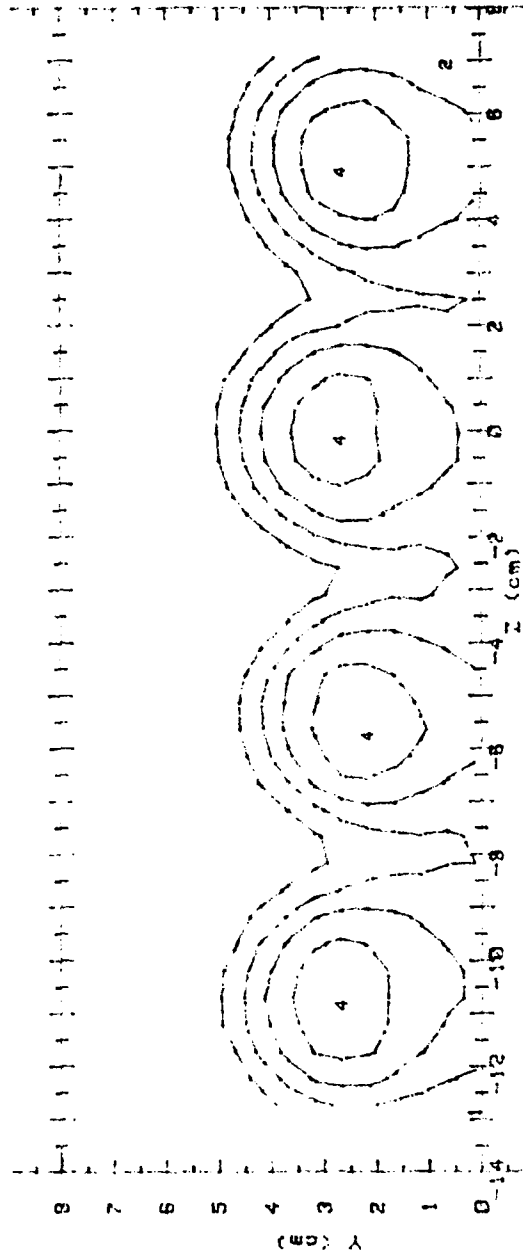
T - Tfs(CELCIUS) RANGES 1 ROW m=1.0 x/d = 43.7

0 :	< .5	5 :	2.5 < 3
1 :	.5 < 1	6 :	3 < 3.5
2 :	1 < 1.5	7 :	3.5 < 4
3 :	1.5 < 2	8 :	4 < 4.5
4 :	2 < 2.5	9 :	4.5

Figure 102. Streamwise Injectant Distribution, Simple Angle, 1 row, m=1.0, x/d=43.7.

RUN #122790.2212

T -- Tfs



T - Tfs (CELCIUS) RANGES 1 ROW m=1.0 x/d = 85.2

0 :	< .5	5 :	2.5 < 3
1 :	.5 < 1	6 :	3 < 3.5
2 :	1 < 1.5	7 :	3.5 < 4
3 :	1.5 < 2	8 :	4 < 4.5
4 :	2 < 2.5	9 :	4.5

Figure 103. Streamwise Injectant Distribution, Simple Angle, 1 row, $m=1.0$, $x/d=85.2$.

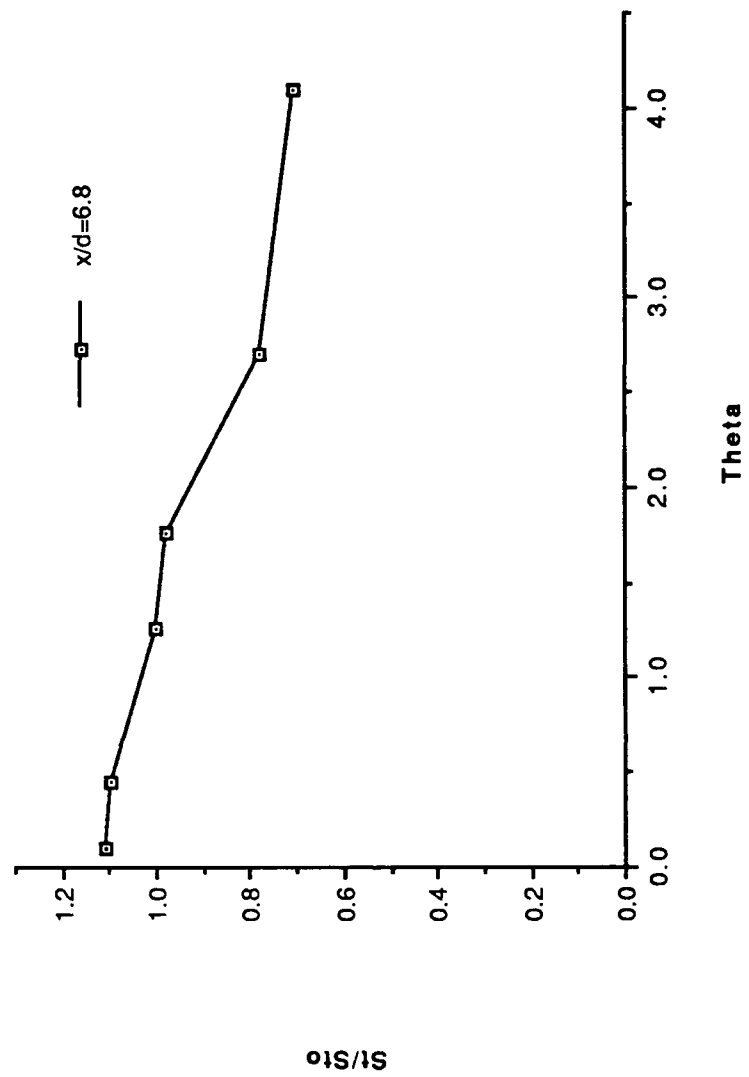


Figure 104. St/St_0 vs θ , Simple Angle, 1 row, $m=1.5$, $x/d=6.8$, $z=0.0$.

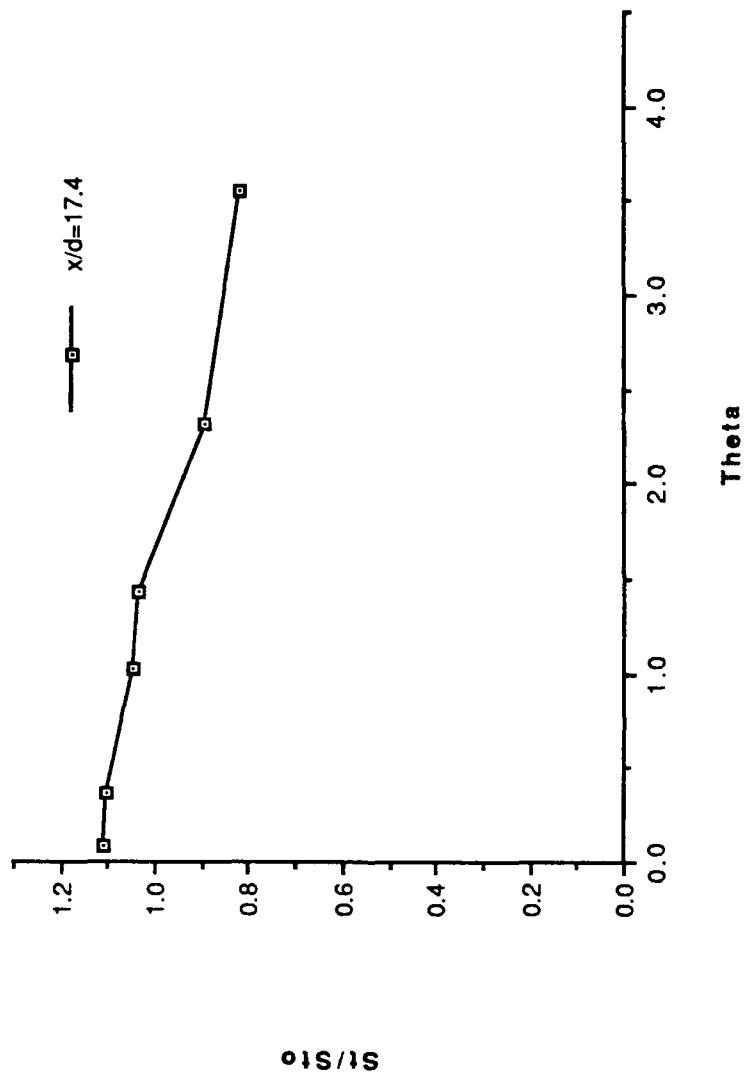


Figure 105. St/St_0 vs θ , Simple Angle, 1 row, $m=1.5$, $x/d=17.4$, $z=0.0$.

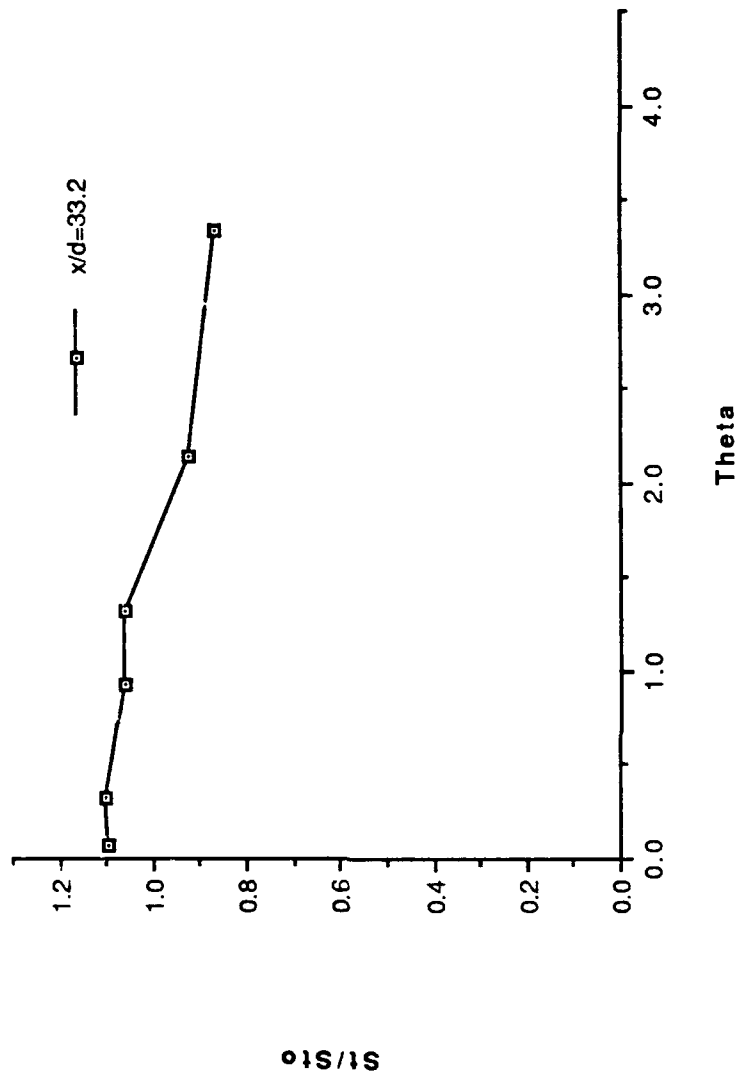


Figure 106. St/St_0 vs θ , Simple Angle, 1 row, $m=1.5$, $x/d=33.2$, $z=0.0$.

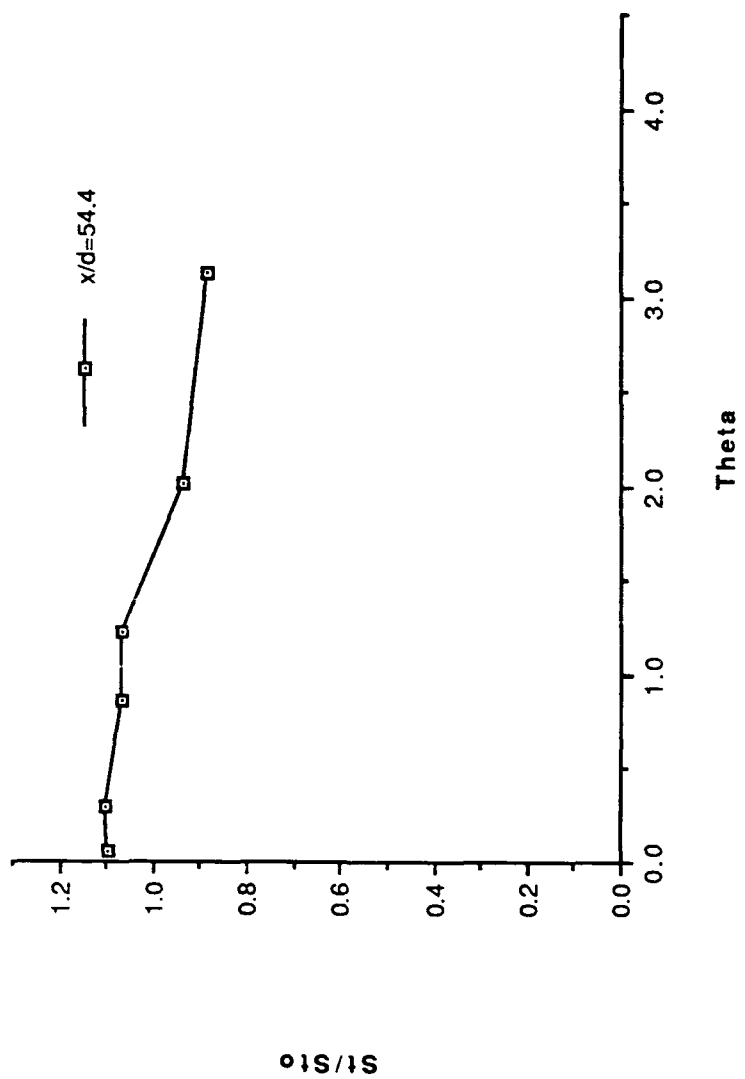


Figure 107. St/St_0 vs θ , Simple Angle, 1 row, $m=1.5$, $x/d=54.4$, $z=0.0$.

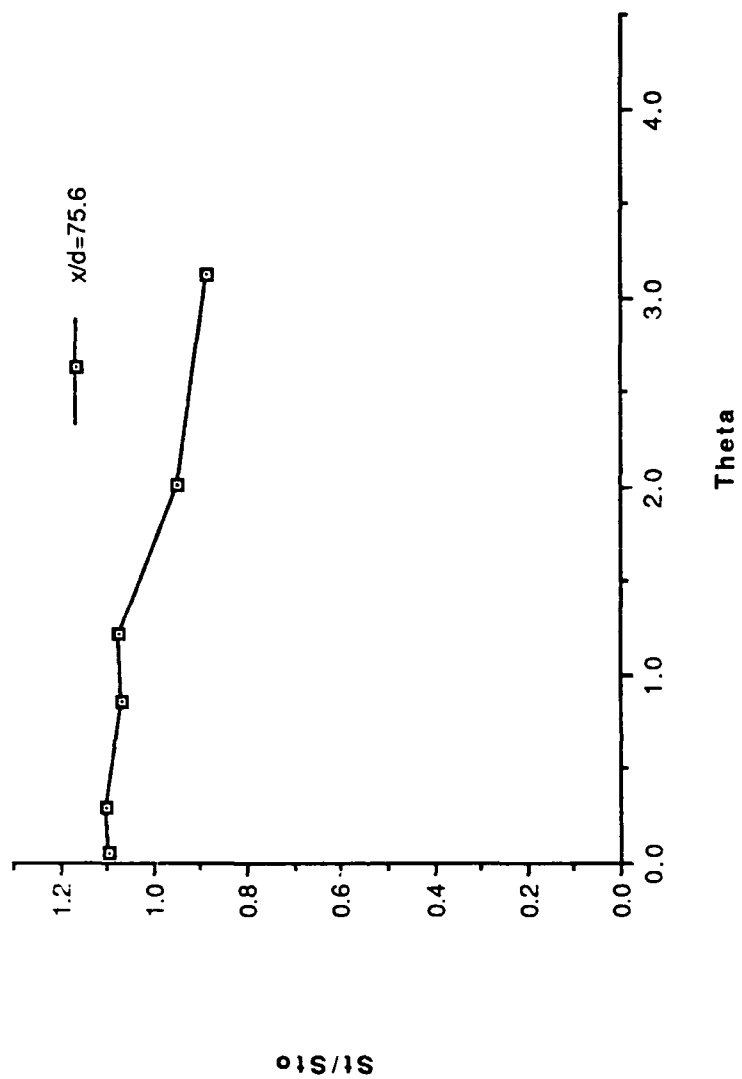


Figure 108. St/St_0 vs θ , Simple Angle, 1 row, $m=1.5$, $x/d=75.6$, $z=0.0$.

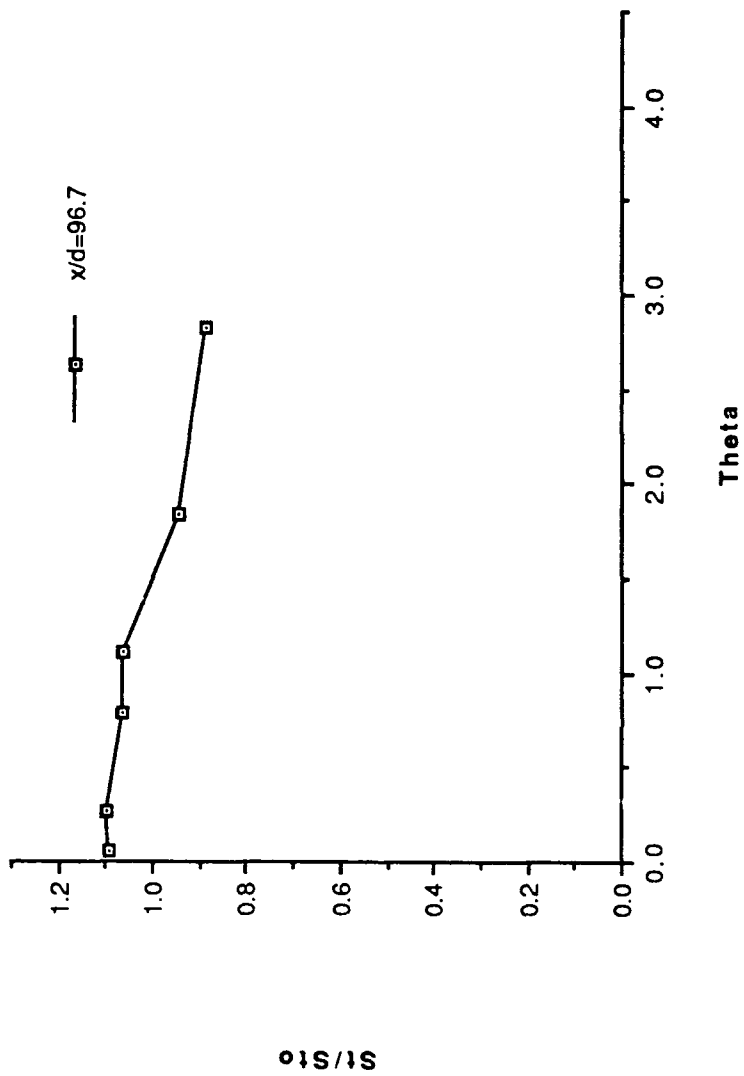


Figure 109. St/St_0 vs θ , Simple Angle, 1 row, $m=1.5$, $x/d=96.7$, $z=0.0$.

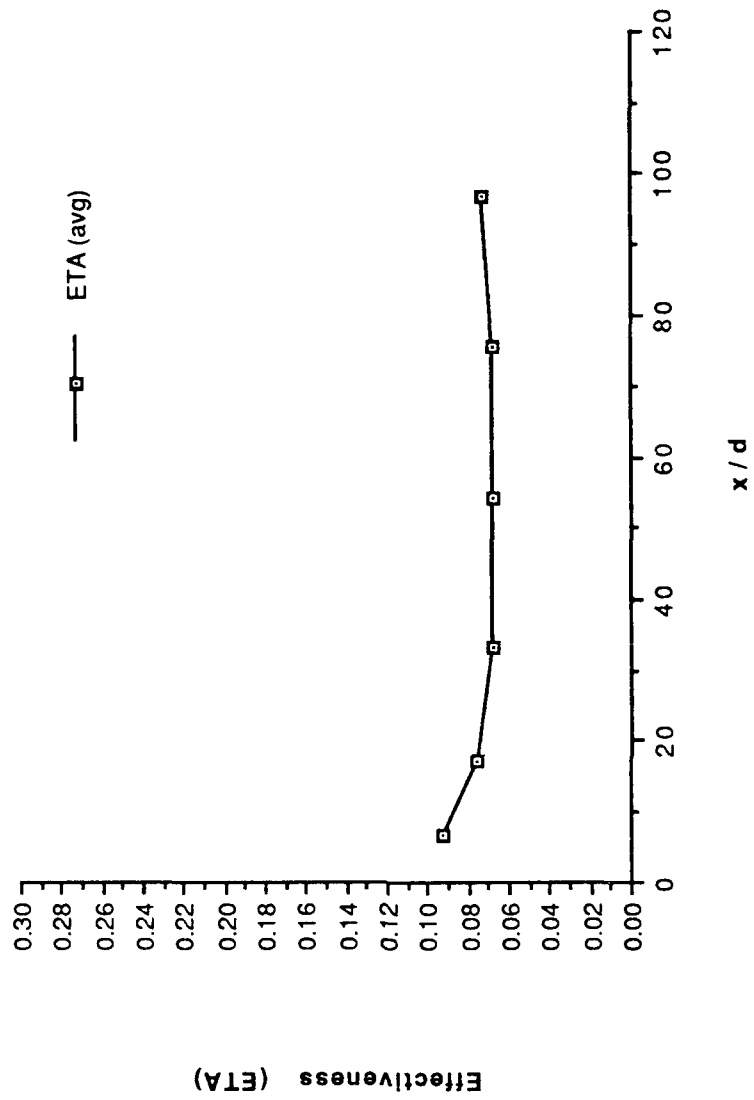


Figure 110. η , vs x/d , Simple Angle, 1 row, $m=1.5$, Spanwise Average.

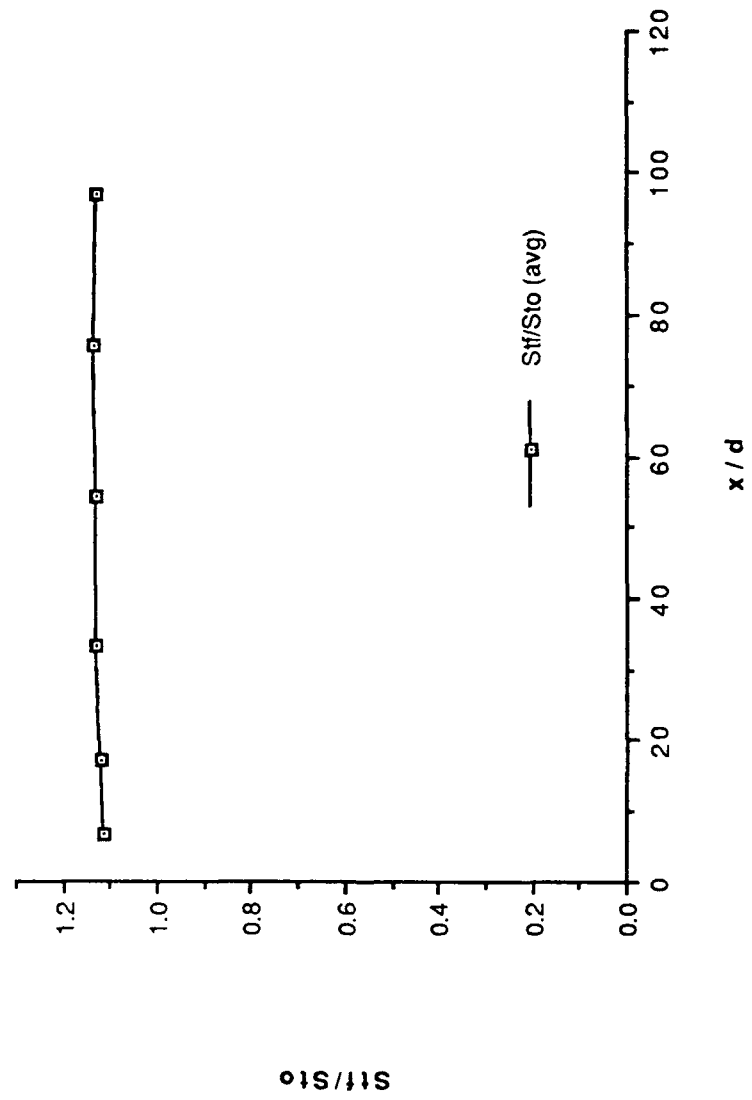


Figure 111. St_f/St_0 vs x/d , Simple Angle, 1 row, $m=1.5$, Spanwise Average.

FILM-COOLING EFFECTIVENESS

DATE = 10291.0000
 1 ROW SIMPLE ANGLE
 BLOWING RATIO = 1.5
 F.S. VELOCITY = 10 M/S

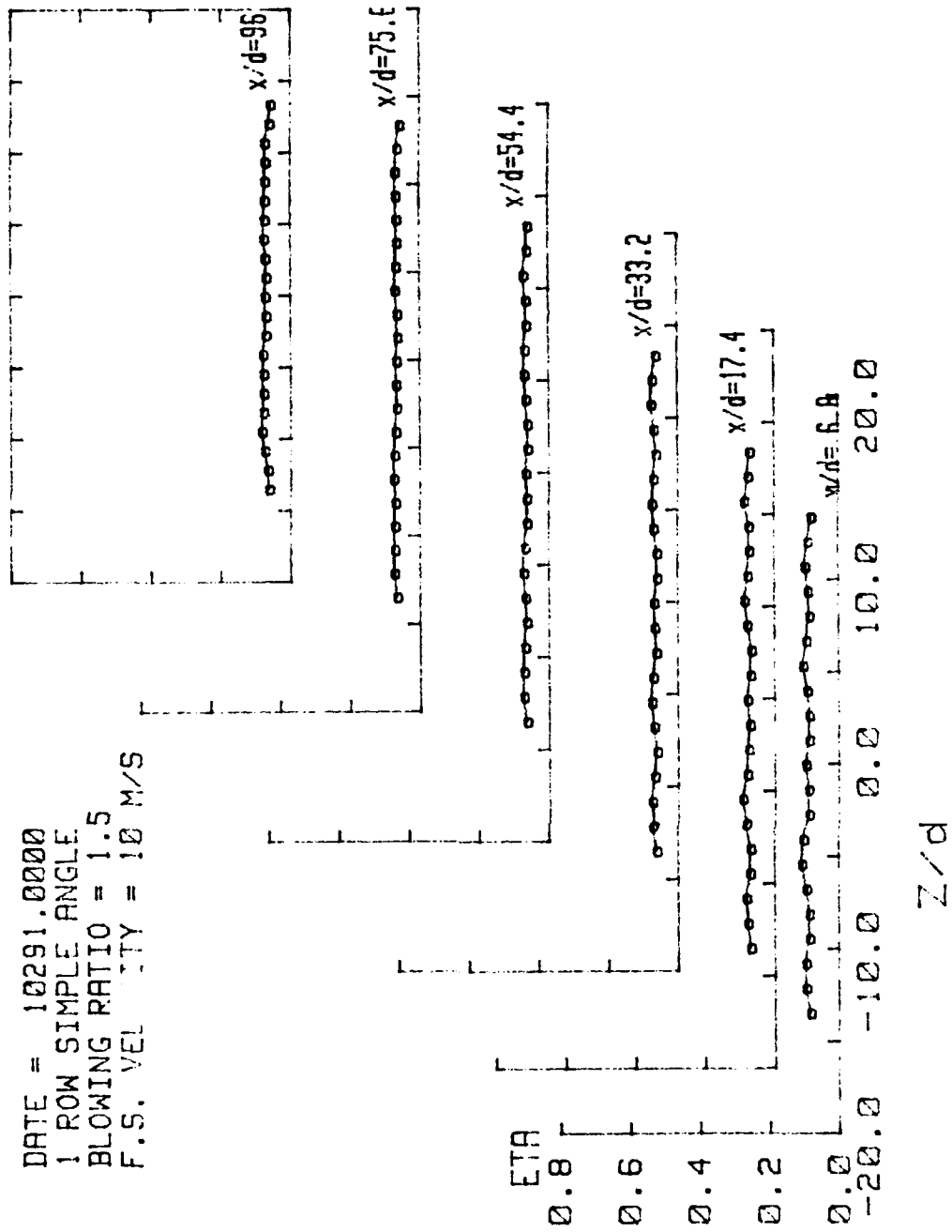


Figure 112. Spanwise Variation of η , Simple Angle, 1 row, $m=1.5$.

STANTON NUMBER RATIOS

DATE = 10291.1508
 THETA=1.626
 BLOWING RATIO = 1.5
 F.S. VELOCITY = 10 M/S

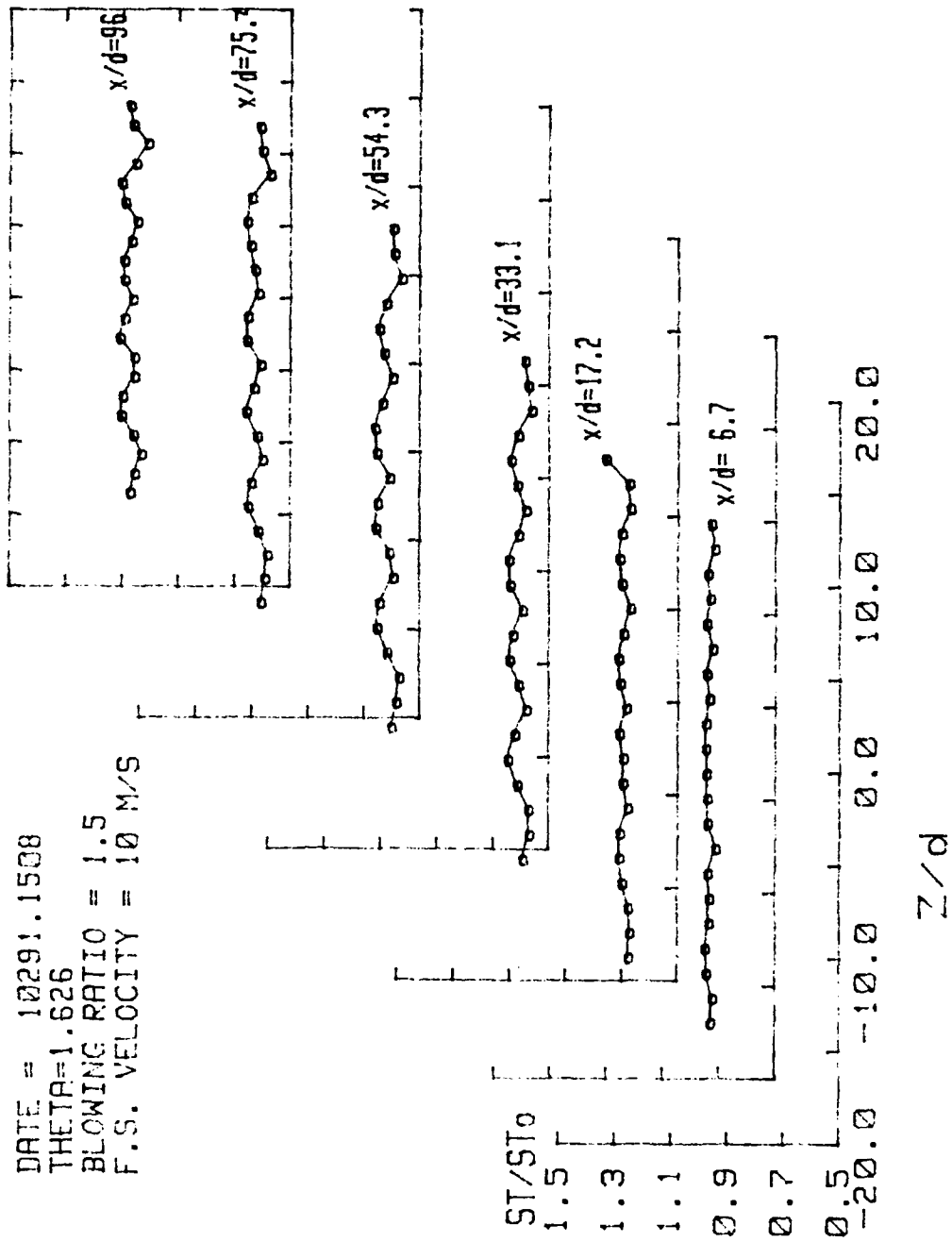


Figure 113. Spanwise Variation of St/St_0 , Simple Angle, 1 row, $m=1.5$, $\theta=1.626$.

ISO-ENERGETIC STANTON # RATIO

DATE = 10291.0000
 1 ROW SIMPLE ANGLE
 BLOWING RATIO = 1.5
 F.S. VELOCITY = 10 M/S

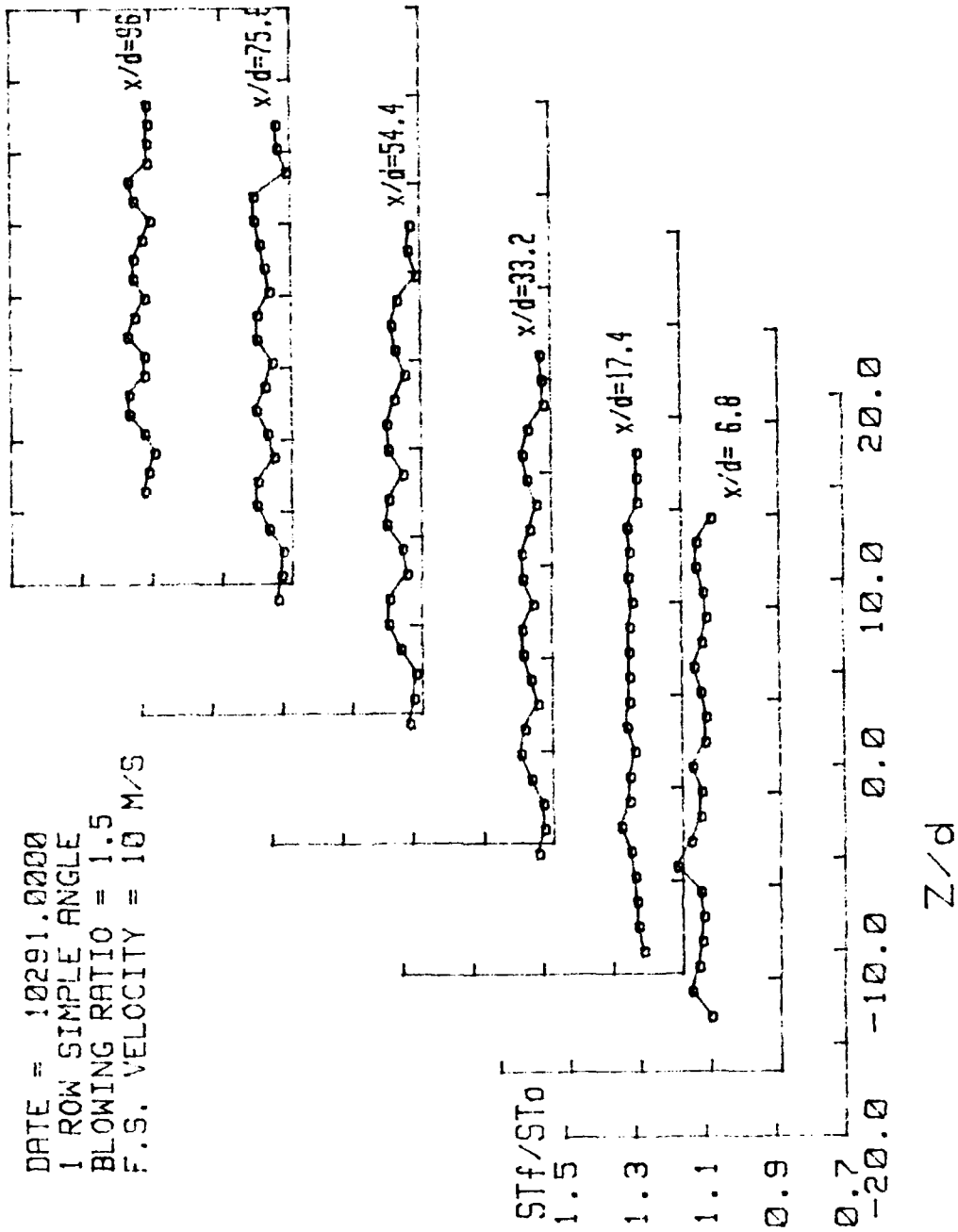
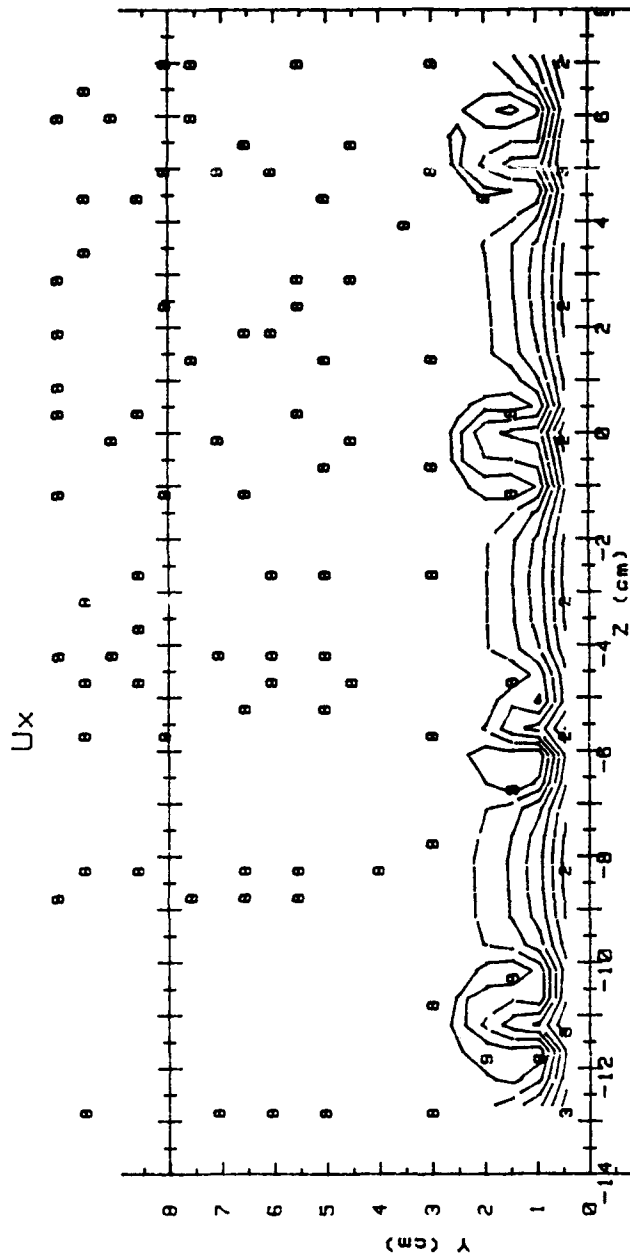


Figure 114. Spanwise Variation of St_f/St_0 , Simple Angle, 1 row, $m=1.5$.

RUN #11691.0737

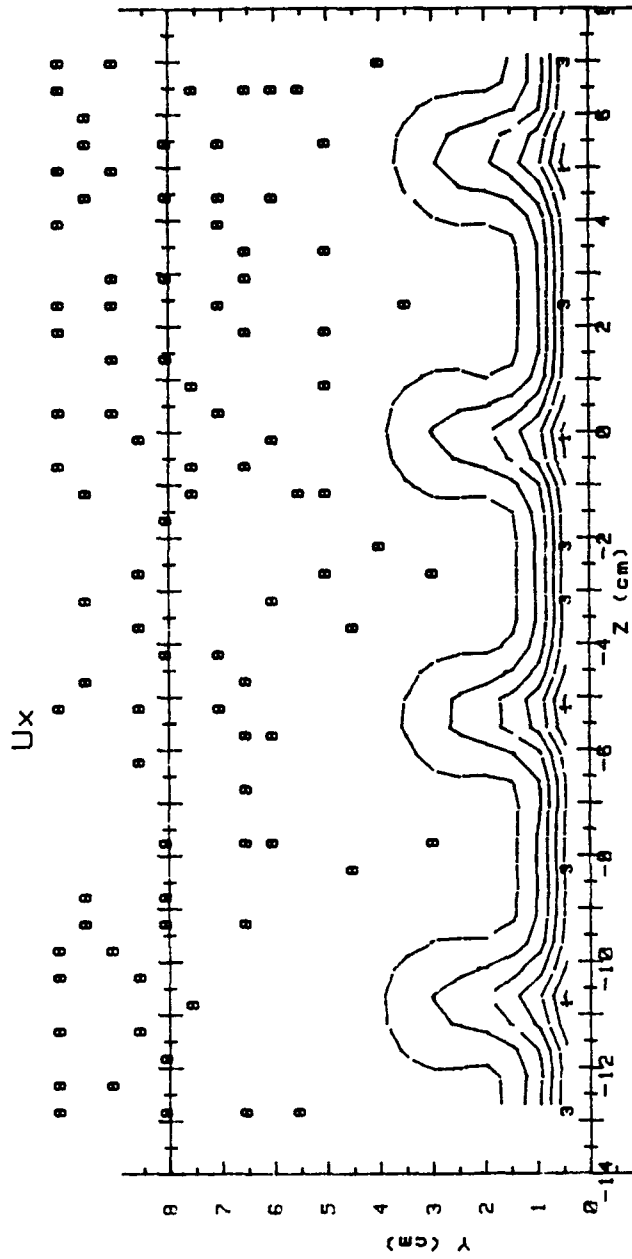


Ux(m/s) RANGES 1 ROW m=1.5 x/d = 9.4

0 :	< 6.5	5 :	8.5 < 9
1 :	6.5 < 7	6 :	9 < 9.5
2 :	7 < 7.5	7 :	9.5 < 10
3 :	7.5 < 8	8 :	10 < 10.5
4 :	8 < 8.5	9 :	10.5 < 11
		10 :	11

Figure 115. Streamwise Velocity Field, Simple, 1 row, m=1.5, x/d=9.4.

RUN #11291.1922

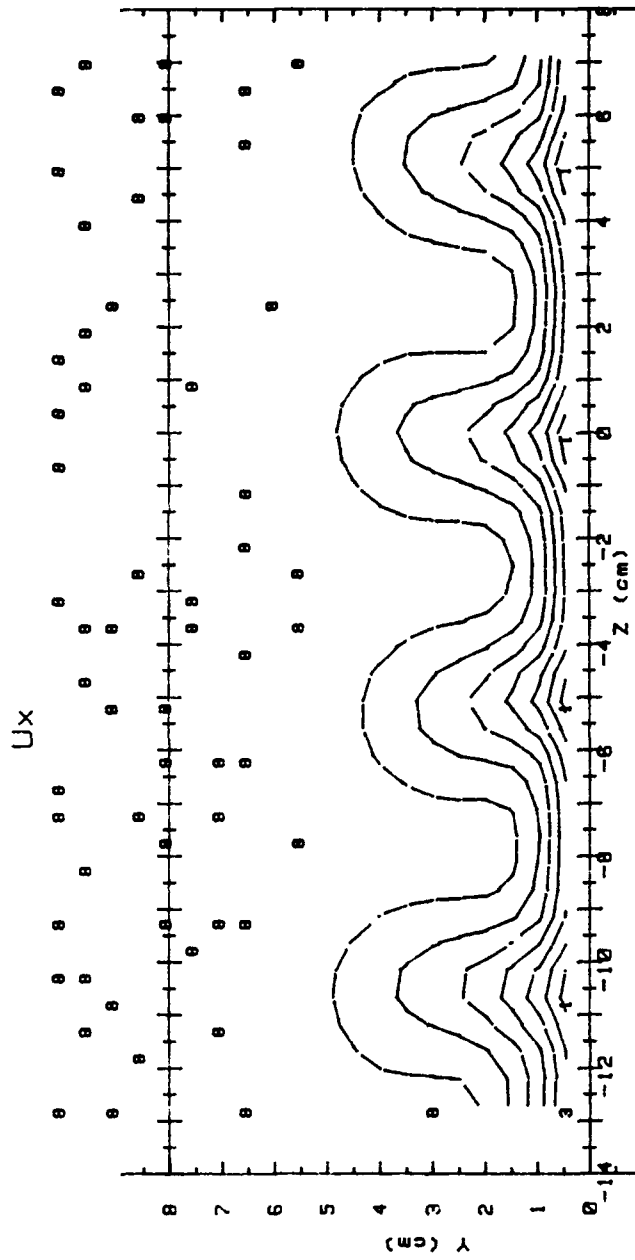


Ux(m/s) RANGES 1 ROW m=1.5 x/d = 43.7

0 :	< 6.5	5 :	8.5 < 9
1 :	6.5 < 7	6 :	9 < 9.5
2 :	7 < 7.5	7 :	9.5 < 10
3 :	7.5 < 8	8 :	10 < 10.5
4 :	8 < 8.5	9 :	10.5 < 11
		10 :	11

Figure 116. Streamwise Velocity Field, Simple Angle, 1 row, m=1.5, x/d=43.7.

RUN #10991.2125



Ux (m/s) RANGES 1 ROM m=1.5 x/d = 85.2

0 :	< 6.5	5 :	8.5 < 9
1 :	6.5 < 7	6 :	9 < 9.5
2 :	7 < 7.5	7 :	9.5 < 10
3 :	7.5 < 8	8 :	10 < 10.5
4 :	8 < 8.5	9 :	10.5 < 11
		10 :	> 11

Figure 117. Streamwise Velocity Field, Simple Angle, 1 row, m=1.5, x/d=85.2.

RUN #11691.0737

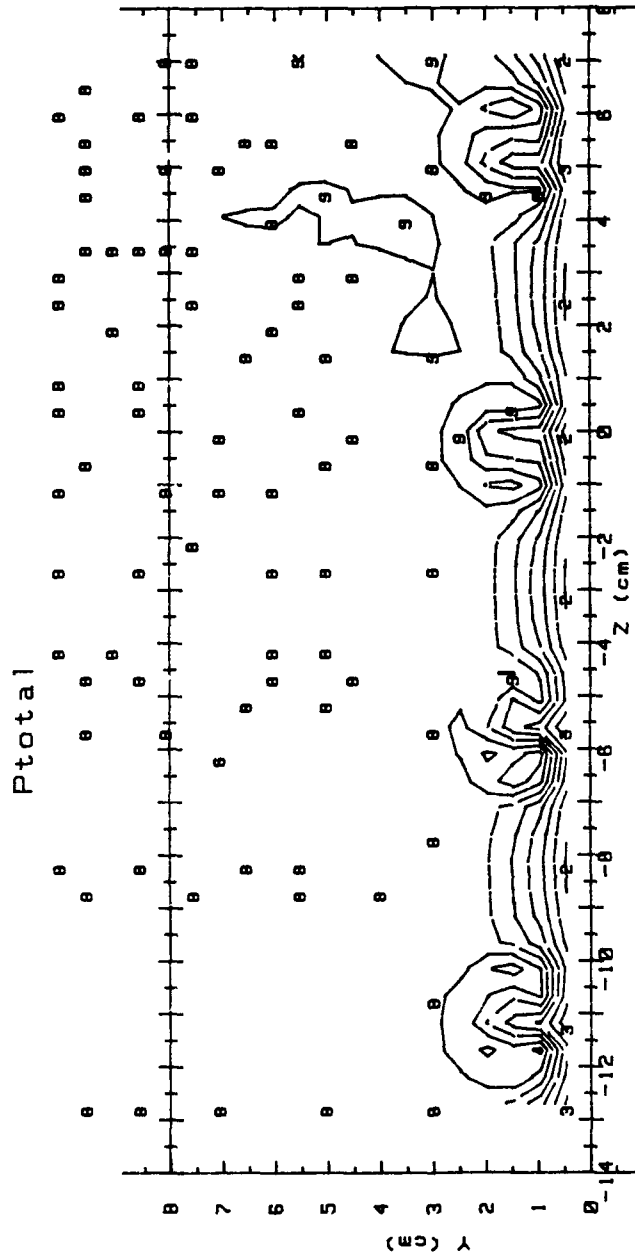
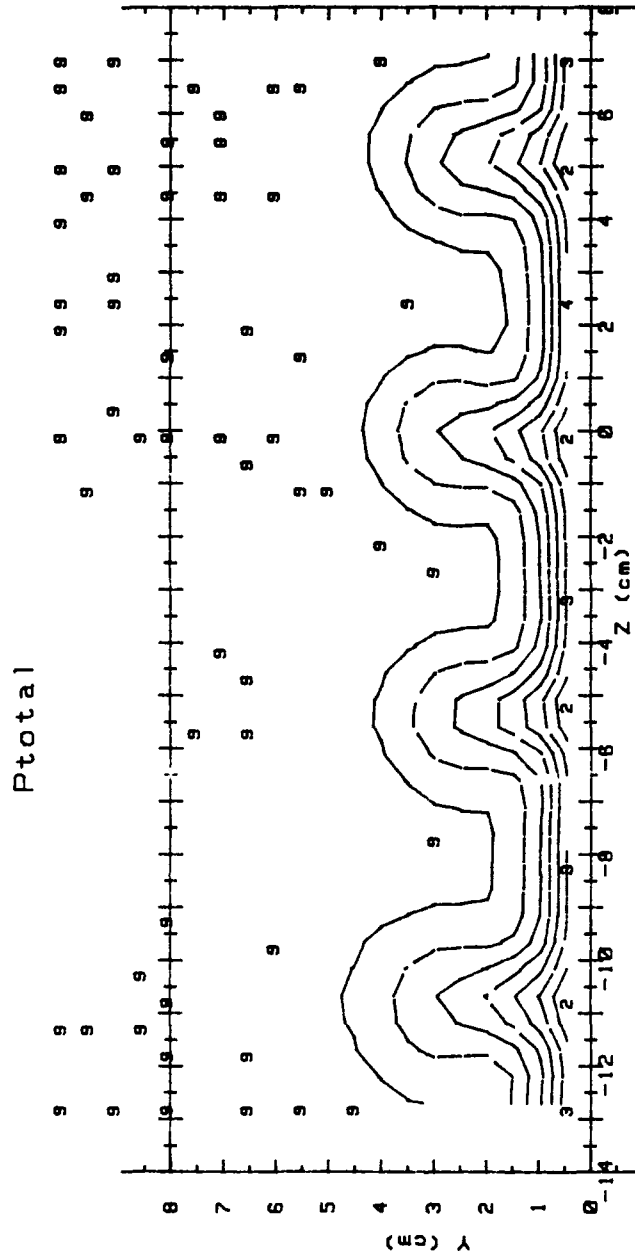


Figure 118. Streamwise Pressure Field, Simple Angle, 1 row, $m=1.5$, $x/d=9.4$.

RUN #11291.1922

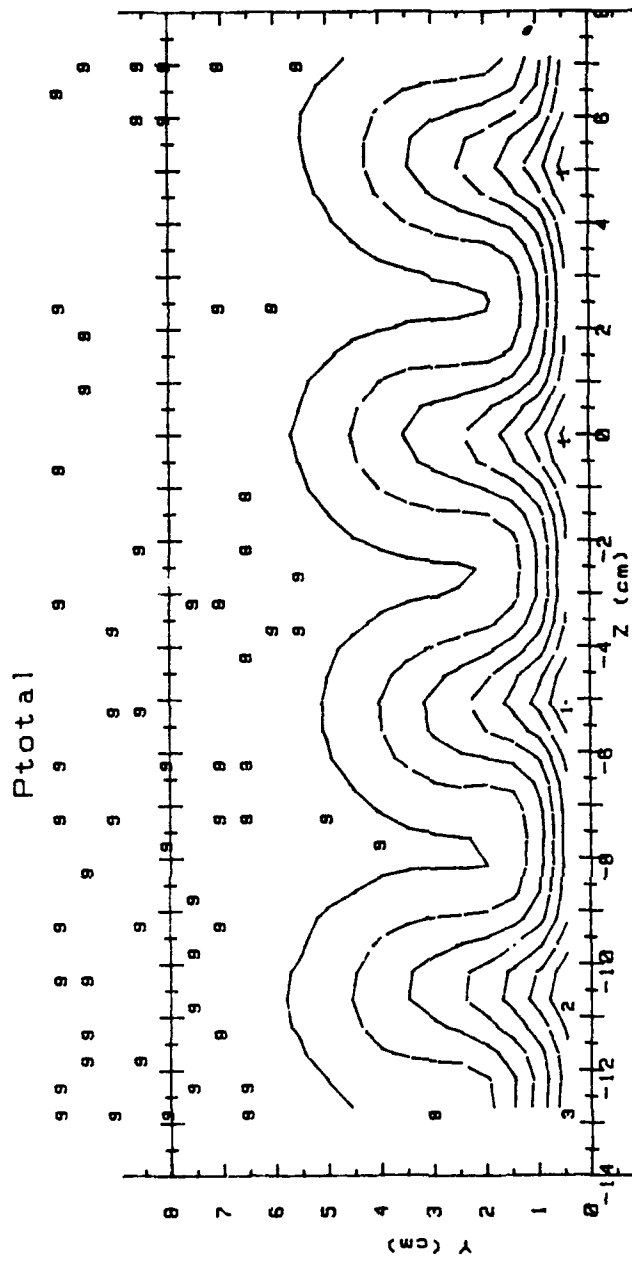


Ptotal(Pascals) RANGES 1 ROW m=1.5 x/d=43.7

- 0 : < 25
- 1 : 25 < 30
- 2 : 30 < 35
- 3 : 35 < 40
- 4 : 40 < 45
- 5 : 45 < 50
- 6 : 50 < 55
- 7 : 55 < 60
- 8 : 60 < 65
- 9 : 65 < 70
- 10 : 70

Figure 119. Streamwise Pressure Field, Simple Angle, 1 row, m=1.5, x/d=43.7.

RUN #10991.2125



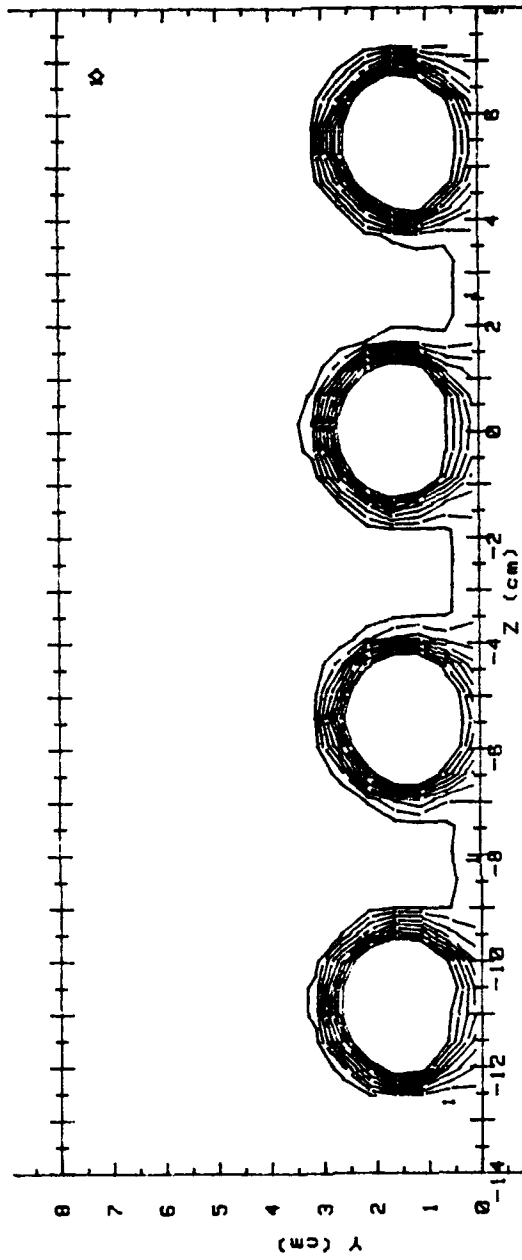
Ptotal(Pascals) RANGES 1 ROW m=1.5 x/d= 85.2

0 :	< 25	5 :	45 < 50
1 :	25 < 30	6 :	50 < 55
2 :	30 < 35	7 :	55 < 60
3 :	35 < 40	8 :	60 < 65
4 :	40 < 45	9 :	65 < 70
		10 :	70

Figure 120. Streamwise Pressure Field, Simple Angle, 1 row, $m=1.5$, $x/d=85.2$.

RUN #10891.0129

T - Tfs



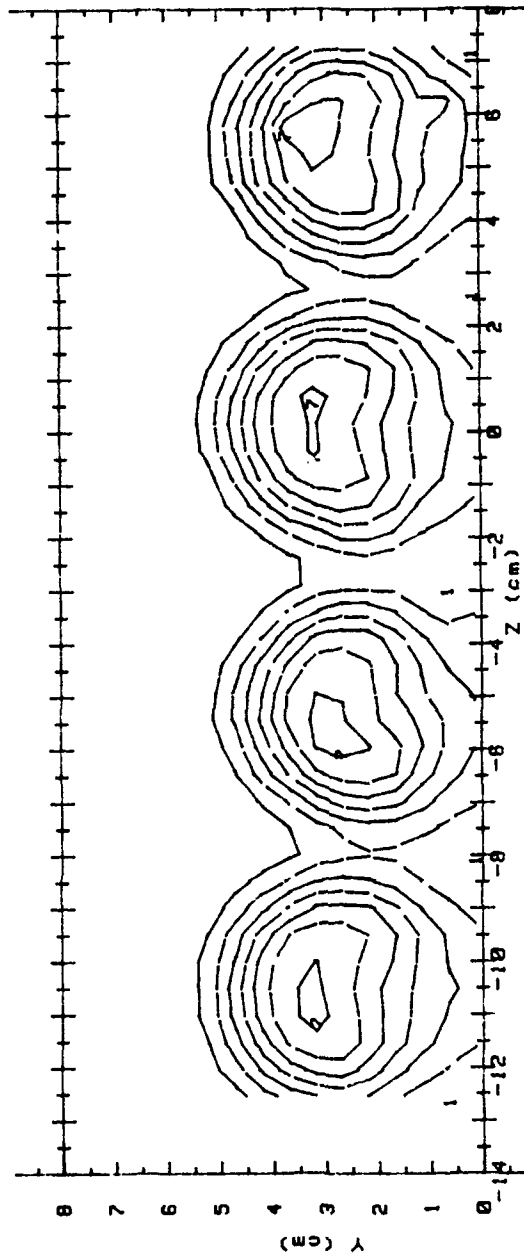
T - Tfs (CELCIUS) RANGES 1 ROW m=1.5 x/d = 9.4

0 :	< .5	5 :	2.5 < 3
1 :	.5 < 1	6 :	3 < 3.5
2 :	1 < 1.5	7 :	3.5 < 4
3 :	1.5 < 2	8 :	4 < 4.5
4 :	2 < 2.5	9 :	4.5

Figure 121. Streamwise Injectant Distribution, Simple Angle, 1 row, $m=1.5$, $x/d=9.4$.

RUN #10891.0838

T - Tfs



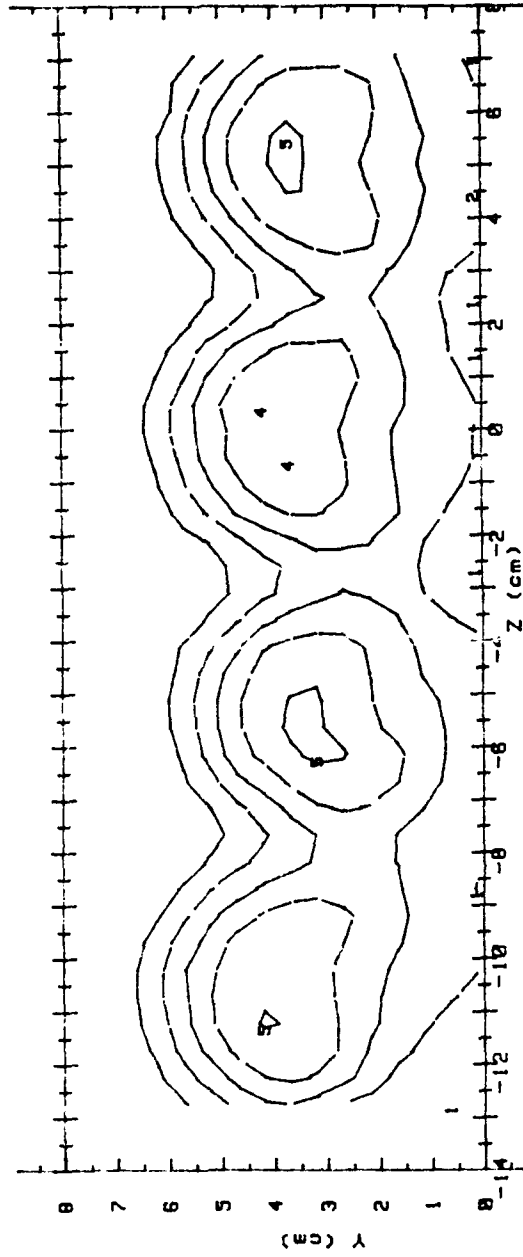
T - Tfs (CELCIUS) RANGES 1 ROW m=1.5 x/d = 43.7

0 :	< .5	5 :	> 2.5 < 3
1 :	> .5 < 1	6 :	> 3 < 3.5
2 :	> 1 < 1.5	7 :	> 3.5 < 4
3 :	> 1.5 < 2	8 :	> 4 < 4.5
4 :	> 2 < 2.5	9 :	> 4.5

Figure 122. Streamwise Injectant Distribution, Simple Angle, 1 row, $m=1.5$, $x/d=43.7$.

RUN #10891.1256

T - Tfs



T - Tfs(CELCIUS) RANGES 1 ROW m=1.5 x/d = 85.2

0 :	< .5	5 :	2.5 < 3
1 :	.5 < 1	6 :	3 < 3.5
2 :	1 < 1.5	7 :	3.5 < 4
3 :	1.5 < 2	8 :	4 < 4.5
4 :	2 < 2.5	9 :	4.5

Figure 123. Streamwise Injectant Distribution, Simple Angle, 1 row, $m=1.5$, $x/d=85.2$.

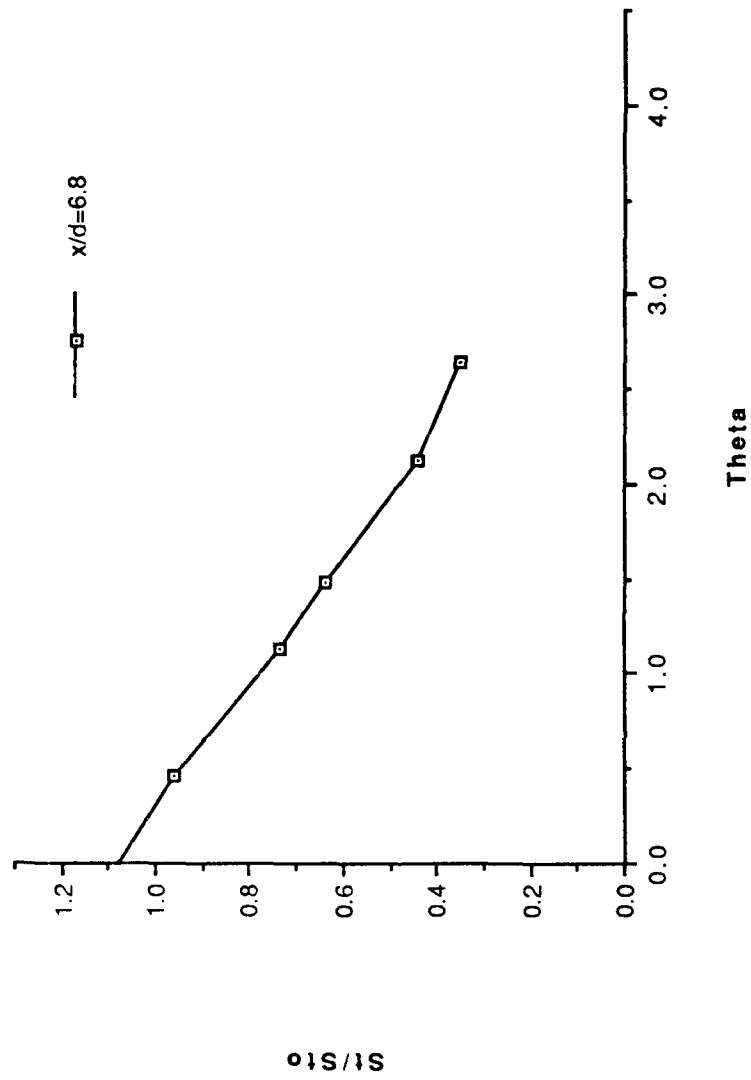


Figure 124. St/St_0 vs θ , Simple Angle, 2 rows, $m=0.5$, $x/d=6.8$, $z=0.0$.

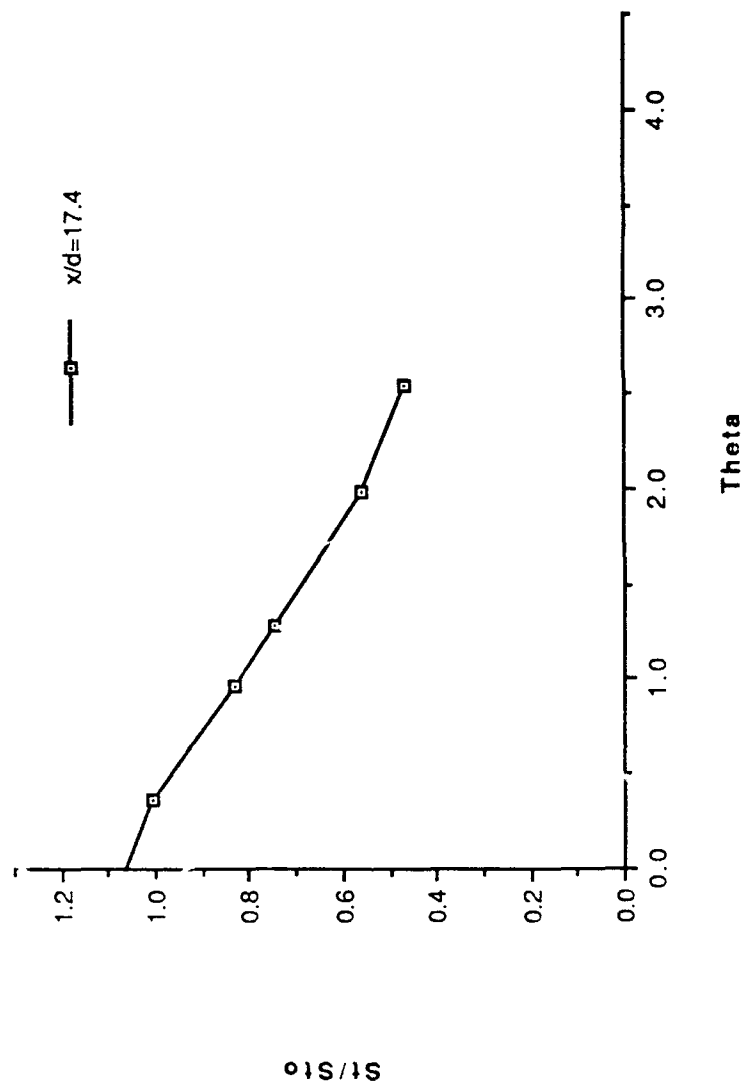


Figure 125. St/St_0 vs θ , Simple Angle, 2 rows, $m=0.5$, $x/d=17.4$, $z=0.0$.

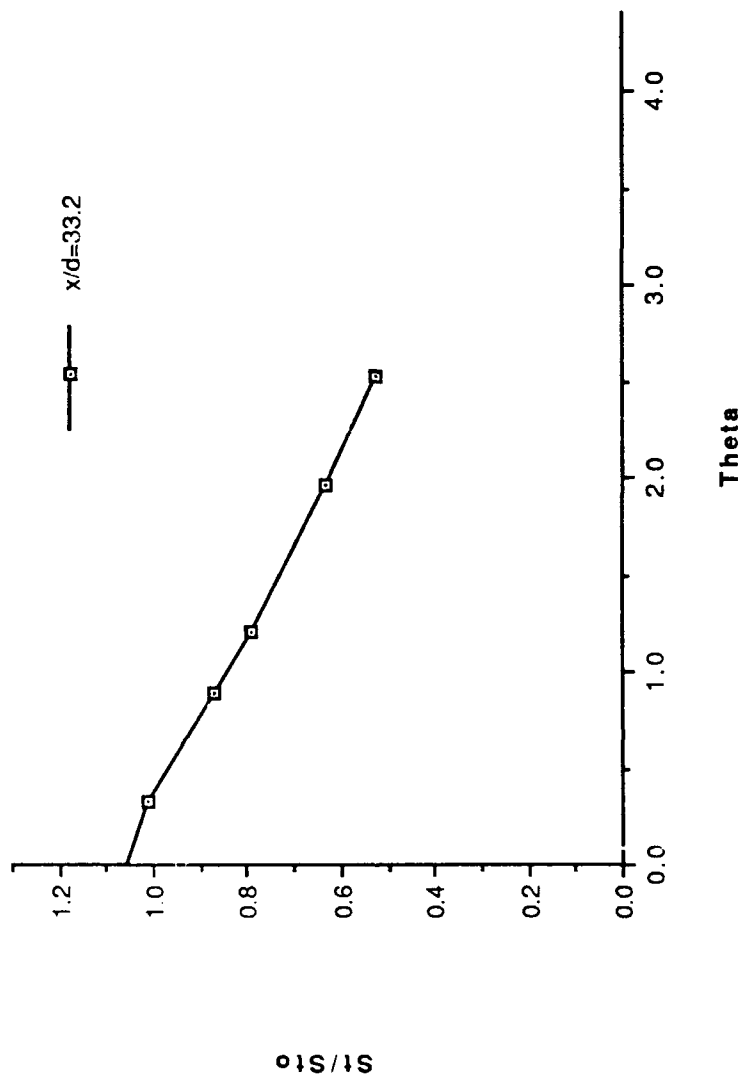


Figure 126. St/St_0 vs θ , Simple Angle, 2 rows, $m=0.5$, $x/d=33.2$, $z=0.0$.

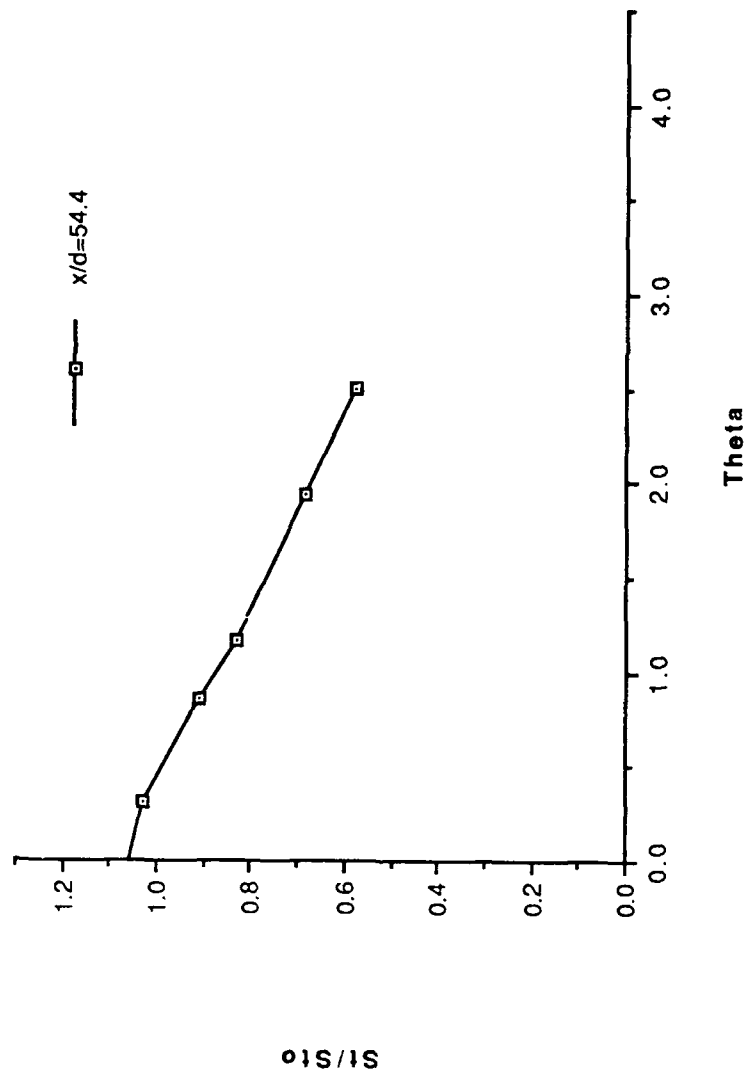


Figure 127. St/St_0 vs θ , Simple Angle, 2 rows, $m=0.5$, $x/d=54.4$, $z=0.0$.

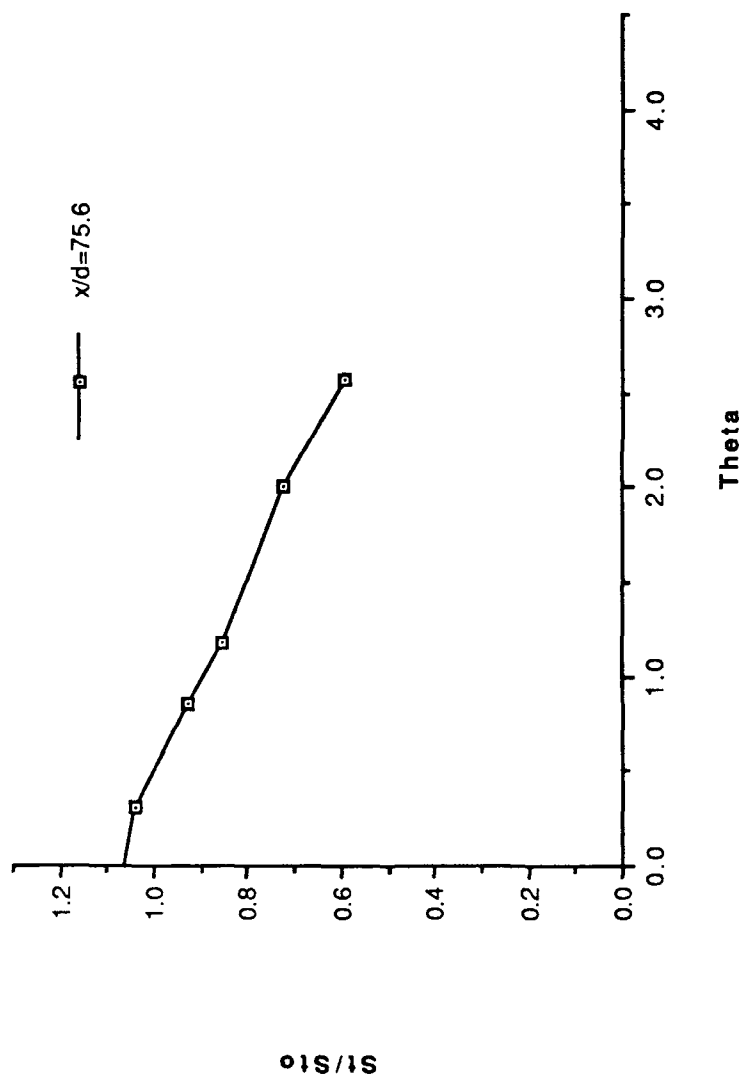


Figure 128. St/St_0 vs θ , Simple Angle, 2 rows, $m=0.5$, $x/d=75.6$, $z=0.0$.

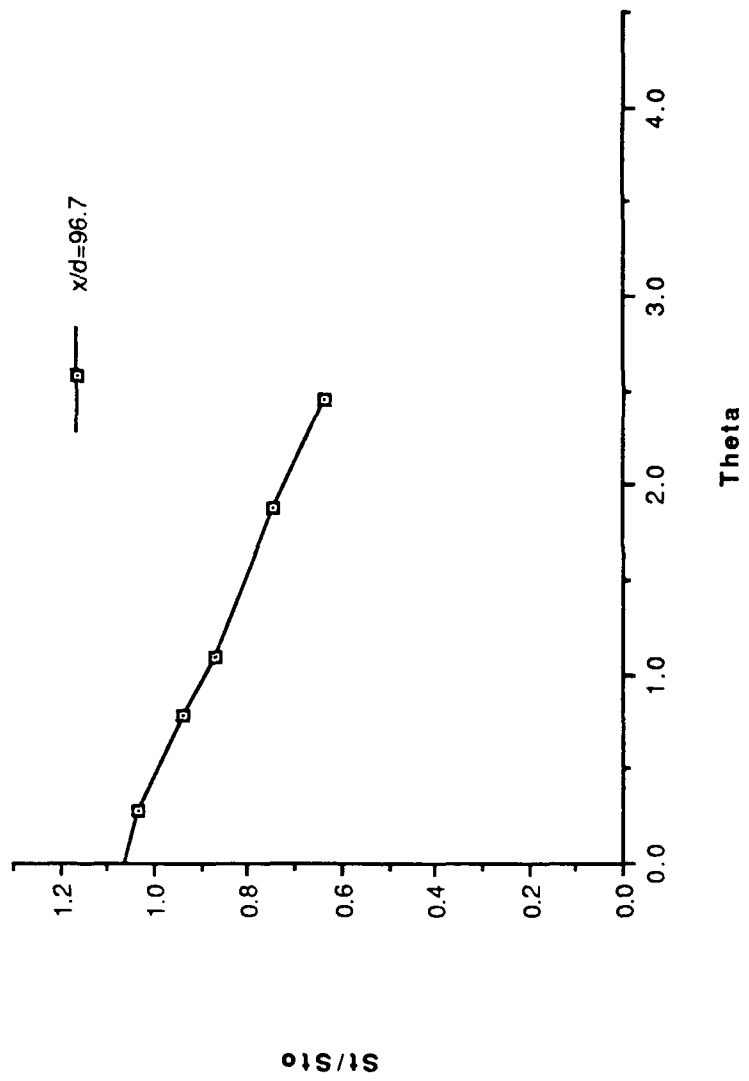


Figure 129. St/St_0 vs θ , Simple Angle, 2 rows, $m=0.5$, $x/d=96.7$, $z=0.0$.

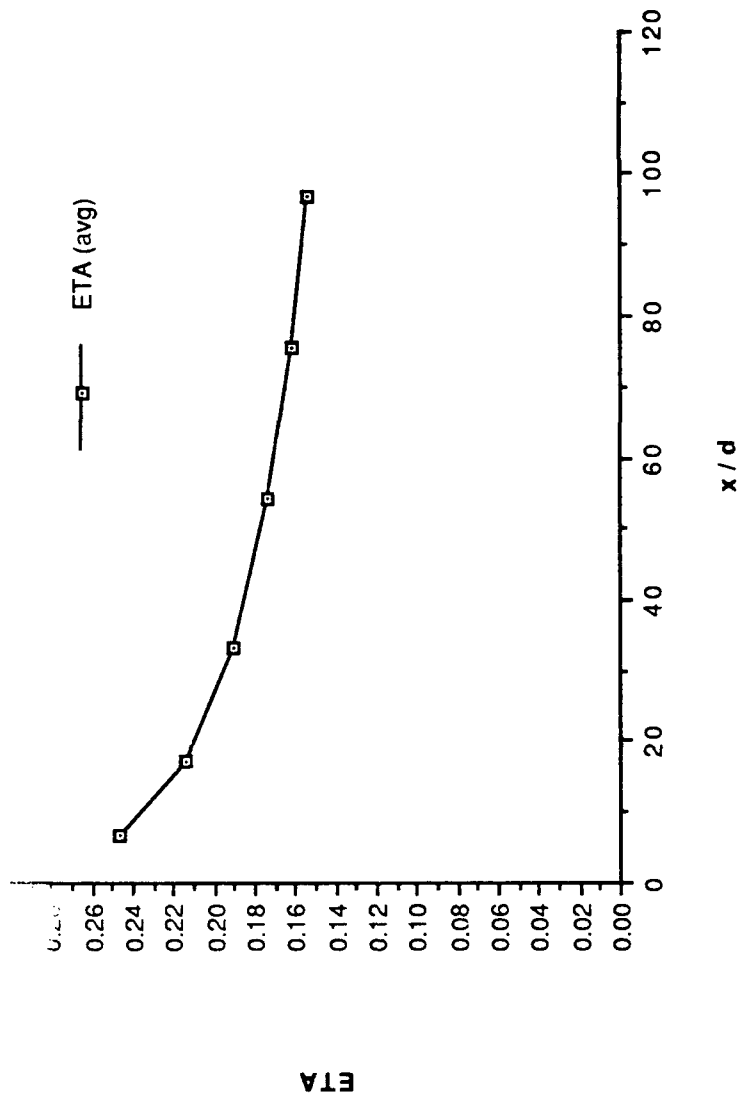


Figure 130. η , vs x/d , Simple Angle, 2 rows, $m=0.5$, Spanwise Average.

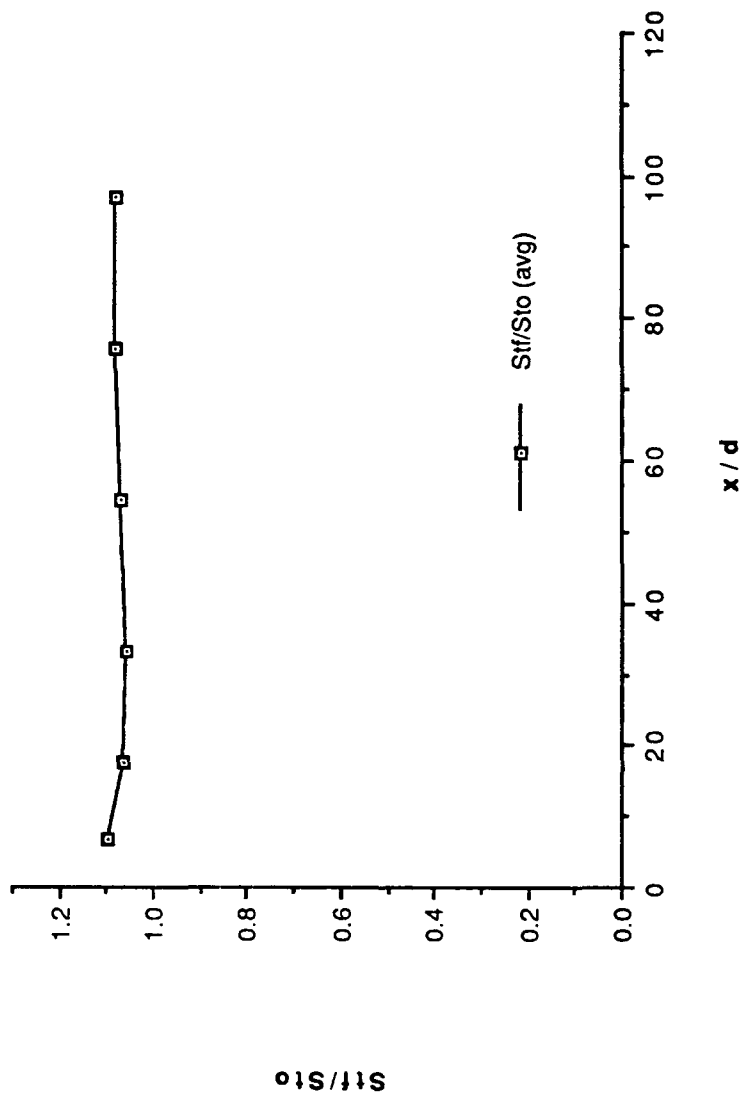


Figure 131. St_f/St_0 vs x/d , Simple Angle, 2 rows, $m=0.5$, Spanwise Average.

FILM-COOLING EFFECTIVENESS

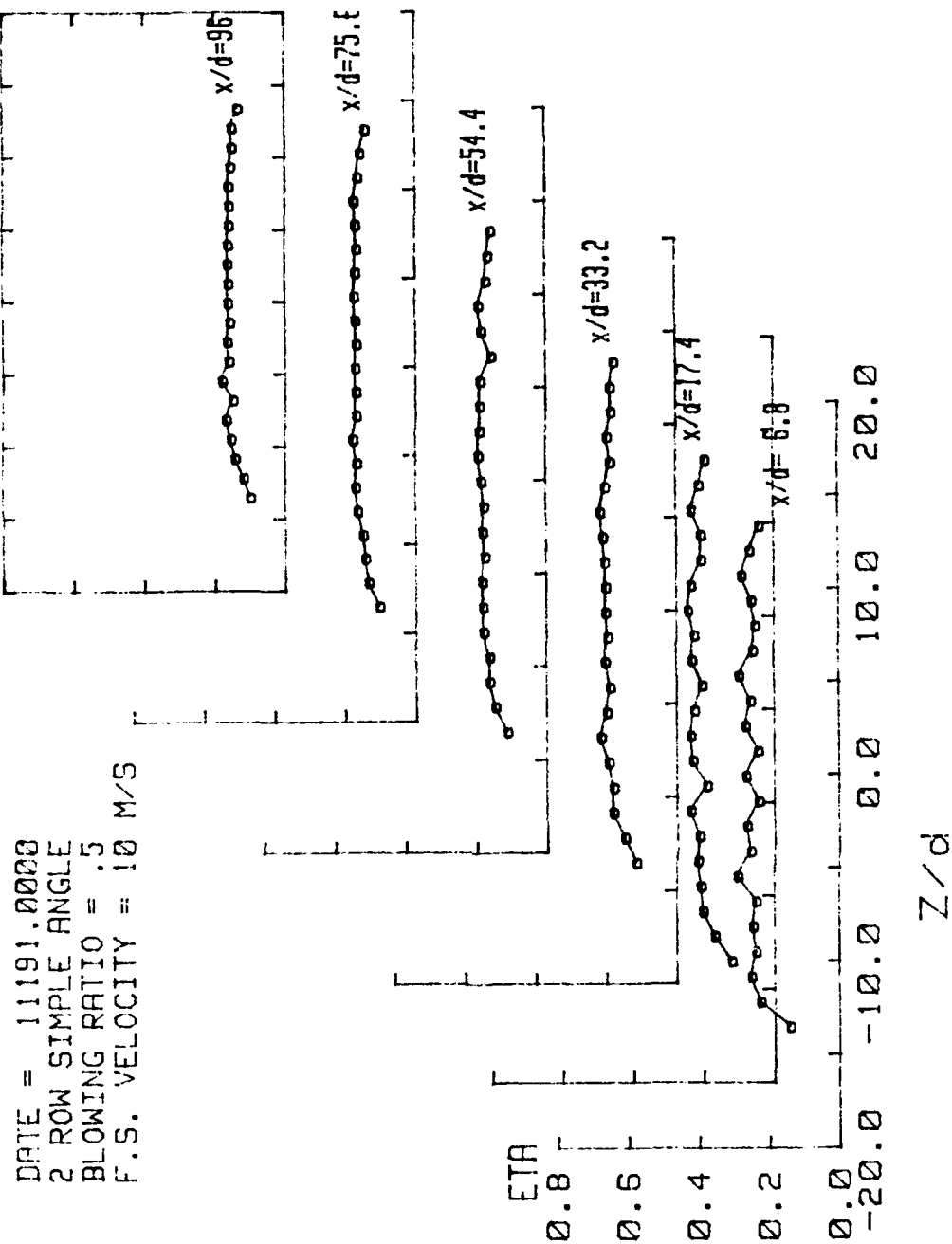


Figure 132. Spanwise Variation of η , Simple Angle, 2 rows, $m=0.5$.

STANTON NUMBER RATIOS

DATE = 11191.1247
 THETA=1.450
 BLOWING RATIO = .5
 F.S. VELOCITY = 10 M/S

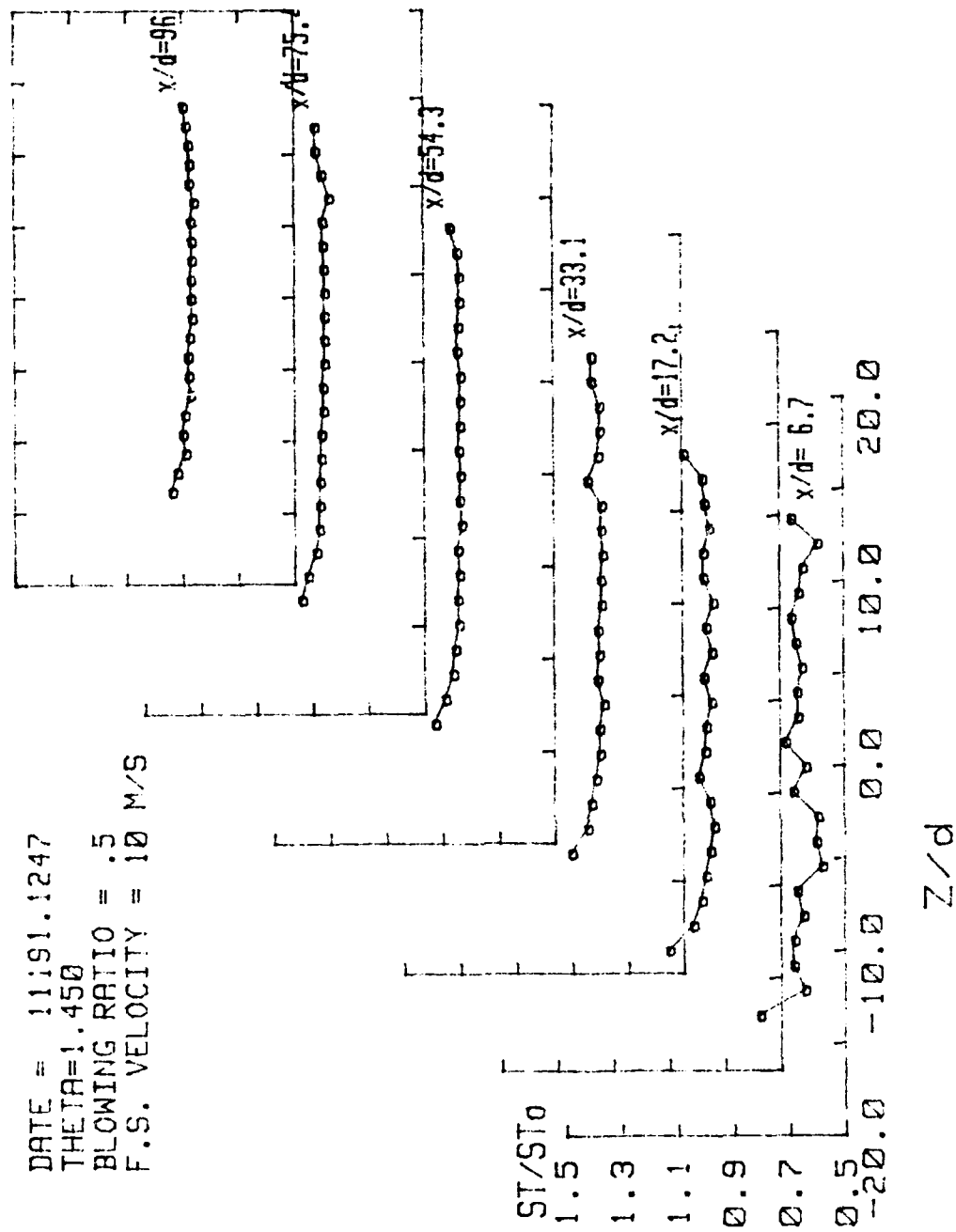


Figure 133. Spanwise Variation of St/St_0 , Simple Angle, 2 rows, $m=0.5$, $\theta=1.450$.

ISO-ENERGETIC STANTON # RATIO

DATE = 11191.0000
 2 ROW SIMPLE ANGLE
 BLOWING RATIO = .5
 F.S. VELOCITY = 10 M/S

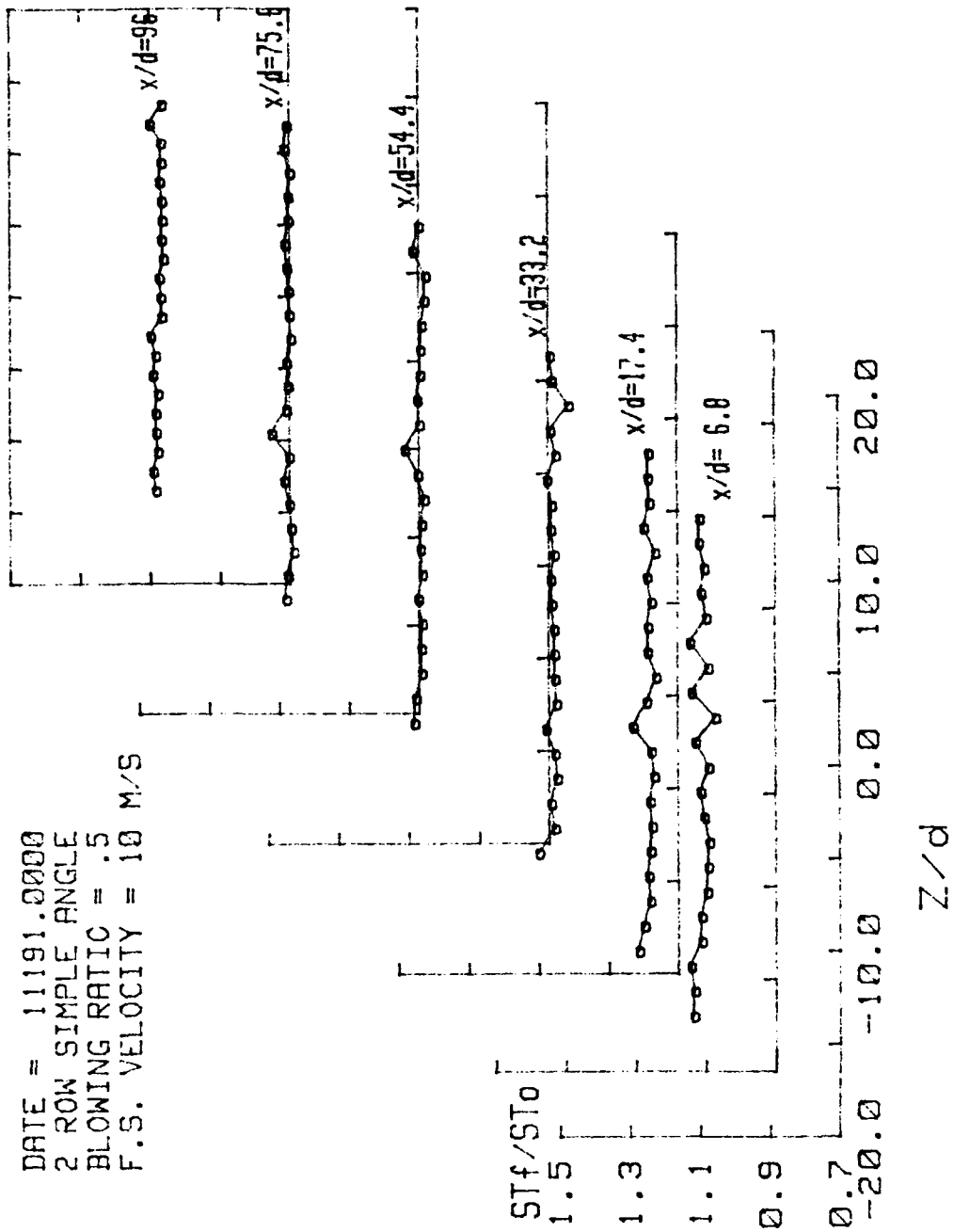
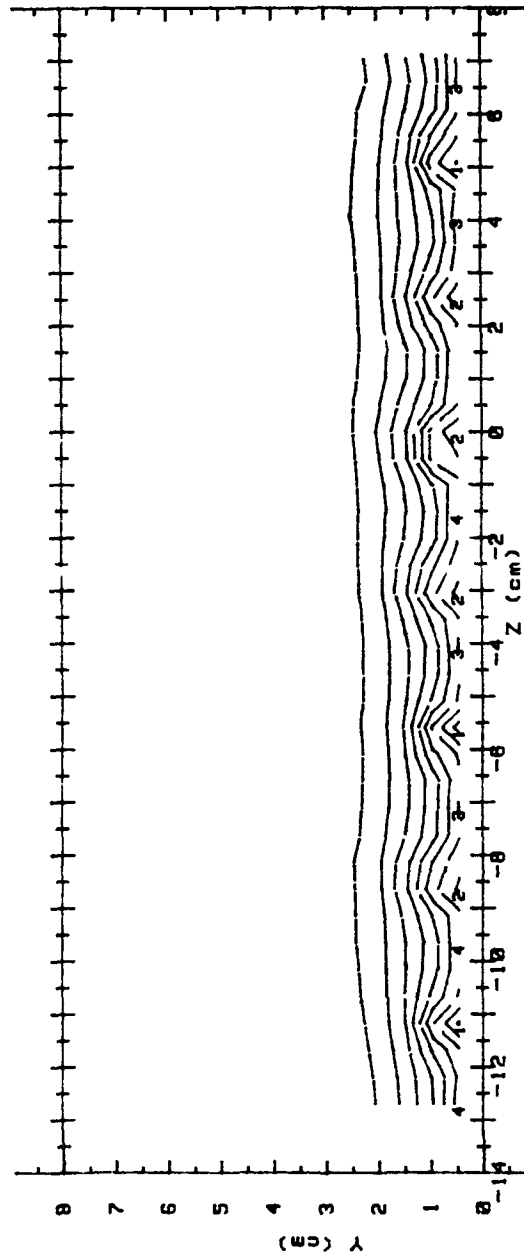


Figure 134. Spanwise Variation of St_f/St_0 , Simple Angle, 2 rows, $m=0.5$.

RUN #11891.0734

Ux



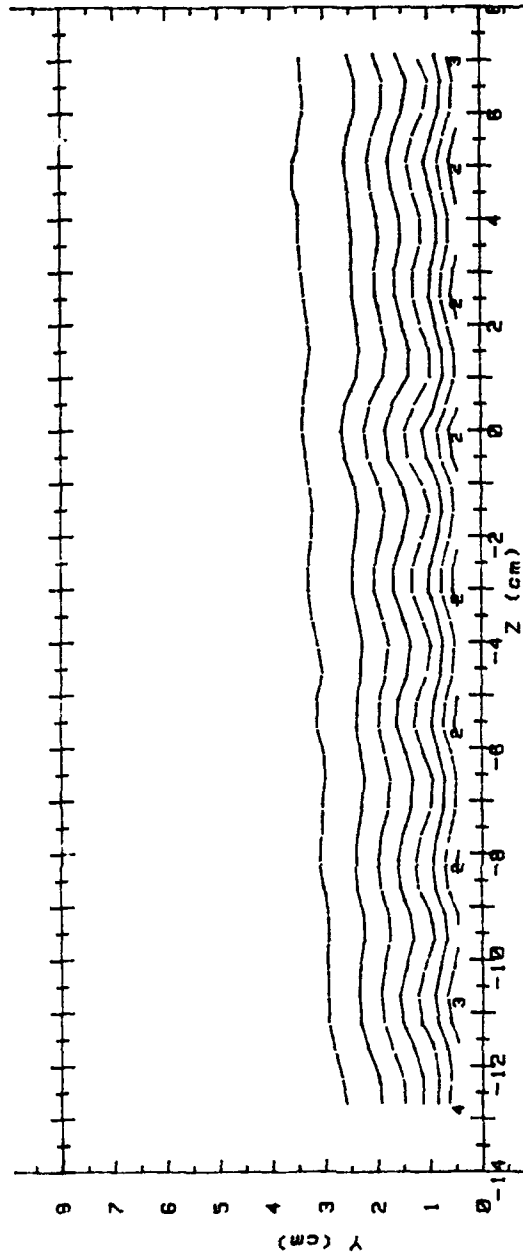
Ux (m/s) RANGES 2 ROW m=0.5 x/d = 9.4

0 :	< 5.5	5 :	7.5 < 8
1 :	5.5 < 6	6 :	8 < 8.5
2 :	6 < 6.5	7 :	8.5 < 9
3 :	6.5 < 7	8 :	9 < 9.5
4 :	7 < 7.5	9 :	9.5 < 10
		10 :	> 10

Figure 135. Streamwise Velocity Field, Simple, 2 rows, $m=0.5$, $x/d=9.4$.

RUN #12091.0857

Ux



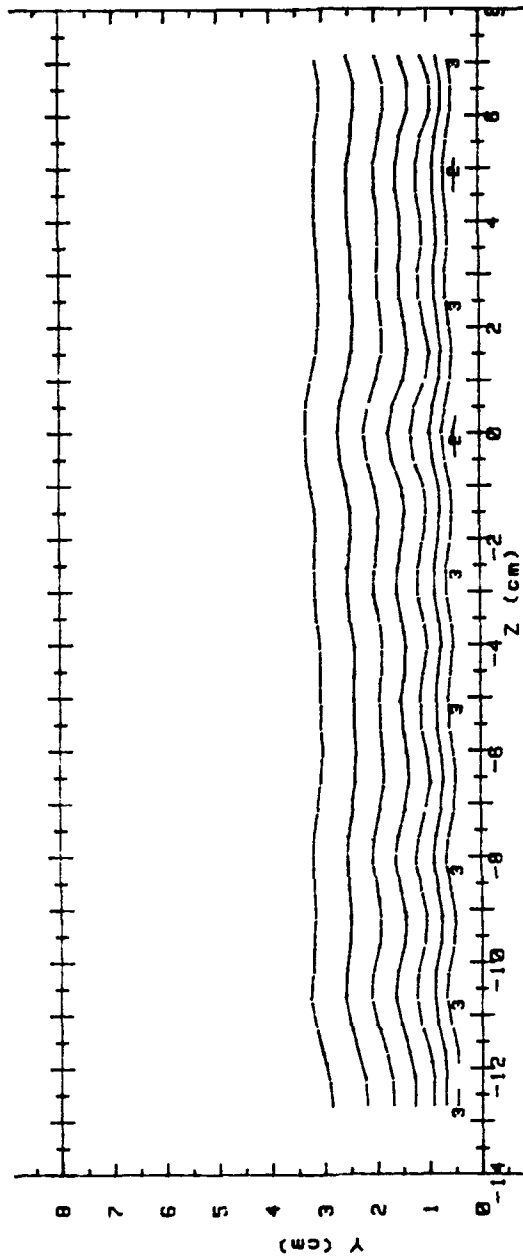
Ux(m/s) RANGES 2 ROW m=0.5 x/d = 43.7

0 :	< 5.5	5 :	7.5 < 8
1 :	5.5 < 6	6 :	8 < 8.5
2 :	6 < 6.5	7 :	8.5 < 9
3 :	6.5 < 7	8 :	9 < 9.5
4 :	7 < 7.5	9 :	9.5 < 10
		10 :	> 10

Figure 136. Streamwise Velocity Field, Simple Angle, 2 rows, $m=0.5$, $x/d=43.7$.

RUN #12291.1632

Ux



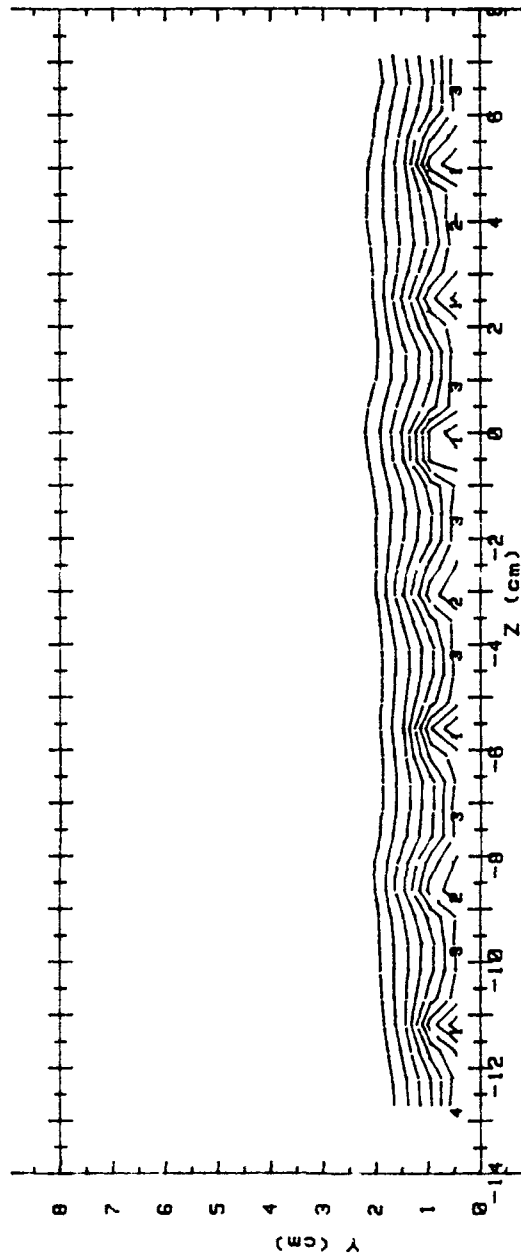
Ux(m/s) RANGES 2 ROW m=0.5 x/d = 85.2

0 :	< 5.5	5 :	7.5 < 8
1 :	5.5 < 6	6 :	8 < 8.5
2 :	6 < 6.5	7 :	8.5 < 9
3 :	6.5 < 7	8 :	9 < 9.5
4 :	7 < 7.5	9 :	9.5 < 10
		10 :	10

Figure 137. Streamwise Velocity Field, Simple Angle, 2 rows, $m=0.5$, $x/d=85.2$.

RUN #11891.0734

Ptotal



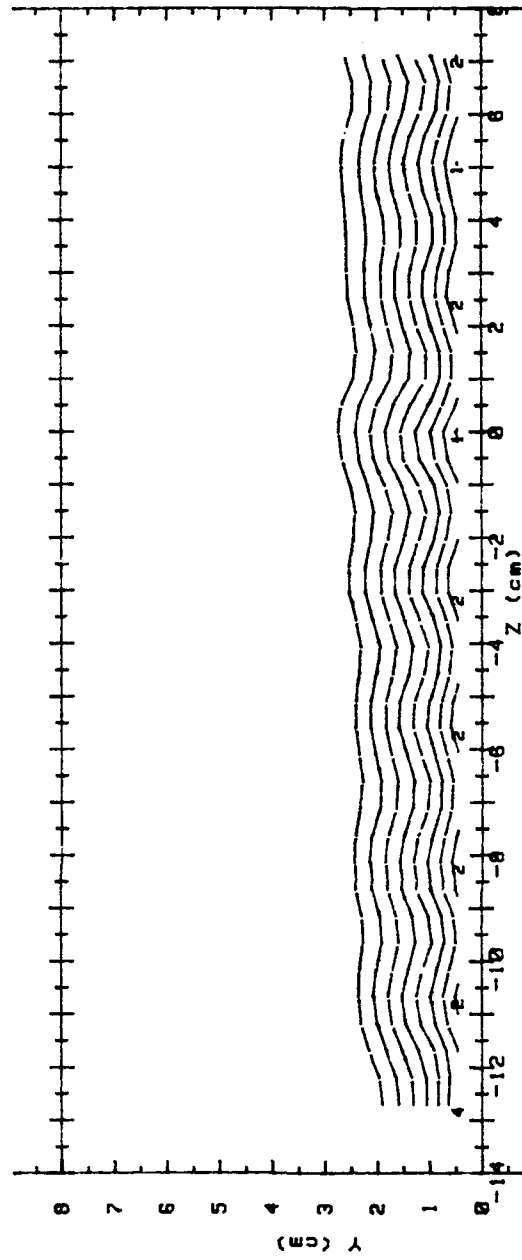
Ptotal(Pascals) RANGES 2 ROW m=0.5 x/d= 9.4

0 :	< 20	5 :	36 < 40
1 :	20 < 24	6 :	40 < 44
2 :	24 < 28	7 :	44 < 48
3 :	28 < 32	8 :	48 < 52
4 :	32 < 36	9 :	52 < 56
		10 :	> 56

Figure 138. Streamwise Pressure Field, Simple Angle, 2 rows, $m=0.5$, $x/d=9.4$.

RUN #12091.0857

Ptotal



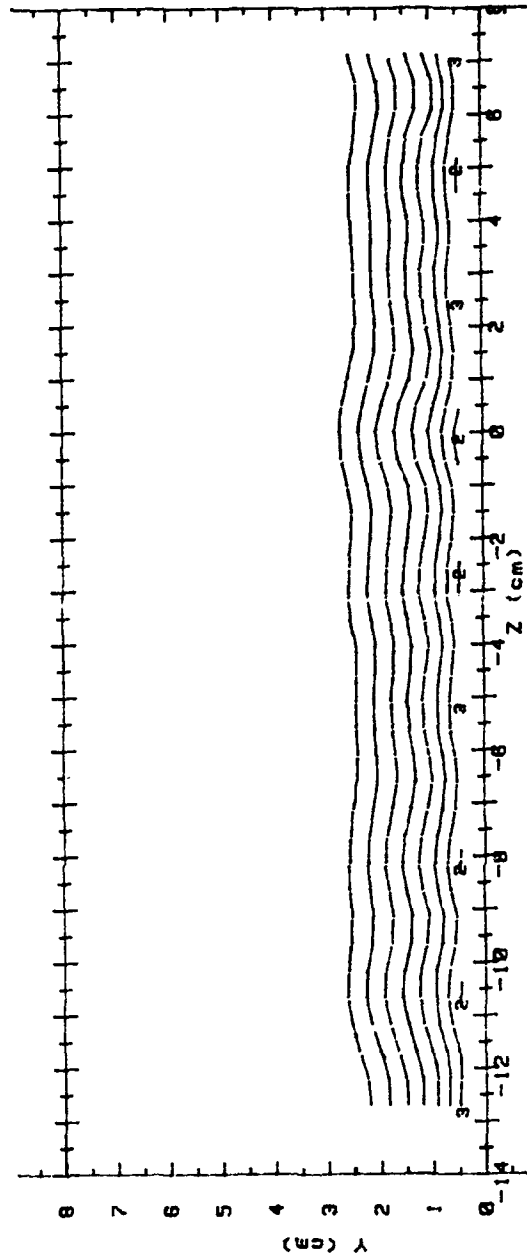
Ptotal(Pascals) RANGES 2 ROW m=0.5 x/d= 43.7

0 :	< 20	5 :	36 < 40
1 :	20 < 24	6 :	40 < 44
2 :	24 < 28	7 :	44 < 48
3 :	28 < 32	8 :	48 < 52
4 :	32 < 36	9 :	52 < 56
		10 :	56

Figure 139. Streamwise Pressure Field, Simple Angle, 2 rows, $m=0.5$, $x/d=43.7$.

RUN #12291.1632

Ptotal



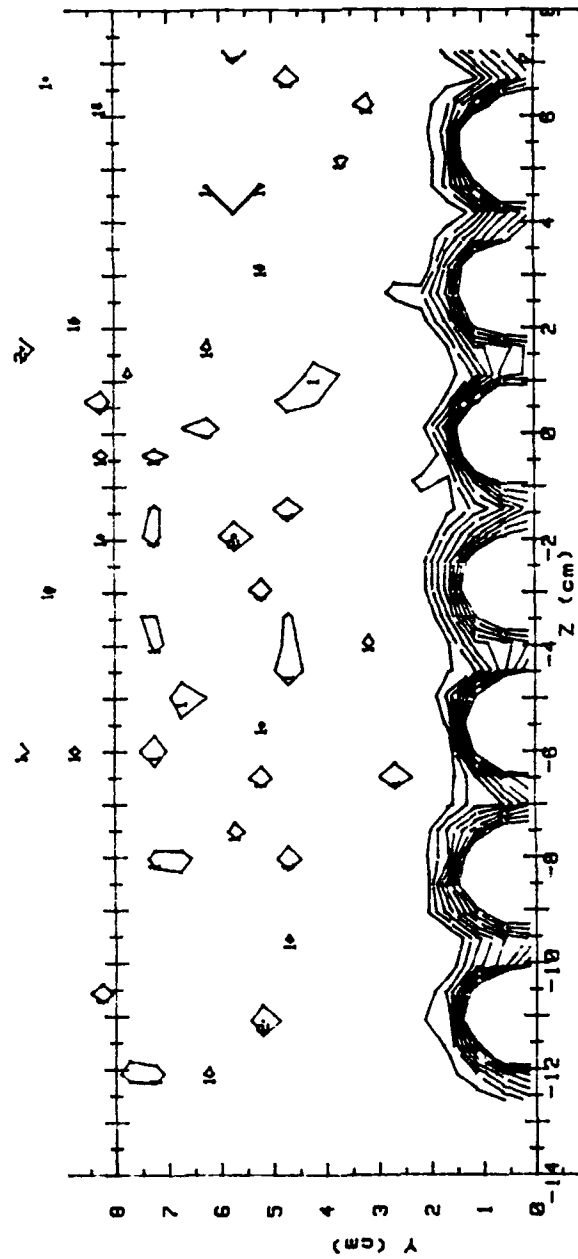
Ptotal(Pascals) RANGES 2 ROW m=0.5 x/d=85.2

0 :	< 20	5 :	36 < 40
1 :	20 < 24	6 :	40 < 44
2 :	24 < 28	7 :	44 < 48
3 :	28 < 32	8 :	48 < 52
4 :	32 < 36	9 :	52 < 56
		10 :	> 56

Figure 140. Streamwise Pressure Field, Simple Angle, 2 rows, $m=0.5$, $x/d=85.2$.

RUN #12691.0943

T - Tfs



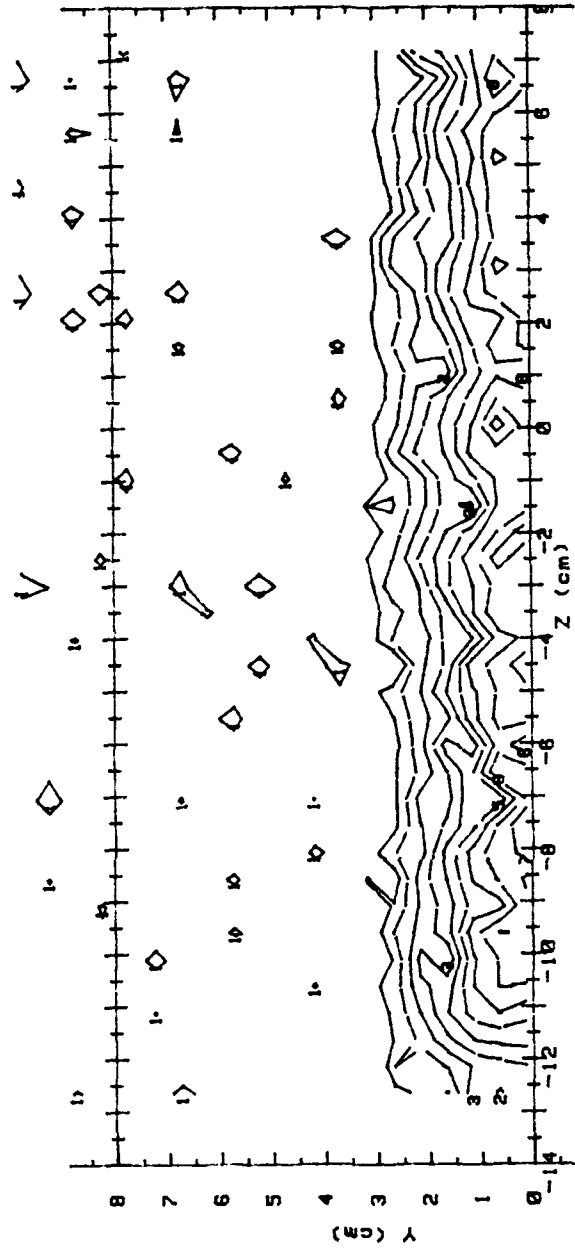
T - Tfs (CELCIUS) RANGES 2 ROW m=0.5 x/d = 9.4

0 :	< .5	5 :	2.5 < 3
1 :	.5 < 1	6 :	3 < 3.5
2 :	1 < 1.5	7 :	3.5 < 4
3 :	1.5 < 2	8 :	4 < 4.5
4 :	2 < 2.5	9 :	4.5

Figure 141. Streamwise Injectant Distribution, Simple Angle, 2 rows, $m=0.5$, $x/d=9.4$.

RUN #12591.1211

T - Tfs



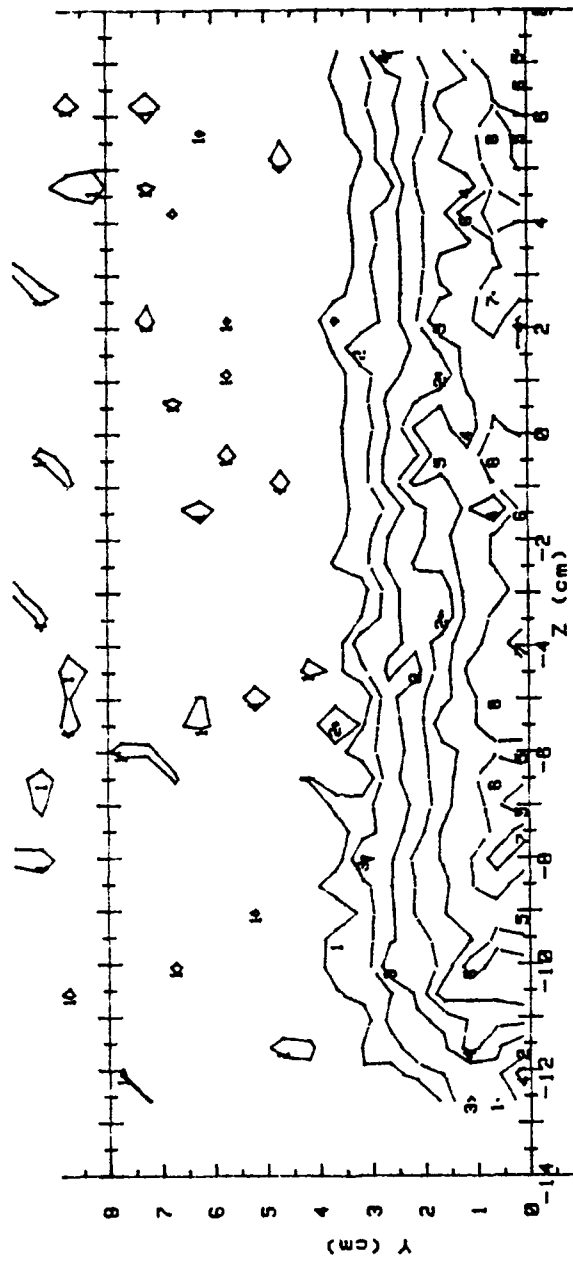
T - Tfs (CELCIUS) RANGES 2 ROW m=0.5 x/d = 43.7

- 0 : < .5
- 1 : .5 < 1
- 2 : 1 < 1.5
- 3 : 1.5 < 2
- 4 : 2 < 2.5
- 5 : 2.5 < 3
- 6 : 3 < 3.5
- 7 : 3.5 < 4
- 8 : 4 < 4.5
- 9 : 4.5

Figure 142. Streamwise Injectant Distribution, Simple Angle, 2 rows, m=0.5, x/d=43.7.

RUN #12591.0804

T - Tfs



T - Tfs (CELCIUS) RANGES 2 ROW m=0.5 x/d = 85.2

0 :	< .5	5 :	2.5 < 3
1 :	.5 < 1	6 :	3 < 3.5
2 :	1 < 1.5	7 :	3.5 < 4
3 :	1.5 < 2	8 :	4 < 4.5
4 :	2 < 2.5	9 :	4.5

Figure 143. Streamwise Injectant Distribution, Simple Angle, 2 rows, m=0.5, x/d=85.2.

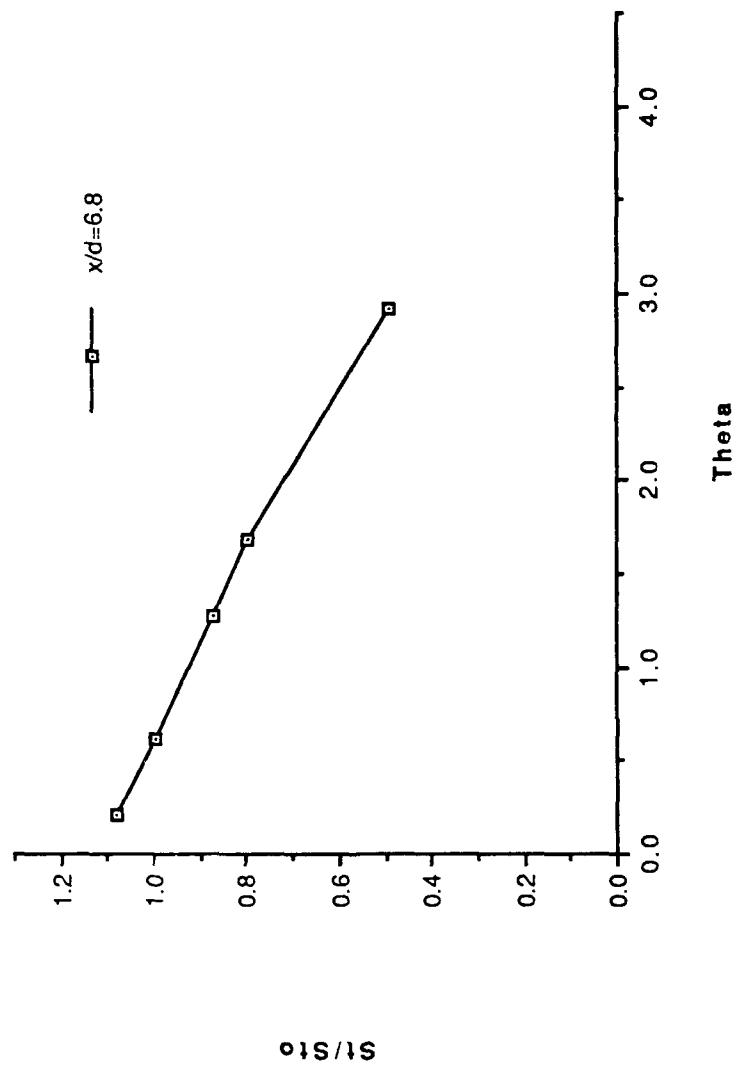


Figure 144. St/St_0 vs θ , Simple Angle, 2 rows, $m=1.0$, $x/d=6.8$, $z=0.0$.

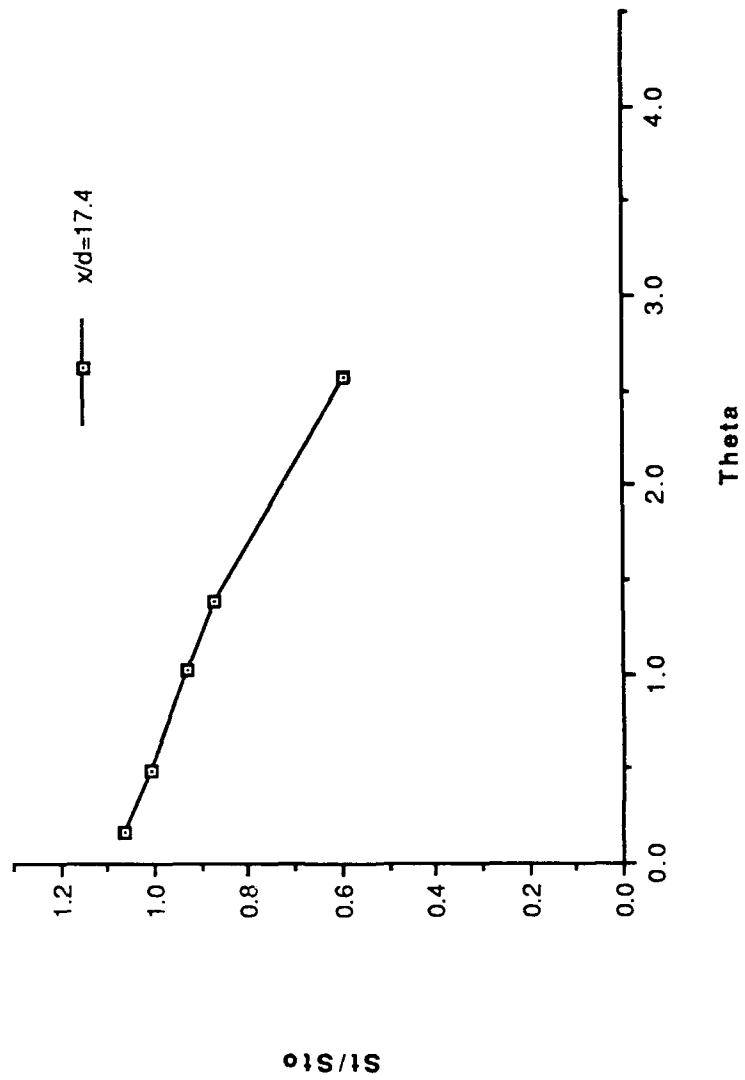


Figure 145. St/St_0 vs θ , Simple Angle, 2 rows, $m=1.0$, $x/d=17.4$, $z=0.0$.

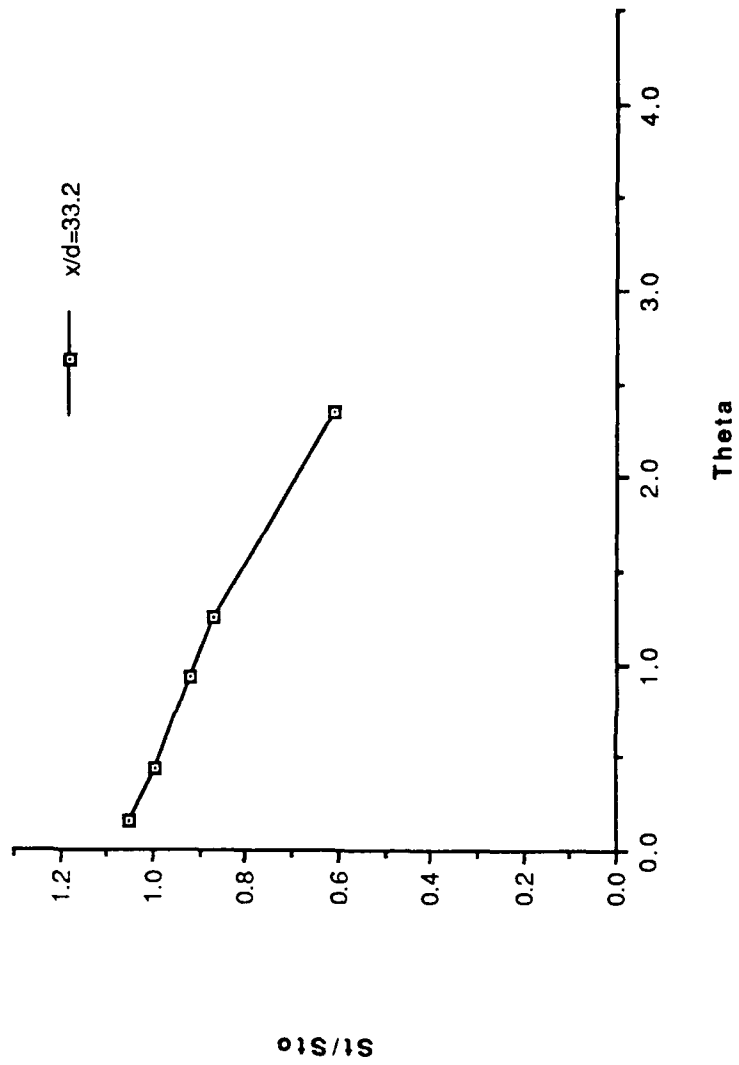


Figure 146. St/St_0 vs θ , Simple Angle, 2 rows, $m=1.0$, $x/d=33.2$, $z=0.0$.

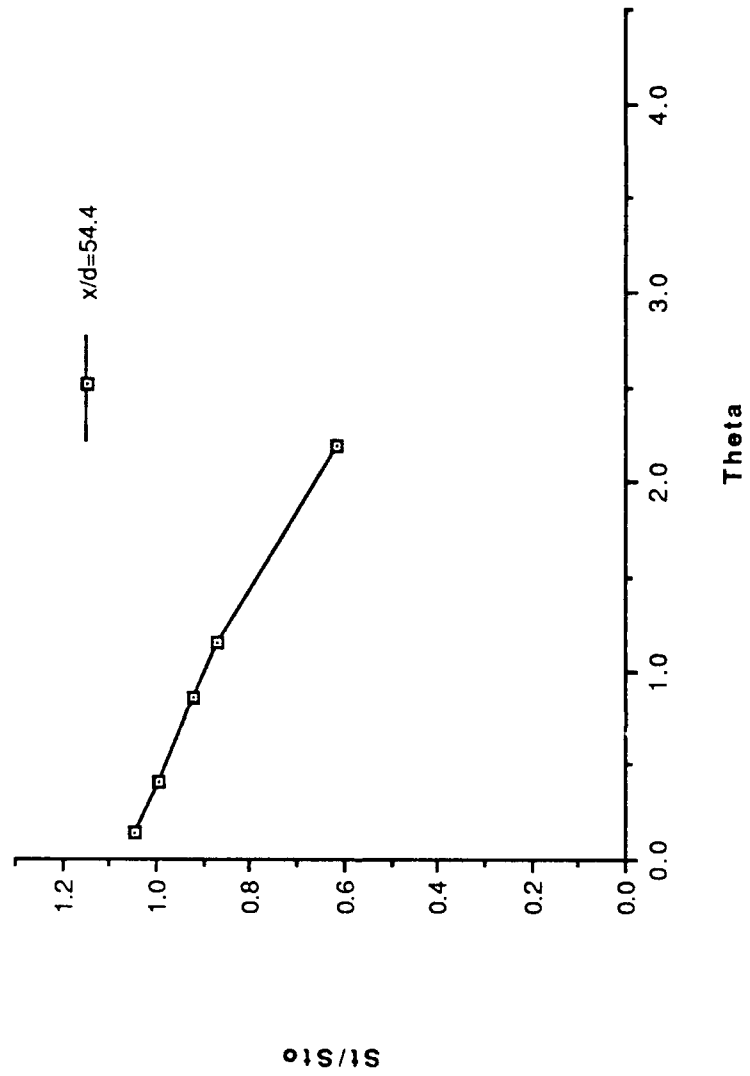


Figure 147. St/St_0 vs θ , Simple Angle, 2 rows, $m=1.0$, $x/d=54.4$, $z=0.0$.

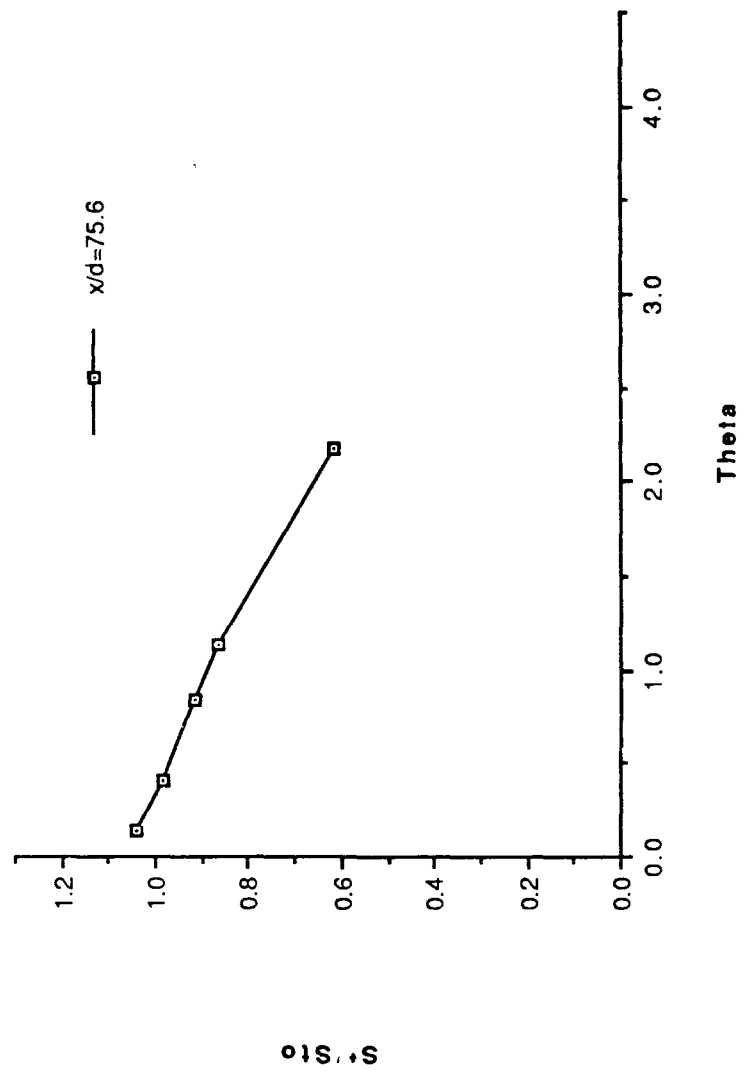


Figure 148. St/St_0 vs θ , Simple Angle, 2 rows, $m=1.0$, $x/d=75.6$, $z=0.0$.

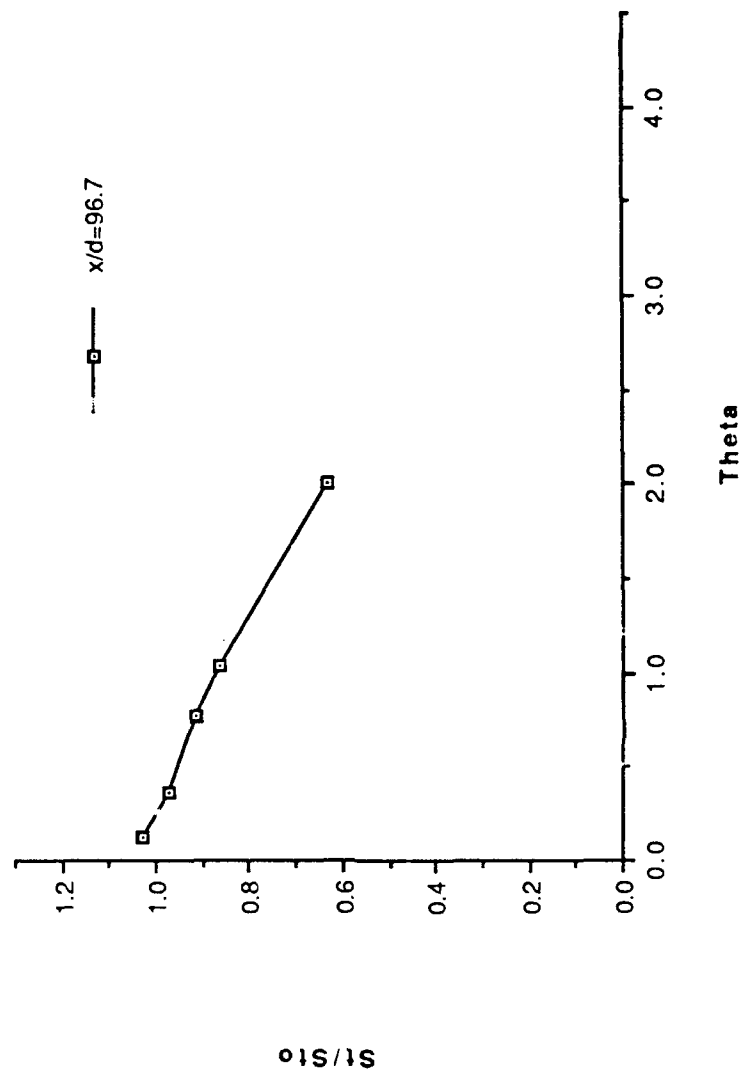


Figure 149. St/St_0 vs θ , Simple Angle, 2 rows, $m=1.0$, $x/d=96.7$, $z=0.0$.

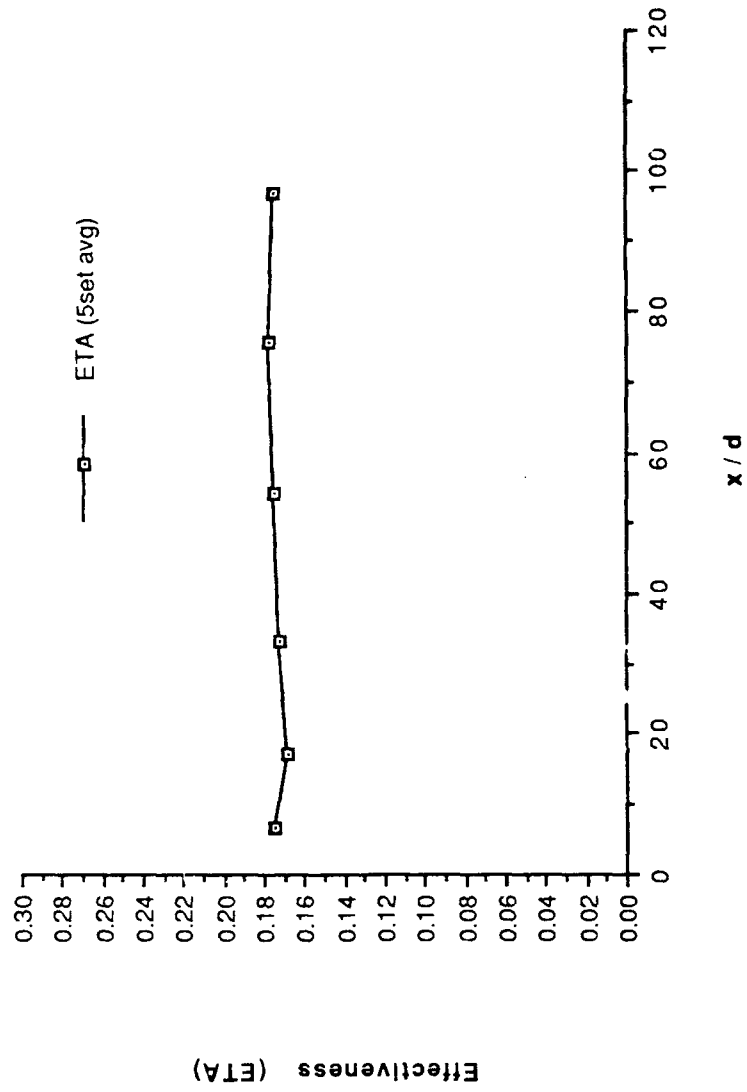


Figure 150. η , vs x/d , Simple Angle, 2 rows, $m=1.0$, Spanwise Average.

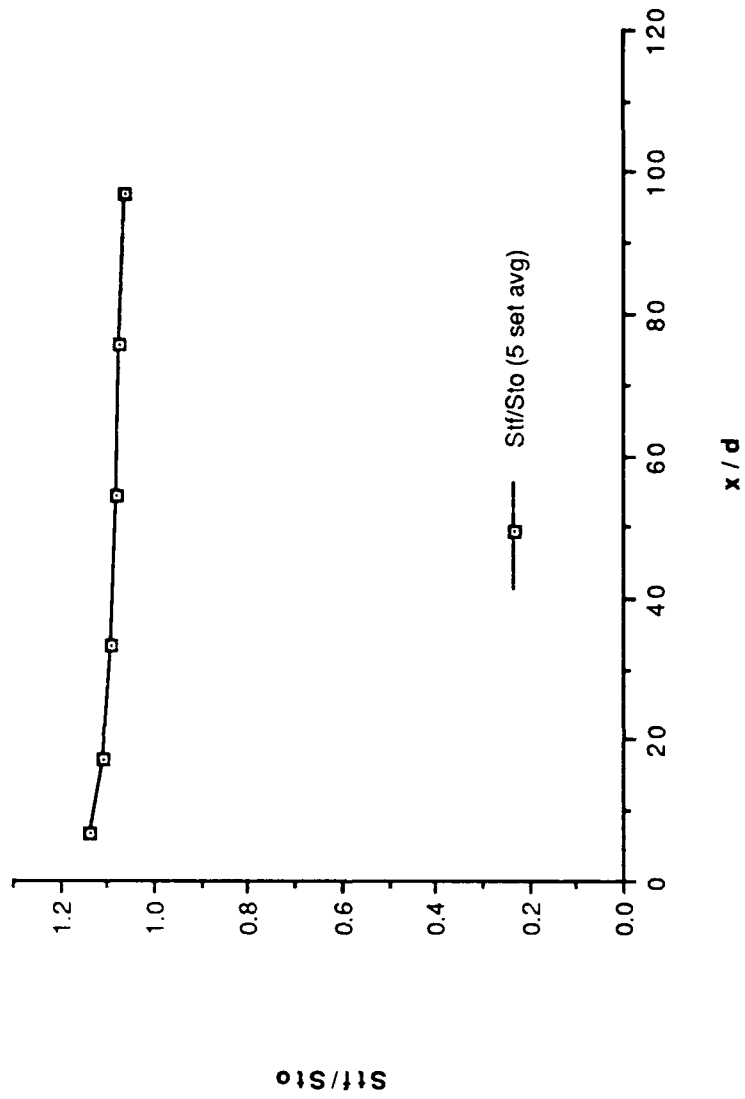


Figure 151. St_f/St_0 vs x/d , Simple Angle, 2 rows, $m=1.0$, Spanwise Average.

FILM-COOLING EFFECTIVENESS

DATE = 11091.0000
 2 ROW SIMPLE ANGLE
 BLOWING RATIO = 1
 F.S. VELOCITY = 10 M/S

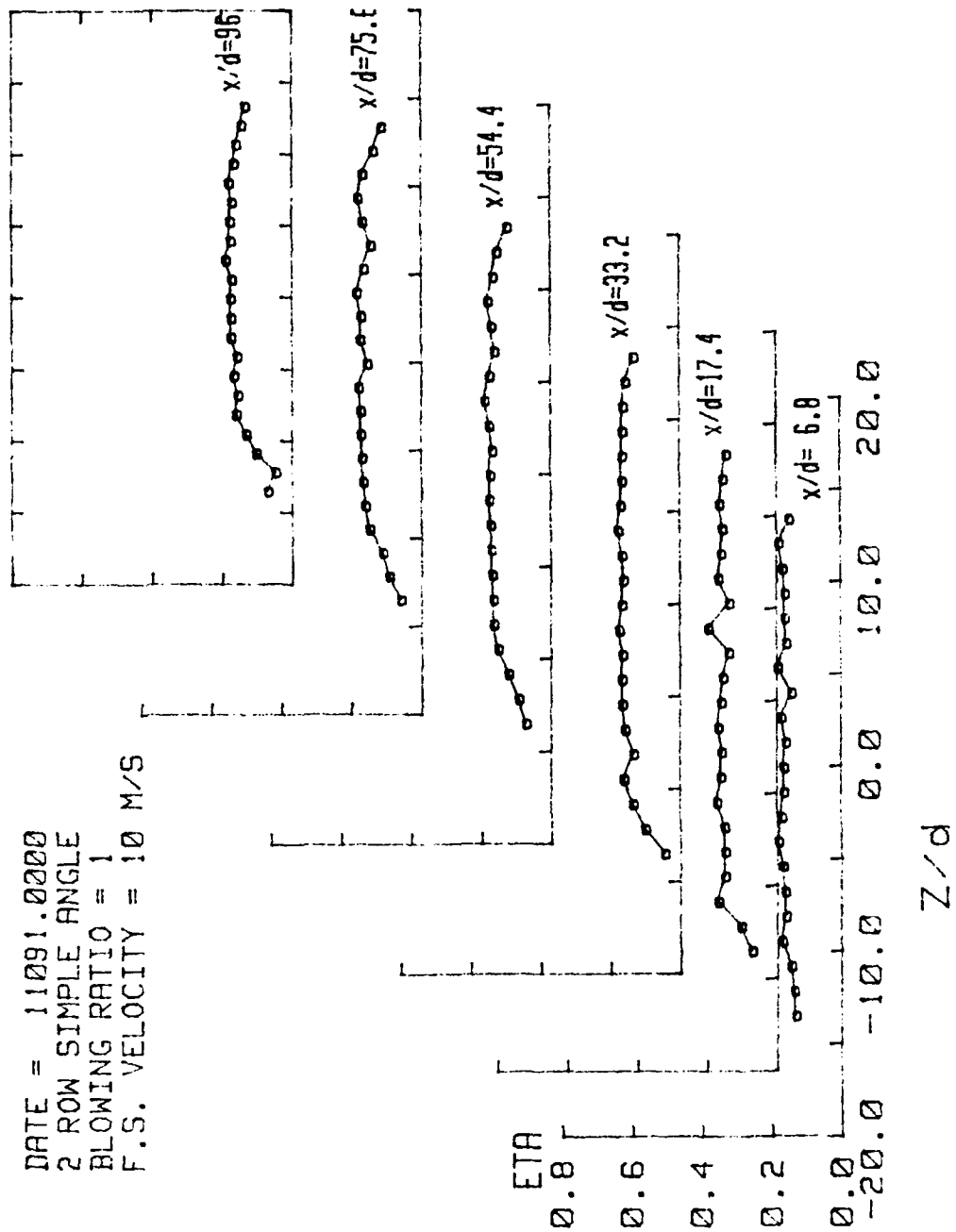


Figure 152. Spanwise Variation of η , Simple Angle, 2 rows, $m=1.0$.

STANTON NUMBER RATIOS

DATE = 11091.1413
 THETA=1.500
 BLOWING RATIO = 1
 F.S. VELOCITY = 10 M/S

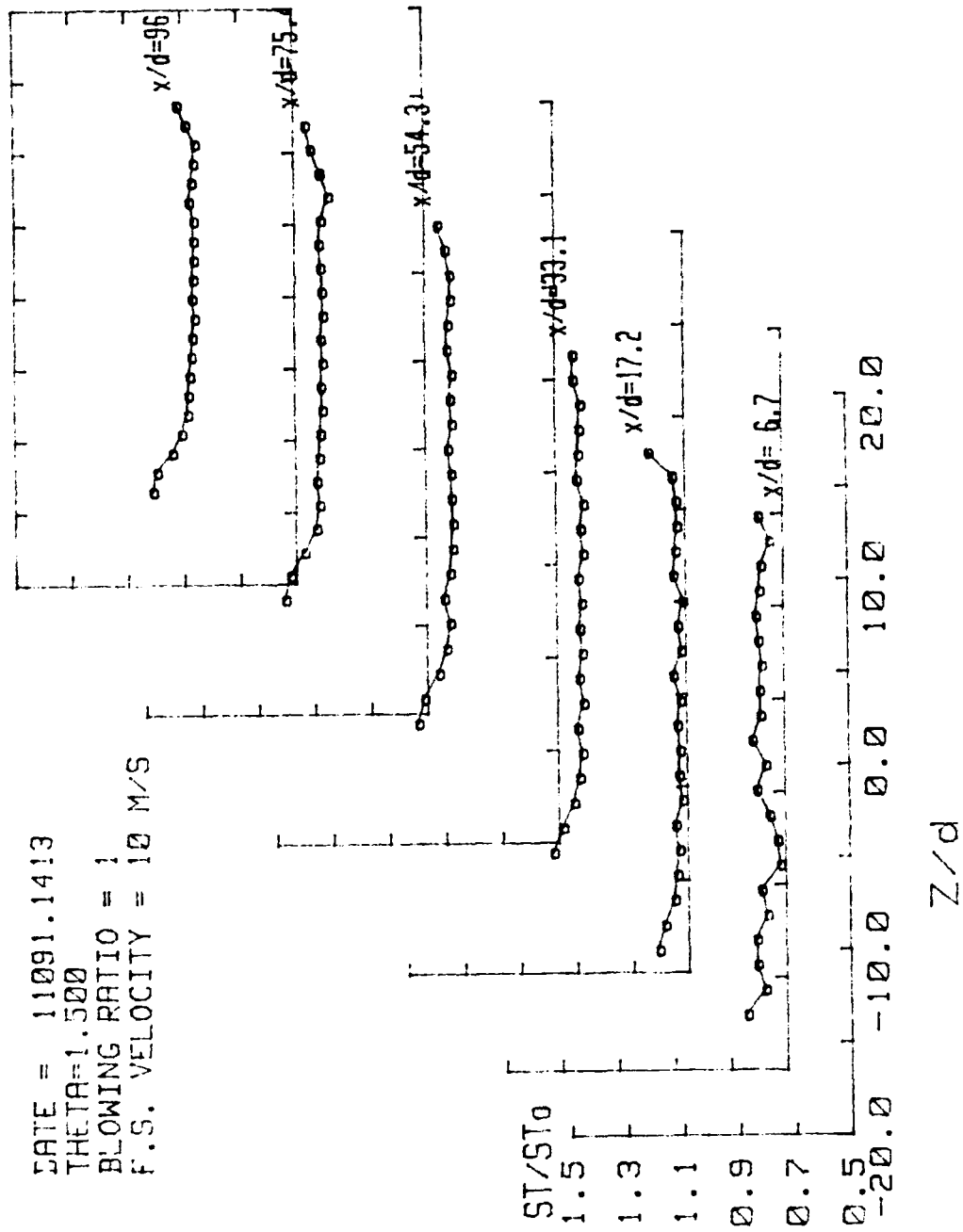


Figure 153. Spanwise Variation of St/St_0 , Simple Angle, 2 rows, $m=1.0$, $\theta=1.500$.

ISO-ENERGETIC STANTON # RATIO

DATE = 11091.0000
 2 ROW SIMPLE ANGLE
 BLOWING RATIO = 1
 F.S. VELOCITY = 10 M/S

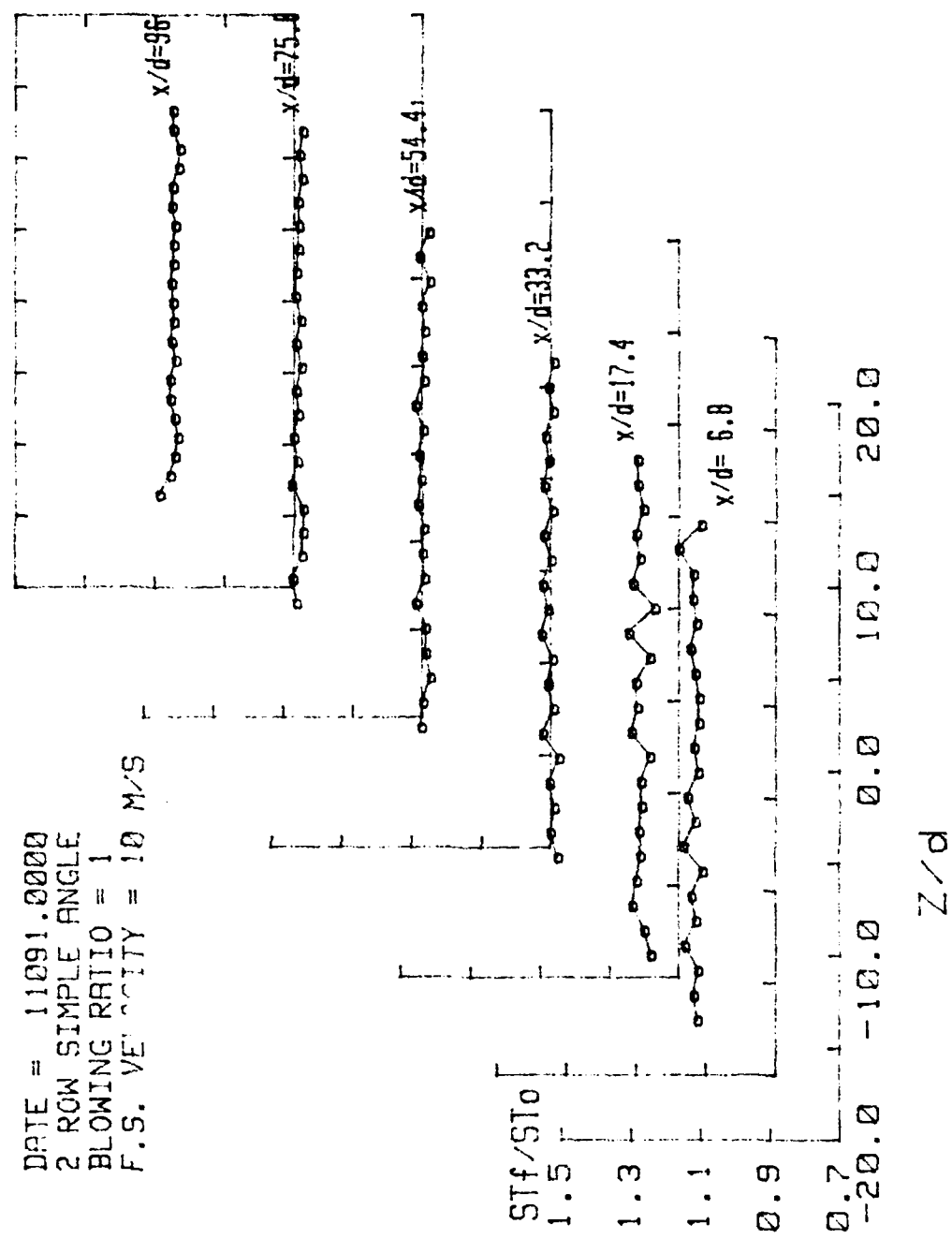
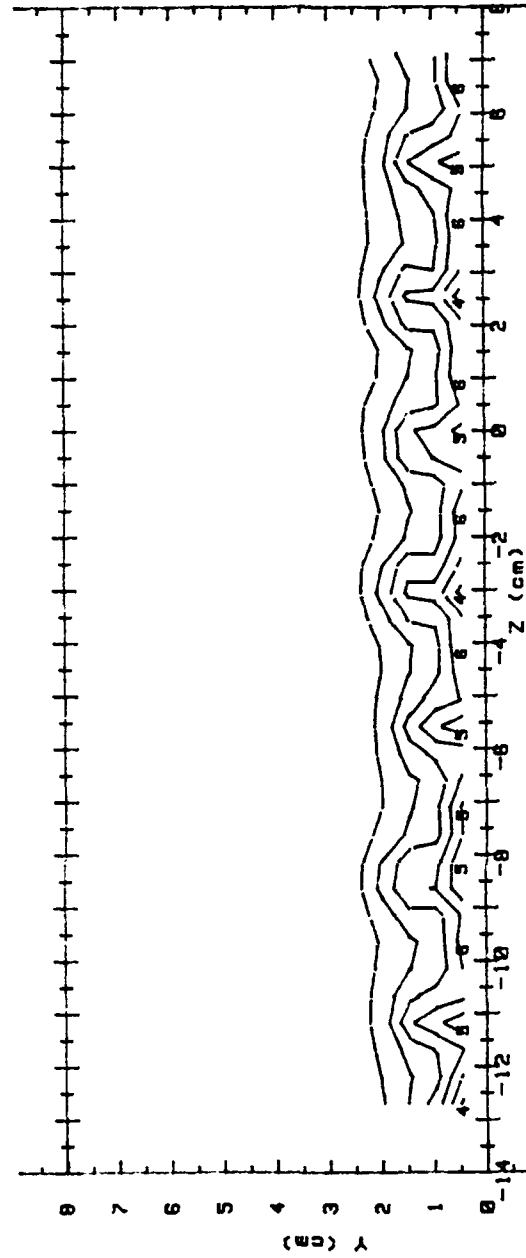


Figure 154. Spanwise Variation of St_f/St_0 , Simple Angle, 2 rows, $m=1.0$.

RUN #11891.1838

Ux



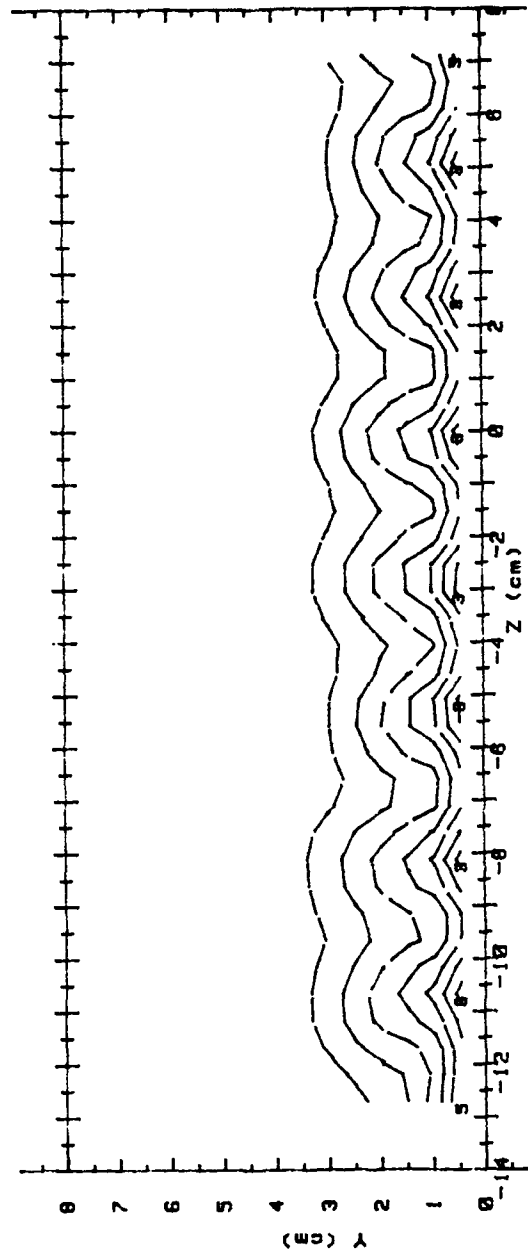
Ux(m/s) RANGES 2 ROW m=1.0 x/d = 9.4

0 :	< 5.5	5 :	7.5 < 8
1 :	5.5 < 6	6 :	8 < 8.5
2 :	6 < 6.5	7 :	8.5 < 9
3 :	6.5 < 7	8 :	9 < 9.5
4 :	7 < 7.5	9 :	9.5 < 10
		10 :	> 10

Figure 155. Streamwise Velocity Field, Simple, 2 rows, m=1.0, x/d=9.4.

RUN #12091.1924

Ux



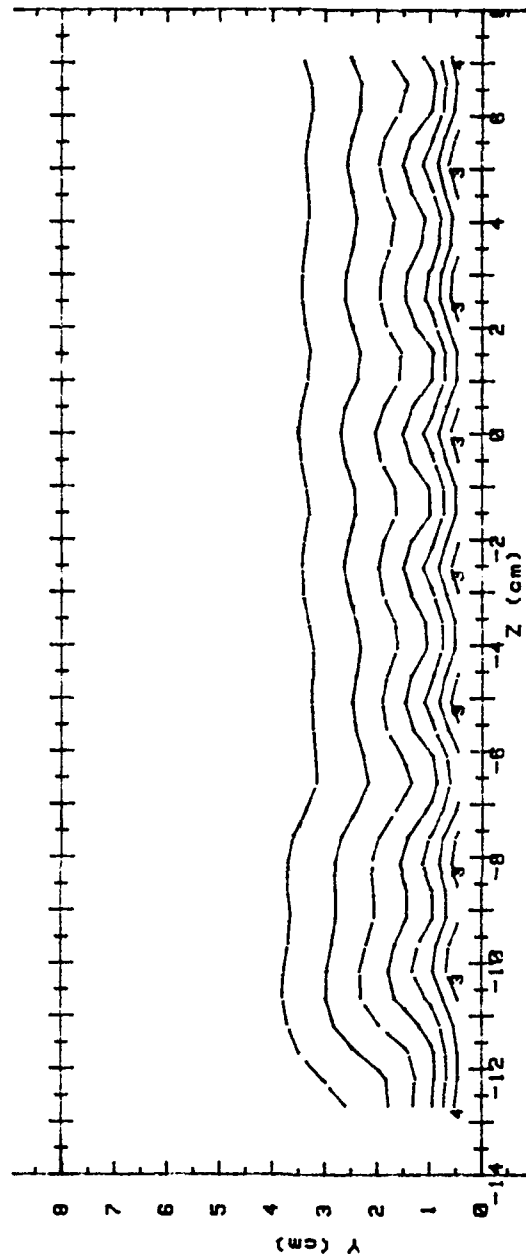
Ux (m/s) RANGES 2 ROW m=1.0 x/d = 43.7

0 :	< 5.5	5 :	7.5 < 8
1 :	5.5 < 6	6 :	8 < 8.5
2 :	6 < 6.5	7 :	8.5 < 9
3 :	6.5 < 7	8 :	9 < 9.5
4 :	7 < 7.5	9 :	9.5 < 10
		10 :	10

Figure 156. Streamwise Velocity Field, Simple Angle, 2 rows, $m=1.0$, $x/d=43.7$.

RUN #12391.1758

Ux

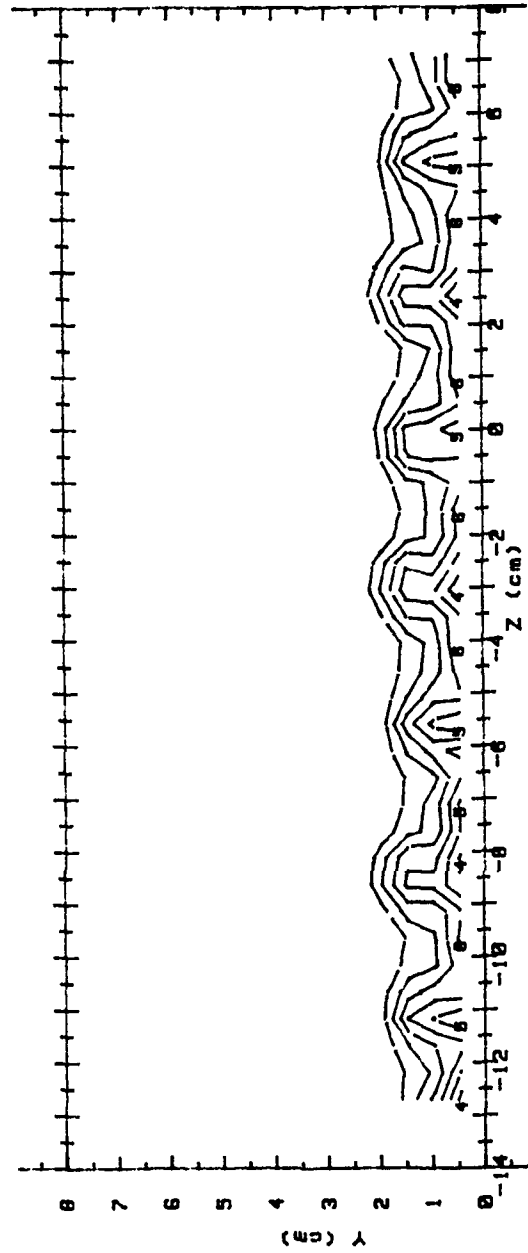


Ux (m/s) RANGES 2 ROW m=1.0 x/d = 85.2

0 :	< 5.5	5 :	7.5 < 8
1 :	5.5 < 6	6 :	8 < 8.5
2 :	6 < 6.5	7 :	8.5 < 9
3 :	6.5 < 7	8 :	9 < 9.5
4 :	7 < 7.5	9 :	9.5 < 10
		10 :	10

Figure 157. Streamwise Velocity Field, Simple Angle, 2 rows, $m=1.0$, $x/d=85.2$.

RUN #11891.1838
 Ptotal



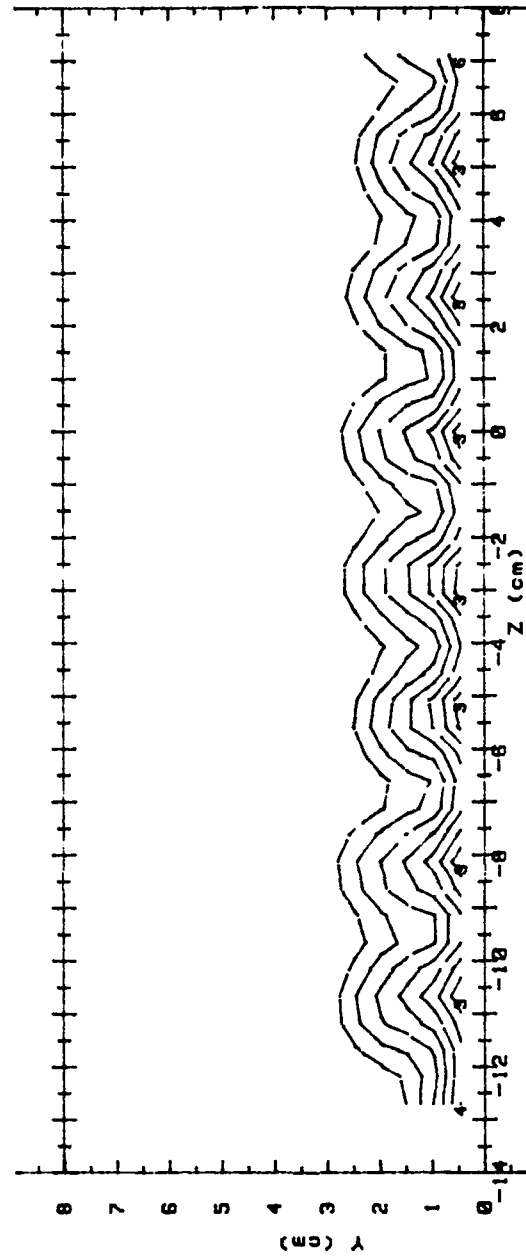
Ptotal(Pascals) RANGES 2 ROW m=1.0 x/d=9.4

0 :	< 20	5 :	36 < 40
1 :	20 < 24	6 :	40 < 44
2 :	24 < 28	7 :	44 < 48
3 :	28 < 32	8 :	48 < 52
4 :	32 < 36	9 :	52 < 56
		10 :	56

Figure 158. Streamwise Pressure Field, Simple Angle, 2 rows, $m=1.0$, $x/d=9.4$.

RUN #12091.1924

Ptotal



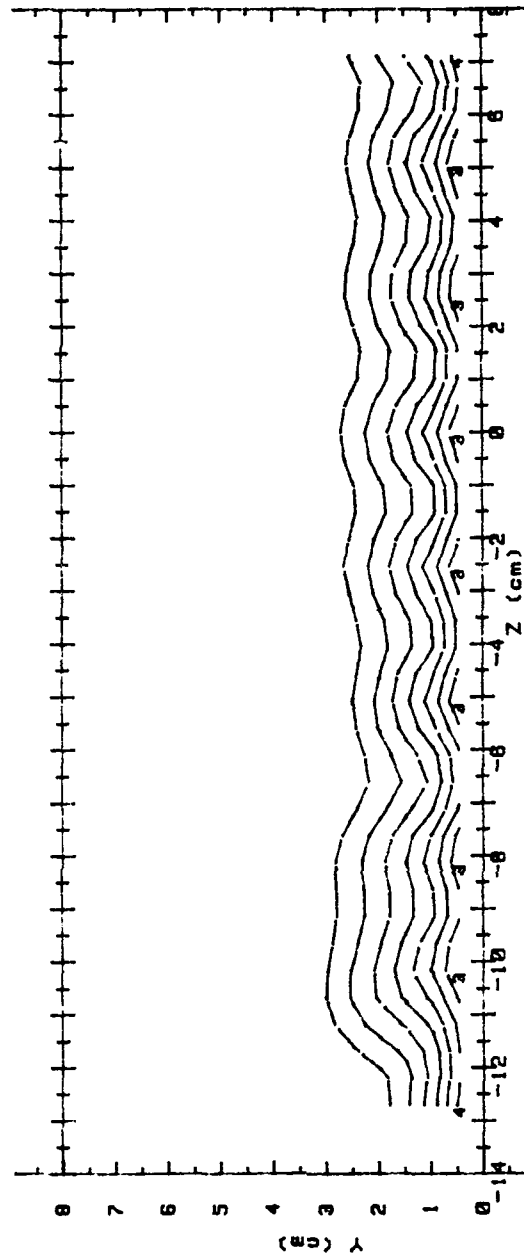
Ptotal (Pascals) RANGE: 2 ROW m=1.0 x/d= 43.7

0 :	< 20	5 :	36 < 40
1 :	20 < 24	6 :	40 < 44
2 :	24 < 28	7 :	44 < 48
3 :	28 < 32	8 :	48 < 52
4 :	32 < 36	9 :	52 < 56
		10 :	56

Figure 159. Streamwise Pressure Field, Simple Angle, 2 rows, $m=1.0$, $x/d=43.7$.

RUN #12391.1758

Ptotal



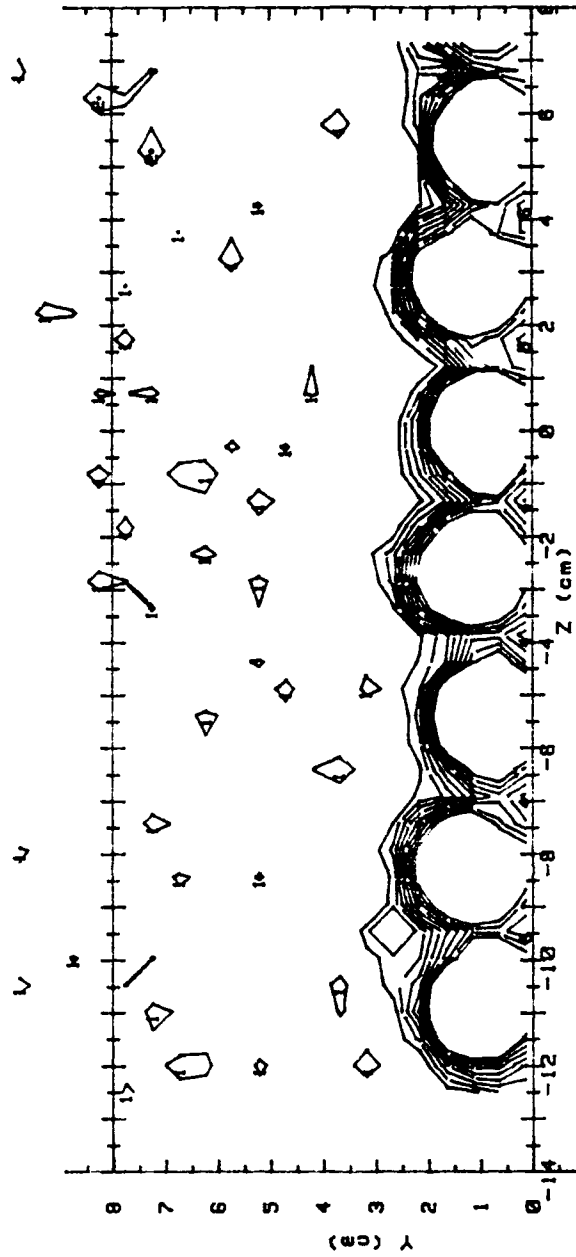
Ptotal (Pascals) RANGES 2 ROW m=1.0 x/d=85.2

0 : < 20
1 : 20 < 24
2 : 24 < 28
3 : 28 < 32
4 : 32 < 36
5 : 36 < 40
6 : 40 < 44
7 : 44 < 48
8 : 48 < 52
9 : 52 < 56
10 : > 56

Figure 160. Streamwise Pressure Field, Simple Angle, 2 rows, $m=1.0$, $x/d=85.2$.

RUN #12691.1425

T - Tfs



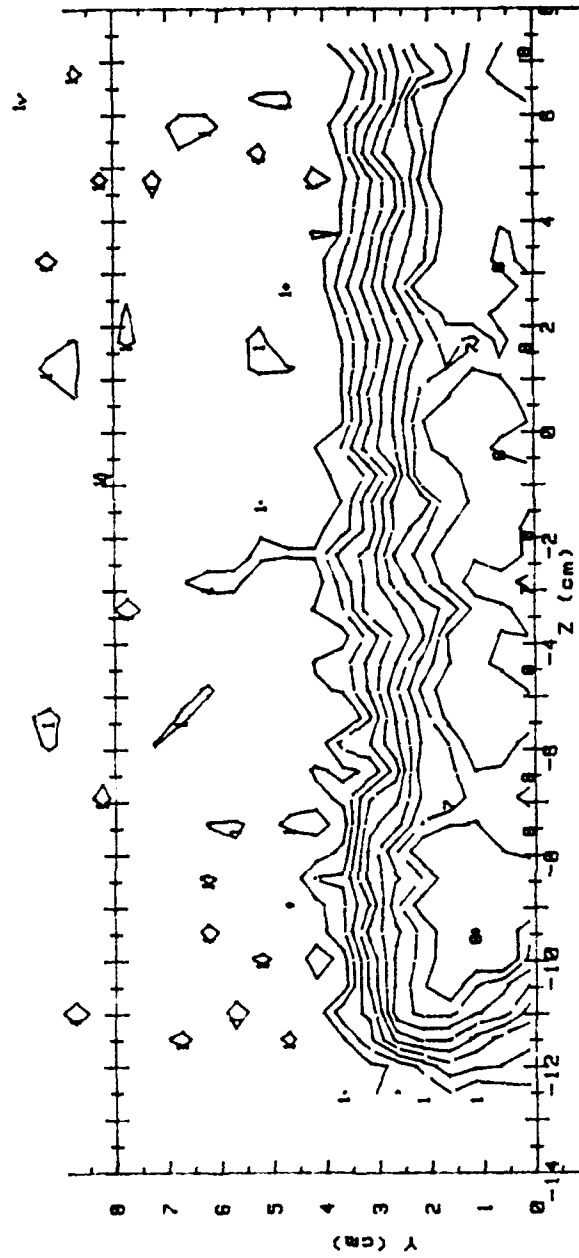
T - Tfs(CELCIUS) RANGES 2 ROW m=1.0 x/d = 9.4

0 :	< .5	5 :	> 2.5 < 3
1 :	> .5 < 1	6 :	> 3 < 3.5
2 :	> 1 < 1.5	7 :	> 3.5 < 4
3 :	> 1.5 < 2	8 :	> 4 < 4.5
4 :	> 2 < 2.5	9 :	> 4.5

Figure 161. Streamwise Injectant Distribution, Simple Angle, 2 rows, $m=1.0$, $x/d=9.4$.

RUN #12791.1033

T - Tfs



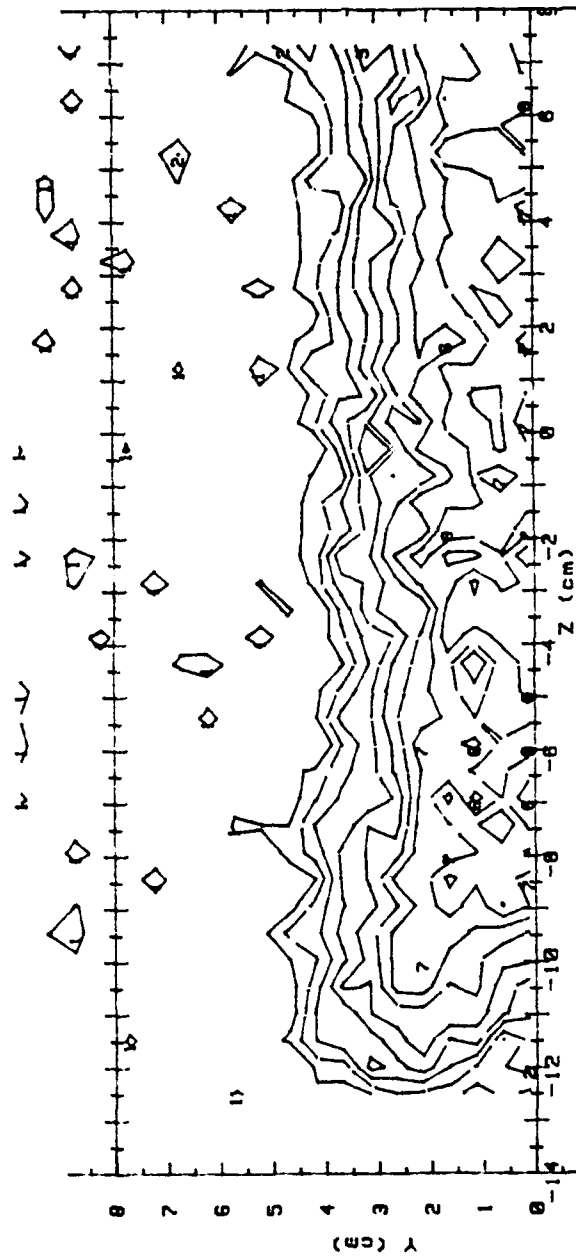
T - Tfs(CELCIUS) RANGES 2 ROW m=1.0 x/d = 43.7

0 :	< .5	5 :	> 2.5	< 3	
1 :	> .5	< 1	6 :	> 3	< 3.5
2 :	> 1	< 1.5	7 :	> 3.5	< 4
3 :	> 1.5	< 2	8 :	> 4	< 4.5
4 :	> 2	< 2.5	9 :	> 4.5	

Figure 162. Streamwise Injectant Distribution, Simple Angle, 2 rows, $m=1.0$, $x/d=43.7$.

RUN #12791.1505

T - Tfs



T - Tfs(CELCIUS) RANGES 2 ROW m=1.0 x/d = L..2

0 :	< .5	5 :	2.5 < 3
1 :	.5 < 1	6 :	3 < 3.5
2 :	1 < 1.5	7 :	3.5 < 4
3 :	1.5 < 2	8 :	4 < 4.5
4 :	2 < 2.5	9 :	4.5

Figure 163. Streamwise Injectant Distribution, Simple Angle, 2 rows, $m=1.0$, $x/d=85.2$.

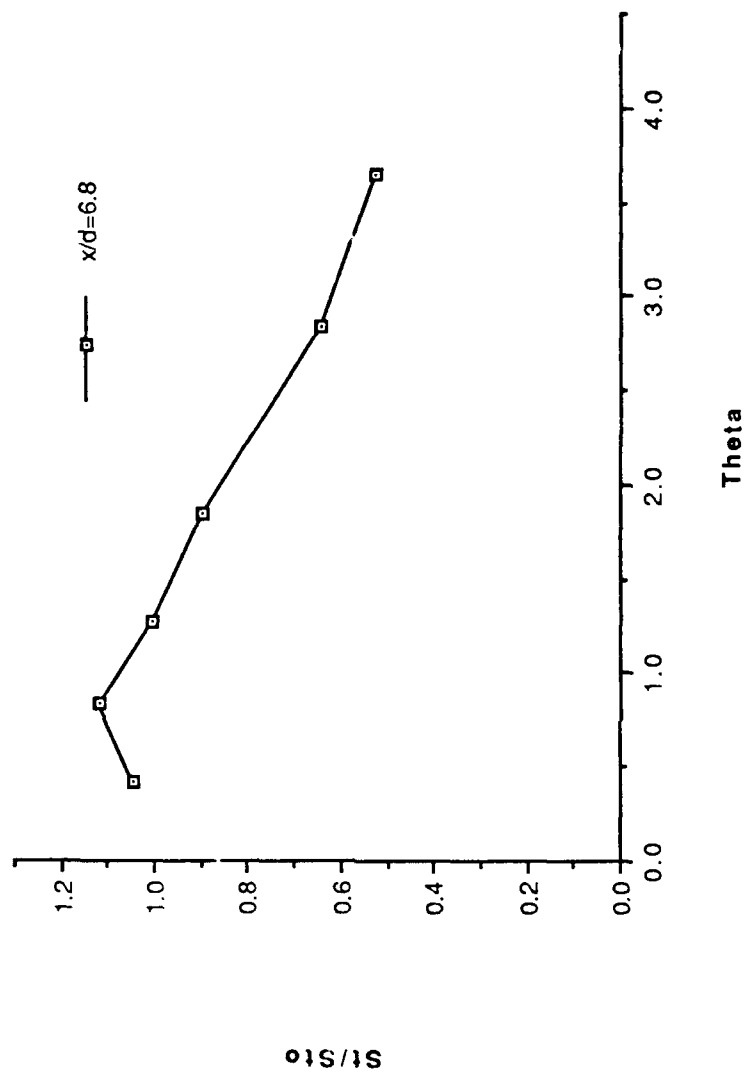


Figure 164. St/St_0 vs θ , Simple Angle, 2 rows, $m=1.5$, $x/d=6.8$, $z=0.0$.

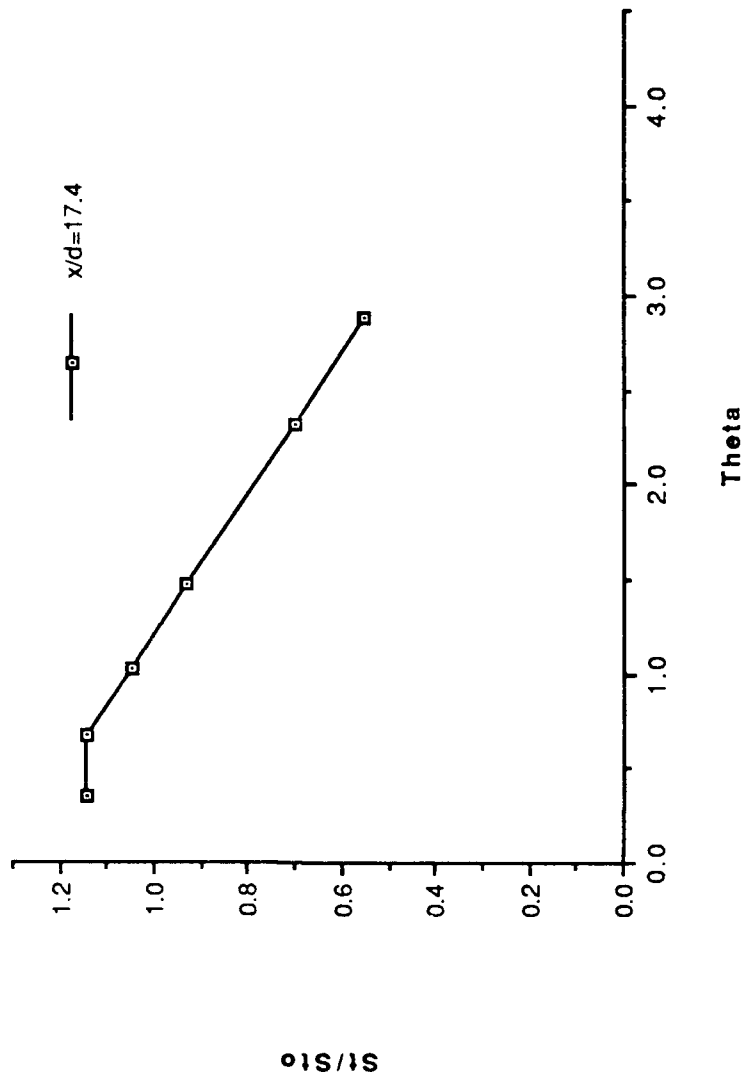


Figure 165. St/St_0 vs θ , Simple Angle, 2 rows, $m=1.5$, $x/d=17.4$, $z=0.0$.

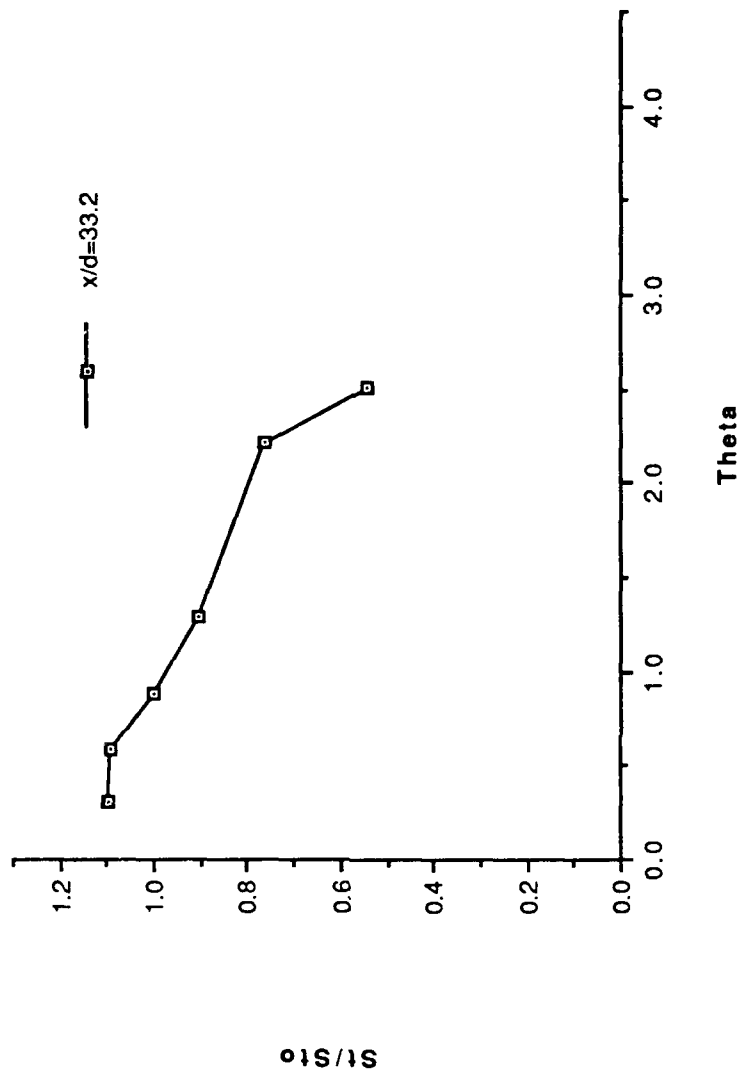


Figure 166. St/St_0 vs θ , Simple Angle, 2 rows, $m=1.5$, $x/d=33.2$, $z=0.0$.

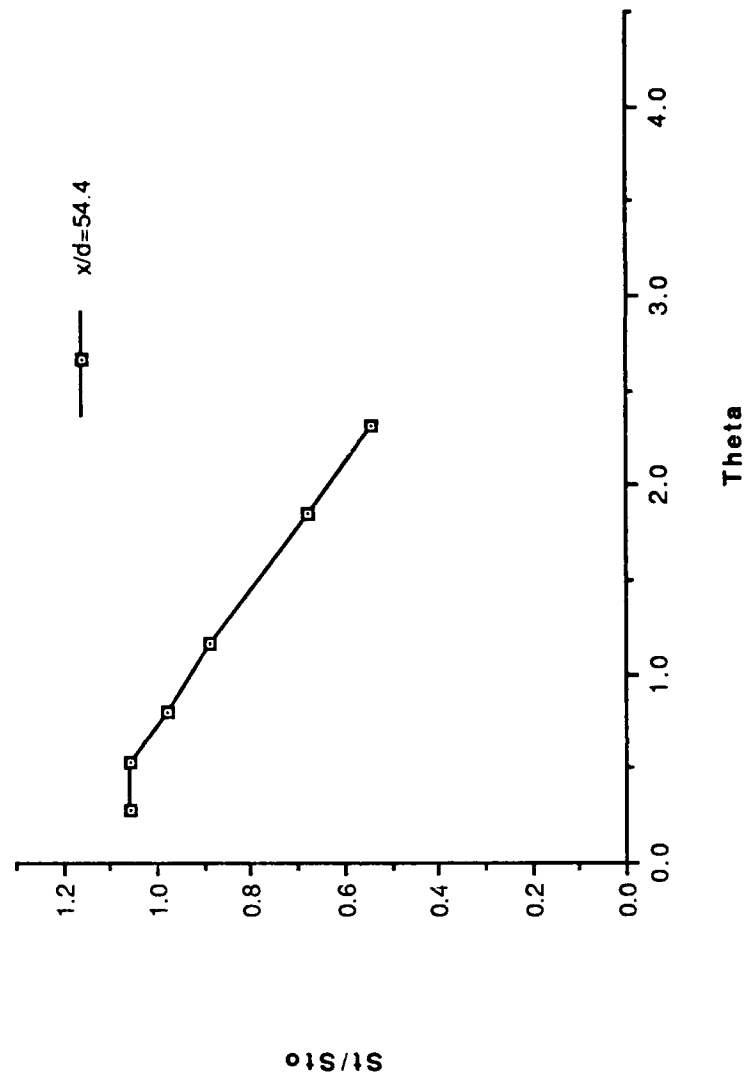


Figure 167. St/St_0 vs θ , Simple Angle, 2 rows, $m=1.5$, $x/d=54.4$, $z=0.0$.

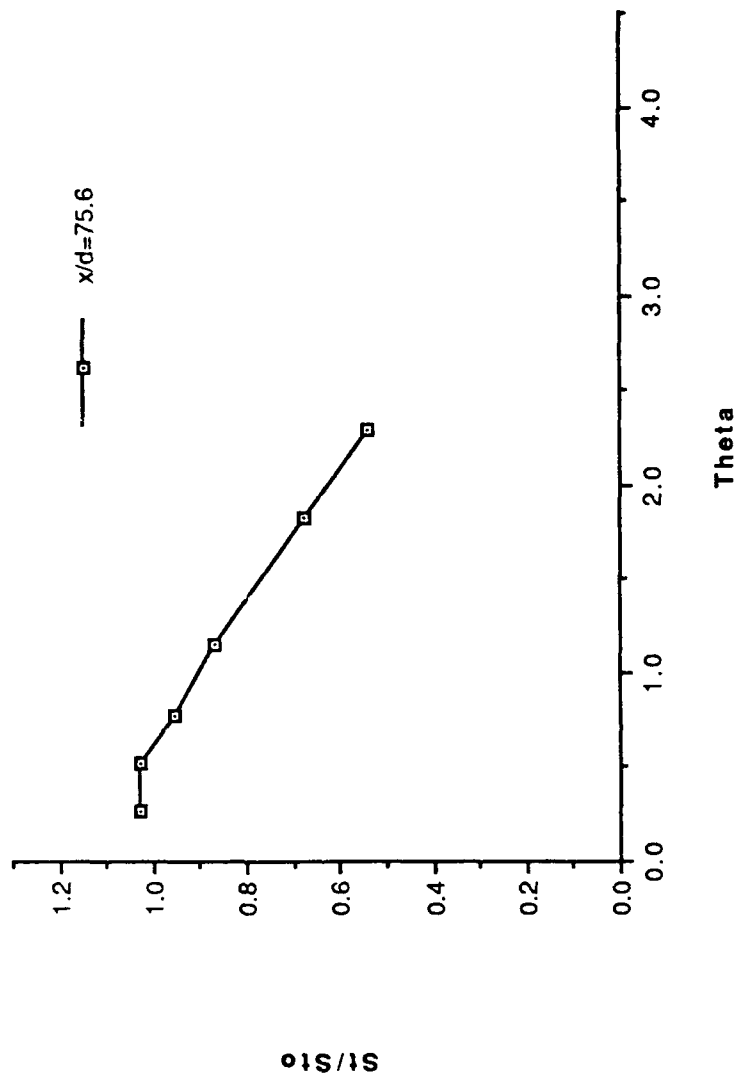


Figure 168. St/St_0 vs θ , Simple Angle, 2 rows, $m=1.5$, $x/d=75.6$, $z=0.0$.

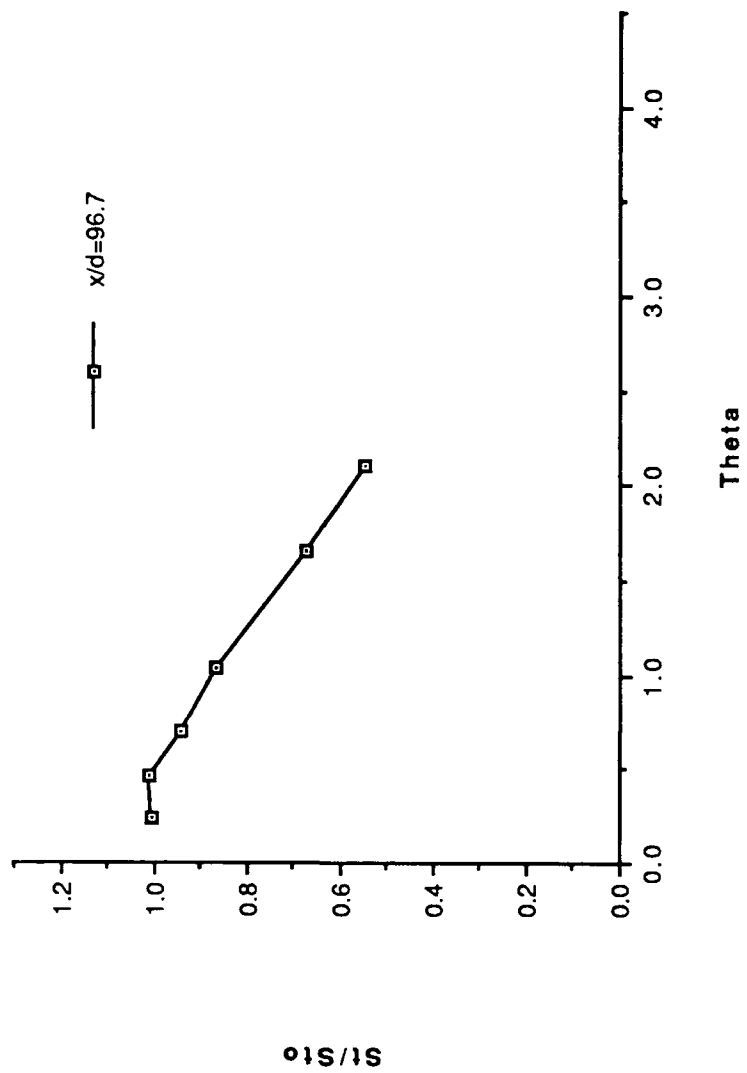


Figure 169. St/St_0 vs θ , Simple Angle, 2 rows, $m=1.5$, $x/d=96.7$, $z=0.0$.

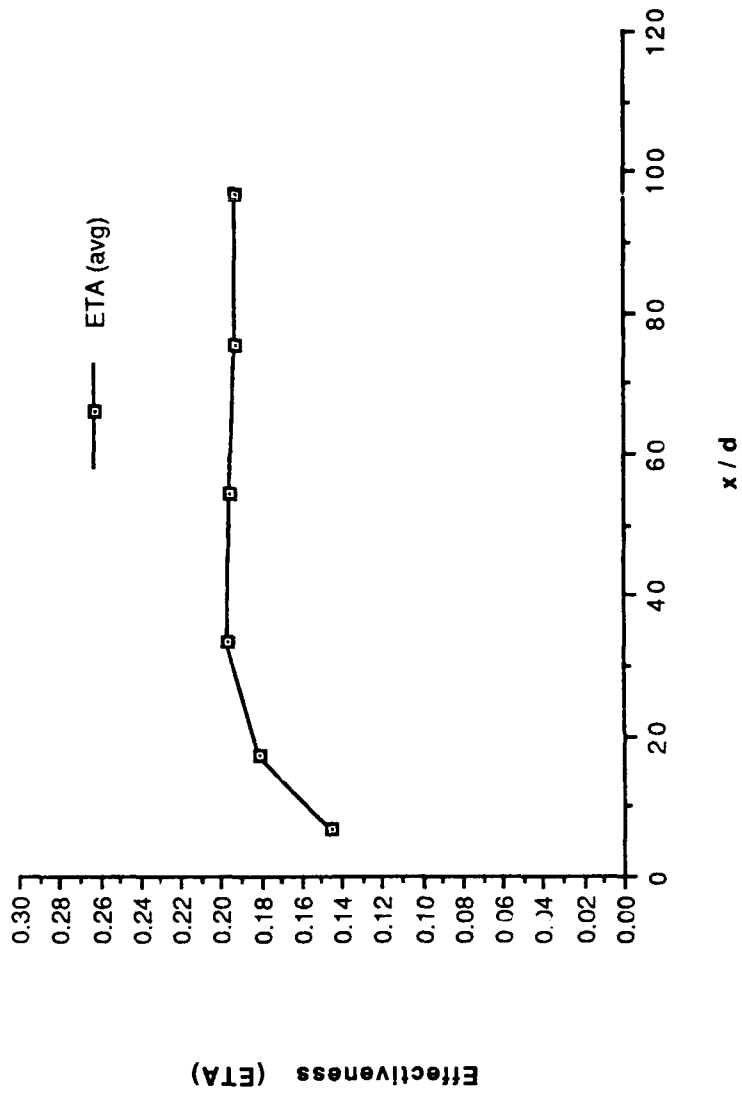


Figure 170. η , vs x/d , Simple Angle, 2 rows, $m=1.5$, Spanwise Average.

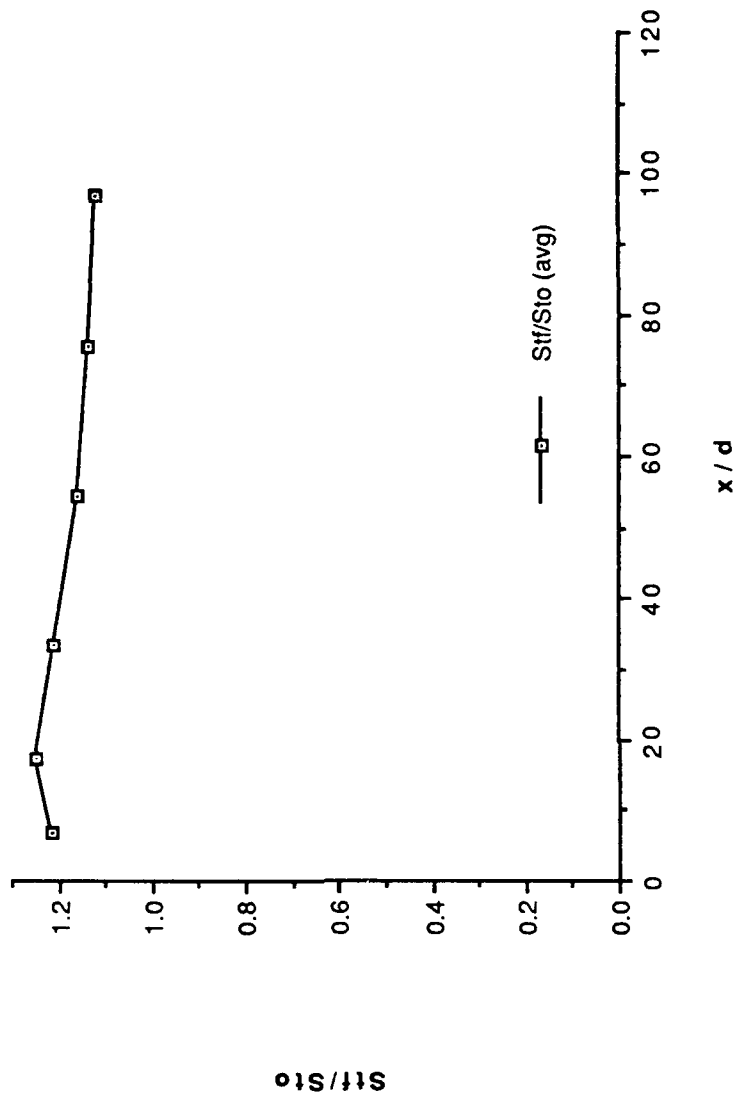


Figure 171. St_f/St_0 vs x/d , Simple Angle, 2 rows, $m=1.5$, Spanwise Average.

FILM-COOLING EFFECTIVENESS

DATE = 11591.0000
 2 ROW SIMPLE ANGLE
 BLOWING RATIO = 1.5
 F.S. VELOCITY = 10 M/S

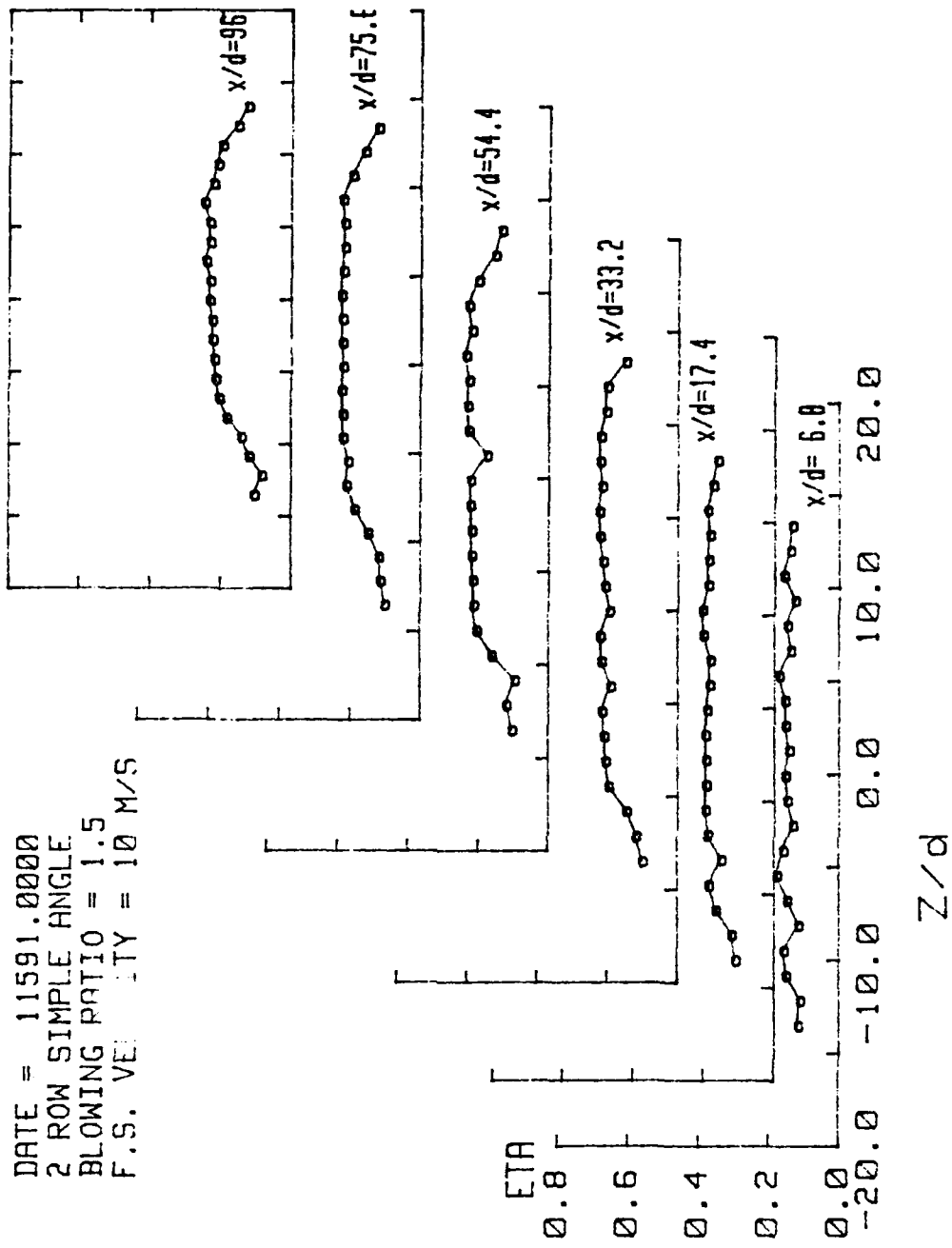


Figure 172. Spanwise Variation of η , Simple Angle, 2 rows, $m=1.5$.

STANTON NUMBER RATIOS

DATE = 11591.1411
 THETA=1.574
 BLOWING RATIO = 1.5
 F.S. VELOCITY = 10 M/S

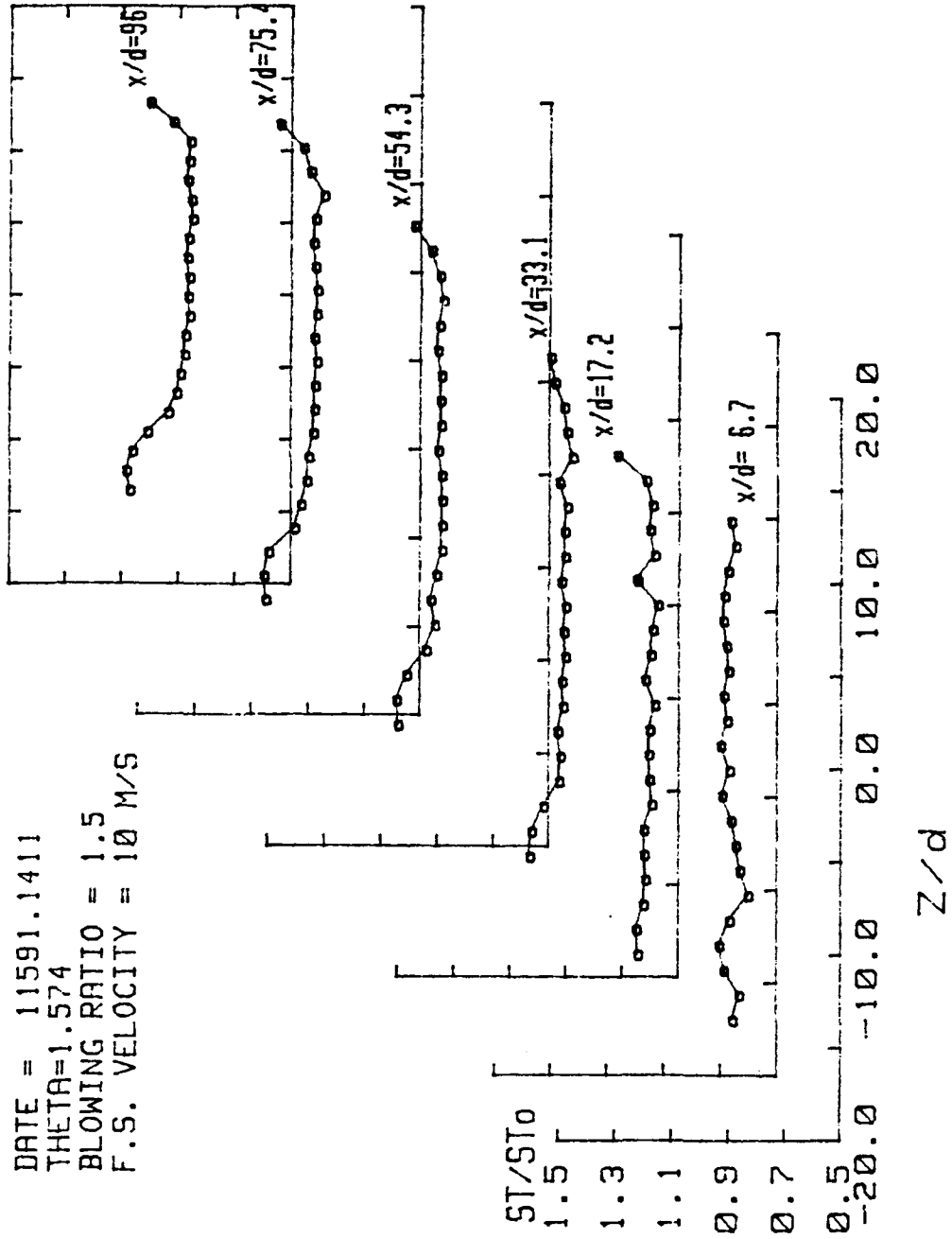


Figure 173. Spanwise Variation of St/St_0 , Simple Angle, 2 rows, $m=1.5$, $\theta=1.574$.

ISO-ENERGETIC STANTON # RATIO

DATE = 11591.0000
 2 ROW SIMPLE ANGLE
 BLOWING RATIO = 1.5
 F.S. VELOCITY = 10 M/S

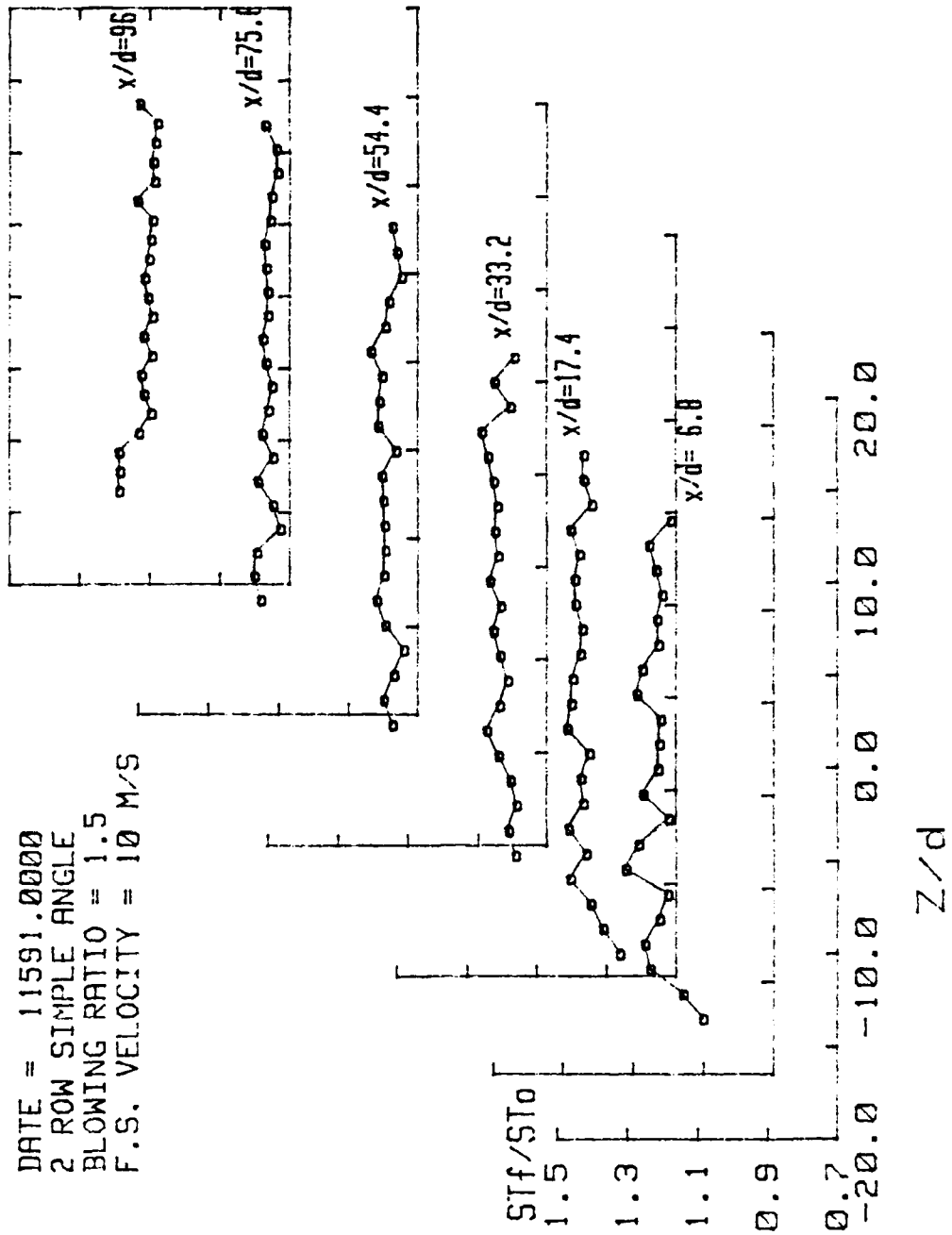
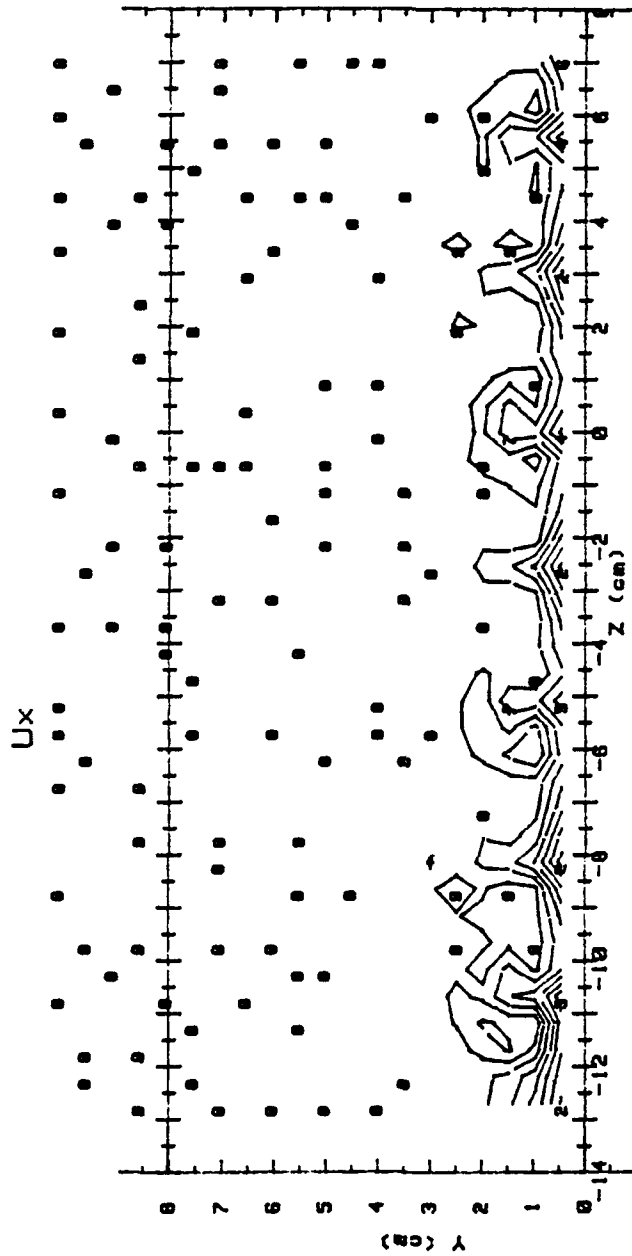


Figure 174. Spanwise Variation of St_f/St_0 , Simple Angle, 2 rows, $m=1.5$.

RUN #13191.1921

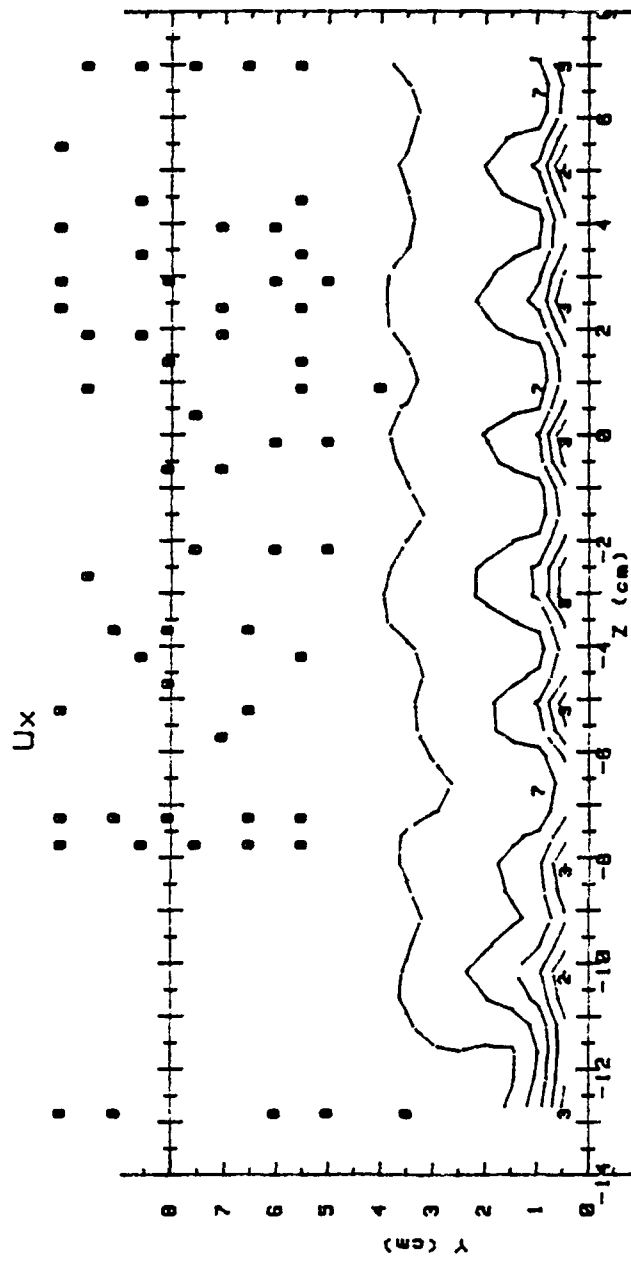


Ux (m/s) RANGES 2 ROW m=1.5 x/d = 9.4

0 :	< 6.5	5 :	6.5 < 9
1 :	6.5 < 7	6 :	8 < 9.5
2 :	7 < 7.5	7 :	8.5 < 10
3 :	7.5 < 8	8 :	10 < 10.5
4 :	8 < 8.5	9 :	10.5 < 11
		10 :	11

Figure 175. Streamwise Velocity Field, Simple, 2 rows, m=1.5, x/d=9.4.

RUN #20191.0810

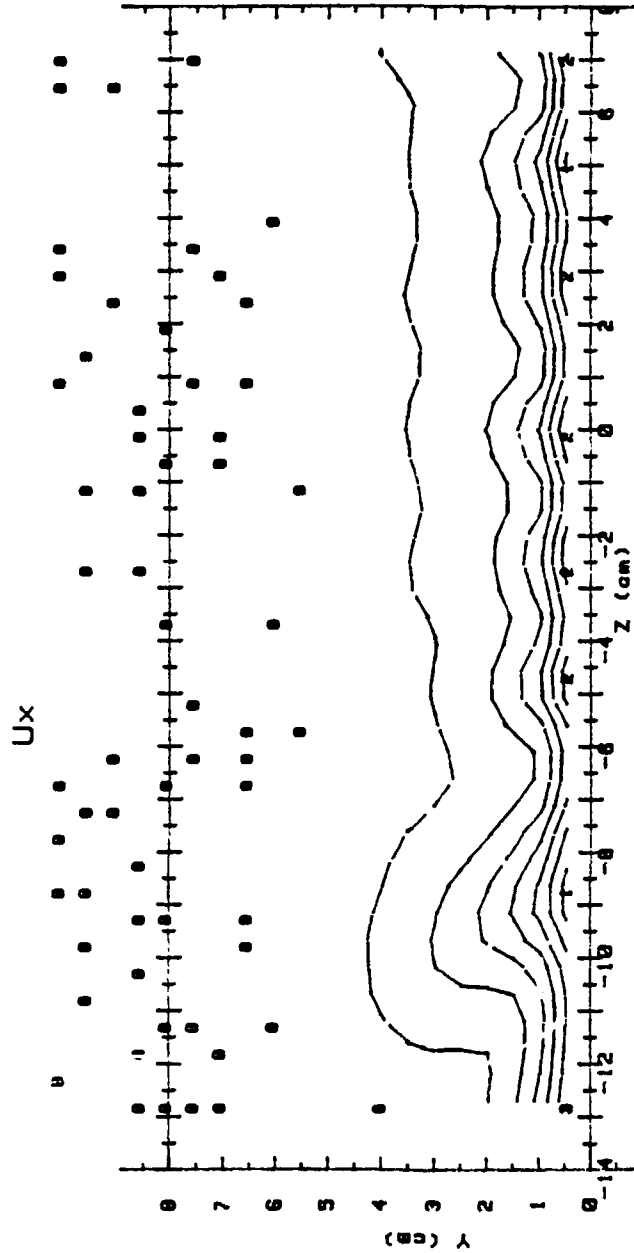


Ux (m/s) RANGES 2 ROW m=1.5 x/d = 43.7

0 1	< 6.5	5 1	8.5 < 9
1 1	6.5 < 7	6 1	9 < 8.5
2 1	7 < 7.5	7 1	9.5 < 10
3 1	7.5 < 8	8 1	10 < 10.5
4 1	8 < 8.5	9 1	10.5 < 11
		10 1	11

Figure 176. Streamwise Velocity Field, Simple Angle, 2 rows, $m=1.5$, $x/d=43.7$.

RUN #20:91.1848

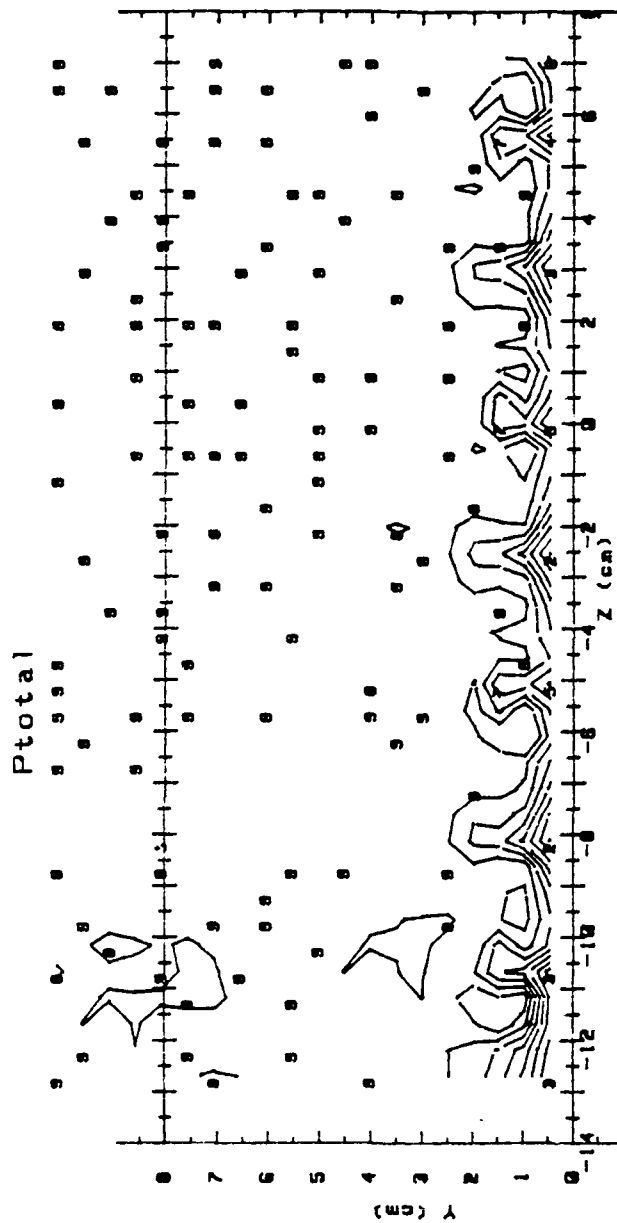


Ux (m/s) RANGES 2 ROW m=1.5 x/d = 85.2

0	< 6.5	5	8.5 < 9
1	6.5 < 7	6	9 < 9.5
2	7 < 7.5	7	9.5 < 10
3	7.5 < 8	8	10 < 10.5
4	8 < 8.5	9	10.5 < 11
		10	11

Figure 177. Streamwise Velocity Field, Simple Angle, 2 rows, $m=1.5$, $x/d=85.2$.

RUN #13191.1921

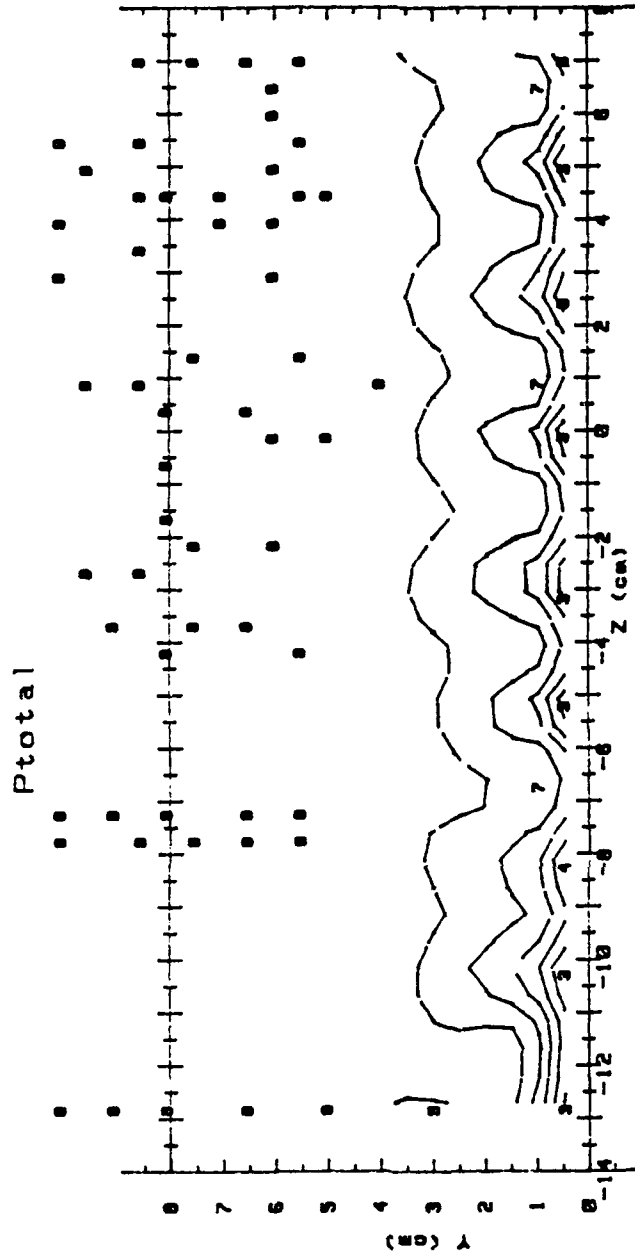


Ptotal(Pascals) RANGES 2 ROW m=1.5 x/d=9.4

0 1	< 25	5 1	45 < 50
1 1	25 < 30	6 1	50 < 55
2 1	30 < 35	7 1	55 < 60
3 1	35 < 40	8 1	60 < 65
4 1	40 < 45	9 1	65 < 70
		10 1	70

Figure 178. Streamwise Pressure Field, Simple Angle, 2 rows, $m=1.5$, $x/d=9.4$.

RUN #20191.0818

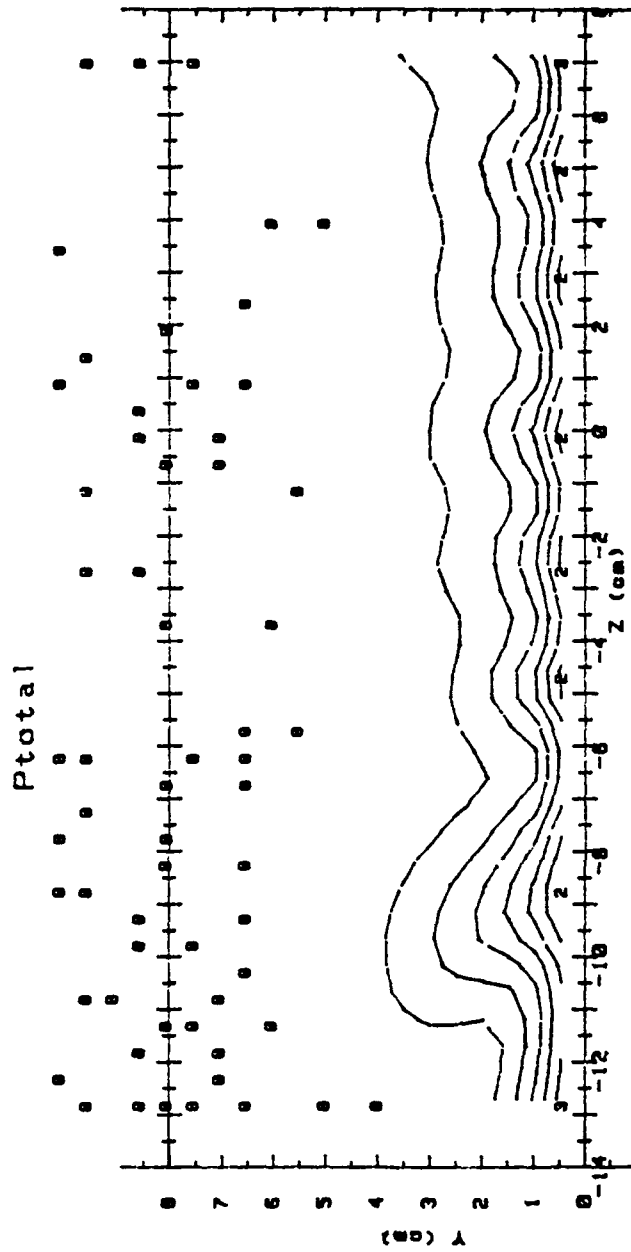


Ptotal(Pascals) RANGES 2 ROW m=1.5 x/d= 43.7

0	< 25	5	> 45	< 50	
1	> 25	< 30	6	> 50	< 55
2	> 30	< 35	7	> 55	< 60
3	> 35	< 40	8	> 60	< 65
4	> 40	< 45	9	> 65	< 70
			10	> 70	

Figure 179. Streamwise Pressure Field, Simple Angle, 2 rows, $m=1.5$, $x/d=43.7$.

RUN #20191.1848



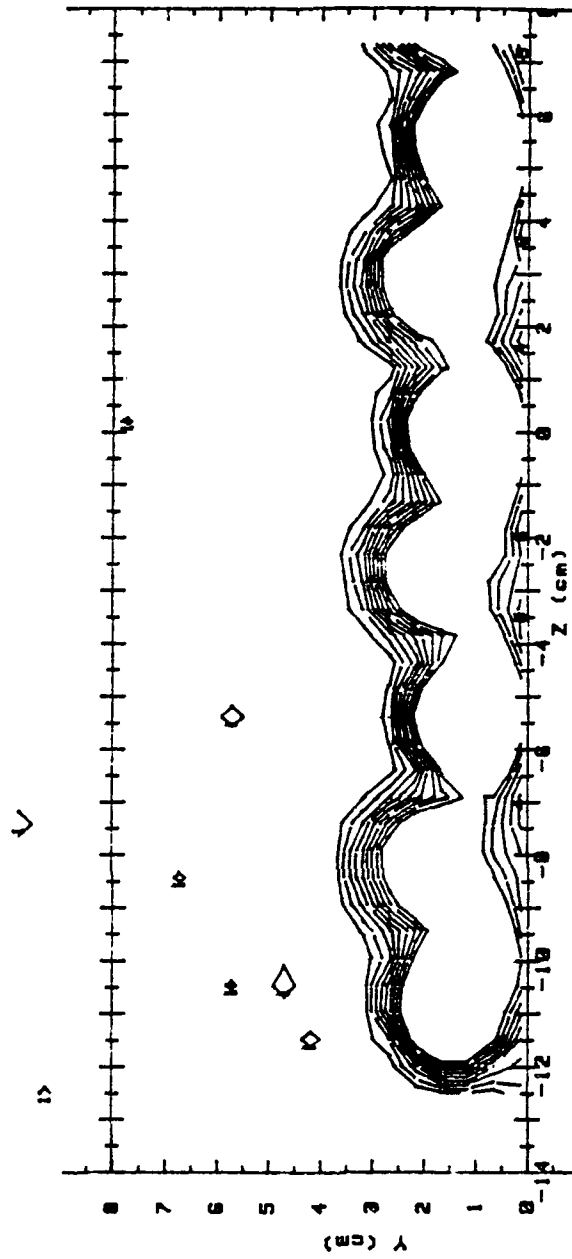
Ptotal(Pascals) RANGES 2 ROW m=1.5 x/d= 85.2

0 1	< 25	5 1	45	< 58	
1 1	25	< 30	6 1	50	< 55
2 1	30	< 35	7 1	55	< 60
3 1	35	< 40	8 1	60	< 65
4 1	40	< 45	9 1	65	< 70
			10 1	70	

Figure 180. Streamwise Pressure Field, Simple Angle, 2 rows, $m=1.5$, $x/d=85.2$.

RUN #12991.1125

T - Tfs



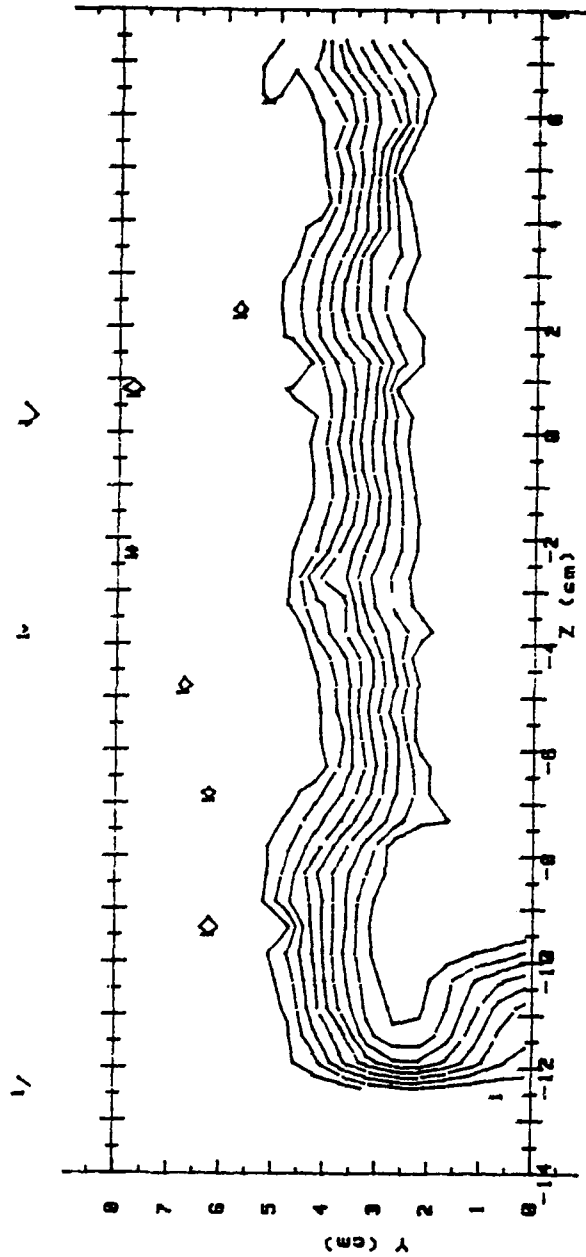
T - Tfs(CELCIUS) RANGES 2 ROW m=1.5 x/d = 9.4

0 :	< .5	5 :	2.5 < 3
1 :	.5 < 1	6 :	3 < 3.5
2 :	1 < 1.5	7 :	3.5 < 4
3 :	1.5 < 2	8 :	4 < 4.5
4 :	2 < 2.5	9 :	4.5

Figure 181. Streamwise Injectant Distribution, Simple Angle, 2 rows, m=1.5, x/d=9.4.

RUN #12891.1542

T -- Tfs



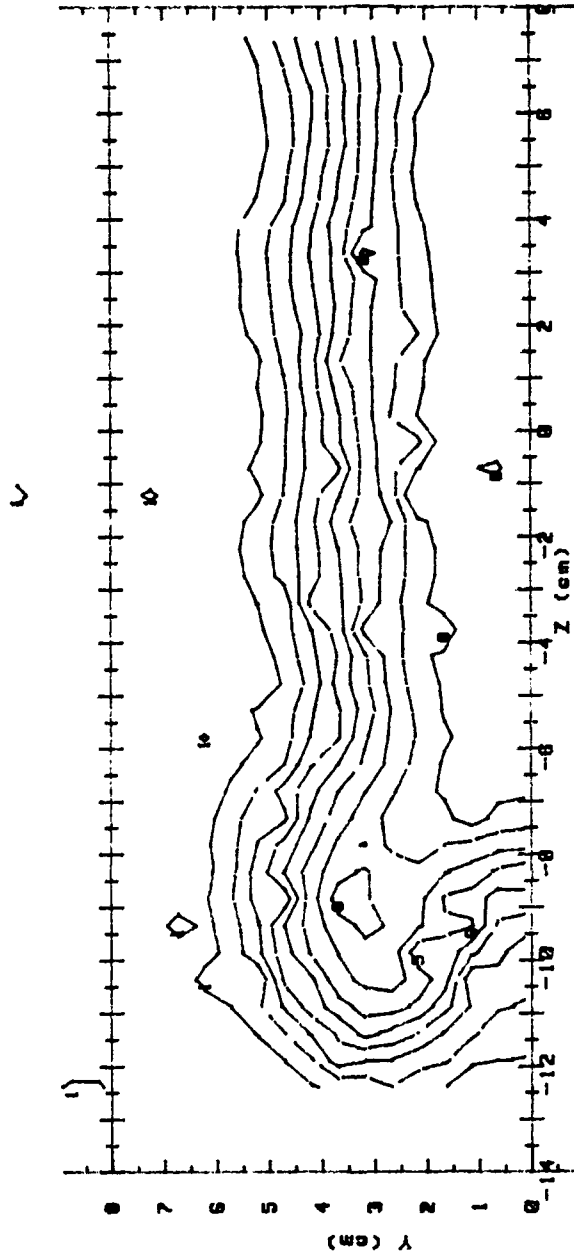
T -- Tfs(CELCIUS) RANGES 2 ROW m=1.5 x/d = 43.7

0	:	<	.5	5	:	>	2.5	<	3
1	:	>	.5	<	1	6	:	>	3
2	:	>	1	<	1.5	7	:	>	3.5
3	:	>	1.5	<	2	8	:	>	4
4	:	>	2	<	2.5	9	:	>	4.5

Figure 182. Streamwise Injectant Distribution, Simple Angle, 2 rows, $m=1.5$, $x/d=43.7$.

RUN #12891.1125

T - Tfs



T - Tfs(CELCIUS) RANGES 2 ROW m=1.5 x/d = 85.2

- 0 1 < .5
- 1 1 > .5 < 1
- 2 1 > 1 < 1.5
- 3 1 > 1.5 < 2
- 4 1 > 2 < 2.5
- 5 1 > 2.5 < 3
- 6 1 > 3 < 3.5
- 7 1 > 3.5 < 4
- 8 1 > 4 < 4.5
- 9 1 > 4.5

Figure 183. Streamwise Injectant Distribution, Simple Angle, 2 rows, m=1.5, x/d=85.2.

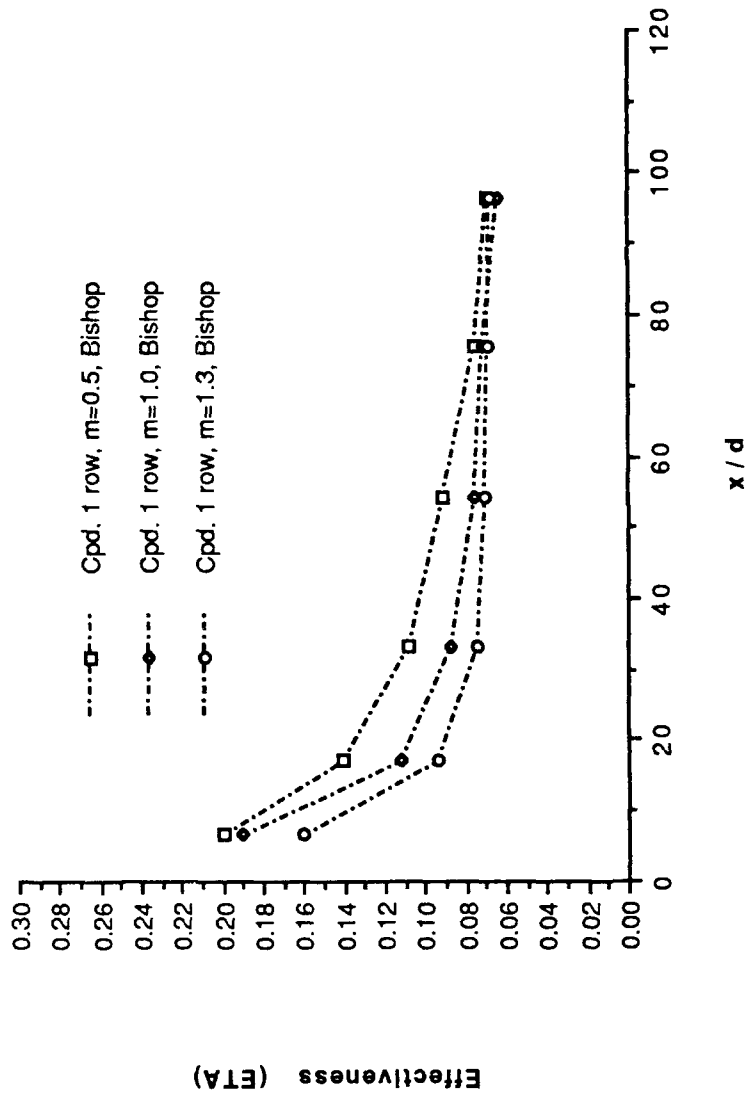


Figure 184. Comparison of η for Compound Angle Injection System at Different Blow Ratios, 1 row Bishop [Ref. 6].

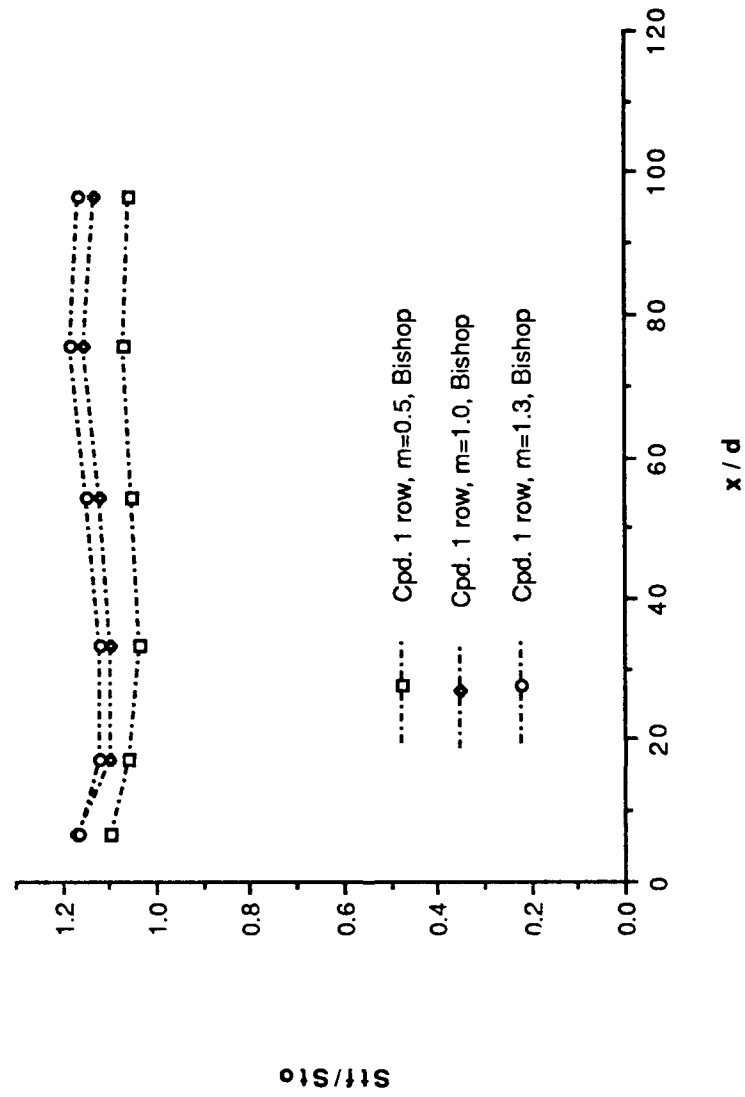


Figure 185. Comparison of Stf/Sto , for Compound Angle Injection System at Different Blow Ratios, 1 row Bishop [Ref. 6].

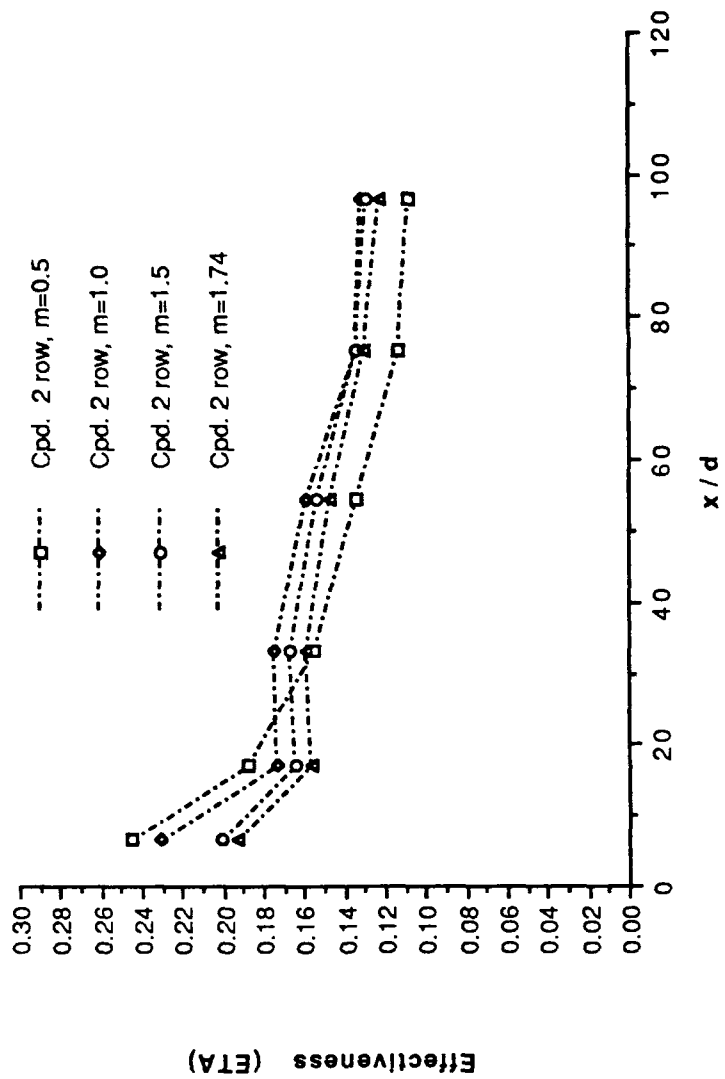


Figure 186. Comparison of η for Compound Angle Injection System at Different Blow Ratios, 2 rows.

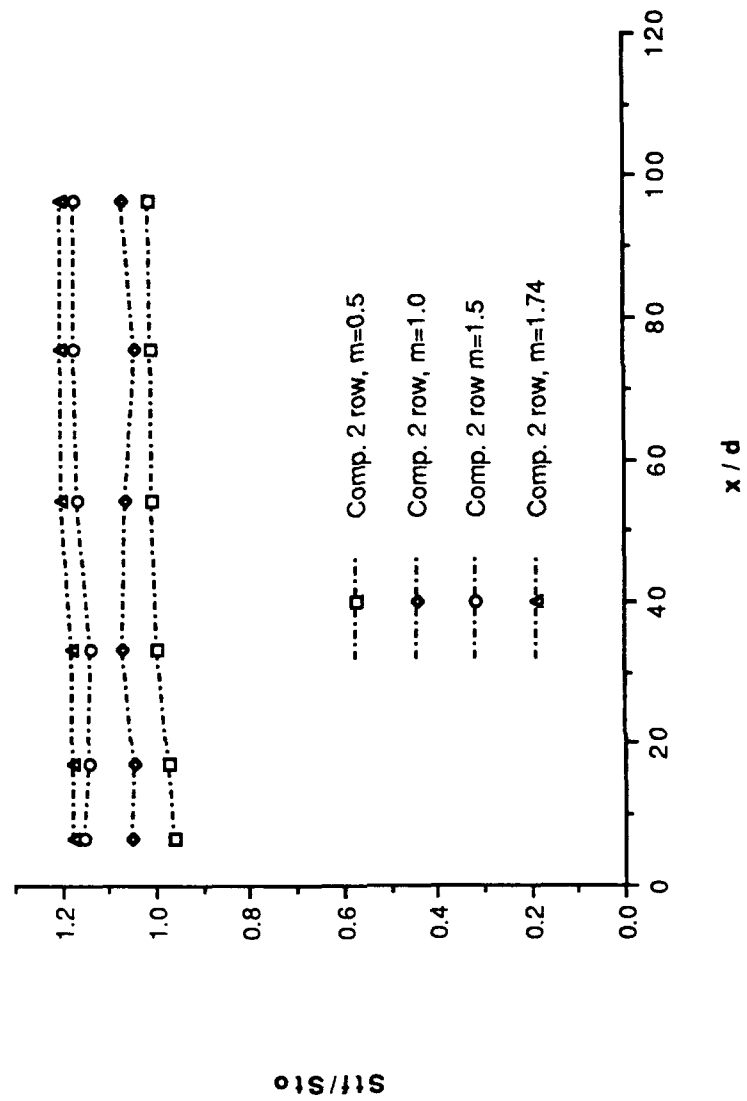


Figure 187. Comparison of Stf/Sto , for Compound Angle Injection System at Different Blow Ratios, 2 rows.

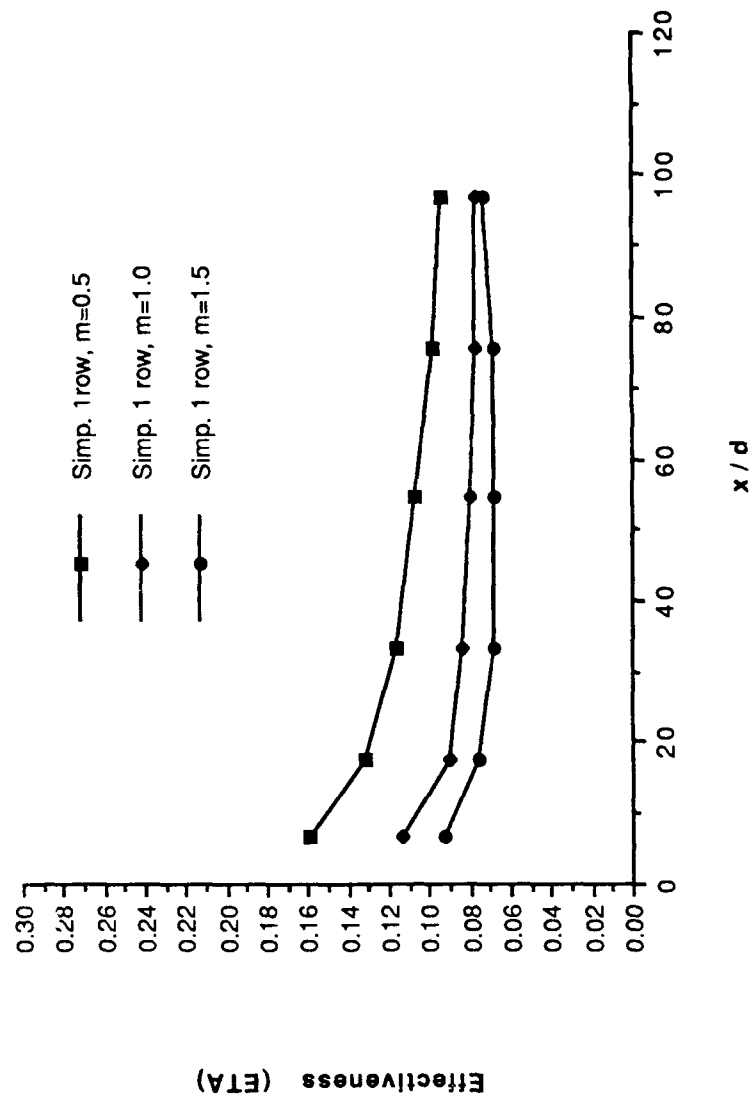


Figure 188. Comparison of η for Simple Angle Injection System at Different Blow Ratios, 1 row.

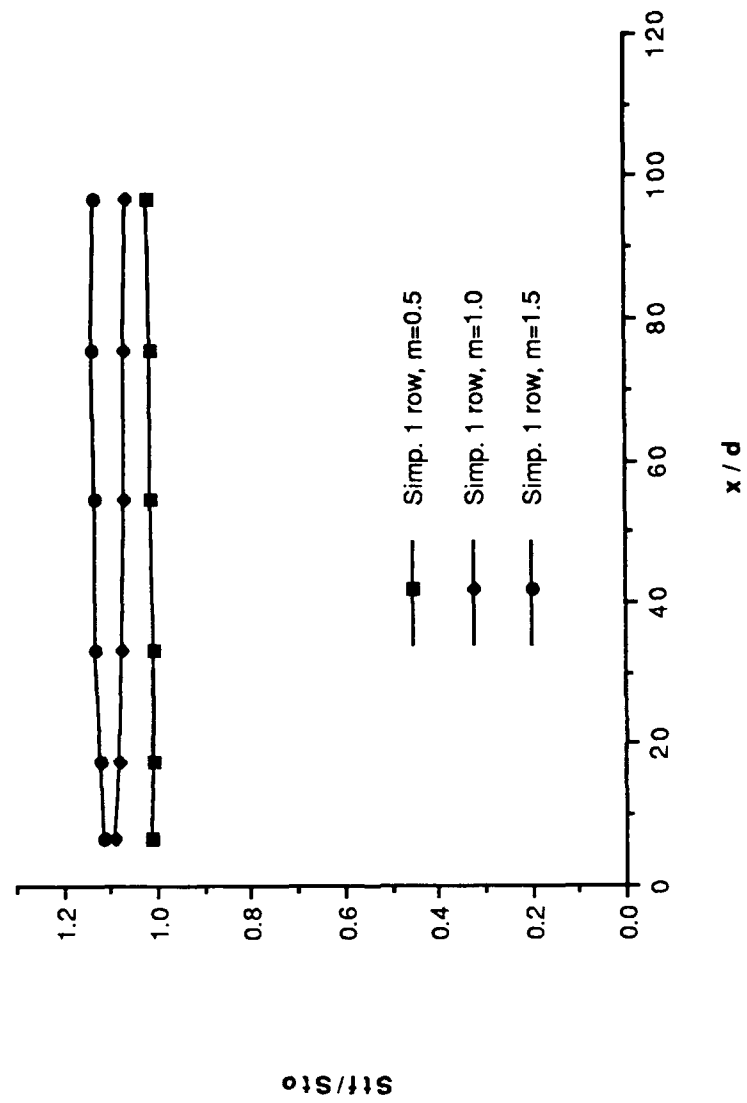


Figure 189. Comparison of Stf/Sto , for Simple Angle Injection System at Different Blow Ratios, 1 row.

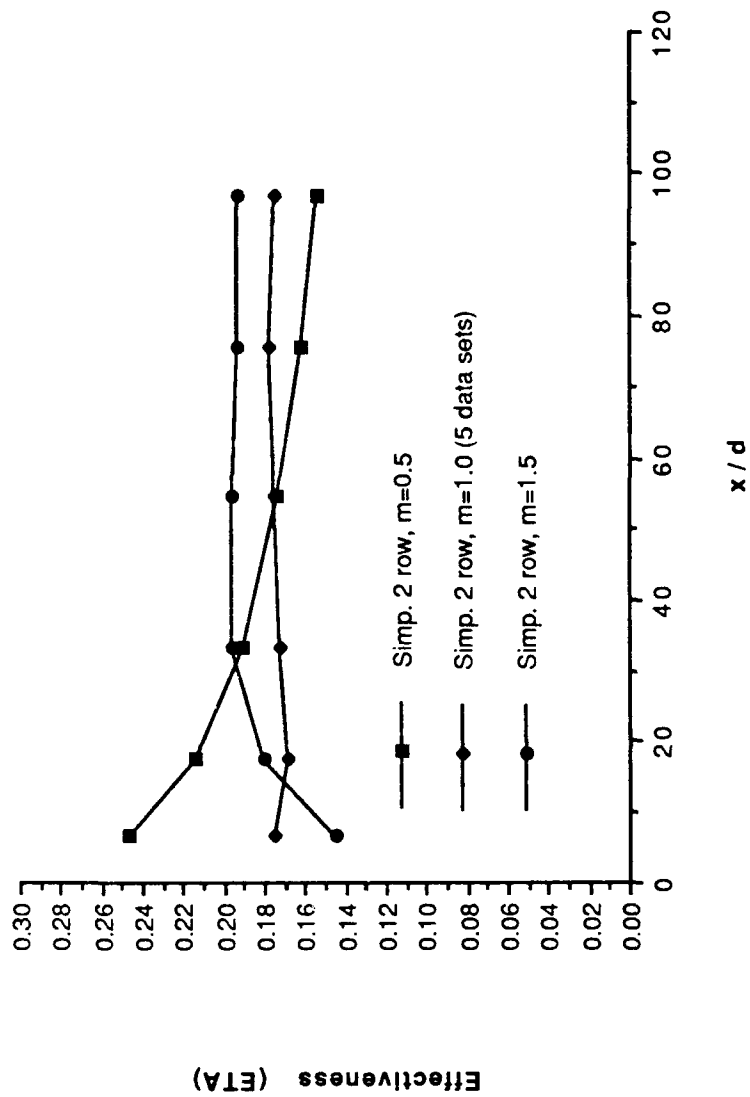


Figure 190. Comparison of η for Simple Angle Injection System at Different Blow Ratios, 2 rows.

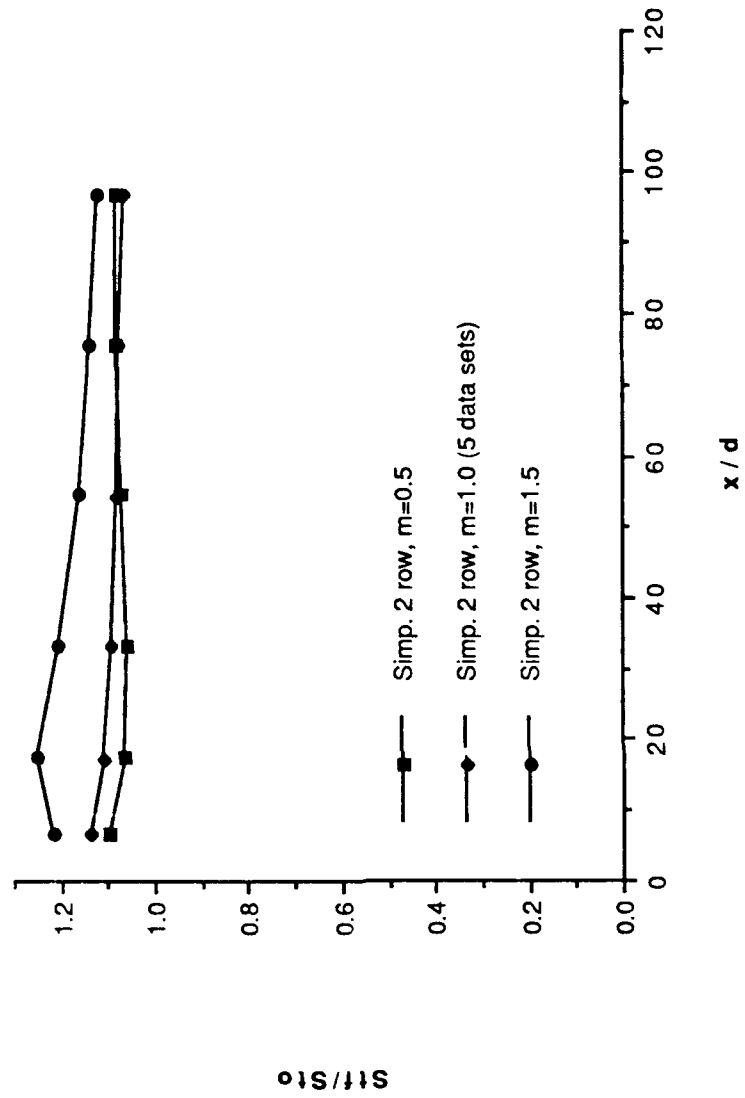


Figure 191. Comparison of Stf/Sto , for Simple Angle Injection System at Different Blow Ratios, 2 rows.

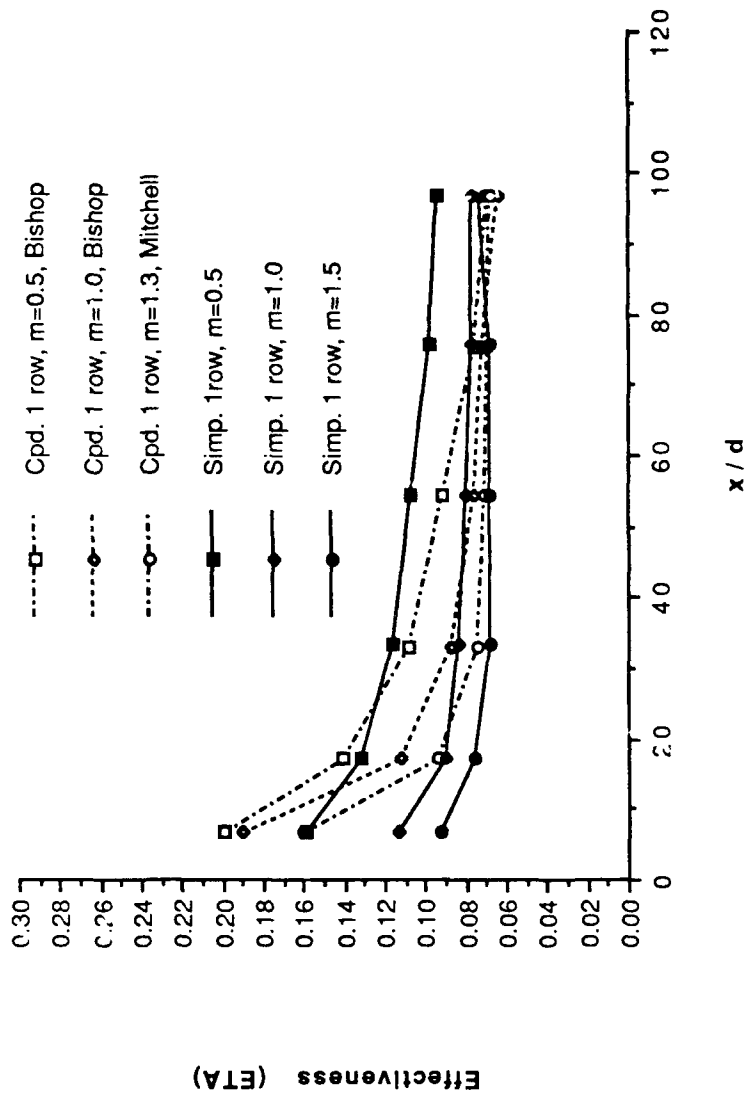


Figure 192. Comparison of η of Compound Angle Injection System to Simple Angle Injection System, 1 row.

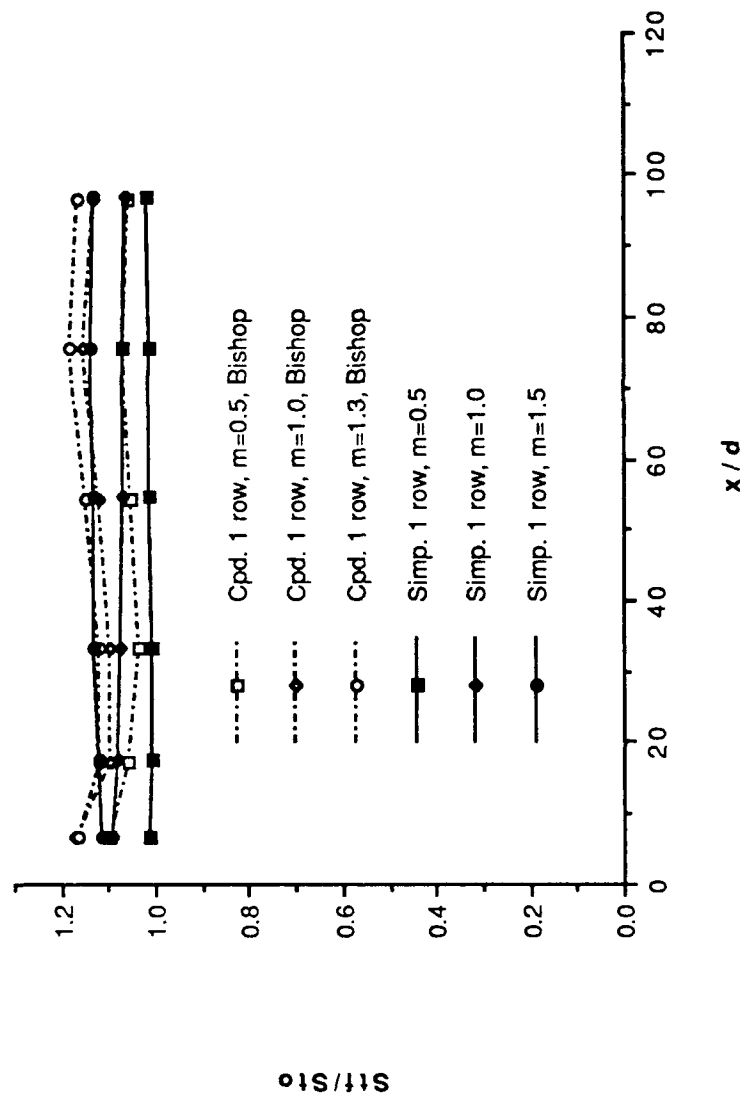


Figure 193 Comparison of Stf/Sto , of Compound Angle Injection System to Simple Angle Injection System, 1 row.

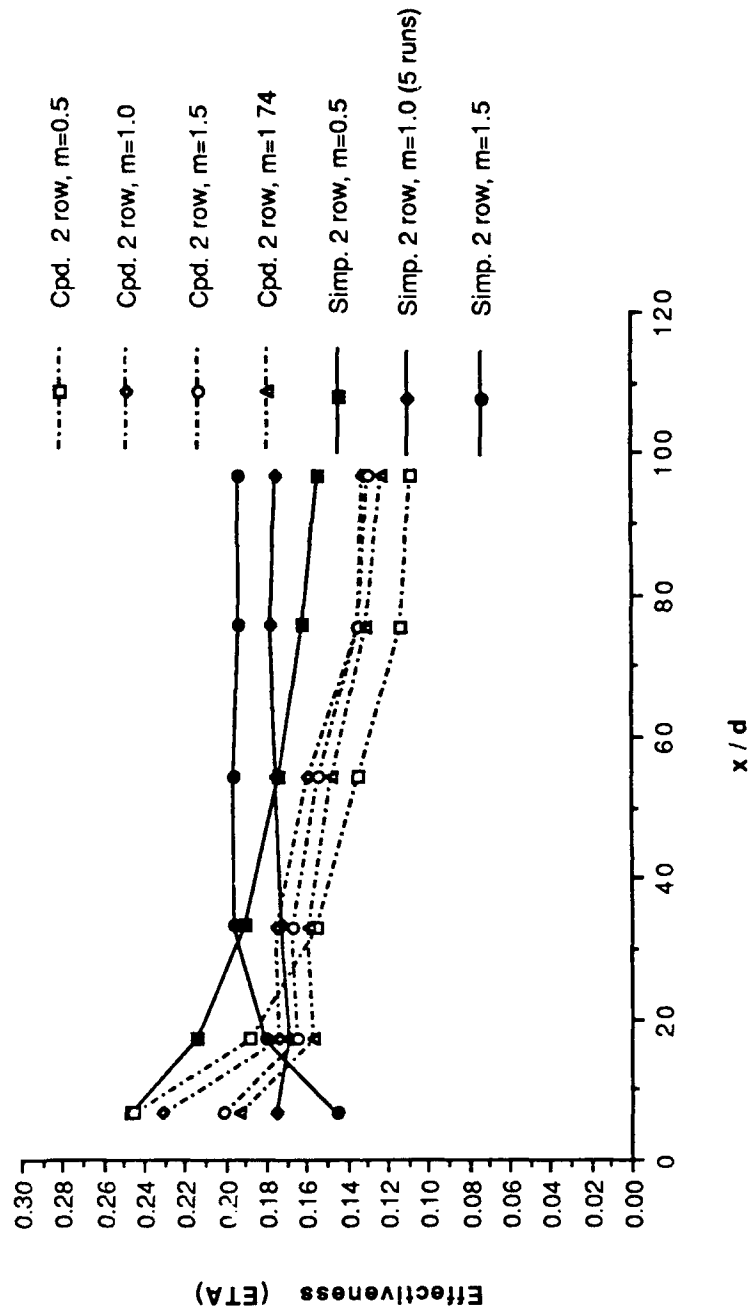


Figure 194. Comparison of η of Compound Angle Injection System to Simple Angle Injection System, 2 rows.

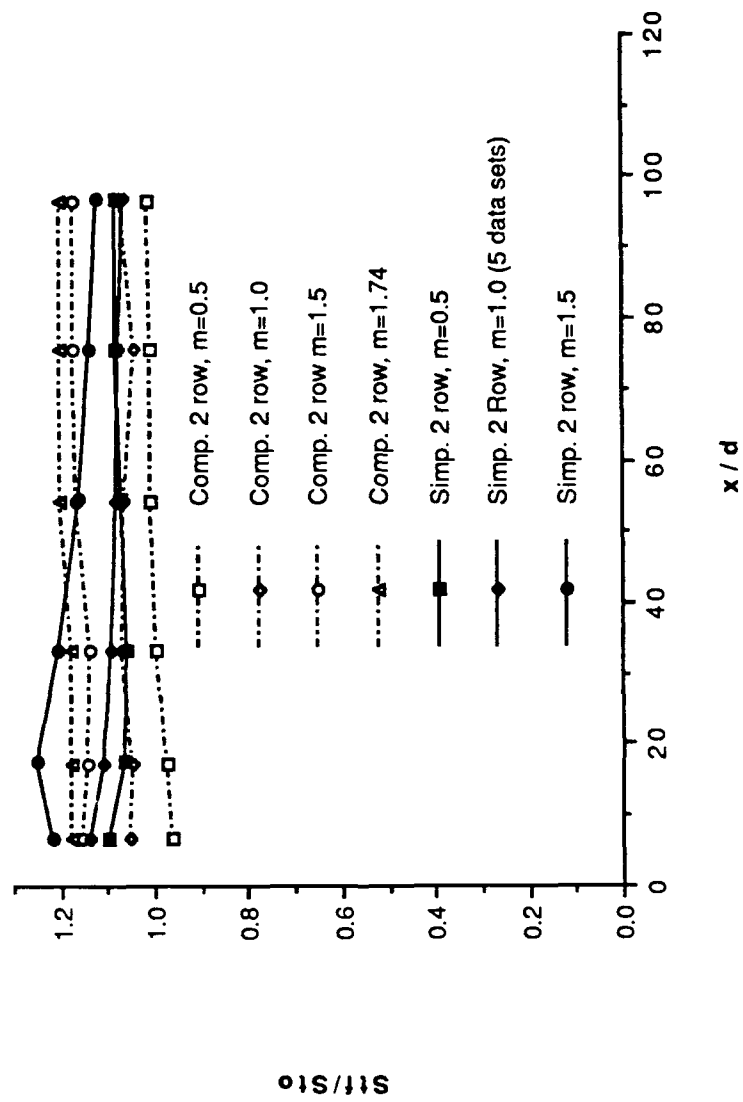


Figure 195 Comparison of Stf/Sto , of Compound Angle Injection System to Simple Angle Injection System. 2 rows.

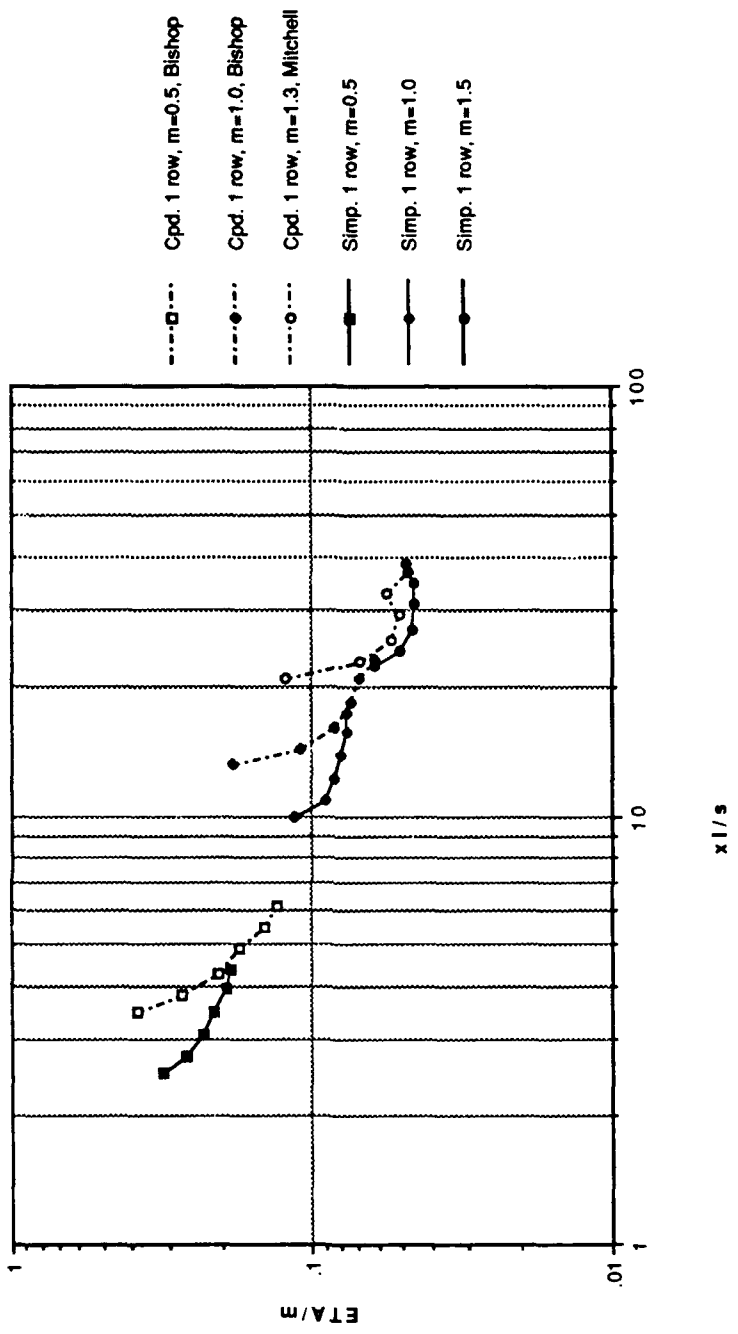


Figure 196 ETA/m vs xI/s , Compound Angle Injection System vs Simple Angle Injection System, 1 row.

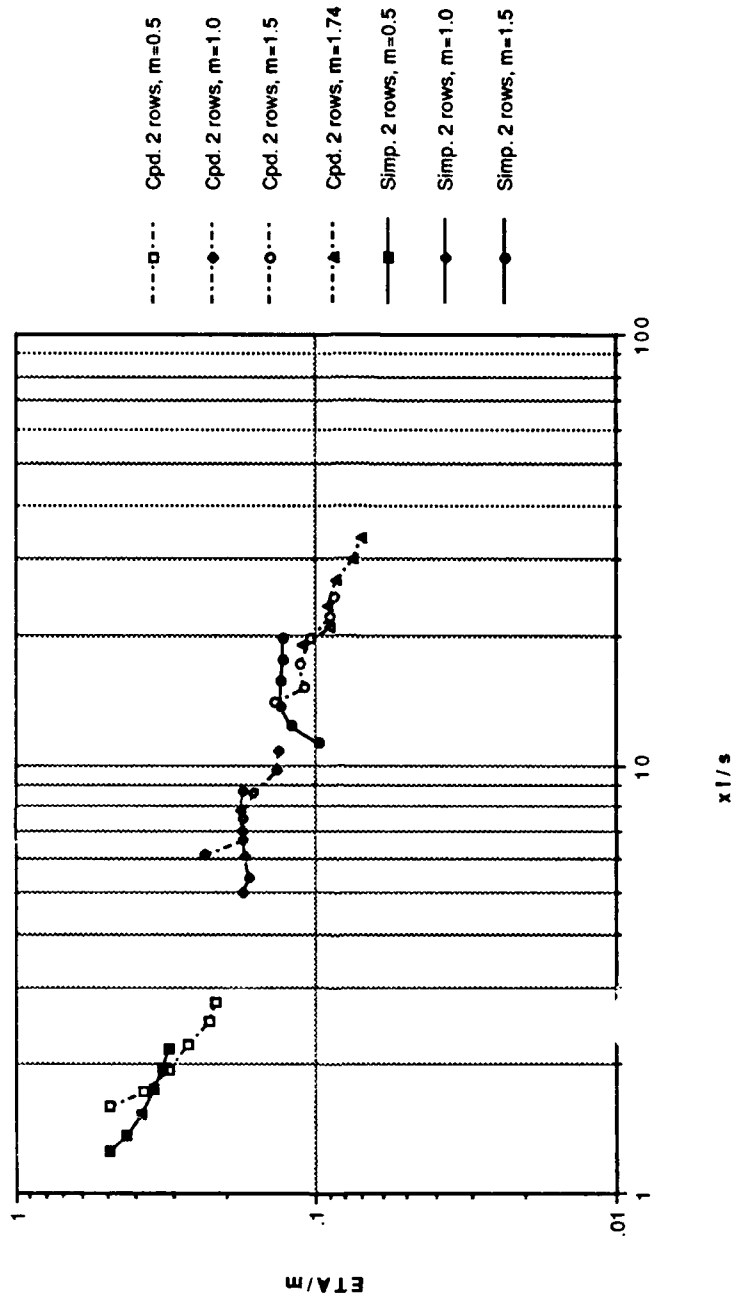


Figure 197 ETA/m vs xI/s, Compound Angle Injection System vs Simple Angle Injection System, 2 rows.

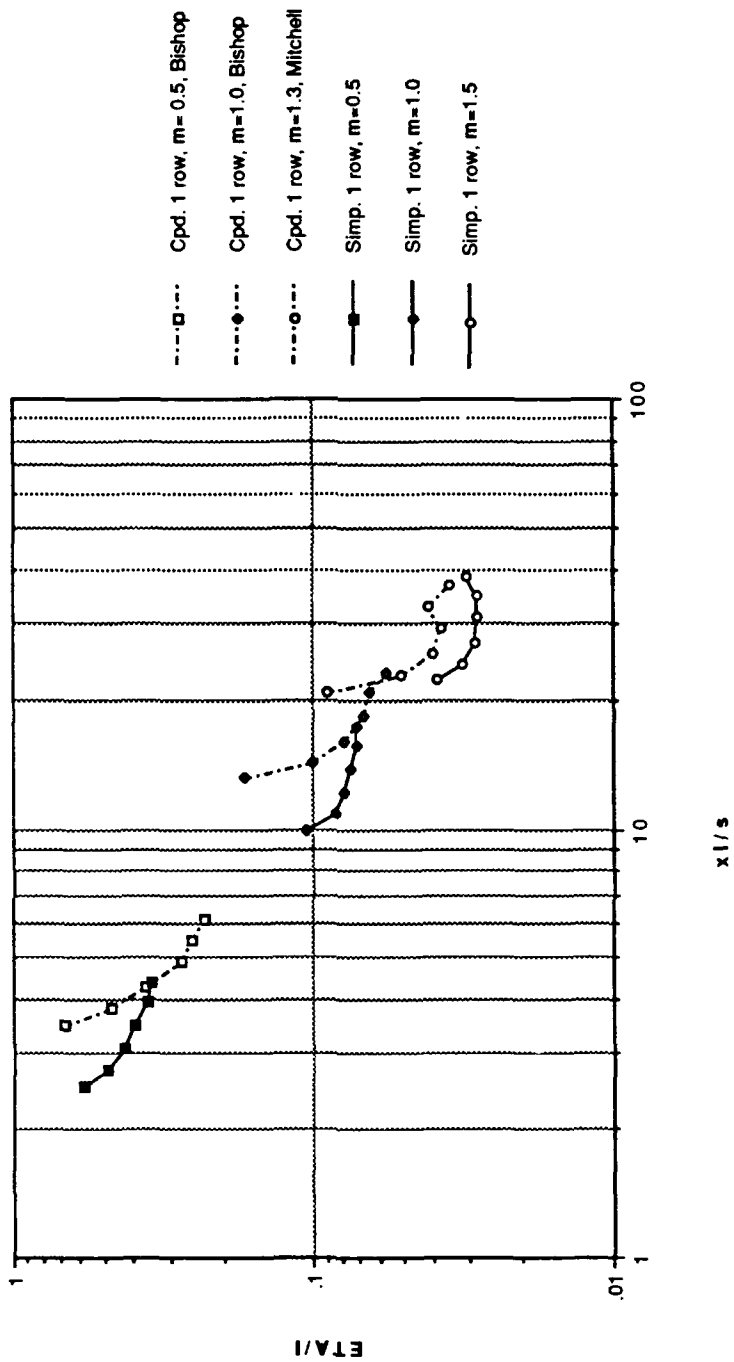


Figure 198 $\eta I / I$ vs $x I / s$, Compound Angle Injection System vs Simple Angle Injection System, 1 row.

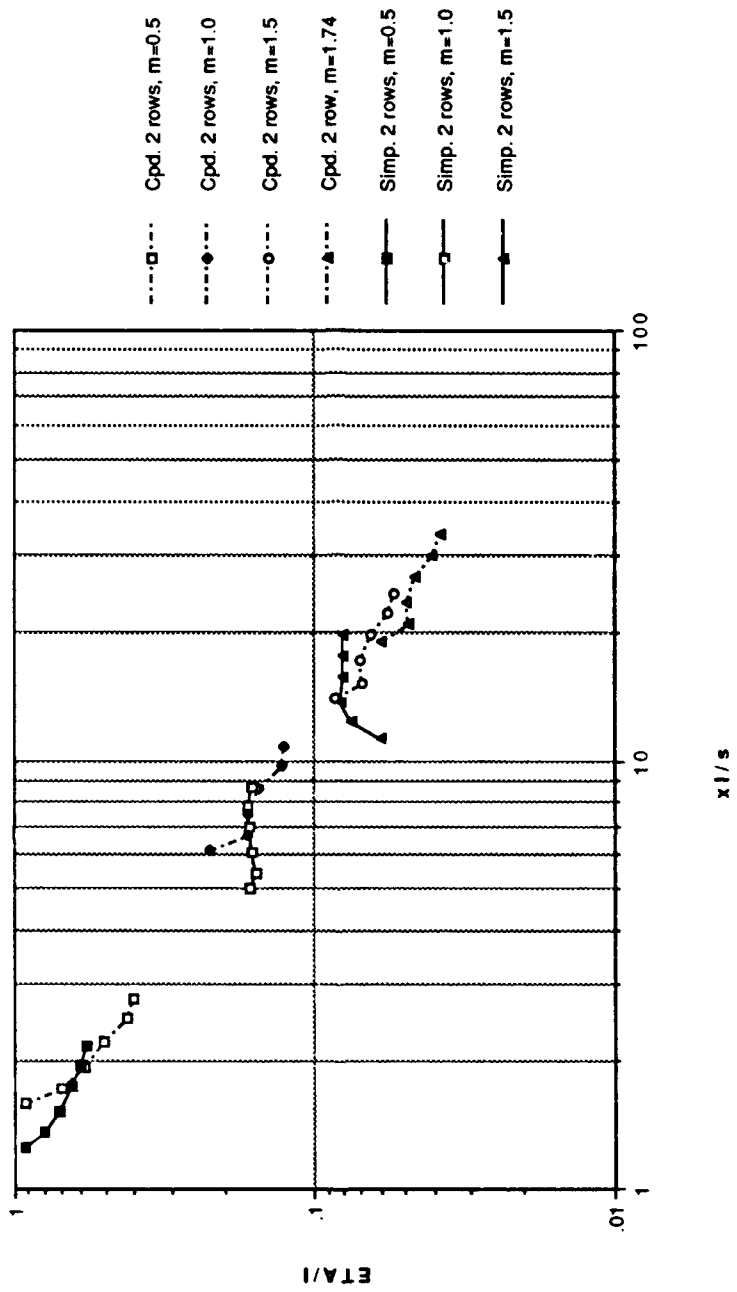


Figure 199 ETA/I vs xI/s , Compound Angle Injection System vs Simple Angle Injection System, 2 rows.

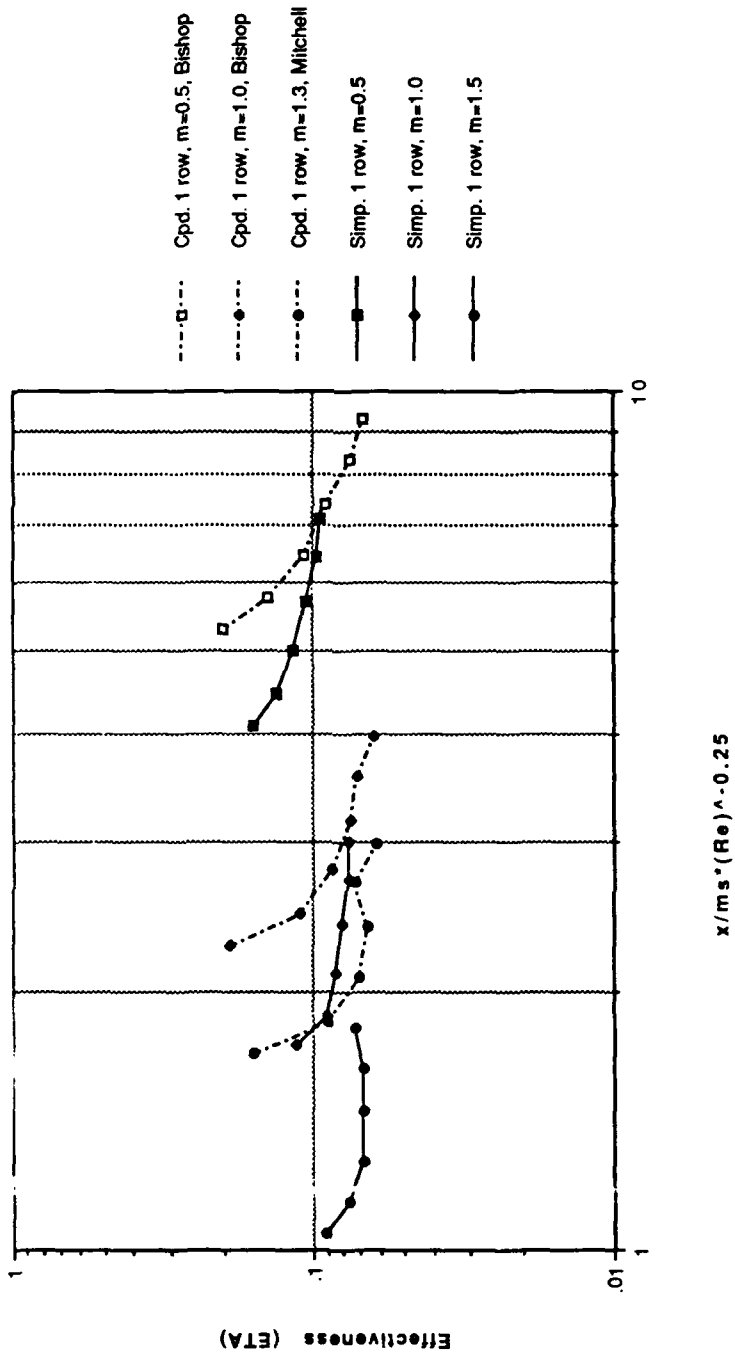


Figure 200 η vs $x/(ms) \cdot Re^{-0.25}$, Compound Angle Injection System vs Simple Angle Injection System, 1 row.

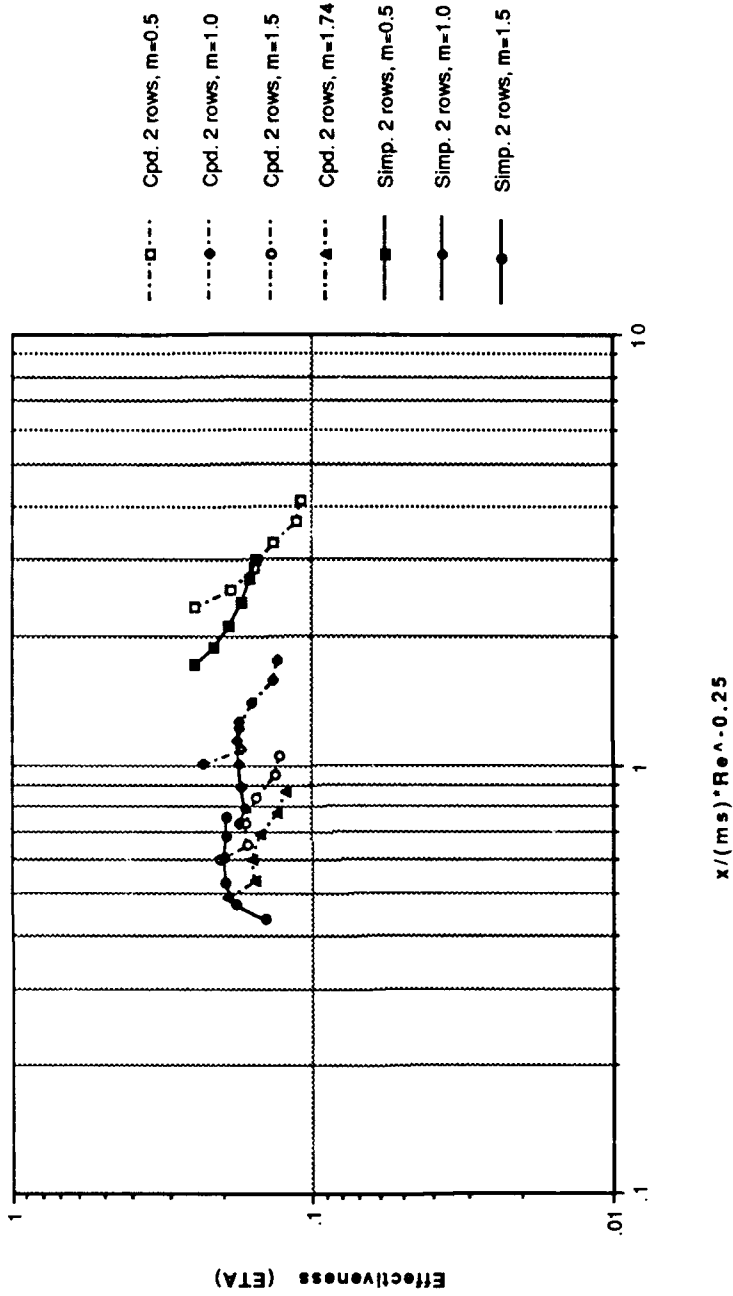


Figure 201 ETA vs $x/(ms) \cdot Re^{-0.25}$, Compound Angle Injection System vs Simple Angle Injection System, 2 rows.

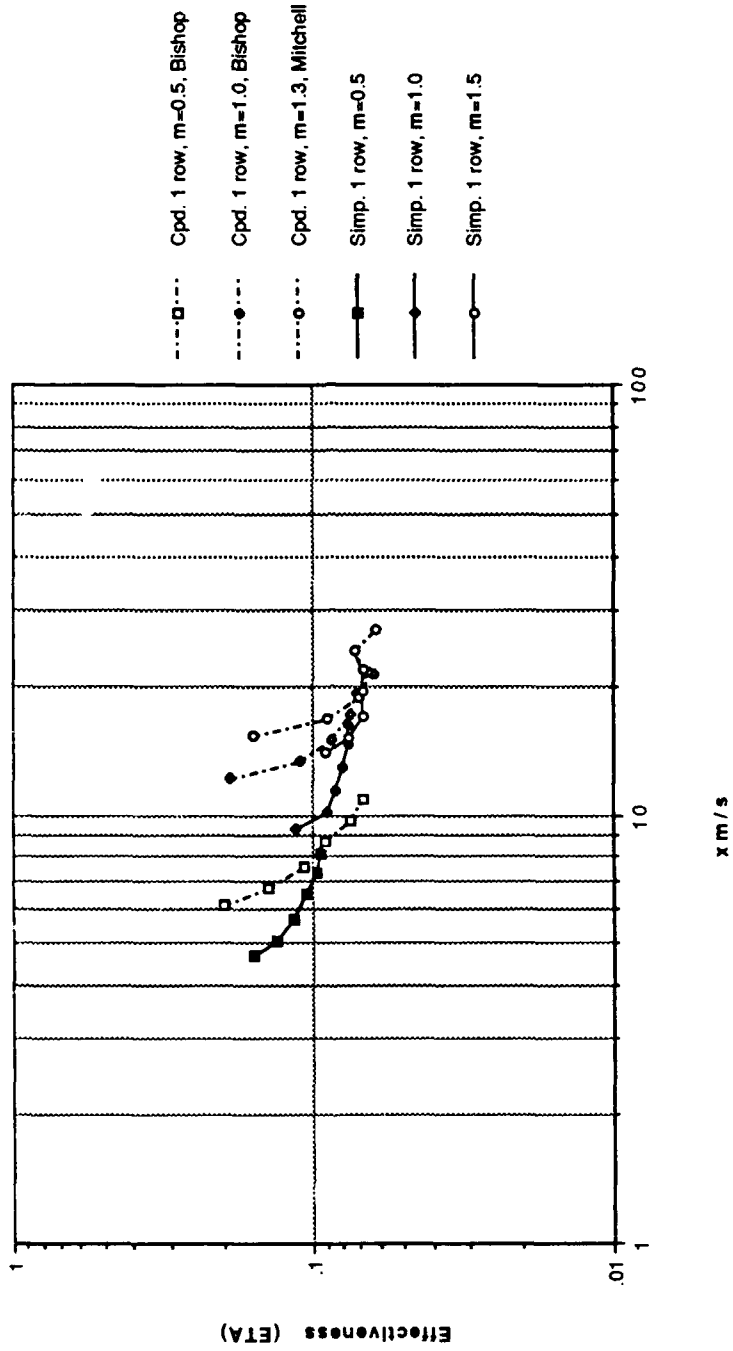


Figure 202 ETA vs xm/s , Compound Angle Injection System vs Simple Angle Injection System, 1 row.

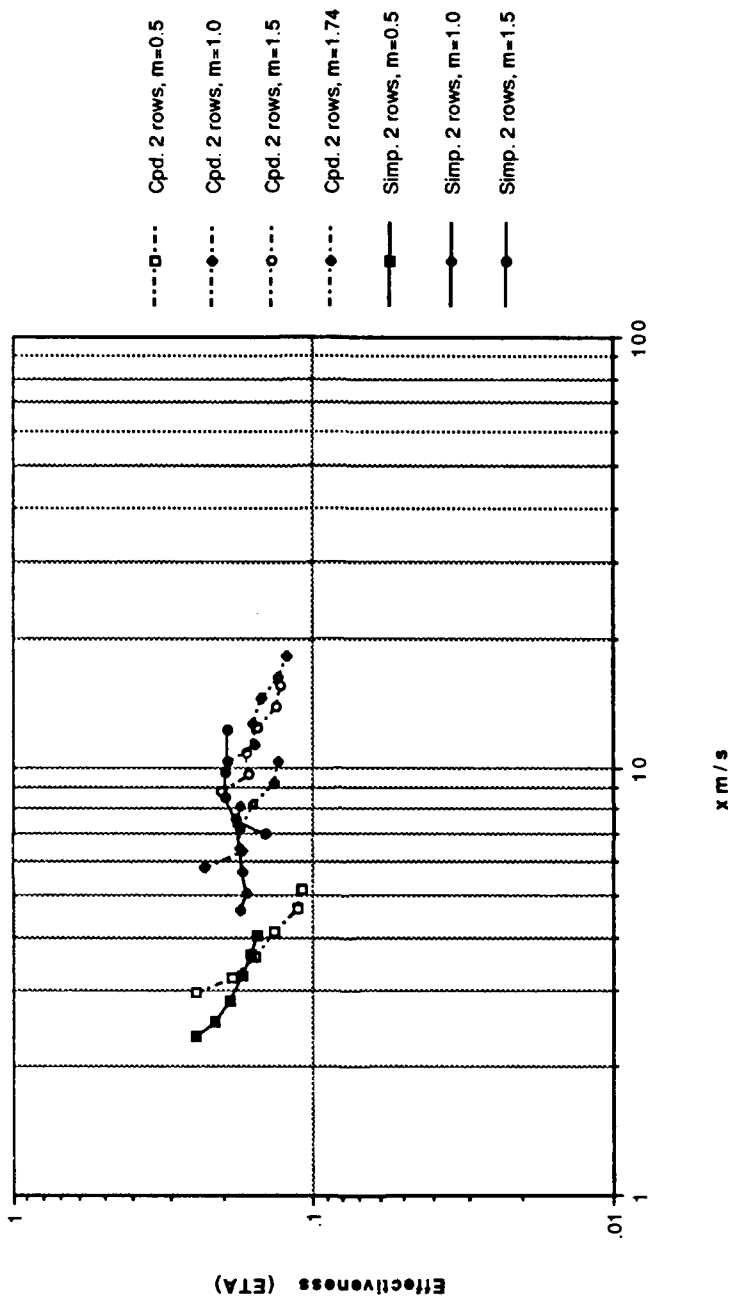


Figure 203 ETA vs xm/s, Compound Angle Injection System vs Simple Angle Injection System, 2 rows.

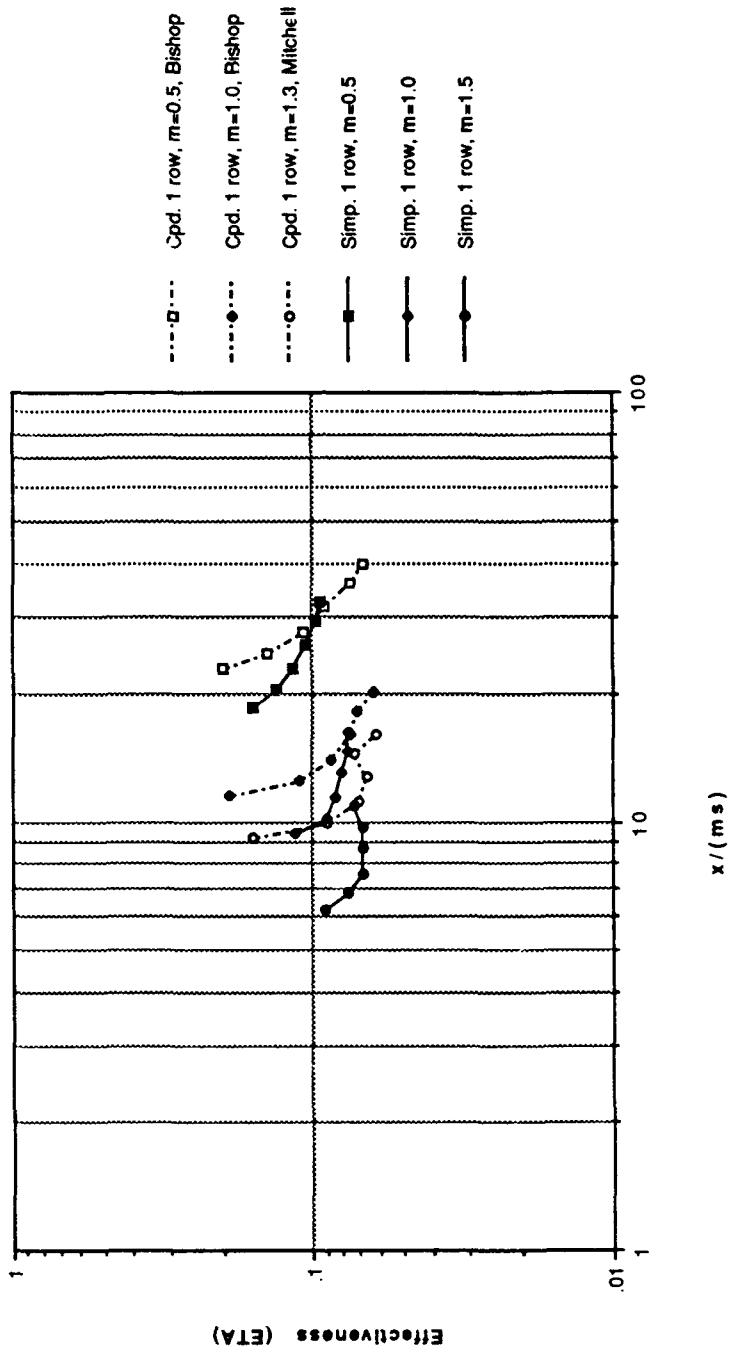


Figure 204 ETA vs x/(ms), Compound Angle Injection System vs Simple Angle Injection System, 1 row.

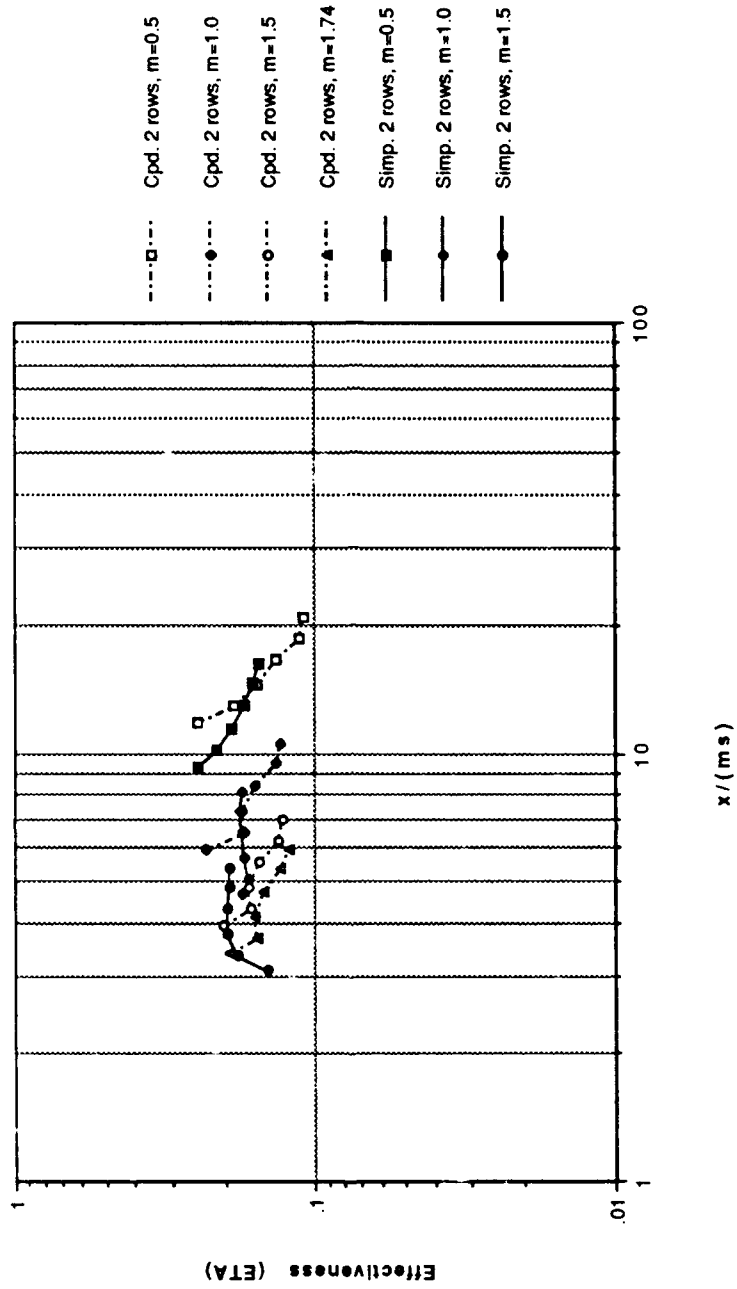


Figure 205 ETA vs x/(ms), Compound Angle Injection System vs Simple Angle Injection System, 2 rows.

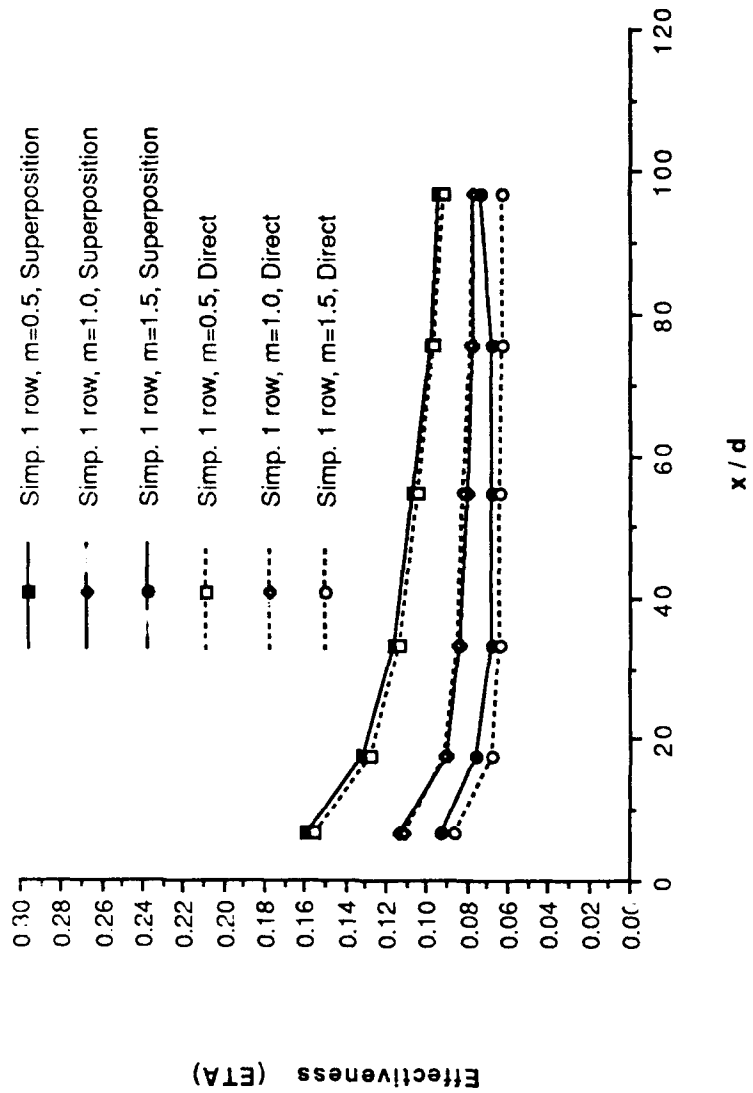


Figure 206. η vs x/d . Superposition vs. Direct Measurement.

APPENDIX B

UNCERTAINTY ANALYSIS

An uncertainty analysis, by Schwartz [Ref. 8], was accomplished on the input parameters and variables used for this study. A 95% confidence interval was utilized. Table I contains a summary of the parameters and their uncertainties :

TABLE I. EXPERIMENTAL UNCERTAINTIES FOR MEASURED QUANTITIES

<u>Quantity (units)</u>	<u>Typical Nominal Value</u>	<u>Experimental Uncertainty</u>
T_{∞} (°C)	18.0	0.13
T_w (°C)	40.0	0.21
P_{ambient} (mm Hg)	760	0.71
ρ_{∞} (kg/m ³)	1.23	0.009
U_{∞} (m/s)	10.0	0.06
C_p [J/(kg K)]	1006	1
$q_w A$ (W)	270	10.5
h [W/(m ² K)]	24.2	1.03
St	0.00196	0.000086
St/St_0	1.05	0.058
A (m ²)	0.558	0.0065
m	0.98	0.05
x/d	54.6	0.36

APPENDIX C

DATA ACQUISITION, PROCESSING AND PLOTTING PROGRAMS

1. Mean Velocity Survey Software :

FIVEHOLE1 : This program acquires pressure data from each of the five transducers associated with the probe. The FIVEHOLE1 program controls the MITAS motor controller which, in turn, controls the automatic traversing device on which the five hole probe is mounted. An 800 point pressure survey is conducted in the Y-Z plane normal to the freestream flow. Two data files, FIVx and FIVPx, are created. The FIVx data file consists of mean velocity, center port pressure, average pressure of the four peripheral ports, and the yaw and pitch coefficients for each of the 800 locations sampled. The FIVx data file consists of the pressures P1 through P5 sensed by each of the five pressure probe sensing ports, the average pressure of the four peripheral ports and the mean velocity, for each of the 800 survey locations.

PADJUST : This program accesses the FIVPx data file created by FIVEHOLE1 and adjusts the pressures to account for spatial resolution problems. *Pressure correction is performed using a curve fit to move the measurement location to the center sensing port location.* The output file of PADJUST is FIVxA.

VELOCITY : This program accesses FIVxA, the data file created by

PADJUST, and computes U_x , U_y and U_z velocity components. The output file of VELOCITY is V_x .

UX3 : This program accesses V_x , the data file created by VELOCITY, and plots streamwise velocity (U_x) contours of the Y-Z plane surveyed by the five hole pressure probe.

PTOT3 : This program accesses V_x , data file created by VELOCITY, and plots total pressure contours of the surveyed Y-Z plane.

2. Mean Temperature Survey Software :

ROVER1 : This program acquires flow temperature data from the "roving" thermocouple mounted on the automatic traversing device. The traversing device is controlled by the MITAS controller which is, in turn, controlled by this program. The output data file consists of differential temperatures ($T_{\text{Rover}} - T_{\infty}$) for each of the 800 survey locations in the Y-Z plane. The output file of ROVER1 is TEM_x .

PLTMP3 : This program uses the differential temperature data file TEM_x , created by ROVER1 and plots differential temperature contours of the surveyed Y-Z plane.

3. Heat Transfer Measurement Software (No Film Cooling) :

STANTON3 : This program acquires multiple channel thermocouple data for heat transfer measurements with no film cooling. It creates two output data files, TDATA and IDATA. The TDATA file consists of the 126 test plate thermocouple temperatures. The IDATA file records run number, test plate voltage and current, ambient pressure, pressure differential, ambient temperature, freestream velocity, air density and freestream temperature.

STANTON4 : STANTON4 accesses TDATA and IDATA files created by STANTON3 and calculates heat transfer coefficients and Stanton numbers for each of the 126 thermocouple locations. This program also calculates the average Reynolds number for each thermocouple row. STANTON4 creates three output files. These files are HDATA, SDATA, and STAV. The HDATA file consists of the local heat transfer coefficient, the Stanton number and the X and Z coordinates for each of the 126 test plate thermocouples. The SDATA file contains only the Stanton number values calculated for each thermocouple location. STAV contains the X location and the average Reynolds and Stanton numbers for each of the six thermocouple rows.

4. Heat Transfer Measurement Software (with Film Cooling) :

SETCONDV2: This program is used to set conditions for heat transfer data acquisition when film cooling is employed. SETCONDV2 determines injection velocity, Reynolds number, blowing ratio (m) and non-dimensional temperature (θ). It requires user input from the terminal of freestream conditions, rotometer percent flow and injection plenum differential pressure.

STANFC1B : This program is used when film cooling is employed to acquire multiple channel thermocouple data for heat transfer measurements. STANFC1B creates three data files : a temperature data file (Tx), a terminal input data file (Cx), and a film cooling data file (CFCx). The temperature data file consists of the 126 test plate thermocouple temperatures. The terminal input data file records the identical information contained in the IDATA file of STANTON3, as discussed earlier. The film cooling data file contains the injection rotometer percent flow and the injection plenum differential pressure.

STANFC2A : This program accesses the temperature, terminal input and film cooling data files created by STANFC1B. The program calculates Stanton number values for the 126 thermocouple locations and creates a single output file (FCx) containing these values.

EFFFC2B : This program is a modification of STANFC2A. This program accesses the temperature, terminal input and film cooling data files created by STANFC1B. In addition, it accesses an output file created by STANFC2A, (FCx), and directly calculates adiabatic effectiveness without power being applied to the test bed.

STANR1 : This program reads three Stanton number data files and creates a single output file containing two Stanton number ratios for each of the 126 thermocouple locations. The required input data files are : SDATA file created by STANTON4 containing baseline Stanton numbers for no film cooling and

two FCx data files created by STANFC2A containing Stanton numbers with film cooling. The output file of STANR1 is STRx.

FLMEFFV2 : This program processes Stanton number data and calculates the local and spanwise averaged film cooling effectiveness and iso-energetic Stanton number ratios. The program reads several files and creates two output files. The program reads the SDATA file created by STANTON4 which contains the baseline Stanton numbers for no film cooling, and up to six FCx, Tx and Cx files created by STANFC2A, and STANFC2B. One of the two output data files contains the local effectiveness and iso-energetic Stanton number ratios and the other output file contains the spanwise averaged effectiveness and iso-energetic Stanton number ratios.

3DSTGETA : This program accesses the files created by FLMEFFV2 and plots the spanwise variation of effectiveness in three-dimensional form.

3DSTGSTH : This program accesses the files created by FLMEFFV2 and plots the spanwise variation of the iso-energetic Stanton number ratio in three-dimensional form.

3DSTRST : This program accesses STRx, the Stanton number ratio file created by STANR1, and plots the spanwise variations of the Stanton number ratios in three-dimensional form.

APPENDIX D

DATA FILE DIRECTORY

1. Heat Transfer Data:

A. STANTON3 / STANTON4 data files -- (no film cooling) :

pTDATAxx ---- temperature data file
pIDATAxx ---- user terminal input data file
pHDATAxx ---- heat transfer coefficient data file
pSDATAxx ---- local Stanton number data file

<u>Data Run #</u>	<u>Data File</u>	<u>Experimental Conditions</u>
100490.1415	TDATA1 IDATA1 HDATA1 SDATA1	Compound Angle Tp-Tf=20.3 deg C no film-cooling
101390.1436	TDATA3 IDATA3 HDATA3 SDATA3	Compound Angle Tp-Tf=5.3 deg C no film cooling
121490.1027	2TDATA1 2IDATA1 2HDATA1 2SDATA1	Simple Angle Tp-Tf=19.8 deg C no film cooling
101390.1436	2TDATA9 2IDATA9 2HDATA9 2SDATA9	Simple Angle Tp-Tf=7.7 deg C no film cooling

B. STANFC1B / STANFC2A data files -- (film-cooling)

pTxx ---- temperature data file
 pCxx ---- user terminal input data file
 pCFCxx ---- film-cooling parameters data file
 pFCxx ---- local Stanton number data file

COMPOUND ANGLE, 2 ROWS

<u>Data Run #</u>	<u>Data File</u>	<u>Experimental Conditions</u>
102990.1434	T46 C46 CFC46 FC46	Compound Angle 2 rows, m=0.5, theta=0.02
102990.1600	T47 C47 CFC47 FC47	Compound Angle 2 rows, m=0.5, theta=0.81
102990.1730	T49 C49 CFC49 FC49	Compound Angle 2 rows, m=0.5, theta=1.09
102990.1848	T50 C50 CFC50 FC50	Compound Angle 2 rows, m=0.5, theta=1.26
103090.1233	T51 C51 CFC51 FC51	Compound Angle 2 rows, m=0.5, theta=2.67
103090.1507	T53	Compound Angle

	C53 CFC53 FC53	2 rows, $m=0.5$, $\theta=3.30$
100990.1552	T11 C11 CFC11 FC11	Compound Angle 2 rows, $m=1.0$, $\theta=0.54$
100990.1856	T16 C16 CFC16 FC16	Compound Angle 2 rows, $m=1.0$, $\theta=1.08$
100990.2018	T18 C18 CFC18 FC18	Compound Angle 2 rows, $m=1.0$, $\theta=1.44$
101090.1313	T21 C21 CFC21 FC21	Compound Angle 2 rows, $m=1.0$, $\theta=2.30$
100990.1607	T25 C25 CFC25 FC25	Compound Angle 2 rows, $m=1.0$, $\theta=3.0$
102290.1334	T28 C28 CFC28 FC28	Compound Angle 2 rows, $m=1.0$, $\theta=0.20$
102490.1429	T30 C30 CFC30 FC30	Compound Angle 2 rows, $m=1.5$, $\theta=0.52$

102490.1552	T32 C32 CFC32 FC32	Compound Angle 2 rows, $m=1.5$, $\theta=0.78$
102490.1804	T34 C34 CFC34 FC34	Compound Angle 2 rows, $m=1.5$, $\theta=1.00$
102590.1438	T40 C40 CFC40 FC40	Compound Angle 2 rows, $m=1.5$, $\theta=1.430$
102690.1227	T42 C42 CFC42 FC42	Compound Angle 2 rows, $m=1.5$, $\theta=2.54$
102690.1416	T44 C44 CFC44 FC44	Compound Angle 2 rows, $m=1.5$, $\theta=3.11$
103190.1143	T55 C55 CFC55 FC55	Compound Angle 2 rows, $m=1.74$, $\theta=1.36$
110190.1645	T57 C57 CFC57 FC57	Compound Angle 2 rows, $m=1.74$, $\theta=0.95$
110190.1857	T58 C58	Compound Angle 2 rows, $m=1.74$, $\theta=0.75$

	CFC58 FC58	
110190.2018	T59 C59 CFC59 FC59	Compound Angle 2 rows, $m=1.74$, $\theta=0.59$
110290.1206	T60 C60 CFC60 FC60	Compound Angle 2 rows, $m=1.74$, $\theta=3.43$
110290.1342	T61 C61 CFC61 FC61	Compound Angle 2 rows, $m=1.74$, $\theta=2.78$

SIMPLE ANGLE, 1 ROW

010491.1019	2T14 2C14 2CFC14 2FC14	Simple Angle 1 row, $m=0.5$, $\theta=-0.02$
010491.1242	2T15 2C15 2CFC15 2FC15	Simple Angle 1 row, $m=0.5$, $\theta=0.47$
010491.1436	2T16 2C16 2CFC16 2FC16	Simple Angle 1 row, $m=0.5$, $\theta=1.17$
010491.1556	2T17	Simple Angle

	2C17 2CFC17 2FC17	1 row, $m=0.5$, $\theta=1.48$
010491.1718	2T18 2C18 2CFC18 2FC18	Simple Angle 1 row, $m=0.5$, $\theta=3.12$
010491.1811	2T19 2C19 2CFC19 2FC19	Simple Angle 1 row, $m=0.5$, $\theta=2.53$
122090.1128	2T2 2C2 2CFC2 2FC2	Simple Angle 1 row, $m=1.0$, $\theta=0.36$
122090.1237	2T3 2C3 2CFC3 2FC3	Simple Angle 1 row, $m=1.0$, $\theta=0.72$
122090.140	2T4 2C4 2CFC4 2FC4	Simple Angle 1 row, $m=1.0$, $\theta=1.12$
122090.1601	2T5 2C5 2CFC5 2FC5	Simple Angle 1 row, $m=1.0$, $\theta=1.64$
122190.1506	2T6 2C6 2CFC6 2FC6	Simple Angle 1 row, $m=1.0$, $\theta=3.19$

122190.1624	2T7 2C7 2CFC7 2FC7	Simple Angle 1 row, m=1.0, theta=2.56
010291.1145	2T8 2C8 2CFC8 2FC8	Simple Angle 1 row, m=1.5, theta=0.09
010291.1304	2T9 2C9 2CFC9 2FC9	Simple Angle 1 row, m=1.5, theta=0.40
010291.1428	2T10 2C10 2CFC10 2FC10	Simple Angle 1 row, m=1.5, theta=1.15
010291.1508	2T11 2C11 2CFC11 2FC11	Simple Angle 1 row, m=1.5, theta=1.63
010291.1621	2T12 2C12 2CFC12 2FC12	Simple Angle 1 row, m=1.5, theta=3.40
010291.1658	2T13 2C13 2CFC13 2FC13	Simple Angle 1 row, m=1.5, theta=2.57

SIMPLE ANGLE, 2 ROWS

011191.1039	2T30 2C30 2CFC30 2FC30	Simple Angle 2 rows, $m=0.5$, $\theta=-0.05$
011191.1115	2T31 2C31 2CFC31 2FC31	Simple Angle 2 rows, $m=0.5$, $\theta=0.41$
011191.1209	2T32 2C32 2CFC32 2FC32	Simple Angle 2 rows, $m=0.5$, $\theta=1.09$
011191.1247	2T33 2C33 2CFC33 2FC33	Simple Angle 2 rows, $m=0.5$, $\theta=1.45$
011191.1419	2T34 2C34 2CFC34 2FC34	Simple Angle 2 rows, $m=0.5$, $\theta=2.90$
011191.1505	2T35 2C35 2CFC35 2FC35	Simple Angle 2 rows, $m=0.5$, $\theta=2.31$
011091.1103	2T24 2C24 2CFC24 2FC24	Simple Angle 2 rows, $m=1.0$, $\theta=0.18$
011091.1105	2T25	Simple Angle

	2C25 2CFC25 2FC25	2 rows, $m=1.0$, $\theta=0.53$
011091.1301	2T26 2C26 2CFC26 2FC26	Simple Angle 2 rows, $m=1.0$, $\theta=1.12$
011091.1413	2T27 2C27 2CFC27 2FC27	Simple Angle 2 rows, $m=1.0$, $\theta=1.50$
011091.1540	2T28 2C28 2CFC28 2FC28	Simple Angle 2 rows, $m=1.0$, $\theta=2.70$
011091.1619	2T29 2C29 2CFC29 2FC29	Simple Angle 2 rows, $m=1.0$, $\theta=3.10$
011591.1113	2T36 2C36 2CFC36 2FC36	Simple Angle 2 rows, $m=1.5$, $\theta=0.37$
011591.1154	2T37 2C37 2CFC37 2FC37	Simple Angle 2 rows, $m=1.5$, $\theta=0.71$
011591.1301	2T38 2C38 2CFC38 2FC38	Simple Angle 2 rows, $m=1.5$, $\theta=1.08$

011591.1411	2T39 2C39 2CFC39 2FC39	Simple Angle 2 rows, m=1.5, theta=1.57
011591.1453	2T40 2C40 2CFC40 2FC40	Simple Angle 2 rows, m=1.5, theta=3.00
011591.1542	2T41 2C41 2CFC41 2FC41	Simple Angle 2 rows, m=1.5, theta=2.43

C. FILM EFFECTIVENESS DATA

Generating Program : FLMEFFV2

pFCxx ---- local effectiveness data file
 pSPAxx ---- spanwise average effectiveness data file

COMPOUND ANGLE, 2 ROWS

<u>Data Run #</u>	<u>Data File</u>	<u>Experimental Conditions</u>
102990.1434	FEFF5	Compound Angle.
102990.1600	SPA5	2 rows, m=0.5
102990.1730		
102990.1848		
103090.1233		
103090.1507		

100990.1552	FEFF2	Compound Angle
100990.1856	SPA2	2 rows, m=1.0
100990.2018		
101090.1313		
101090.1607		
102290.1344		

102490.1429	FEFF4	Compound Angle
102490.1552	SPA4	2 rows, m=1.5
102490.1804		
102590.1938		
102590.1227		
102690.1416		

103190.1143	FEFF6	Compound Angle
110190.1645	SPA6	2 rows, m=1.74
110190.1857		
110190.2018		
110290.1206		
110290.1342		

SIMPLE ANGLE 1 ROW

010491.1019	2FEFF3	Simple Angle
010491.1247	2SPA3	1 row, m=0.5
010491.1436		
010491.1556		
010491.1718		
010491.1811		

122090.1128	2FEFF1	Simple Angle
122090.1237	2SPA1	1 row, m=1.0
122090.1401		
122090.1601		
122190.1506		
122190.1624		

010291.1145	2FEFF2	Simple Angle
010291.1304	2SPA2	1 row, m=1.5
010291.1428		
010291.1508		
010291.1621		
010291.1658		

SIMPLE ANGLE 2 ROWS

011191.1039	2FEFF4	Simple Angle
011191.1115	2SPA4	2 rows, m=0.5
011191.1209		
011191.1247		
011191.1419		
011191.1505		

011091.1103	2FEFF5	Simple Angle
011091.1205	2SPA5	2 rows, m=1.0
011091.1301		
011091.1413		
011091.1540		
011091.1619		

011591.11	2FEFF6	Simple Angle
011591.1154	2SPA6	2 rows, m=1.5
011591.1301		
011591.1411		
011591.1453		
011591.1542		

D. FILM EFFECTIVENESS DATA FROM DIRECT MEASUREMENT

Generating Program : EFFF2B

pNFCxx ---- local effectiveness data file

SIMPLE ANGLE, 1 ROW

<u>Data Run #</u>	<u>Data File</u>	<u>Experimental Conditions</u>
010791.1636	2NFC20B	1 row, m=0.5
021391.1719	2NFC44B	1 row, m=1.0
010891.0821	2NFC22B	1 row, m=1.5

E. STANTON NUMBER RATIO FILES

Generating Program : STANR1

pSTRxx ---- Film-coolig data file

COMPOUND ANGLE, 2 ROWS

<u>Data Run #</u>	<u>Data File</u>	<u>Experimental Conditions</u>
102990.1848	STR1	2 rows, m=0.5, theta=1.26
100990.2018	STR2	2 rows, m=1.0, theta=1.44
102590.1438	STR3	2 rows, m=1.5, theta=1.43
103190.1143	STR4	2 rows, m=1.74, theta=1.36

SIMPLE ANGLE, 1 ROW

<u>Data Run #</u>	<u>Data File</u>	<u>Experimental Conditions</u>
010491.1556	2STR3	1 row, m=0.5, theta=1.48
122090.1601	2STR1	1 row, m=1.0, theta=1.64
010291.1508	2STR2	1 row, m=1.5, theta=1.63

SIMPLE ANGLE, 2 ROWS

<u>Data Run #</u>	<u>Data File</u>	<u>Experimental Conditions</u>
011191.1247	2STR5	2 rows, m=0.5, theta=1.45
011091.1413	2STR4	2 rows, m=1.0, theta=1.50
011591.1411	2STR6	2 rows, m=1.5, theta=1.57

F. MEAN VELOCITY DATA :

COMPOUND ANGLE, 2 ROWS

<u>Data Run #</u>	<u>Data File</u>	<u>Generating Program</u>	<u>Experimental Conditions</u>
112590.0905	FIV2 FIVP2 FIV2A V2	FIVEHOLE1 FIVEHOLE1 PADJUST VELOCITY	2 rows, m=1.0 x/d = 9.4
112090.0900	FIV1 FIVP1 FIV1A V1	FIVEHOLE1 FIVEHOLE1 PADJUST VELOCITY	2 rows, m=1.0 x/d = 43.7
111590.1400	FIV0 FIVP0 FIV0A V0	FIVEHOLE1 FIVEHOLE1 PADJUST VELOCITY	2 rows, m=1.0 x/d = 85.2

SIMPLE ANGLE, 1 ROW

<u>Data Run #</u>	<u>Data File</u>	<u>Generating Program</u>	<u>Experimental Conditions</u>
011491.0844	2FIV7 2FIVP7 2FIV7A 2V7	FIVEHOLE1 FIVEHOLE1 PADJUST VELOCITY	1 row, m=0.5 x/d = 9.4

011291.0831	2FIV5 2FIVP5 2FIV5A 2V5	FIVEHOLE1 FIVEHOLE1 PADJUST VELOCITY	1 row, m=0.5 x/d = 43.7
010991.1106	2FIV3 2FIVP3 2FIV3A 2V3	FIVEHOLE1 FIVEHOLE1 PADJUST VELOCITY	1 row, m=0.5 x/d = 85.2
122390.1646	2FIV2 2FIVP2 2FIV2A 2V2	FIVEHOLE1 FIVEHOLE1 PADJUST VELOCITY	1 row, m=1.0 x/d = 9.4
122290.1815	2FIV1 2FIVP1 2FIV1A 2V1	FIVEHOLE1 FIVEHOLE1 PADJUST VELOCITY	1 row, m=1.0 x/d = 43.7
122290.0655	2FIV0 2FIVP0 2FIV0A 2V0	FIVEHOLE1 FIVEHOLE1 PADJUST VELOCITY	1 row, m=1.0 x/d = 85.2
011691.0737	2FIV8 2FIVP8 2FIV8A 2V8	FIVEHOLE1 FIVEHOLE1 PADJUST VELOCITY	1 row, m=1.5 x/d = 9.4
011291.1922	2FIV6 2FIVP6 2FIV6A 2V6	FIVEHOLE1 FIVEHOLE1 PADJUST VELOCITY	1 row, m=1.5 x/d = 43.7
010991.2125	2FIV4 2FIVP4	FIVEHOLE1 FIVEHOLE1	1 row, m=1.5 x/d = 85.2

2FIV4A PADJUST
2V4 VELOCITY

SIMPLE ANGLE, 2 ROWS

<u>Data Run #</u>	<u>Data File</u>	<u>Generating Program</u>	<u>Experimental Conditions</u>
011891.0734	2FIV9 2FIVP9 2FIV9A 2V9	FIVEHOLE1 FIVEHOLE1 PADJUST VELOCITY	2 rows, m=0.5 x/d = 9.4
012091.0857	2FIV12 2FIVP12 2FIV12A 2V12	FIVEHOLE1 FIVEHOLE1 PADJUST VELOCITY	2 rows, m=0.5 x/d = 43.7
012291.1632	2FIV15 2FIVP15 2FIV15A 2V15	FIVEHOLE1 FIVEHOLE1 PADJUST VELOCITY	2 rows, m=0.5 x/d = 85.2
011891.1838	2FIV10 2FIVP10 2FIV10A 2V10	FIVEHOLE1 FIVEHOLE1 PADJUST VELOCITY	2 rows, m=1.0 x/d = 9.4
012091.1924	2FIV13 2FIVP13 2FIV13A 2V13	FIVEHOLE1 FIVEHOLE1 PADJUST VELOCITY	2 rows, m=1.0 x/d = 43.7
012391.1758	2FIV16 2FIVP16 2FIV16A 2V16	FIVEHOLE1 FIVEHOLE1 PADJUST VELOCITY	2 rows, m=1.0 x/d = 85.2

011991.0735	2FIV11 2FIVP11 2FIV11A 2V11	FIVEHOLE1 FIVEHOLE1 PADJUST VELOCITY	2 rows, m=1.5 x/d = 9.4
012191.0808	2FIV14 2FIVP14 2FIV14A 2V14	FIVEHOLE1 FIVEHOLE1 PADJUST VELOCITY	2 rows, m=1.5 x/d = 43.7
012491.0821	2FIV17 2FIVP17 2FIV17A 2V17	FIVEHOLE1 FIVEHOLE1 PADJUST VELOCITY	2 rows, m=1.5 x/d = 85.2

G. Mean Temperature Survey Data :

Generating Program : ROVER1

COMPOUND ANGLE

<u>Data Run #</u>	<u>Data File</u>	<u>Experimental Conditions</u>
120590.1535	TEM0	2 rows, m=1.0, x/d=9.4
120590.1535	TEM1	2 rows, m=1.0, x/d=43.7
120690.1045	TEM2	2 rows, m=1.0, x/d=85.2

SIMPLE ANGLE, 1 ROW

<u>Data Run #</u>	<u>Data File</u>	<u>Experimental Conditions</u>
-------------------	------------------	--------------------------------

120590.1535	2TEM5	1 row, m=0.5, x/d=9.4
120590.1535	2TEM4	1 row, m=0.5, x/d=43.7
120690.1045	2TEM3	1 row, m=0.5, x/d=85.2
120590.1535	2TEM0	1 row, m=1.0, x/d=9.4
120590.1535	2TEM1	1 row, m=1.0, x/d=43.7
120690.1045	2TEM2	1 row, m=1.0, x/d=85.2
120590.1535	2TEM6	1 row, m=1.5, x/d=9.4
120590.1535	2TEM7	1 row, m=1.5, x/d=43.7
120690.1045	2TEM8	1 row, m=1.5, x/d=85.2

SIMPLE ANGLE, 2 ROW

<u>Data Run #</u>	<u>Data File</u>	<u>Experimental Conditions</u>
012691.0943	2TEM11	2 rows, m=0.5, x/d=9.4
012591.1211	2TEM10	2 rows, m=0.5, x/d=43.7
012591.0807	2TEM9	2 rows, m=0.5, x/d=85.2
012691.1425	2TEM12	2 rows, m=1.0, x/d=9.4
012691.1033	2TEM13	2 rows, m=1.0, x/d=43.7
012791.1505	2TEM14	2 rows, m=1.0, x/d=85.2
012991.1125	2TEM17	2 rows, m=1.5, x/d=9.4
012891.1542	2TEM16	2 rows, m=1.5, x/d=43.7
012891.1125	2TEM15	2 rows, m=1.5, x/d=85.2

REFERENCES

1. Metzger, D.E., Carper, H.J. and Swank, L.R., "Heat Transfer with Film Cooling Near Nontangential Injection Slots", *Journal of Engineering for Power*, pp. 157-163, April 1968.
2. Ortiz, A., *The Thermal Behavior of Film Cooled Turbulent Boundary Layers as Affected by Longitudinal Vortices*, M.E. Thesis, Naval Postgraduate School, Monterey, California, September 1987.
3. Ligrani, P. M., Ortiz, A., Joseph, S. L. and Evans, D.L., "Effects of Embedded Vortices on Film-Cooled Turbulent Boundary Layers", ASME-88-GT-170, ASME Gas Turbine and Aeroengine Congress and Exposition, Amsterdam, The Netherlands, June 1988, also *ASME Transactions -- Journal of Turbomachinery*, Vol. 111, pp. 71-77, 1989.
4. Williams, W., *Effects of an Embedded Vortex on a Single Film-Cooling Jet in a Turbulent Boundary Layer*, M.S. Thesis, Naval Postgraduate School, Monterey, California, June 1988.
5. Craig, D. W., *Effect of Vortex Circulation on Injectant from a Single Film-Cooling Hole in a Turbulent Boundary Layer*, M.S. Thesis, Naval Postgraduate School, Monterey, California, June 1989.
6. Bishop, D., *Heat Transfer, Adiabatic Effectiveness and Injectant Distributions Downstream of Single and Double Rows of Film Cooling Holes with Compound Angles*, M.S. Thesis, Naval Postgraduate School, Monterey, California, September 1990.
7. Mitchell, S., *The Effects of Embedded Longitudinal Vortices on Heat Transfer in a Turbulent Boundary Layer with Film Cooling from Holes with Compound Angles*, M.S. Thesis, Naval Postgraduate School, Monterey, California, September 1990.
8. Schwartz, G. E., *Control of Embedded Vortices Using Wall Jets*, M.S. Thesis, Naval Postgraduate School, Monterey, California, September 1988.
9. Joseph, S. L., *The Effects of an Embedded Vortex on a Film-Cooled Turbulent Boundary Layer*, M.E. Thesis, Naval Postgraduate School, Monterey, California, December 1986.

10. Kays, W. M. and Crawford, M. E., *Convective Heat and Mass Transfer*, Second Edition, p. 216, McGraw-Hill Book Company, 1980.
11. Mick, W. J. and Mayle, R. E., "Stagnation Film Cooling and Heat Transfer, Including Its Effects Within the Hole Pattern", *ASME Transactions -- Journal of Turbomachinery*, Vol. 110, pp. 66-72, 1988.

INITIAL DISTRIBUTION LIST

- | | | |
|----|--|---|
| 1. | Defense Technical Information Center
Cameron Station
Alexandria, Virginia 22304-6145 | 2 |
| 2. | Library, Code 52
Naval Postgraduate School
Monterey, California 93943-5002 | 2 |
| 3. | Professor P. M. Ligrani, Code MELi
Department of Mechanical Engineering
Naval Postgraduate School
Monterey, California 93943-5000 | |
| . | Department Chairman, Code ME
Department of Mechanical Engineering
Naval Postgraduate School
Monterey, California 93943-5000 | 1 |
| 5. | Dr. Bill Troha
Components Branch
Turbine Engine Division
Aero Propulsion Laboratory
Department of the Air Force
Air Force Wright Aeronautical Laboratories
Wright-Patterson Air Force Base, Ohio 45433 | 4 |
| 6. | Naval Engineering Curricular Officer, Code 34
Department of Mechanical Engineering
Naval Postgraduate School
Monterey, California 93943-5000 | 1 |
| 7. | Professor C. S. Subramanian, Code MESu
Department of Mechanical Engineering
Naval Postgraduate School
Monterey, California 93943-5000 | 1 |
| 8. | LT. Salvatore Ciriello, Jr.
RR#1 Hilltop Drive
North Salem, New York 10560 | 1 |